The Organic-Metal Interface

Design of an Inverse Photoemission Spectrometer for the Investigation of the Energy Level Alignment and the Electronic Structure

Von der Fakultät für Mathematik, Informatik und Naturwissenschaften der RWTH Aachen University zur Erlangung des akademischen Grades einer Doktorin der Naturwissenschaften genehmigte Dissertation

vorgelegt von
Diplom-Physikerin
Carolin Claudia Jacobi
aus Fulda

Berichter: Univ.-Prof. Dr. rer. nat. Matthias Wuttig
Univ.-Prof. Dr. rer. nat. Joachim Mayer

Tag der mündlichen Prüfung: 03.03.2017

Diese Dissertation ist auf den Internetseiten der Universitätsbibliothek online verfügbar.

‘So eine Arbeit wird eigentlich nie fertig,
man muss sie für fertig erklären,
wenn man nach Zeit und
Umständen das Möglichste getan hat.’
Johann Wolfgang von Goethe,
Italienische Reise II, Neapel,
Caserta, 16. März 1787

Abstract

The development of organic-based devices has received considerable interest over the past few years and has led to commercial products that are, nowadays, indispensable in daily live. In the course of device design, organic-metal as well as organic-organic interfaces play crucial roles for charge injection and transport in these devices. In order to further improve the device performance, their electronic structure, chemical properties, and electrical behaviour must be fully characterised and understood. The present work is embedded in this context with a special focus on the organic-metal interface. Four distinct topics are addressed:

(I) First an inverse photoemission spectrometer was constructed and successfully put into operation in the course of the thesis presented. Inverse photoemission spectroscopy (IPES) enables investigation of the unoccupied part of the density of states. Thus, combining it with ultra-violet photoelectron spectroscopy (UPS) the complete density of states can be probed. During preparation of the thesis presented, both methods have been applied in order to study the frontier electronic states of noble metal and organic surfaces.

(II) A discussion on the electronic structure of the metallic substrates builds the groundwork in order to understand the effects occurring at the organic-metal interface. Since the electronic states of noble metal surfaces are well-known, the presented data serve, furthermore, as prove that the IPE spectrometer is properly working and obtains reliable results.

(III) Before the focus is put on the organic-metal interface, also the electronic structures of bulk-like thin films are discussed. In this context, a combined UPS/IPES study was applied to the molecule of interest namely N,N'-dimethyl-3,4,9,10-perylene dicarboximide (DiMe-PTCDI or PTCDI-C_1). Its electronic structure is compared to the measured electronic states of its core molecule perylene and to two perylene derivatives – 3,4,9,10-perylene-tetracarboxylic acid dianhydride (PTCDA) and N,N'-dioctyl-3,4,9,10-perylene dicarboximide (PTCDI-C_8). The obtained results reveal that due to the high-lying LUMO of perylene with respect to Fermi level E_F, there is a large injection barrier for electrons from metal electrodes. As a consequence, perylene shows mainly p-type electrical transport. Furthermore, it is presented that substitution of perylene with electron-withdrawing anhydride or imide groups significantly lowers the molecular orbitals with respect to the vacuum level. Here, the impact on the electron affinity is much stronger than on the ionisation energy. Thus, PTCDA as well as DiMe-PTCDI and PTCDI-C_8 possess a low-lying LUMO with respect to E_F resulting

in an n-type behaviour of these molecules. The replacement of the oxygen atom in the anhydride group of PTCDA by the less polar methylimide group in the case of DiMe-PTCDI leads to a small increase in energy of the molecular orbitals with respect to the vacuum level. This results in a slightly smaller electron affinity as well as in a decreased ionisation energy in the case of DiMe-PTCDI. The lengthening of the alkyl chain, when going from DiMe-PTCDI (PTCDI-C_1) to PTCDI-C_8, has only a minor impact on the electronic structure.

(IV) Last but not least, the effects occurring at the interface between DiMe-PTCDI and the noble metals silver and copper is studied regarding its chemical and electronic interaction. Therefore, additionally to UPS and IPES measurements also X-ray photoelectron spectroscopy (XPS) is applied. Furthermore, the growth behaviour of the DiMe-PTCDI molecules on the respective substrate is investigated with atomic force microscopy (AFM). On silver, DiMe-PTCDI shows Volmer-Weber growth. Furthermore, a strong chemisorption between the DiMe-PTCDI molecules and the underlying silver substrate is observed. This strong chemical interaction leads to the formation of a covalent bond between the molecule and its substrate. The formation of the covalent bond, in turn, results in a filling of the LUMO of the isolated molecule and thus becomes the HOMO of the thin film. For DiMe-PTCDI grown on copper, Volmer-Weber growth and LUMO filling is also observed. However, XPS measurements reveal a weaker chemical interaction in comparison to DiMe-PTCDI grown on silver. While in the latter case the whole functional group – the oxygen and nitrogen atoms – contributes to the interaction with the substrate, for DiMe-PTCDI grown on copper a chemical interaction with the underlying substrate is only observed for the nitrogen atoms.

Kurzfassung

Deutsche Übersetzung des Originaltitels:

"Die Organik-Metall Grenzfläche –
Design eines inversen Photoemissionsspektrometers zur Untersuchung des Energieniveauausgleichs und der elektronischen Struktur"

In den letzten Jahren, rief die Entwicklung (opto-)elektronischer Bauteile, welche sich die Eigenschaften organischer Halbleiter zu Nutze machen, großes wissenschaftliches Interesse hervor. Diese Entwicklung hat heutzutage zu kommerziell erhältlichen Produkten geführt, die aus dem Alltag nicht mehr wegzudenken sind. Im Zuge der Bauteilkonzeption spielen Organik-Metall und Organik-Organik Grenzflächen bei der Ladungsinjektion und dem Transport in diesen Geräten eine entscheidende Rolle. Um die Geräteleistung weiter verbessern zu können, müssen die elektronische Struktur, die chemischen Eigenschaften und das elektrische Verhalten dieser Grenzflächen vollständig charakterisiert und verstanden werden. Die vorliegende Arbeit gliedert sich in diesen Kontext ein. Dabei liegt der besondere Fokus auf der Organik-Metall Grenzfläche. Es werden vier verschiedene Themen behandelt:

(I) Zunächst wurde im Rahmen der vorliegenden Arbeit ein inverses Photoemissionsspektrometer konstruiert und erfolgreich in Betrieb genommen. Die inverse Photoemissionsspektroskopie (IPES) ermöglicht die Untersuchung des unbesetzten Teils der Zustandsdichte. Somit kann in Kombination mit der ultravioletten Photoelektronspektroskopie (UPS) die komplette Zustandsdichte des zu untersuchenden Materials vermessen werden. Während der Vorbereitung der vorliegenden Arbeit wurden diese beide Methoden (UPS/IPES) angewandt, um die elektronischen Zustände an der Grenzfläche zwischen Edelmetallen und organischen Halbleitern zu untersuchen.

(II) Eine Diskussion über die elektronische Struktur der metallischen Substrate bildet die Grundlage, um die an der Organik-Metall Grenzfläche auftretenden Effekte besser zu verstehen. Die vorgestellten Daten dienen ferner als Nachweis, dass mit Hilfe des IPE-Spektrometers verlässliche und belastbare Ergebnisse erzielt werden können.

(III) Vor der Fokussierung auf die Grenzfläche zwischen dem organischen Halbleiter und der Metalloberfläche wird die elektronische Struktur von organischen Dünnfilmen, welche Bulk-Eigenschaften besitzen, diskutiert. In diesem Zusammenhang wurde eine UPS-/IPES-Studie

an dem Molekül N,N'-dimethyl-3,4,9,10-perylene dicarboximide (DiMe-PTCDI oder PTCDI-C_1), auf dem das Hauptaugenmerk der vorgelegten Arbeit liegt, durchgeführt. Des Weiteren werden die Ergebnisse mit den elektronischen Zuständen des Kernmoleküls Perylen und mit zwei Perylenderivaten – 3,4,9,10-perylene-tetracarboxylic acid dianhydride (PTCDA) und N,N'-dioctyl-3,4,9,10-perylene dicarboximide (PTCDI-C_8) –, welche ebenfalls im Rahmen der Arbeit vermessen wurden, verglichen. Die erhaltenen Ergebnisse offenbaren, dass Perylen aufgrund der hohen Position des LUMOs relativ zum Fermi Niveau E_F eine hohe Injektionsbarriere für Elektronen aufweist. Als Folge weist Perylen hauptsächlich p-Typ-Transport auf. Weiterhin ist gezeigt, dass die Substitution von Perylen mit einer elektronenanziehenden Anhydrid- oder Imidgruppe die molekularen Orbitale in Bezug auf das Vakuumniveau signifikant senkt. Hierbei ist der Einfluss auf die Elektronenaffinität viel stärker als auf die Ionisationsenergie. Somit besitzen sowohl PTCDA als auch DiMe-PTCDI und PTCDI-C_8 relativ zu E_F ein niedrig liegendes LUMO, was zu n-Typ-Verhalten der Moleküle führt. Der Austausch des Sauerstoffatoms in der Anhydridgruppe von PTCDA durch die weniger polare Methylimidgruppe im Falle von DiMe-PTCDI führt zu einer geringen Erhöhung der Molekülorbitale in Bezug auf das Vakuumniveau. Aus diesem Grund weist DiMe-PTCDI eine geringfügig kleinere Elektronenaffinität sowie eine verringerte Ionisierungsenergie auf. Die Verlängerung der Alkylkette im Vergleich von DiMe-PTCDI (PTCDI-C_1) mit PTCDI-C_8 hat hingegen nur einen sehr geringen Einfluss auf die elektronische Struktur.

(IV) Zu guter Letzt werden die Effekte, welche an der Grenzfläche zwischen DiMe-PTCDI und den Edelmetallen Silber und Kupfer auftretenden, bezüglich ihrer chemischen und elektronischen Wechselwirkungen diskutiert. Daher wurde für diese Untersuchung zusätzlich zu den UPS- und IPES-Messungen auch Röntgen-Photoelektronspektroskopie (XPS) eingesetzt. Weiterhin wurde das Wachstumsverhalten der DiMe-PTCDI Moleküle auf dem jeweiligen Substrat mit Rasterkraftmikroskopie (AFM) untersucht. Auf Silber zeigt DiMe-PTCDI Volmer-Weber-Wachstum. Ferner wird eine starke Chemisorption zwischen den DiMe-PTCDI Molekülen und dem darunter liegenden Silbersubstrat beobachtet. Diese starke chemische Wechselwirkung bewirkt die Bildung einer kovalenten Bindung zwischen dem Molekül und dem Substrat. Die Bildung der kovalenten Bindung wiederum führt zum Auffüllen des LUMOs des isolierten Moleküls, welches somit zum HOMO des Dünnfilms wird. Für das auf Kupfer gewachsene DiMe-PTCDI werden ebenfalls Volmer-Weber-Wachstum und das Auffüllen des LUMOs beobachtet. Allerdings offenbaren die Ergebnisse der XPS-Messungen eine schwächere chemische Wechselwirkung im Vergleich zu dem auf Silber gewachsenem DiMe-PTCDI. Während im letzteren Fall die ganze funktionelle Gruppe – die Sauerstoff- und Stickstoffatome – zur Wechselwirkung mit dem Substrat beiträgt, wird für DiMe-PTCDI auf Kupfer eine chemische Wechselwirkung mit dem darunterliegenden Substrat nur für die Stickstoffatome beobachtet.

List of Symbols

a	Radius of the anode of the gaseous ionisation detector
$\vec{A}$	Magnetic vector potential
α	Fine structure constant, $\alpha = e^2/\hbar c = 1/137$, or polarisation angle
$a^+_{\vec{q},\alpha}$ and $a_{\vec{q},\alpha}$	Operators that create or annihilate a photon in the state $(\vec{q}, \alpha)$, respectively
b	Radius of the cathode of the gaseous ionisation detector
$\beta(E)$	Probability of a non-radiative decay of the electron into its final state caused by inelastic electron-electron interactions
C	Capacitance
c_i	Probability of an electron coupling into an unoccupied electronic state i
c	Speed of light in vacuum, $c = 299792458\,\mathrm{m/s}$
d_CA	Distance between the cathode of the electron gun to its anode
ΔE_IPES	Total experimental resolution of the IPE spectrometer
ΔE_kin	Resolution of the kinetic energy of the electron beam
$\Delta k_{\|\|}$	Momentum resolution in the direction of $\vec{k}_{\|\|}$
$\Delta\Theta$	Angular resolution, or beam divergence of the electron beam provided by the electron gun
$\mathrm{d}\Omega$	Solid angle
d_window	Shortest distance between the window face and the photon bandpass detector

$(\mathrm{d}\sigma/\mathrm{d}\Omega)_{\mathrm{IPE}}$, $(\mathrm{d}\sigma/\mathrm{d}\Omega)_{\mathrm{PE}}$	Change in cross-section per steradian of a photon or electron, respectively
EA	Electron affinity
E_{B}	Binding energy
E_{cutoff}	Energetic position of the secondary electron cutoff
E_{EE}	Electron energy
E_{F}	Fermi level or Fermi energy
E_{f}	Energy of the final state
E_{i}	Energy of the initial state
E_{kin}	Kinetic energy
e	Elementary charge, $e = 1.60 \cdot 10^{-19}\,\mathrm{C}$
E_n	Binding energy of a surface state
E_{opt}	Optical band gap
$\hat{\epsilon}^{(\alpha)}$	Linear polarisation vector whose direction depends on the propagation vector $\vec{q}$
E_{t}	Transport band gap
E_{Vac}	Vacuum level or vacuum energy
h	Planck constant, $h = 4.14 \cdot 10^{-15}\,\mathrm{eVs}$
$\hbar$	Reduced Planck constant, $\hbar = h/2\pi = 6.58 \cdot 10^{-16}\,\mathrm{eVs}$
H'	Hamiltonian describing the interaction between a photon and an electron
$\hbar\omega$	Energy of a photon or particle with angular frequency ω
I_{E}	Emission current of the electron gun
IE	Ionisations energy
I_{ES}	Source current of the electron gun
I_{S}	Sample current
I_{SCL}	Emission current of the electron gun operated in the space charge limited region
I_{TL}	Emission current of the electron gun operated in the temperature limited region
J_{SCL}	Emission current density of the electron gun operated in the space charge limited region

J_{TL}	Emission current density of the electron gun operated in the temperature limited region
k_{B}	Boltzmann constant, $k_{\mathrm{B}} = 8.62 \cdot 10^{-5}\,\mathrm{eV/K}$
$\vec{k}$	Wave vector of an electron
$\vec{k}_{\mathrm{f}}$	Wave vector of an electron in the final state
$\vec{k}_{\mathrm{i}}$	Wave vector of an electron in the initial state
$\vec{k}_{\|\|}$	Parallel component of the wave vector $\vec{k}$
$\vec{k}_{\perp}$	Perpendicular component of the wave vector $\vec{k}$
l	Angular momentum of the continuum electron, or length
λ	Inelastic mean free path of electrons
L_{coll}	Mean free path between two molecular collisions
λ_e	Electron wavelength
λ_{i}	Lonization path, i.e. the distance in field direction the electron has to travel to gain enough energy between two successive ionizations within the photon bandpass detector
λ_{m}	Mean free path of an electron
λ_p	Photon wavelengths
m_{e}	Electron rest mass, $m_{\mathrm{e}} = 9.11 \cdot 10^{-31}\,\mathrm{kg}$
$\overline{N}$	Averaged, normalised count rate
$\sqrt{\overline{N}}$	Square root of the averaged, normalised count rate $\overline{N}$
ω	Angular frequency
$\Omega_{\mathrm{detection}}$	Solid angle of photon detection
Φ	Work function
p_{GM}	Total pressure of the gas mixture filled into a Geiger-Müller counter
Φ_{C}, Φ_{B}	Phase changes occurring upon reflection at a crystal surface (index C) and a barrier potential (index B), respectively

Φ_{EC}	Work function of the cathode of the electron gun
$\vec{p}_{\mathrm{f,i}}$	Momentum matrix element between initial and final states
p_{Prop}	Total pressure of the acetone gas filled into a proportional counter
$\Psi_{\mathrm{f}}(\vec{r})$	IPE final state of the electron by emitting a photon with the wave vector $\vec{q}$
$\Psi_{\mathrm{fe}}(\vec{r})$	PE final state of the emitted electron
$\Psi_{\mathrm{i}}(\vec{r})$	IPE initial state comprised of a free electron
$\Psi_{\mathrm{occ}}(\vec{r})$	PE initial state of an electron in an occupied level after the absorption of an incoming photon with the wave vector $\vec{q}$
$\vec{q}$	Wave vector of a photon
r	Radial distance
r_{C}	Critical radius at which gas multiplication begins
r_{A}	Radius of the aperture of the anode of the electron gun
r_{C}, r_{B}	Real parts of the reflection coefficients related to a reflection at a crystal surface (index C) and a barrier potential (index B), respectively
$\rho_{\mathrm{photon}}(E)$, $\rho_{\mathrm{electron}}(E)$	Photon or electron density of states of the energy E, respectively
r_{window}	Radius of the window of the photon bandpass detector
σ_{exp}	Experimental standard deviation
σ_{el}	Variance of the electron energy distribution
σ_{opt}	Variance of the optical bandpass of the detector
σ_{tot}	Variance of the total energy resolution of the IPE spectrometer
T	Temperature
τ	Time constant, $\tau = RC$
t_{C}	Charge collection time
T_{ES}	Temperature of the cathode of the electron gun
Θ	Angle of incidence

t_{ml}	Monolayer formation time
Θ_{n}	Number of monolayers
U	Voltage
u	Change of the applied voltage within the gaseous ionisation detector
U_{detector}	High voltage applied between the two electrodes of the gaseous ionisation detector
U_{T}	Threshold voltage at which gas multiplication begins
U_{trigger}	Discrimation level of the counting device in the radiation detector
U_{A}	Voltage applied to the 1^{st} anode
U_{d}	Difference between the voltage applied to the cathode of the electron gun and its anode voltage
U_{SV}	Starting voltage of the photon bandpass detector, at which the first counts can be measured
U_{EE}	Voltage applied in order to accelerated or decelerated the electrons to their final energy $E_{\mathrm{EE}} = e \cdot U_{\mathrm{EE}}$
U_{F}	Voltage applied to the focus
U_{G}	Voltage applied to the grid
U_{OP}	Operation voltage of the photon bandpass detector
U_{ES}	Voltage applied to the cathode/source
U_{XD}	Voltage applied to the X-direction deflection plate
U_{YD}	Voltage applied to the Y-direction deflection plate
V_{p}, V_{e}	Photon's or electron's normalisation volume
W_{IPE}, W_{PE}	Transition rate of IPE or PE, respectively

Contents

Abstract iii

Kurzfassung v

List of Symbols vii

1 Introduction 1

I An Introduction to Direct and Inverse Photoemission Spectroscopy

2 Photoelectron Spectroscopy 11
2.1 Aspects of Photoemission Theory 12
2.2 Experimental Setup 16

3 Inverse Photoemission Spectroscopy 19
3.1 Theoretical Considerations 21
3.2 Energetics in IPES 24
3.3 Angle-Resolved IPES 26
3.4 Surface States 29
3.5 Technical Requirements 35

II The Inverse Photoemission Spectrometer

4 Design of the IPE Spectrometer 43
4.1 Sample Handling Chamber 44
4.2 Analysis Chamber for the Inverse Photoemission Spectrometer 48

5 Characterisation of the IPE Spectrometer 57
5.1 Characterisation of the Electron Gun 57
5.2 Characterisation of the Photon Bandpass Detector 64

5.3 Apparatus Function and Total Energy Resolution 87

III The Interface between Metals and Organic Semiconductors

6 Electronic Structure of Noble Metals 93

7 Electronic Structure of Organic Semiconductors - Bulk-like Thin Films 103
7.1 The Electronic Structure of Aromatic Molecules 103
7.2 Perylene and Perylene Derivatives – An Example: DiMe-PTCDI 107
7.3 Perylene and Perylene Derivatives – A Comparison 111
7.4 Summary 115

8 Interface Formation between DiMe-PTCDI Molecules and a Noble Metal Surface 117
8.1 The Interface between DiMe-PTCDI and Silver 118
8.2 The Interface between DiMe-PTCDI and Copper 133

IV Conclusion

9 Summary and Outlook 143

V Appendix

A Supporting Information on the Gaseous Radiation Detector . III

B Supporting Information on the Crystal and Electronic Structure of Noble Metal Surfaces V

C Supporting Information on the Electronic Structure of Organic Semiconductors - Bulk-like Thin Films a Comparison IX

D Supporting Information on the Interface Formation between DiMe-PTCDI Molecules and Silver XIII

E Supporting Information on the Interface Formation between DiMe-PTCDI Molecules and Copper XV

List of Acronyms XIX

List of Figures XXI

List of Tables XXV

Bibliography XXVII

Acknowledgments LI

1. Introduction

Since fundamental properties like electroluminescence or photoconductivity have been discovered in organic semiconductors in the middle of the 20th century [1, 2], organic optoelectronic devices have gained considerable interest over the last decades: in 1986, the first two-layered organic photovoltaic cell (OPVC) was developed by *Ching W. Tang* [3]. Only one year later, also the first organic light-emitting diode (OLED) and the first organic thin-film transistor (OTFT) were presented [4, 5]. Then, in the year 2000, the growing research on new conductive molecular materials has been honoured with the Nobel Prize for *Alan Jay Heeger*, *Alan Graham MacDiarmid* and *Hideki Shirakawa* 'for their discovery of electrically conductive polymers' [6].

Nowadays, organic optoelectronic devices are indispensable in daily live. OLEDs, for example, are being found in mobile phones, 'wearables', digital cameras, virtual reality (VR) headsets, tablets, laptops and TVs for almost ten years now. The advantage of organic semiconductors such as low cost, flexibility, stretchability, reliability, good environmental credentials, etc. thereby allows to think of future applications like flexible screens for electronic newspapers or mobile phones [7, 8]. It has been suggested that Samsung may release its first bendable smartphone in the year 2017 [9–11].
Especially, the OLED display sector is counted among the fastest growing ones in the world [12]. IDTechEx forecasts a growth of the total market for printed, flexible and organic electronics from USD26.54 billion in 2016 to USD69.03 billion in 2026. Therein, the majority will be achieved in OLED display technology with USD57 billion followed by OLED lighting with USD2.2 billion in 2026 [13–15].

An OLED consists of one or several thin organic layers, which serve as emission layer (green part of Figure 1.1). The total organic layer thickness is in the order of tens to hundreds nanometres. Two electrodes, of which at least one is transparent in the visible range for the out-coupling of light, sandwich the emission layer. In order to run an OLED, the device has to be biased. Consequently, an electric current is implemented through the emission layer leading to the aforementioned phenomenon of electroluminescence. The working principle of an OLED is illustrated in Figure 1.1: electrons (-) and holes (+) are injected at the interface between their respective inorganic contact electrode and the organic layer. Thereafter, they traverse the emission layer (green part) until they recombine and form an exciton (black ellipse). The localised exciton is formed by the coupling of an electron-hole pair. By emitting a photon, this exciton decays. The contacts, i.e. anode and cathode, are depicted by their high

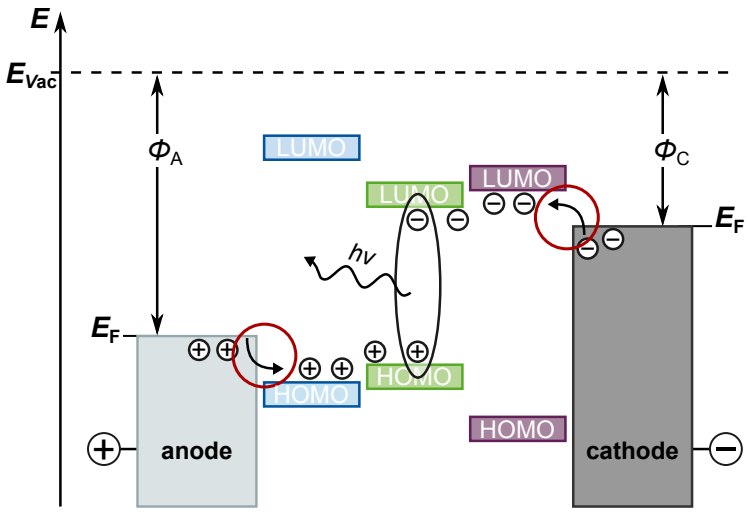

Figure 1.1 | Working principle of an OLED stack: commonly, holes and electrons are injected from the anode and cathode, respectively. Thereafter, they are transported to the middle layer (green part), where they recombine and form an exciton (black ellipse). By emitting a photon, this exciton decays. The contacts, i.e. anode and cathode, are depicted by their work function Φ_A and Φ_C, respectively. In order to ensure an effective charge transfer into the frontier molecular levels (highest occupied molecular orbital (HOMO) and lowest unoccupied molecular orbital (LUMO)), the energy level alignment at the interfaces (red circles) is critical. Frequently, several layers (blue and violet parts) of different organic semiconductors are used in order to separate charge injection and transport from the region of exciton formation and recombination. Hence, this multilayer concept requires an optimisation of the energy level alignment not only at the organic-metal, but also at the organic-organic interface. All energy levels are referenced to the vacuum level E_{Vac}. (This picture is reprinted from [16] with kind permission.)

and low work functions Φ_A and Φ_C, respectively.

In order to ensure an effective charge transfer into the frontier molecular levels and, thereby to minimise the operation voltage, the energy level alignment (ELA) at the interfaces between the inorganic contact electrode and the organic layer (exemplarily marked by the red circles) is very critical. As mentioned before, an OLED consists commonly of more than one organic layer, which are exemplarily represented by the blue and violet coloured rectangles. These additional layers are required to separate the region of charge injection and transport from that of exciton formation and recombination [17]: by the design of such organic heterojunctions, it is ensured that one charge carrier is transported across the interface, while at the same time the opposite charge is blocked. This multilayer concept requires optimisation of the energy level alignment not only at the organic-metal, but also at the organic-organic interfaces. Besides the interfaces discussed above, an interference is occurring from the fact that the emission layer is positioned within a cavity resonator. This resonator consists of the electrodes, which act as mirrors, and the internal organic dielectric layers [18]. Therefore, this interface also has to be optimised in order to ensure an effective charge transport. Summarising, the function and the efficiency of organic optoelectronic devices critically depend on the electronic structure at the interfaces within these devices [17, 19, 20]. Thus, understanding the energy level alignment and the underlying effects, which are discussed in more detail

below, is one key issue when thinking of further improving these devices.

The study of the electronic structure at interfaces, especially at the organic-metal interface, is also interesting from a fundamental point of view [21]. Here, two different scientific fields – solid-state physics and molecular science – have to be matched: on the one hand, in metals, the atoms are metallically bound while delocalised electrons are distributed over the whole crystal [22]; on the other hand, molecules exhibit strong intramolecular covalent bonds, too, but the intermolecular bonds are commonly formed by weak van der Waals bonds [23]. Furthermore, in $\pi-$conjugated[1] molecules, which are in the focus of the study in the thesis presented, the electrons are delocalised within each molecule, but the energy bands are just weakly dispersive [21]. Consequently, the electrons are distributed over not more than the adjacent molecules and are often assumed as being strongly localised at the molecule.

In order to characterise the interface energetics, most commonly the position of the Fermi level E_F of the electrode, the highest occupied molecular orbital (HOMO) and the lowest unoccupied molecular orbital (LUMO) are investigated [17]. HOMO and LUMO are the frontier orbitals of organic semiconductors. In addition, the energetic difference between E_F and HOMO defines the hole injection barrier (HIB), while the energy between E_F and LUMO gives the electron injection barrier (EIB). Their energetic difference defines the transport gap, which is an important parameter for device applications and is discussed in the course of this thesis.

During the last years, the research group at the I. Institute of Physics (IA) of the RWTH Aachen University has gained a deep understanding of interface effects, which can occur at an organic-metal interface. Meanwhile, questions about how to tailor the work function alignment in order to gain a better charge injection and questions about a universal work function modification could successfully be answered [16, 24]. So far, these studies were based on direct photoelectron spectroscopy (PES). Consequently, the impact on the electron injection barrier forced by a surface modification could only be measured indirectly up to now. Furthermore, the precise position of the LUMO stayed completely unknown, which made statements about the energy level alignment in device applications quite difficult. Thus, the need of a spectrometer that is able to measure the unoccupied density of states had become essential.

> *Therefore, an inverse photoemission (IPE) spectrometer was newly constructed and set up into operation within the scope of the thesis presented.*

Inverse photoemission spectroscopy (IPES) is one of the most powerful techniques to obtain information on the density of unoccupied electronic states above the Fermi level [17, 25, 26]. This technique can be seen as complementary to the well-established direct photoelectron spectroscopy which mainly probes occupied states below the Fermi level. The principle of photoelectron spectroscopy is shortly introduced in Chapter 2 in the first part of the thesis presented. In IPES, a beam of electrons with the kinetic energy E_kin is directed onto a sample. These electrons couple to high lying unoccupied electronic states. Thereafter, they decay

[1] The term conjugation is used as a description of delocalised π-electron systems.

either radiatively or non-radiatively into low-lying unoccupied states. If the decay is radiative, the emitted photons are detected and an energy spectrum of the unoccupied density of electronic states is recorded. Thus, results obtained with inverse photoemission spectroscopy allow to immediately track the electron injection barrier of the organic thin film and provide an overall view on the electronic structure of the interface investigated if combined with PES. The density of unoccupied states can also be probed with other spectroscopies like x-ray absorption near-edge structure (XANES), near-edge x-ray absorption (NEXAFS) or two-photon spectroscopy (2PPE). In comparison to the first two methods, the major advantage of IPES and 2PPE is the capability of angle-resolved photoemission in order to completely characterise electronic states in energy and momentum space [27, 28]. However, while, 2PPE shows a higher energetic resolution, it only covers a small part of the Brillouin zone due to the low photon energy which is used for such an experiment. In contrast, IPES allows for studying the dispersion of unoccupied states with sufficient accuracy for the entire Brillouin zone. Nevertheless, the energetic resolution of IPES is smaller than that of PES or 2PPE by one to two orders of magnitude [29]. This is mainly caused by the cross section of IPES being several orders of magnitude lower in IPES compared to that of the photoemission of an electron [25, 27, 29]. Consequently, energy resolution and signal intensity must be compromised in the design of an IPE spectrometer.
In this context, a detailed overview of both the theoretical and experimental aspects of the IPE technique are given in Chapter 3. Part II comprises the design of the spectrometer as well as the experimental characterisation. Especially, the experimental aspects given in Chapter 3 are essential to understand the various design choices outlined in Chapter 4, in which the spectrometer and its components are described. In Chapter 5, the experimental characteristics of the electron gun and the photon detector as well as the apparatus function and the total energy resolution of the spectrometer itself are discussed. Therein, also general aspects of the photon detector are summarised, which are helpful to understand the behaviour of this detector type.

The third part of the thesis presented deals with the electronic structure of noble metals as well as the organic molecule perylene and its derivatives. Therein, the focus is placed on the energy level alignment at organic-metal interfaces and the underlying effects. But before discussing about interface effects at organic-metal interfaces, the electronic structure of the metal substrates has to be well-understood.

> *Therefore, the electronic structure of the noble metals Gold and copper was investigated by applying ultraviolet photoelectron spectroscopy (UPS) and also inverse photoemission spectroscopy (IPES).*

The results are analysed in Chapter 6. Since the electronic structure of noble metals is already well-understood in literature, this chapter also serves as *prove that IPE spectrometer built in the course of this thesis is properly working and obtains reliable results*.

As stated before, the energy level alignments (ELAs) of HOMO and LUMO at the interface with respect to the substrate Fermi level are one of the key factors for the device performance in the field of organic electronics [30–34]. Simply speaking, when a molecule is brought in

contact to a metal surface, the Fermi level of the metal is required to lie within the band gap between HOMO and LUMO of the organic semiconductor and, thus, the energy levels have to align. Over the past several decades a great deal of work has been devoted in order to gain a deeper understanding of the processes determining the ELA at such an interfaces. In order to describe the limiting cases of this alignment mechanism, the two simplest models, which are commonly applied, are:

i The Schottky-Mott limit: when the organic molecules are brought in contact with the substrate, no charge transfer occurs across the organic-metal interface before reaching equilibrium. Then, the vacuum levels directly match and all energy levels simply align without any shift [34].

ii The Fermi-level pinning: in this case, charge carriers spontaneously begin to flow from the organic material at the interface into the metal substrate. As this flow continues, an interfacial dipole is formed that down-shifts or up-shifts the vacuum level. As a consequence, one edge of the frontier molecular orbitals (MOs) or a newly formed charge transfer (CT) states is pinned relative to the energetic position of the Fermi level of the metal [34].

Furthermore, a few more mechanisms can also play an important role in the alignment process like the electron 'push-back' effect[2] [30, 34, 35], the formation of interface dipoles [30, 37, 38], the chemical interaction between the substrate and the adsorbate [39, 40], the adsorption-induced change of the molecular geometry [41–45] and surface-induced aromatic stabilisation (SIAS) [32, 46, 47].
Nowadays, it is well accepted that the ELA is not only controlled by the work function Φ_{metal} of the metal substrate and the electron affinity (EA) and the ionisation energy (IE) each of the organic molecule. The order and the arrangement of molecules on the metal surface also critically affect the ELA as well as the flexibility of the molecular skeleton and the chemical structure of the molecule [46, 48, 49].

But before investigating the ELA at organic-metal interfaces, the question arises:

> *How does a change of the functional group influence the electronic structure in general way?*

To answer this, the electronic structure of bulk-like thin films of perylene and its derivatives 3,4,9,10-perylene-tetracarboxylic acid dianhydride (PTCDA), N,N'-dimethyl-3,4,9,10-perylene dicarboximide (DiMe-PTCDI or PTCDI-C_1) and N,N'-dioctyl-3,4,9,10-perylene dicarboximide (PTCDI-C_8) were investigated by applying ultraviolet photoelectron spectroscopy and inverse photoemission spectroscopy. The chemical structure of these molecules is shown in Figure 1.2. An answer on an additional question about *the influence of the chain length on the electronic structure* can be given by comparing DiMe-PTCDI and PTCDI-C_8. The results are presented and discussed in Chapter 7.

[2] Regardless of potential charge transfer or dipole formation, the adsorption of organic molecules on metals is always accompanied by a reduction of the work function of the metal substrate. This is caused by a quantum mechanical phenomenon referred to Pauli repulsion between electrons of the same spin [34–36].

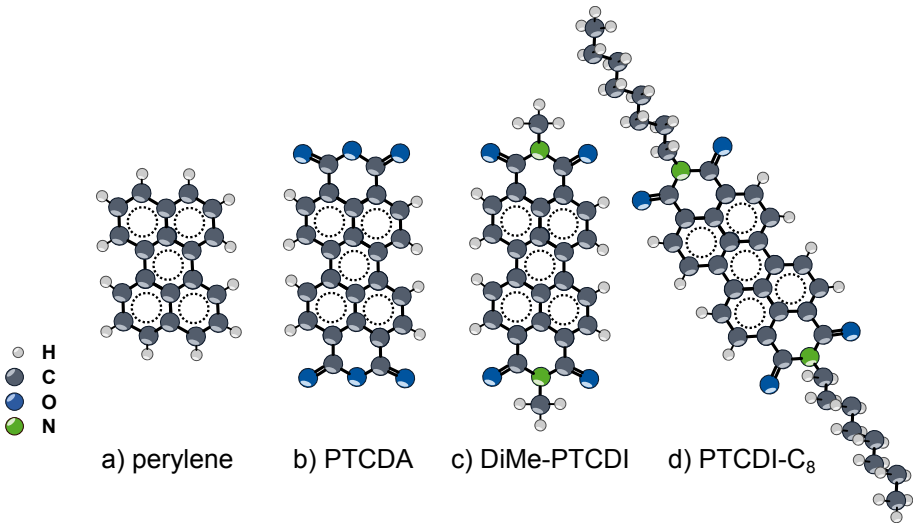

Figure 1.2 | Chemical structures of the perylene derivatives PTCDA, DiMe-PTCDI and PTCDI-C_8:
(a) The perylene molecule, which is very well-studied, belongs to the polynuclear aromatic hydrocarbons (PAH). It is an organic p-type semiconductor [50], which is applied in transistor devices [51]. In addition, it is also utilised as blue-emitting dopant material in OLEDs [52].
(b) The molecule 3,4,9,10-perylene-tetracarboxylic acid dianhydride (PTCDA) is one of the most intensively studied organic semiconductors. Its structure is based on a perylene core, to which two electron withdrawing anhydride side groups are added. PTCDA is thermally stable and very pure. Well-ordered thin films can easily be grown by organic molecular beam deposition (OMBD) on various inorganic substrates.
(c) The molecule N,N'-dimethyl-3,4,9,10-perylene dicarboximide (DiMe-PTCDI) is very similar to PTCDA, but the bridging oxygen atom of the anhydride group is replaced by a methylimide (N-CH_3) group. It is used as a pigment in industry [53]. Moreover, it is a promising n-type material for OPVCs and OFETs [54–56].
(d) Like DiMe-PTCDI, N,N'-dioctyl-3,4,9,10-perylene dicarboximide (PTCDI-C_8) is also a promising n-type material for the utilisation in OPVCs and OFETs [57–59]. It consists of two alkyl chains with 8 carbon atoms each, which are substituted to the imide group attached to the perylene core.

PTCDA is one of the most intensively studied molecules and serves as a prototype molecule in the context of ELA in the current thesis [41, 60–64]. It features a perylene core substituted with two electron withdrawing anhydride side groups (O=C–O–C=O).
The class of N,N'-substituted perylene-3,4,9,10-perylene dicarboximides (PTCDIs) are promising n-type molecules, which have already been successfully implemented in OFETs and OPVs [54–59]. Like PTCDA, they are exhibiting a perylene core, but each anhydride side groups is replaced by an imide group (O=C–N–C=O). Although the promising properties of the PTCDIs are deeply studied in the context of device application, a detailed study about the interface energetics at PTCDI-metal contact interfaces has not been published. However, knowledge on the interface effects arising when a PTCDI molecule is brought in contact with a metal is crucial for further device studies. Hence, answering the following questions is part of the current thesis:

> *How do the energy levels of DiMe-PTCDI, which is the molecule of focus in the thesis presented, align at the DiMe-PTCDI-metal interface? Which interface effects*

can explain the observed alignment?

In this context, the electronic structure of DiMe-PTCDI grown on silver and copper thin films is investigated as a function of the thin film thickness of the organic layer: in order to gain information on the energetic position of the frontier MOs, ultraviolet photoelectron spectroscopy and also inverse photoemission spectroscopy have been applied. This combination of complementary techniques has not been employed before in the discussed context of DiMe-PTCDI-metal interfaces. Additionally, x-ray photoelectron spectroscopy (XPS) has been utilised in order to monitor possible consequences of the interface effects on the chemical structure of the organic adsorbates. The results are presented and discussed in Chapter 8.

An Introduction to Direct and Inverse Photoemission Spectroscopy

2. Photoelectron Spectroscopy

Photoelectron spectroscopy (PES) performed with UV (UPS) or with X-ray photons (XPS) is the technique of high significance for the investigation of the electronic and chemical structure of materials [26]. Thus, in combination with its complementary method inverse photoemission spectroscopy (IPES) introduced in the next chapter, PES is the key technique utilised in this thesis in order to analyse and understand the chemical and electronic properties of solid surfaces.

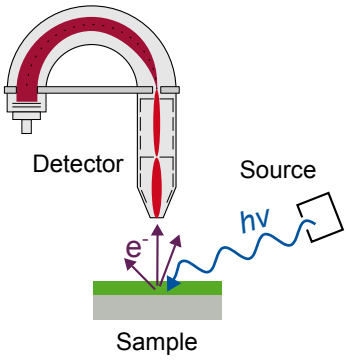

Figure 2.1 | Schematic illustration of a PES experiment: mono-energetic light (blue), which is provided by either a gas-discharge lamp, an X-ray tube or a synchrotron-radiation source, impinges on a sample surface (green) in order to excite the electrons into vacuum (violet). These photoelectrons are then analysed with respect to their kinetic energy and their momentum in an electron-energy analyser.

Photoelectron spectroscopy is based on the well-known photoelectric effect, which was first observed by *H. Hertz* in 1887 and theoretically explained by *A. Einstein* in 1905 [65, 66]: a sample, gas or the surface of a solid, is irradiated by monochromatic photons, which are provided by either a gas-discharge lamp, an X-ray tube or a synchrotron-radiation source (see Figure 2.1). These photons excite electrons from occupied states into empty states. If the energy of the photon is sufficient to release an electron into vacuum, the kinetic energy of the photoelectron can be detected by an electron-energy analyser. Thereby, the kinetic energy E_{kin} is given by

$$E_{\mathrm{kin}} = h\nu - E_{\mathrm{B}} - \Phi, \tag{2.1}$$

where the binding energy E_{B} of the electron refers to the Fermi level E_{F}. Furthermore, a minimum energy barrier Φ has to be overcome in order to liberate the electron into the vacuum. It is also known as work function of a surface.

In this chapter, first the theoretical aspects of photoelectron spectroscopy are briefly explained. The discussion of the underlying mechanisms is based the textbooks 'Photoelectron Spectroscopy' written by *S. Hüfner* [67] and 'Solid surfaces, interfaces and thin films' by *H. Lüth* [26], to which the interested reader is referred for a detailed description. The second section of this chapter then concentrates on the experimental setup.

2.1. Aspects of Photoemission Theory

Basic Principle

Figure 2.2 illustrates the energetic processes in a photoelectron measurement. In the left part, a schematic energy-level diagram of a metal is shown, while, the energy distribution of the photoemitted electrons is sketched on the right side. The solid sample features core levels as well as a valence band. The Fermi energy E_F is located in the valence band and has an energy spacing of Φ to the vacuum level E_Vac.
Empty states, which are located in the crystal above the vacuum level, are populated via optical excitation with photons of a fixed energy $\hbar\omega$. After leaving the surface, the electrons have an energy of

$$E_\mathrm{kin} = \hbar\omega - E_\mathrm{i} - \Phi, \tag{2.2}$$

where E_i is the binding energy of the initial state and Φ represents the work function, which has to be overcome by electrons in order to reach the vacuum states. The corresponding energy distribution of the photoexcited electrons is measured outside of the sample. It yields an image of the distribution of the occupied crystal states – valence and core level states depending on the value of $\hbar\omega$. In the PES experiment, the measured distribution of sharp peaks is superimposed by a background originating from electrons that have lost quasi-continuous amounts of E_kin due to scattering processes in the crystal (not illustrated in Figure 2.2). This background is called secondary electron background (see also 'The 'Three-Step Model' of PES' - 'Second step' on the following pages).

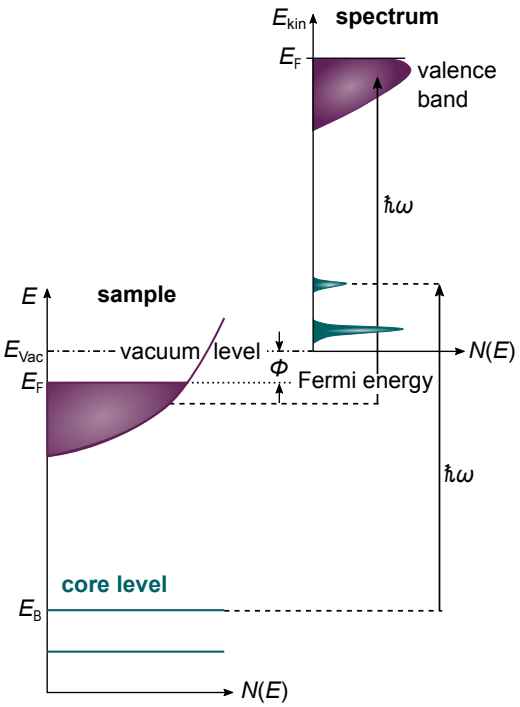

Figure 2.2 | Illustration of the energetic processes in a photoelectron measurement: monoenergetic photons impinge on the sample with an energy of $\hbar\omega$. They excite electrons into unoccupied quasi-continuous electron states within the crystal. These electrons can migrate to the surface, where they are transmitted into vacuum. Thereafter, they are detected in the photoelectron measurement as free electrons with a kinetic energy E_kin. Thus, the abscissa for the photoelectrons is E_kin with its zero at the vacuum level E_Vac of the sample ($E_\mathrm{kin} = \hbar\omega - |E_\mathrm{B}| - \Phi$). However, the binding energy E_B of the electrons is of greater interest, so that the spectra are usually plotted against this measure.

The 'Three-Step Model' of PES

In principle, a full quantum-mechanical approach with a 'one-step process' is required in order to describe the photoelectron process correctly. Therein, the electron is accurately described by a Bloch wave that decays inside the solid, but moves freely in vacuum [66, 68, 69]. Another approach, which is the less accurate, but simpler and more instructive, is the commonly used 'three-step model' [70, 71]. In spite of being purely phenomenological, it has been proven to successfully explain the fundamental principles of photoemission by dividing the complete process into three parts:

i. Optical excitation of an electron from an initial into a final electronic state within the solid.

ii. Transport of the excited electron to the surface of the solid.

iii. Emission of the electron from the solid into the vacuum. Thereby, the electron traverses the surface.

First step

In the first step, *Fermi*'s golden rule expresses the transition probability W for optical excitation of an electron from an initial to a final Bloch state, $\left|i,\vec{k}\right\rangle$ and $\left\langle f,\vec{k}\right|$, respectively:

$$W_{\mathrm{fi}} = \frac{2\pi}{\hbar}\left|\left\langle f,\vec{k}\right|\mathcal{H}\left|i,\vec{k}\right\rangle\right|^2 \delta\left(E_{\mathrm{f}}\left(\vec{k}\right) - E_{\mathrm{i}}\left(\vec{k}\right) - \hbar\omega\right) \tag{2.3}$$

$$= \frac{2\pi}{\hbar} m_{\mathrm{fi}} \delta\left(E_{\mathrm{f}} - E_{\mathrm{i}} - \hbar\omega\right). \tag{2.4}$$

Here, the δ-function involves the energy conservation for the excitation of an electron from an initial state E_{i} into the final state E_{f} of the electronic band structure. In a first approximation, only direct transitions with a nearly unchanged wave vector $\vec{k}$ are considered. Furthermore, the perturbation operator $\mathcal{H}$ of the matrix element m_{fi} is given by the momentum operator $\vec{p}$ and the vector potential $\vec{A}$ of the incident electromagnetic wave in the dipole approximation:

$$\mathcal{H} = \frac{e}{2m_{\mathrm{e}}}\left(\vec{A}\cdot\vec{p} + \vec{p}\cdot\vec{A}\right) \cong \frac{e}{m}\left(\vec{A}\cdot\vec{p}\right). \tag{2.5}$$

Outside of the solid, only electrons with E_{kin} larger than the vacuum energy $E_{\mathrm{Vac}} = E_{\mathrm{F}} + \Phi$ as well as a final state $\vec{k}$-vector pointing outwards from the surface ($k_\perp > 0$) can be detected. In the case of $k_\perp > 0$, the internal electron current density, which is directed towards the surface with an energy E_{kin} and a wave vector around $\vec{k}$, is given by

$$I^{\mathrm{int}}\left(E_{\mathrm{kin}}, \hbar\omega, \vec{k}\right) \propto \sum_{\mathrm{fi}} m_{\mathrm{fi}} \mathrm{f}(E_{\mathrm{i}}) \delta\left(E_{\mathrm{f}} - E_{\mathrm{i}} - \hbar\omega\right) \delta\left(E_{\mathrm{kin}} - E_{\mathrm{f}}\left(\vec{k}\right)\right). \tag{2.6}$$

In order to detect the energy E_{kin} involving the adjustment of the energy window of the electron detector, the energy $E_{\mathrm{f}}\left(\vec{k}\right)$ of the final state has to equal E_{kin}. The Fermi function,

which ensures that the initial state E_i is occupied, is denoted by $\mathrm{f}(E_\mathrm{i})$.

Second step

In the 'three-step' model, the second step comprises the propagation of the electrons, which are described by Equation (2.6), to the surface. During this propagation, some electrons lose a part of their energy E_f via inelastic scattering with electrons or plasmons. These electrons have lost the information about their initial electronic level E_i. They contribute to the continuous background found in a photoelectron spectrum, which is called secondary electron background. The amount of secondary electrons is influenced by many parameters such as crystallinity of the solid material, surface roughness, temperature (i.e. phonon scattering), contamination of the surface, material species and more.
The probability of an electron reaching the surface without undergoing inelastic scattering is given by the inelastic mean free path λ (IMPF). The IMFP depends on the electrons kinetic energy E_kin as well as on the material the electron is traveling through [72]. The propagation to the surface can be described in a simplifying manner by the transport probability $D\left(E_\mathrm{kin}, \vec{k}\right)$

$$D\left(E_\mathrm{kin}, \vec{k}\right) \propto \lambda\left(E_\mathrm{kin}, \vec{k}\right). \tag{2.7}$$

With typical values for the λ in the range of a few Å for UPS and up to a few tens of Å for XPS, the experimental information depth is also limited to the first few nanometres, when using photoelectron techniques. As a consequence of the second step, photoelectron spectroscopy is a surface sensitive technique.

Third step

Finally in the third step, the transmission of the photoexcited electron through the surface into vacuum is treated as scattering of a Bloch electron wave from the surface atom. Another possibility to solve this problem is matching of the internal Bloch wave functions to free-electron wave functions outside on the vacuum side. This is called LEED problem. In both cases, the transmission of the electron through the surface into vacuum calls for the

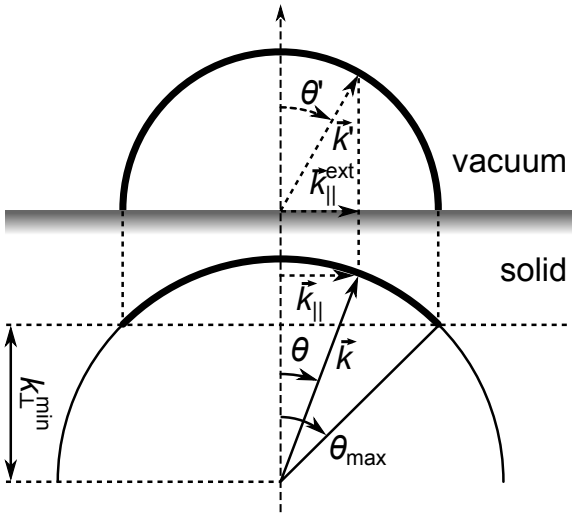

Figure 2.3 | Escape condition for the photoexcited electron: this sketch defines the angular region from which the electrons are able to escape the surface. The thick solid lines show the internal and external escape cones, respectively. Because of the condition that the photoelectron has to have a minimum kinetic energy and, therefore, a minimum wave vector component $k_\perp^\mathrm{min}$ in direction perpendicular to the surface, a maximal escape angle Θ_max can be defined. The wave vector $\vec{k}'$ is defined by $\vec{k}' = \vec{p}/\hbar$ outside of the solid. (This graphic is freely adapted from [16, 67].)

conservation of its wave vector component parallel to the surface (see Figure 2.3), because of the 2D translational symmetry

$$\vec{k}_{||}^{\text{ext}} = \vec{k}_{||} + \vec{G}. \tag{2.8}$$

Here, $\vec{k}$ represents the wave vector of the electron inside the crystal and $\vec{G}$ is the reciprocal lattice vector. During the transmission through the surface, the wave vectors component normal to the surface $\vec{k}_{\perp}$ is not conserved. In the vacuum, $\vec{k}_{\perp}$ is always smaller than inside the solid (see Figure 2.3).
The value of $\vec{k}_{||}^{\text{ext}}$ is determined by the requirement of energy conservation

$$E_{\text{kin}} = \frac{\hbar^2 k^{\text{ext}^2}}{2m_{\text{e}}} = \frac{\hbar^2}{2m_{\text{e}}}\left(k_{\perp}^{\text{ext}^2} + k_{||}^{\text{ext}^2}\right) = E_{\text{f}} - E_{\text{Vac}}, \tag{2.9}$$

which can also be rewritten to Equation (2.1) with $\Phi = E_{\text{Vac}} - E_{\text{F}}$ and E_{B} as the positive binding energy referred to the Fermi level E_{F}

$$\hbar\omega = E_{\text{f}} - E_{\text{i}} = E_{\text{kin}} + \Phi + E_{\text{B}}. \tag{2.10}$$

Here, the wave vector component parallel to the surface on the vacuum side can be determined from experimental parameters

$$k_{||}^{\text{ext}} = \sqrt{\frac{2m_{\text{e}}}{\hbar^2}}\sqrt{\hbar\omega - E_{\text{B}} - \Phi}\sin(\Theta) = \sqrt{\frac{2m_{\text{e}}}{\hbar^2}E_{\text{kin}}}\sin(\Theta). \tag{2.11}$$

According to Equation (2.8), Equation (2.11) directly yields the internal wave vector component $k_{||}$.
As mentioned above, the vector component $\vec{k}_{\perp}$ is not conserved[1]. The outside component is given by the energy conservation in Equation (2.9)

$$k_{\perp}^{\text{ext}} = \sqrt{\frac{2m_{\text{e}}}{\hbar^2}E_{\text{kin}} - \left(\vec{k}_{||} + \vec{G}_{||}\right)^2} = \sqrt{\frac{2m_{\text{e}}}{\hbar^2}E_{\text{kin}}}\cos(\Theta). \tag{2.12}$$

In the third step of the 'three-step model', the transmission of the electrons through the surface, can be formally expressed by the transmission rate

$$T\left(E_{\text{kin}}, \vec{k}\right)\delta\left(\vec{k}_{||} + \vec{G} - \vec{k}_{||}^{\text{ext}}\right). \tag{2.13}$$

A simple approach is given by the assumption that $T\left(E, \vec{k}\right)$ is a constant $R \leq 1$ with

$$T\left(E_{\text{kin}}, \vec{k}\right) = \begin{cases} 0 & \text{for } k_{\perp}^{\text{ext}^2} = \dfrac{2m_{\text{e}}}{\hbar^2}\left(E_{\text{f}} - E_{\text{Vac}}\right) - \left(\vec{k}_{||} + \vec{G}_{||}\right)^2 < 0, \\ R & \text{for } k_{\perp}^{\text{ext}^2} = \dfrac{2m_{\text{e}}}{\hbar^2}\left(E_{\text{f}} - E_{\text{Vac}}\right) - \left(\vec{k}_{||} + \vec{G}_{||}\right)^2 > 0. \end{cases} \tag{2.14}$$

[1] The inner wave vector component $k_{\perp}$ cannot obtained without a detailed knowledge of the electronic band structure for $E_{\text{kin}} > E_{\text{Vac}}$ and of the inner microscopic surface potential V_0, which is usually not exactly known.

Consequently, only electrons with a positive wave vector component $k_{\perp}^{\text{ext}}$ can be observed in PES. All other electrons are internally reflected because their kinetic energy is not sufficient to overcome the surface barrier.

By combining Equation (2.4), (2.6), (2.7), (2.13) with (2.14) the external emission current derived from the 'three-step model' is determined by

$$I^{\text{ext}}\left(E_{\text{kin}}, \hbar\omega, \vec{k}_{||}^{\text{ext}}\right) = I^{\text{int}}\left(E_{\text{kin}}, \hbar\omega, \vec{k}\right) D\left(E_{\text{kin}}, \vec{k}\right) T\left(E_{\text{kin}}, \vec{k}\right) \delta\left(\vec{k}_{||} + \vec{G} - \vec{k}_{||}^{\text{ext}}\right) \tag{2.15}$$

$$\propto \sum_{\text{f,i}} m_{\text{f,i}} \text{f}\left(E_{\text{i}}\left(\vec{k}\right)\right) \delta\left(E_{\text{f}}\left(\vec{k}\right) - E_{\text{i}}\left(\vec{k}\right) - \hbar\omega\right) \delta\left(E_{\text{kin}} - E_{\text{f}}\left(\vec{k}\right)\right) \tag{2.16}$$

$$\times\, \delta\left(\vec{k}_{||} + \vec{G}_{||} - \vec{k}_{||}^{\text{ext}}\right) D\left(E_{\text{kin}}, \vec{k}\right) T\left(E_{\text{kin}}, \vec{k}_{||}\right). \tag{2.17}$$

The delta-function in Equation (2.17) represents all initial and final states. Consequently, a spectrum obtained with photoelectron spectroscopy projects the density of states (DOS(E_{i})) assessable with a photon energy $\hbar\omega$. Electrons with different angular momenta contribute differently to the intensity, because the angular momentum of the initial state is stored in the matrix element $m_{\text{f,i}}$. Consequently, angle-resolved photoelectron spectroscopy (ARPES) offers the opportunity to investigate the band structure of a sample.

2.2. Experimental Setup

All photoelectron spectra presented in this thesis have been obtained at the ORPHEUS cluster system at the I. Institute of Physics (IA) at the RWTH Aachen University. ORPHEUS (organic photoemission ultra-high vacuum system) is a custom-built ultra-high vacuum (UHV) setup which combines the preparation with the characterisation of organic-metal thin films.

Light Sources

Ultraviolet gas discharge lamp

The valence band spectra are measured by using the high-intensity UV irradiation of a helium gas discharge lamp[2]. The lamp is flanged to the UHV analysis chamber through a differentially pumped capillary, which supplies the UV light to the sample surface. The source of light is the He discharge, which is induced in a water-cooled chamber. Here, the He I spectral line originating from excitations of the neutral He atom is intense. The energy of the He I spectral line amounts to $21.22\,\text{eV}$. All other spectral lines only give a rise to a minor background so that no monochromator is needed. Operating at a different pressure induces the He II line at an photon energy of $40.82\,\text{eV}$.
In the thesis presented, all UPS spectra are recorded by using the He I spectral line ($21.22\,\text{eV}$).

[2]The used lamp is a UVS 300 – 'Very High Intensity UV Lamp' with the power supply UVS 300-A delivered by *SPECS GmbH*.

X-ray tube

A high-intensity water-cooled X-ray tube[3] is used in combination with an Aluminium anode, which delivers an Al K_α spectral line at $1486.74\,\mathrm{eV}$. The line width of this spectral emission line is about $830\,\mathrm{meV}$, which is too large for fine-structure investigations or the analysis of chemical shifts [26]. Therefore, the X-ray tube is used in combination with a X-ray monochromator[4] which contains a crystalline diffraction mirror as a dispersive element.

Electron-Energy Detector

The PES detector comprises a Specs PHOIBOS 100 system, which is schematically depicted in Figure 2.4. Its working principle is based on collection and separation of photoelectrons by employing a hemispherical energy analyser (HSA)[5]. After photoexcitation, electrons can leave the surface as described in Section 2.1. These electrons are allowed to enter the HSA at an acceptance angle of usually less than $10°$ at a working distance of $40\,\mathrm{mm}$. The sample can be tilted if electrons are of interest, which are ejected under a different angle than that of the surface normal plus-minus the acceptance angle. This possibility of tilting the sample enables the characterisation of band structures (ARPES).
The photoelectrons, which have entered the HSA, are focused by a system of electronic lenses. These lenses are adjusted on the surface of the sample in order to directly collect excited electrons. Thus, after leaving the surface, these electrons are subsequently pointed on the entrance slit of the hemisphere. The lens system retards the kinetic energy E_{kin} of the electrons by an energy value E_{ret}

$$E_{\mathrm{pass}} = E_{\mathrm{kin}} - E_{\mathrm{ret}}, \tag{2.18}$$

where E_{pass} represents the pass energy. In combination with the hemisphere of the HSA, the lens system enables energy separation and resolution: in order to pass the hemisphere

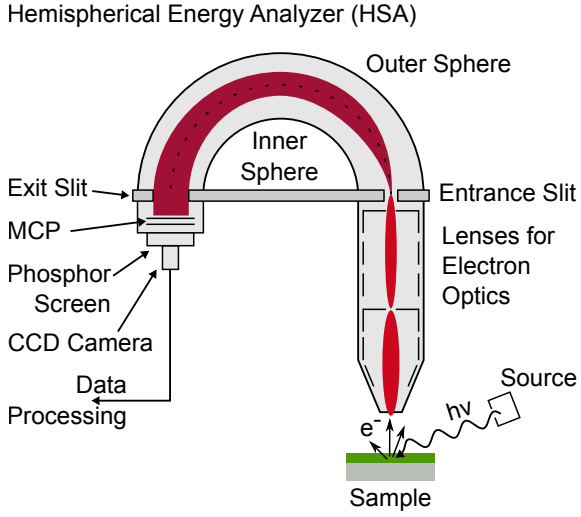

Figure 2.4 | Illustration of a hemispherical energy analyser (HSA) of a photoelectron spectrometer: the photoexcited electrons escape the surface at various angles. However, they are collected just inside a small acceptance angle. Thereafter, the collected electrons are retarded by an electrostatic lens system of the analyser. Thereby, only electrons with a kinetic energy matching the pass energy at the entrance slit of the hemisphere, move through the HSA without deflection. After passing the exit slit of the hemisphere, these electrons are multiplied by micro-channel plates (MCP) and detected by a combination of a phosphor screen and a CCD camera. (This picture is reprinted from [16] with kind permission.)

[3] The used tube is a XR50 M – 'X-ray Source for Focus 500' with the X-ray source control XRC 1000 M delivered by *SPECS GmbH*.
[4] A FOCUS 500 is used as X-Ray monochromator also delivered by *SPECS GmbH*.
[5] The PHOIBOS – 'Hemispherical Energy Analyser Series' is supplied by *SPECS GmbH*.

without deflection, the kinetic energy of the electrons has to equal E_{pass}. The central trajectory in between the inner and outer sphere of the HSA is defined by an electric field $\vec{E}$ that deflects the electrons according to the *Lorentz* force $\vec{F} = q\vec{E}$. Commonly, the fixed analyser transmission (FAT) mode is utilised, in which the pass energy is kept constant. Hence, in order to collect all electrons within the available energy range $\hbar\omega \leq E_{\text{kin}} \leq 0$, the amount of retardation E_{ret} is continuously varied during a photoelectron measurement.

After the electrons have passed the exit slit of the HSA, they are detected by the PHOIBOS CCD[6] detector[7]. This kind of two-dimensional detector is based on two micro-channel plates (MCP) that serve as electron multiplier and a phosphor screen. Impinging electrons locally generate light spots on the screen which are then recorded by a highly sensitive CCD camera. These electrons are thus detected and analysed by the intensity and location of bright pixels on the screen.

[6] CCD is the abbreviation for charge couple device.
[7] The PHOIBOS CCD imaging detector is delivered by *SPECS GmbH*.

3. Inverse Photoemission Spectroscopy

For charge transport through the interface between different materials used in modern devices, the energy level alignment of the frontier electronic states around the Fermi energy E_F is required. Hence, knowledge about these states enables a targeted improvement of modern devices. For the purpose of analysing and understanding the unoccupied electronic states of condensed materials and at interfaces, inverse photoemission spectroscopy (IPES) is a powerful technique. Therefore, its implementation and understanding is of considerable significance for this thesis.

As explained in the previous chapter, in the photoelectron (PE) process, a photon of a discrete energy excites a bound electron of an atom, molecule or solid into the vacuum continuum. By detecting these electrons and analysing their properties, information about the occupied states of the investigated material can be determined. The inverse of this process is utilised in inverse photoemission spectroscopy. Here, an electron of a discrete energy couples to a high-lying unoccupied electronic state. Thereafter, it decays either radiatively or non-radiatively into a low-lying unoccupied state. If the decay is radiative, the emitted photon is detected and an energy spectrum[1] of the unoccupied electronic density of states is obtained. Consequently, the information provided by IPES is complementary to that obtained from PES. Both techniques are compared in Table 3.1.

The principle of inverse photoemission spectroscopy (IPES) was introduced for the first time by *W. Duane* and *F. L. Hunt* in 1915 in order to determine the quotient between Planck's constant and the elementary charge (h/e) with the help of an X-ray tube [73]. Since their experiment was carried out using a fixed monochromator setting, it can be identified as the first isochromat (= constant colour) measurement ever performed. The resolution, however,

Table 3.1 | Conceptual comparison of PES and IPES

	PES	IPES
particles in	photons	electrons
particles out	electrons	photons
information obtained	occupied states	unoccupied states
accessible range	below E_F	above E_F
yield	~10^{-3} electrons/photon (UPS)	~10^{-8} photons/electron

[1] The energy spectrum is drawn as incident electron energy vs. photon counts.

was very poor in these early days, since the experiments were not carried out under proper ultra-high vacuum (UHV) conditions. It then took another 27 years until *P. Ohlin* measured peaks in the short-wavelength limit of the bremsstrahlung spectrum emitted when a monoenergetic beam of electrons irradiated a sample [74]. Thereafter, *B. R. A. Nijober* firstly interpreted them as unfilled electronic states located above the Fermi level in 1946 [75]. After the research on this topic had nearly stopped, *K. Ulmer* and *H. Vernickel* started an experimental isochromat program in order to systematically determine the unoccupied states of samples in 1958 [76]. At first, their samples had to be heated during characterisation to achieve clean surfaces. When 30 years later adequate ultra-high vacuum (UHV) conditions could be achieved, samples with a clean surface were measured at room temperature. Since IPES was first performed by detecting photons with an energy in the X-ray regime, its historical name is bremsstrahlung isochromat spectroscopy (BIS). Today, BIS is only used when measuring the unoccupied states in the X-ray regime, and it is called IPES when photons in the UV region are detected.
The history of inverse photoemission spectroscopy in the ultraviolet energy range is much shorter than spectroscopy using bremsstrahlung. The starting point was the introduction of the Geiger-Müller bandpass ultraviolet photon detector applicable as a detector for the IPES (see also Section 5.2) by *V. Dose* and co-workers in 1977 [77]. Only a few years later, the theoretical work on inverse photoemission (IPE) process was published by *J. B. Pendry* [78, 79].

Figure 3.1 schematically depicts the experimental setup of an IPE spectrometer. An electron gun (coloured in violet) provides a well-collimated and monoenergetic electron beam with energies between 5 eV and 30 eV. Under normal conditions, the electrons (violet squares) enter the sample (green coloured) perpendicularly to the surface. In order to perform angle-

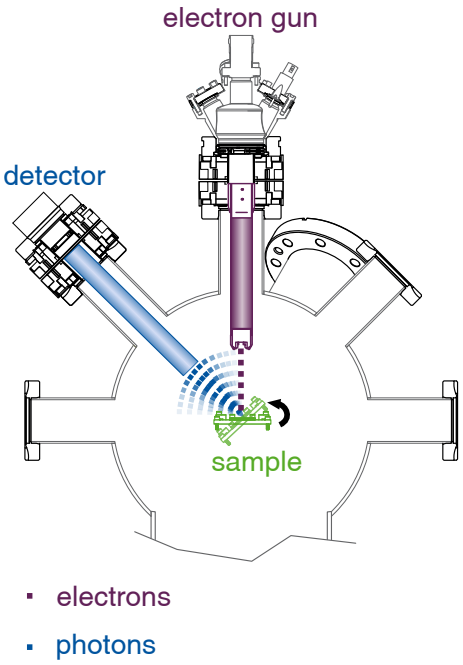

Figure 3.1 | Schematic illustration of an IPES experiment: a beam of low-energy electrons (violet squares), which are provided by the electron gun (violet cylinder), are injected into the sample (green) in order to induce the emission of photons (blue squares). These photons are detected by a Geiger-Müller photon detector (blue cylinder). The sample stage can be tilted to perform angle-resolved studies.

resolved inverse photoemission spectroscopy (AR-IPES) the sample stage can be tilted. A Geiger-Müller photon detector, which is coloured in blue, counts the emitted photons (blue squares). Since the penetration depth of low-energy electrons in the material investigated is only 10 Å to 20 Å [80], IPES is a very surface sensitive technique, which demands UHV conditions.

First, this chapter outlines some theoretical aspects of IPES in comparison to photoelectron spectroscopy (PES) in Section 3.1. Thereafter, the energetics of the IPE process are discussed in Section 3.2. In Section 3.3, angle-resolved inverse photoemission spectroscopy is shortly introduced. Additionally, the existence of image potential induced surface states is explained in Section 3.4, which are a special class of surface states and are inaccessible in PES.
In the course of this doctoral thesis, a IPE spectrometer was designed and successfully put into operation. It is attached to the UHV cluster system 'ORPHEUS' of the I. Institute of Physics (IA) of the RWTH Aachen University. The technical requirements of the electron gun, the detector, the vacuum conditions and the need of a magnetic shielding are presented in Section 3.5.

3.1. Theoretical Considerations

As stated before, an electron entering the surface of a material is able to couple to an unoccupied level, whereafter it decays radiatively or non-radiatively to a tightly bound unoccupied level. If this process takes place by emitting a photon, its energy is given by the energy difference between the initial and final state. The inverse photoemission cross section per steradian, which is related to the probability that such a radiative transition will occur, is derived on the following pages. Thereafter, the result will be compared to the cross section of the photoelectron process by discussing the similarities and the differences between the IPE and the photoelectron process.

The Emission Cross Section

This section is mainly based on the approach of *P. D. Johnson* and *J. W. Davenport* [81], which is equivalent to the original work done by *J. B. Pendry* [78, 79].

The Hamiltonian $\mathcal{H}$ describing the interaction between a photon and an electron by neglecting the spin is given by

$$\mathcal{H} = \frac{e}{2m_{\mathrm{e}}c}\left(\vec{A}\cdot\vec{p}+\vec{p}\cdot\vec{A}\right)+\frac{e^2}{2m_{\mathrm{e}}c^2}\left|\vec{A}\right|^2, \tag{3.1}$$

with $\vec{A}$ denoting the electro magnetic vector potential of the photon and $\vec{p}$ is the momentum the electron. The $\left|\vec{A}\right|^2$ term can also neglected since it leads to second-order processes such as diamagnetism and light scattering. While $\vec{A}$ can be treated as a classical time-dependent perturbation in the case of the photoelectron process (PE process), this is not the case for inverse photoemission. Since photons are created in this process, it is essential to quantise

the electromagnetic field [27, 81]. This is achieved by replacing the classical vector $\vec{A}$ by the field operator $\vec{A}(\vec{x},t)$, which can be written as

$$\vec{A}(\vec{x},t) = 2\pi V_\mathrm{p}^{-1/2} \sum_{\vec{q}} \sum_{\alpha} \frac{\hbar c}{\omega} \left(a^-_{\vec{q},\alpha}(t)\hat{\epsilon}^{(\alpha)} e^{\mathrm{i}\vec{q}\cdot\vec{x}} + a^+_{\vec{q},\alpha}(t)\hat{\epsilon}^{(\alpha)} e^{-\mathrm{i}\vec{q}\cdot\vec{x}} \right). \tag{3.2}$$

Here, the photon has the propagation vector $\vec{q}$, the angular frequency ω and the polarisation angle α. The normalisation volume of the photon is given by V_p and $\hat{\epsilon}^{(\alpha)}$ denotes the linear polarisation vector whose direction depends on $\vec{q}$. The operators $a^+_{\vec{q},\alpha}$ and $a^-_{\vec{q},\alpha}$ describe the creation or annihilation of a photon in the state $(\vec{q},\alpha)$, respectively.
During the IPE process, the electron initially couples to the continuum state $\Psi_\mathrm{i}(\vec{r})$ and recombines to the final state $\Psi_\mathrm{f}(\vec{r})$ by emitting a photon with the wave vector $\vec{q}$. By using first-order perturbation theory, wherein $\mathcal{H}$ is the perturbing operator, the rate W_IPE of a transition from $|\Psi_\mathrm{i}(\vec{r})\rangle$ to $|\Psi_\mathrm{f}(\vec{r}),\vec{q}\rangle$ is then given by *Fermi's* golden rule

$$W_\mathrm{IPE} = \frac{2\pi}{\hbar} \left| \langle \Psi_\mathrm{f}(\vec{r}),\vec{q}| \, \mathcal{H} \, |\Psi_\mathrm{i}(\vec{r})\rangle \right|^2 \rho_\mathrm{photon}(E), \tag{3.3}$$

where the density of states $\rho_\mathrm{photon}(E)$ of the photons with the energy E in the case of emission into the solid state angle $\mathrm{d}\Omega$ can be calculated by

$$\rho_\mathrm{photon}(E) = \frac{V_\mathrm{p}\omega^2}{8\pi^3\hbar c^3}\mathrm{d}\Omega. \tag{3.4}$$

By inserting Equation (3.4) into (3.3) and using Equation (3.1) and (3.2) the transition rate W_IPE becomes

$$W_\mathrm{IPE} = \frac{\omega e^2}{2\pi\hbar m_\mathrm{e}^2 c^3} \left| \langle \Psi_\mathrm{f}(\vec{r}),\vec{q}| \, \hat{\epsilon}\cdot\vec{p} \, |\Psi_\mathrm{i}(\vec{r})\rangle \right|^2 \mathrm{d}\Omega. \tag{3.5}$$

For one electron, the flux j_e is given by

$$j_\mathrm{e} = \frac{\hbar\left|\vec{k}\right|}{m_\mathrm{e}} \frac{1}{V_\mathrm{e}}, \tag{3.6}$$

with V_e denoting the normalisation volume[2] of the electron and m_e being the electron mass. Finally, the inverse photoemission cross section per steradian $(\mathrm{d}\sigma/\mathrm{d}\Omega)_\mathrm{IPE}$ is [81]

$$\left(\frac{\mathrm{d}\sigma}{\mathrm{d}\Omega}\right)_\mathrm{IPE} = \frac{\alpha}{2\pi} \frac{\omega}{m_\mathrm{e}c^2} \frac{1}{\hbar\left|\vec{k}\right|} \left| \langle \Psi_\mathrm{f}(\vec{r}),\vec{q}| \, \hat{\epsilon}\cdot\vec{p} \, |\Psi_\mathrm{i}(\vec{r})\rangle \right|^2, \tag{3.7}$$

where $e^2/\hbar c = \alpha \approx 1/137$ is the fine structure constant. $(\mathrm{d}\sigma/\mathrm{d}\Omega)_\mathrm{IPE}$ yields the probability for radiative transitions upon emission of photons with the wave vector $\vec{q}$ when an electron with the momentum $\vec{k}$ is absorbed by a material.

[2] The continuum electron state is normalised to a box of volume V_e, which does not need to be the same as the photon normalisation box V_p.

Comparison of Inverse Photoemission Spectroscopy and Photoelectron Spectroscopy

At this point, it is interesting to compare the inverse photoemission cross section $(\mathrm{d}\sigma/\mathrm{d}\Omega)_{\mathrm{IPE}}$ of Equation (3.7) with the cross section of the photoelectron process under the assumption that the square magnitudes of the matrix elements for the inverse photoemission and the photoelectron process are the same [27]. For the photoelectron process, the initial state is now an electron in an occupied level below the Fermi energy and the final state is a free electron with momentum $\vec{k}$. The density of states $\rho_{\mathrm{electron}}(E)$ of the emitted electrons can be written as [81]

$$\rho_{\mathrm{electron}}(E) = \frac{V_{\mathrm{e}} m_{\mathrm{e}} \left|\vec{k}\right|}{8\pi^3 \hbar^2}, \tag{3.8}$$

and the incident flux of photons j_{p} is given by [81]

$$j_{\mathrm{p}} = \frac{\omega}{8\pi\hbar c} \frac{1}{V_{\mathrm{p}}}. \tag{3.9}$$

Finally, the cross section per steradian of PE process $(\mathrm{d}\sigma/\mathrm{d}\Omega)_{\mathrm{PE}}$ is [81]

$$\left(\frac{\mathrm{d}\sigma}{\mathrm{d}\Omega}\right)_{\mathrm{PE}} = \frac{\alpha}{2\pi} \frac{\left|\vec{k}\right|}{m_{\mathrm{e}}} \frac{1}{\hbar\omega} \left|\langle \Psi_{\mathrm{fe}}(\vec{r}) | \, \hat{\epsilon} \cdot \vec{p} \, | \Psi_{\mathrm{occ}}(\vec{r}), \vec{q} \rangle\right|^2, \tag{3.10}$$

where $\Psi_{\mathrm{occ}}(\vec{r})$ is now the initial state of an electron in an occupied level below the Fermi energy E_{F} after the absorption of an incoming photon with the wave vector $\vec{q}$. $\Psi_{\mathrm{fe}}(\vec{r})$ is the final state of the emitted electron. The ratio between the two cross sections r thus only expresses the different phase space, which is available for photon or electron creation [27]

$$r = \left(\frac{\mathrm{d}\sigma}{\mathrm{d}\Omega}\right)_{\mathrm{IPE}} \cdot \left(\frac{\mathrm{d}\sigma}{\mathrm{d}\Omega}\right)^{-1}_{\mathrm{PE}} = \frac{\omega^2}{c^2 k^2},$$

which is equal to

$$r = \left(\frac{\lambda_e}{\lambda_p}\right)^2. \tag{3.11}$$

Here, λ_e and λ_p are the wavelengths of the incident electrons and photons, respectively. Summarising, the ratio of the inverse photoemission cross section and the PE process is the ratio of the square of the wavelength of the electron and the photon. At typical energies of $\sim 10\,\mathrm{eV}$ for the vacuum ultraviolet region, λ_e and λ_p amount to $\lambda_e \approx 4\,\text{Å}$ and $\lambda_p \approx 1200\,\text{Å}$, respectively. Consequently, this leads to $r \approx 10^{-5}$, which explains the very low signal levels in IPES (~10^{-8} photons/electron) compared to those achieved by ultra-violet photoelectron spectroscopy (UPS) (~10^{-3} electrons/photon). In the characteristic X-ray range at energies of $\sim 1000\,\mathrm{eV}$, the ratio between X-ray photoelectron spectroscopy (XPS) and IPES is $r \approx 10^{-3}$ [27]. Hence, the expectation of low count rates when performing IPES must be taken into account for the design of an IPE spectrometer.

The ratio of the cross sections is calculated under the assumption that the IPE and the PE process can be treated as time-reversed. In such a case, the square magnitudes of the ma-

trix elements in Equation (3.7) and (3.10) are the same. This is, however, not strictly true, since an electron is removed from the investigated material in PES, whereas the electron is added to the system in IPES. An electron, which approaches an ion, is effected by a long-range Coulomb potential, whereas, an electron approaching a neutral atom experiences a short-range non-Coulombic potential. So, for localised electron states such as those in atoms and molecules, there is a significant difference in the cross section between PES and IPES especially near the threshold region [81]. However, for solids, in which the electron bulk states are delocalised, the removal or the addition of an electron is nearly equivalent. In such a case, the assumption made before is still correct and inverse photoemission spectroscopy can be treated as the time-reversed version of the photoelectron process. In that case, the whole construction of the photoelectron theory, which has been established over years, can be adapted to IPES with hardly any modification [27, 79].

A quantitative treatment of the electromagnetic vector $\vec{A}$, which is associated with polarisation selection rules in PES and IPES, is theoretically difficult. The standard *Fresnel* equations relate values of $\vec{A}$ in vacuum to those in the sample. However, these equations assume an abrupt interface between the vacuum and the medium, which is not correct on the length scale of PES and IPES. Therefore, the spatial variation of $\vec{A}$ has to be calculated in a good agreement to the solution of Maxwell's equations as well as the Schrödinger's equation, which can be achieved by utilising the Jellium approximation [27, 82].

3.2. Energetics in IPES

The formal theory of IPE was propounded by *J. B. Pendry* as a 'one-step' model that treats the IPE process as the time-reversed version of the PE process [78, 79]. It considers three physical steps of the IPE process in one coherent quantum mechanical fashion [27, 83]. These three steps are:

i. the adjustment between the incoming plane wave electron and the electron waves of the solid;

ii. the strong probability of non-radiative inelastic electron decay due to electron-electron interactions with the solid;

iii. the radiative decay of the excited electron.

The major advantage of the 'one-step' model is the simultaneous generation of both bulk-derived and surface-derived features in the spectra. It thereby predicts also the intensities and polarisation sensitivities. In addition, so-called density of states effects are also described by this model [83]. However, the full power of the 'one-step' model is not always required for the understanding of the IPE process and is therefore not discussed in detail here[3].

[3] For further reading, the work of *J. Braun*, *G. Thörner* as well as *G. Borstel* and co-workers is recommended [84–89].

For many intentions it is sufficient to just refer to conservation laws for the energy and the momentum: Figure 3.2 shows a schematic energy level diagram of the IPE process. An electron, which is thermally emitted from the cathode and is thereafter accelerated towards the sample, has the kinetic energy E_{kin} given by

$$E_{\mathrm{kin}} = e \cdot V_{\mathrm{EE}} + \Phi_{\mathrm{C}}. \tag{3.12}$$

Here, V_{EE} represents the acceleration potential of the electron gun with respect to ground potential, i.e. it defines the energy of the electrons E_{EE}. Φ_{C} is the work function of the cathode. When the electron enters the surface of the sample, it couples to a state above the vacuum level $E^{\mathrm{S}}_{\mathrm{Vac}}$. From this initial state with the energy E_{i} the electron decays radiatively into a lower unoccupied electronic final state E_{f}. The energy of the emitted photon $E_{\mathrm{photon}} = \hbar\omega$ amounts to the difference of initial and final state energies. Thus, the conservation law for the energy is given by

$$E_{\mathrm{i}} - E_{\mathrm{f}} - \hbar\omega = 0. \tag{3.13}$$

Consequently, the binding energy E_{B} of the electron in the final state E_{f} reads[4]

$$E_{\mathrm{B}} = \Phi_{\mathrm{S}} + \Delta E - \hbar\omega \tag{3.14}$$

$$= e \cdot V_{\mathrm{EE}} + \Phi_{\mathrm{C}} - \hbar\omega, \tag{3.15}$$

with Φ_{S} representing the work function of the sample and $\Delta E = e \cdot V_{\mathrm{EE}} + \Phi_{\mathrm{C}} - \Phi_{\mathrm{S}}$.

IPE spectra can be obtained in two different ways:

i. keeping the electron beam at a constant energy $E_{\mathrm{kin}} = E_0$, while detecting the full energy range of the emitted photons. This is called the spectroscopic mode. The resulting spectrum shows peaks at $\hbar\omega = E_0 - E_{\mathrm{f}}$.

ii. By utilising the so-called isochromat mode, the energy of the electrons E_{EE} is varied, while only a discrete photon energy of $\hbar\omega_0$ is detected. The intensity of the collected

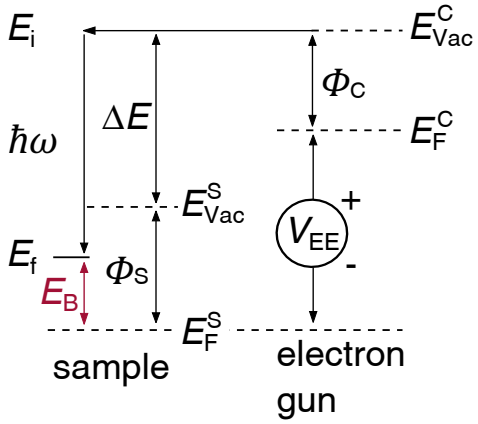

Figure 3.2 | Energetic diagram of the IPE process: Schematic illustrating the energy level diagram of the IPE process. The Fermi energy $E^{\mathrm{C}}_{\mathrm{F}}$ and the vacuum level $E^{\mathrm{C}}_{\mathrm{Vac}}$ of the cathode of the electron gun are shifted by the potential V_{EE}, which accelerates the thermally emitted electrons to the kinetic energy $E_{\mathrm{kin}} = e \cdot V_{\mathrm{EE}} + \Phi_{\mathrm{C}}$. When the electrons enter the samples surface, they couple to a state E_{i}, which lies above the vacuum level $E^{\mathrm{S}}_{\mathrm{Vac}}$. Thereafter, the electrons decay radiatively into a lower unoccupied electronic final state with the energy E_{f}. The energy of the emitted photon is about $E_{\mathrm{photon}} = \hbar\omega$. The final states' binding energy E_{B} of E_{f} with respect to the Fermi energy $E^{\mathrm{S}}_{\mathrm{F}}$ of the sample is then given by $E_{\mathrm{B}} = e \cdot V_{\mathrm{EE}} + \Phi_{\mathrm{C}} - \hbar\omega$.

[4] For the calculation of the binding energy E_{B} in Equation (3.15), the assumption is made that the sample is on ground potential as is the case for most IPE experiments.

photons thus increases at $E_{\mathrm{kin}} = \hbar\omega_0 + E_{\mathrm{f}}$.

In the case of IPE spectra, the energy axis is mostly referred to the Fermi level $E_{\mathrm{F}}^{\mathrm{S}}$ of the sample as in it is also the case for ultra-violet photoelectron spectra. Consequently, in such a spectrum the Fermi level has a binding energy of $E_{\mathrm{B,F}}^{\mathrm{S}} = 0\,\mathrm{eV}$. In order to determine the position of the Fermi level, a reference measurement is required[5] if $E_{\mathrm{F}}^{\mathrm{S}}$ lies within the transport gap of the semiconductor samples for example. From Equation (3.15) it can be concluded that the position of the Fermi level $E_{\mathrm{F}}^{\mathrm{S}}$ is independent of the measured sample

$$\begin{aligned} E_{\mathrm{B,F}}^{\mathrm{S}} &= 0\,\mathrm{eV} \\ &= e \cdot V_{\mathrm{EE,F}} + \Phi_{\mathrm{C}} - \hbar\omega \qquad (3.16) \\ \Longrightarrow e \cdot V_{\mathrm{EE,F}} &= \hbar\omega - \Phi_{\mathrm{C}}. \qquad (3.17) \end{aligned}$$

Hence, the position of the Fermi level only depends on the difference between the photon energy $\hbar\omega$ detected by the photon bandpass detector as well as on the work function Φ_{C} of the cathode material used to generate electrons.

As shown in the following section, measurements of the energetic positions of states as a function of the angle of incidence Θ in angle-resolved IPE can be reduced to $E_{\mathrm{f}}\left(\vec{k}_{||}\right)$, just as in ARPES [90]. The results can then be compared to $E\left(\vec{k}_{||}\right)$ relations that are derived by first-principle theoretical calculations of the bulk band structure or the surface electronic structure.

3.3. Angle-Resolved IPES

For single crystals, the electronic states do not only depend on the energy, but also on the momentum. Therefore, in order to detect all the unoccupied states of the investigated material, the momentum of the incoming electron beam has to be varied. When not only the energy but also the momentum of the electron is changed during the measurement, the experiment is called angle-resolved inverse photoemission spectroscopy (AR-IPES)[6]

The magnitude of the total momentum of the electron just before it reaches the sample is given by the free-electron relation

$$\left|\vec{k}\right| = \frac{\sqrt{2m_{\mathrm{e}}E_{\mathrm{kin}}}}{\hbar}. \qquad (3.18)$$

Due to the virtually infinite translation periodicity of the lattice structure of the crystal parallel to its surface, the component of the incident wave vector of the electron in this direction $\vec{k}_{||}$ is a good quantum number[7] [80]: only the parallel component of the electron wave vector

[5] This measurement is shown in Section 5.3.

[6] Another common name is K-Resolved Inverse photoemission spectroscopy (KRIPES).

[7] $\vec{k}_{\perp}$ is not a good quantum number, because of the existence of the surface and the shortness of the electron penetration depth into sample: consequently, $\vec{k}_{\perp}$ is not necessarily conserved in the optical transition, when the electron decays from its initial to the final state [80].

$\vec{k}_{||}$ is conserved when traversing the vacuum-solid interface

$$\left(\vec{k}_{||}\right)_{\mathrm{f}} = \left(\vec{k}_{||}\right)_{\mathrm{i}} - \vec{G}_{||} + \vec{q}. \tag{3.19}$$

Here, $\vec{G}_{||}$ is the reciprocal lattice vector. For photon energies below $100\,\mathrm{eV}$, the wave vector of the photon $\vec{q}$ remains small compared to the size of the Brillouin zone and is, thus, negligible [91]. The subtraction of a reciprocal lattice vector $\vec{G}_{||}$ is used when plotting the energy bands within the surface Brillouin zone [91]. Hence, a peak in the angle-resolved inverse photoemission spectrum corresponds to an unoccupied state with the energy as given in Equation (3.17) and a parallel momentum equal to that of the incident electron. The magnitude of the momentum parallel to the sample surface $\vec{k}_{||}$ depends on the angle of incidence Θ by

$$\begin{aligned}\left|\vec{k}_{||}\right| &= \left|\vec{k}\right| \cdot \sin(\Theta) \\ &= \frac{\sqrt{2m_{\mathrm{e}}E_{\mathrm{kin}}}}{\hbar}\sin(\Theta).\end{aligned} \tag{3.20}$$

Thus, AR-IPES can be performed by just an additional variation of the angle of incidence of the electron beam relative to the surface normal resulting in a measurement of the complete bandstructure of a single crystal material.

Inverted 'Three-Step' Model

This subsection is mainly based on the work of *D. P. Woodruff* and co-workers [80].

As explained in Section 2.1, the three-step model invented by *C. N. Berglund* and *W. E. Spicer* [71] is much simpler than the more formal approach of the one-step model. For this reason, the three-step model was inverted by *D. P. Woodruff* and co-workers to describe the IPE process [80]:

i. *Penetration through the surface:* the incoming electron couples to the initial unoccupied bulk state of the investigated sample. Thereby, the coupling probability c_{i} to bulk bands is the overlap integral between the initial state wave function and the free electron states in the crystal [92].

ii. *Competition between non-radiative and radiative decay:* the probability $\beta(E)$ of an electron decaying non-radiatively through inelastic electron-electron interaction is high inside the solid. This results in very short penetration depth of $l \lesssim (10-20)\,\text{Å}$ for low-energy electrons. The remaining fraction $(1-\beta(E))$ yields the probability of a radiative decay of the electron into its final state. The photon attenuation lengths are much larger than l, so that all emitted photons contribute to the spectrum gained by IPES. Since the value of $(1-\beta(E))$ is varying hardly over the energy range of interest, it is not taken into account for the first approximation of the ARIPE spectrum.

iii. *Optical de-excitation:* it is assumed that the radiative decay takes place through a direct transition. Thus, an electron occupies a state at $\vec{k}$ in the Brillouin zone at the initial energy $E_\mathrm{i}\left(\vec{k}\right)$ and decays, then, vertically into a final energy $E_\mathrm{f}\left(\vec{k}\right)$. Thereby, the electron's total momentum is conserved and the final state must have the same parallel momentum as the incident electron [67].

The intensity I for incoming electrons with the energy E and for photons with the energy $\hbar\omega$ is given by [92]

$$I\left(E,\hbar\omega\right) \sim \sum_{\mathrm{f,i}} \int_{\Omega} c_\mathrm{i} \underbrace{\left|M_{i,f}\right|^2}_{\mathrm{I.}} \underbrace{\delta\left(E_\mathrm{i}\left(\vec{k}\right) - E_\mathrm{f}\left(\vec{k}\right) - \hbar\omega\right)}_{\mathrm{II.}} \underbrace{\delta\left(E - E_\mathrm{i}\left(\vec{k}\right)\right)}_{\mathrm{III.}} \mathrm{d}^3\vec{k}. \tag{3.21}$$

I. In general, the transition matrix element $M_{i,f}$ is determined by the scalar product of the vector potential $\vec{A}$ (see Equation (3.2)) and the momentum operator $\vec{p}$. For energies well beyond $100\,\mathrm{eV}$, the transition matrix element is just determined by the momentum matrix element $\vec{p}_{f,i}$ between initial and final states, which gives the intensity of the transition and the orientation of the transition dipole [92].

II. The first δ-function generates the energy conservation, which is also given in Equation (3.13).

III. The second δ-function defines the energy of the initial state as the energy of the incoming electron.

The volume of integration Ω over the $\vec{k}$-space depends on the experimental conditions, i.e. angle integrated or angle resolved. For example, for an angle integrated experiment, Ω includes the entire Brillouin zone. Whereas, for an angle resolved experiment, Ω is a narrow rod passing through the origin and being parallel to the surface normal.

In order to determine the energy dispersion curve $E_\mathrm{i}\left(k_{||}\right)$ and $E_\mathrm{f}\left(k_{||}\right)$, generally, the full band structure calculation would be necessary. However, in order to get a first guess on the geometry, the energy dispersion of $E_\mathrm{f}\left(k_{||}\right)$ can be calculated with the help of the two-band nearly-free-electron (NFE) approach under the assumption that the bulk reciprocal lattice vector $\vec{G}$ is perpendicular to the surface [27, 80]

$$E_\mathrm{f}\left(k_{||}\right) = \frac{\hbar^2 k_{||}^2}{2m_\mathrm{e}} + \frac{\left(E_\mathrm{g} + \hbar\omega\right)^2 - 4V_\mathrm{g}^2}{4E_\mathrm{g}}. \tag{3.22}$$

Here, V_g represents the pseudo-potential coefficient which is associated with bulk reciprocal lattice vector $\vec{G}$, and the energy E_g is given by approximately $E_\mathrm{g} = \hbar^2 g^2 / 2m_\mathrm{e}$. The dispersion is free-electron like in $k_{||}$. In addition, the $E_\mathrm{f}\left(k_{||}\right)$ curve shifts when $\hbar\omega$ is varied in case of states which originate from the bulk bandstructure. This fact can be used to distinguish such features in the spectra from surface-derived features, where no such shift is expected. As a

summary, features corresponding to the one-dimensional density of states (1D-DOS) in the direction of $\vec{k}_{||}$ are expected in angle-resolved inverse photoemission data. In case of angle-integrated data, the relaxation of the $\vec{k}_{\perp}$ conservation leads to spectra displaying features of the total density of states (DOS).

3.4. Surface States

Due to the short mean free path of electrons in a solid medium, which is a few nanometres maximum, both PES and IPES are surface sensitive methods. Consequently, not only bulk-induced states but also surface related states are visible in both spectroscopy techniques. In PES, these surface states are commonly crystal-induced Shockley or Tamm states[8]. In IPES and AR-IPES, an additional class of surface states is generated by the image potential. This image potential results from the polarisation charge that is induced by an electron being close to the surface. The Coulomb tail of the image potential gives rise to a Rydberg-like series of the so-called image potential states[9] converging towards the vacuum level. Compared to crystal-induced states, image potential states are expected to have relatively long lifetimes, since their wave function is localised mainly in front of the surface. The section will outline the basics and the properties of surface states and is mainly based on the work *J. B. Pendry* and *P. M. Echenique* and co-workers [95, 96], on secondary sources like [27, 83, 97–99] and on the book of *S. Hüfner* [67].

Historically, the work of *I. Tamm* and that of *W. Shockley* marked the beginning of the field of surface physics of solids in the 1930s. Ten years later, during the 'transistor years', the effect of surface states on the contact potential at the interfaces of a transistor was shown by *W. E. Meyerhof* [100] and hypothesised by *J. Bardeen* [101]. Two experiments by *W. Shockley* and *W. H. Brattain* (in 1947) [102] and *G. L. Pearson* (in 1948) [103] finally proved *Bardeen's* hypothesis and confirmed *Tamm's* and *Schockley's* predictions [104]. In the first experiment by *W. Shockley* and *W. H. Brattain*, the work function difference of two Silicon samples, one of p-type and the other of n-type, was measured. If the Fermi level is located just below the lower edge of the conduction band for the n-type, while for the p-type E_{F} is lying just above the upper edge of the valence band, the difference between the work functions should be equal to the band gap $\Phi_{\mathrm{p}} - \Phi_{\mathrm{n}} = 1.2\,\mathrm{eV}$. *W. Shockley* and *W. H. Brattain* obtained a value of $\Phi'_{\mathrm{p}} - \Phi'_{\mathrm{n}} = 0.6\,\mathrm{eV}$, which is a clear indicator for the existence of surface states [102, 105]. In the second experiment by *W. Shockley* and *G. L. Pearson*, the existence of surface states was proven by the measurement of the conductance on a semiconducting plate in a parallel condenser. It was found that only a small fraction of the induced charge was mobile

[8] In the discussion of surface states, there is generally a distinction between Shockley states [93] and Tamm states [94], which are named after the American physicist *W. Shockley* and the Russian physicist *I. Tamm*. While, Tamm states arise from an asymmetrical surface potential and require an overriding of a threshold perturbation of the surface potential, Shockley states result from the crossing of atomic orbitals or the crossover of adjacent bands. In addition, Shockley states can exist without a surface perturbation and the degree of localisation of the surface modes depends on the width of the gap between the energy bands.

[9] Image potential states are also called 'barrier-induced' surface states or simply 'image states'.

while the most of the charges were trapped in surface states as predicted by the theory before [103, 105].
After the theoretical description of Shockley states and image potential states by *J. B. Pendry* and *P. M. Echenique* in 1978 [95], the assumption that image potential states are observable in IPE spectra was first made by *P. D. Johnson* and *N. V. Smith* in 1983. They proposed the interpretation of a state near the vacuum level E_{Vac} as an unresolved combination of a Rydberg series of image states [106]. One year later, this suggestion was confirmed by four other cooperations by measuring the IPE spectra of mainly noble metals [107–110]. Additional to the confirmation by IPES, the existence of image potential states was proven by pre-emergent fine structures in low-energy electron diffraction (LEED) [97, 111] and in the binding of electrons at the surface of liquid helium [112].

In the model by *J. B. Pendry* and *P. M. Echenique* [95], surface states are considered as electrons, which are trapped between the surface of the crystal at the band gap and the surface barrier potential, which prevents them from escaping into the vacuum. This model is schematically shown in Figure 3.3. The potential in a 'real' crystal upon a 'real' surface potential is approximated by the black curved line. As shown in the following pages, the lowest

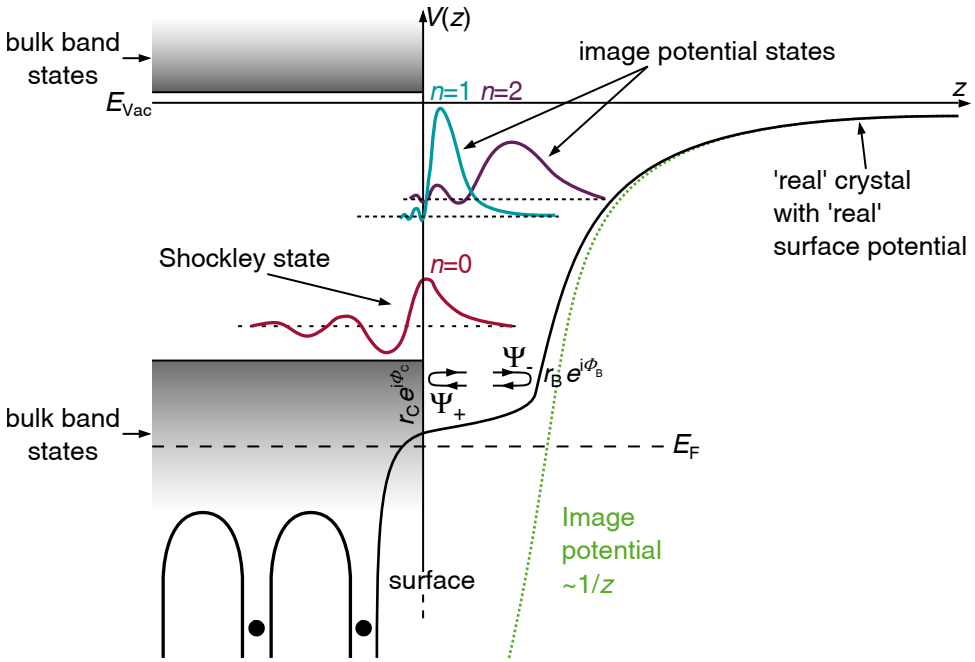

Figure 3.3 | Model of surface states by J. B. Pendry and P. M. Echenique: the black curved line represents an approximation of the potential in a 'real' crystal upon a 'real' surface potential. The maxima of the crystal potential are assumed to be localised between the ions while the minima are at the sites of the ion cores (black dot). An electron is trapped between the crystals surface and its image potential (green dotted line) and is repetitively reflected between these two barriers, which is indicated by the two curved arrows. The lowest order solution $(n = 0)$ of the model gives the Shockley state (red), which can be located above or below near the Fermi energy E_{F}. Higher order solutions $(n \geq 1)$ result in image potential states ($n = 1$ in turquoise and $n = 2$ in violet), which extend out into the vacuum and are located near the vacuum level E_{Vac}. (This picture is freely adapted from [67, 83, 96].)

order solution ($n = 0$) of the model gives the Shockley state (red), which can be located above or below the Fermi energy E_F. Higher order solutions ($n \geq 1$) describe solutions where the electrons are bound outside the crystal surface by their own image potential (green dotted line) resulting in the image potential states (exemplarily: $n = 1$ in turquoise and $n = 2$ in violet). Image potential states extend out into the vacuum and are located near the vacuum level E_{Vac}.

An electron outside the crystal (index C) travels towards (Ψ_+) and away from the surface (Ψ_-) (see Figure 3.3). Thereby, it is multiply reflected at the crystal surface and at the barrier potential, which is equal to its image potential at large distances. When it travels towards the crystal, the reflected beam can be written as

$$\Psi_- = r_C e^{i\Phi_C}\Psi_+, \tag{3.23}$$

while after the reflection at the surface barrier (index B) the beam is given by

$$\Psi_+ = r_B e^{i\Phi_B} r_C e^{i\Phi_C}\Psi_+. \tag{3.24}$$

Here, r_B and r_C are the real parts of the reflection coefficients and Φ_B and Φ_C are the phase changes occurring upon reflection. Thus, $re^{i\Phi}$ is the total reflection coefficient. After summation of repeated reflections, the total amplitude of the electron wave Ψ_+ is proportional to

$$\Psi_+ \propto \left[1 - r_C \cdot r_B \cdot e^{i[\Phi_B+\Phi_C]}\right]^{-1}. \tag{3.25}$$

As a result, bound surface states correspond to the poles of the total amplitude given in Equation (3.25) and occur when the following requirements are fulfilled

$$\text{I. } r_B \cdot r_C = 1 \text{ and} \tag{3.26}$$

$$\text{II. } \Phi_B + \Phi_C = n2\pi, \text{ with n being an integer.} \tag{3.27}$$

The first condition (Equation (3.26)) can alternatively be written as

$$r_B = r_C = 1. \tag{3.28}$$

In physical terms this means: for states with an energy $E < E_{Vac}$, r_B is equal to one and $r_C = 1$ because the states are positioned energetically in a gap of the bandstructure of the crystal.
In order to make further predictions, it is necessary to make assumptions about the crystal wave functions in the band gap as well as about the form of the barrier potential:

$n = 0$ Solution – Shockley States

The wave function $\Psi_{outside}$ in the vacuum is given by

$$\Psi_{outside} = e^{ikz} + e^{-ikz}e^{i\Phi_C}, \tag{3.29}$$

with $k = p + iq$ being a complex wave vector. The form of the wave function Ψ_{inside} in the crystal is given by

$$\Psi_{\text{inside}} = e^{qz}\cos(pz + \delta), \tag{3.30}$$

where δ is a phase parameter that varies from 0 to $-\pi/2$. For matching the wave functions inside and outside the crystal, the matching condition is often written in literature as the logarithmic derivative $[(\mathrm{d}\Psi/\mathrm{d}z)/\Psi]$

$$\left.\frac{\mathrm{d}\Psi/\mathrm{d}z}{\Psi}\right|_{\text{outside}} = \left.\frac{\mathrm{d}\Psi/\mathrm{d}z}{\Psi}\right|_{\text{inside}}, \tag{3.31}$$

With Equation (3.29) and (3.30), the matching condition of Equation (3.31) results in

$$k \cdot \tan(\Phi_{\text{C}}) = -q - p \cdot \tan(\delta) \text{ with} \tag{3.32}$$

$$k = \sqrt{\frac{E_{\text{EE}} \cdot 2m_{\text{e}}}{\hbar^2}}. \tag{3.33}$$

Here, E_{EE} is the energy of the electron. In a rough approximation, q can be set to $q \cong 0$ and $k \cong p$ resulting in: $\Phi_{\text{C}}/2 = -\delta$.

For $n = 0$, the second condition (Equation (3.27)) is $\Phi_{\text{B}} + \Phi_{\text{C}} = 0$. Assuming the potential of the surface to be stepwise instead of a Coulomb-like image potential, the wave function in the crystal is of the type $e^{-ikz} + e^{ikz}e^{i\Phi_{\text{B}}}$ and another one is decaying exponentially into the vacuum with $e^{q'z}$. Applying again the matching condition of Equation (3.31) leads to

$$\tan\left(\frac{1}{2}\Phi_{\text{B}}\right) = -\frac{q'}{k}. \tag{3.34}$$

Inserting Equation (3.34) and $-\Phi_{\text{B}} = \Phi_{\text{C}}$ into Equation (3.32) leads to the matching of the wave functions inside and outside the crystal and this yields[10]:

$$+k\left(\frac{q'}{k}\right) = -q - p \cdot \tan(\delta) \tag{3.35}$$

and

$$q' = -q - p \cdot \tan(\delta). \tag{3.36}$$

Consequently, there are eigenfunctions existent in the band gap of the bandstructure, which exponentially decay into the vacuum but are also located in the crystal, and, thus, represent the crystal-induced surface states, which are also called '$n = 0$ states' or 'Shockley states' [93] (see also Figure 3.3). Image potential states are not present in this solution.

[10] Note that this solution is just valid for semi-infinite crystals. For the assumption of infinite crystals, energy states in the band gap are forbidden because they diverge as $z \longrightarrow \pm\infty$.

$n > 0$ Solution – Image Potential States

As a short reminder: in the model by *J. B. Pendry* and *P. M. Echenique* it is assumed, that electrons are bound in band gaps of a solid by bouncing back and forth between the crystal surface potential and their image potential. Thus, the nature of this barriers is taken into account by considering the phase changes in the scattering process, leading to the second condition (Equation (3.27)) of the existence of surface states

$$\Phi_B + \Phi_C = n2\pi.$$

Since $\Phi_C = -\pi$ for an infinitely high barrier at the crystal surface, Φ_B has to be a function of the energy. The simplest ansatz is $\Phi_B \sim a\,(E_{Vac} - E_n)^b$. In order to start out at $-\pi$ so that Equation (3.27) is fulfilled, Φ_B is determined by

$$\Phi_B = -\pi + a\,(E_{Vac} - E_n)^b\,. \tag{3.37}$$

Combination with $\Phi_B + \Phi_C = n2\pi$ yields

$$a\,(E_{Vac} - E_n)^b = 2\pi(n+1). \tag{3.38}$$

The Coulombic image potential barrier $(\sim 1/4z)$ results then in $E_n \sim 1/n^2$, which is equal to $b = -1/2$. Consequently, Equation (3.38) can be written as

$$E_{Vac} - E_n = \frac{(a/2\pi)^2}{(n+1)^2}. \tag{3.39}$$

By identification of $E_{Vac} - E_n$ with the energy in the Coulomb potential $0.85\,\mathrm{eV}/m^2$ (with $m = 1, 2, ...$), the parameter a can be determined by

$$a = 2\pi\sqrt{(0.85\,\mathrm{eV})}. \tag{3.40}$$

Thus, Equation (3.37) gives

$$\frac{\Phi_B}{\pi} = -1 + \sqrt{\frac{4 \cdot 0.85\,\mathrm{eV}}{E_{Vac} - E_n}} = \sqrt{\frac{3.4\,\mathrm{eV}}{E_{Vac} - E_n}} - 1. \tag{3.41}$$

Assuming that the phase change Φ_C at the crystal surface can also vary ($\Phi_C/\pi = \varepsilon$, with $0 < \varepsilon < 1$) gives

$$\frac{\Phi_B}{\pi} = \varepsilon \text{ or } \frac{\Phi_B}{\pi} + 1 = 2n + 1 - \varepsilon. \tag{3.42}$$

The binding energy of a surface state can be calculated by

$$E_{Vac} - E_n = \frac{0.85\,\mathrm{eV}}{\left(n + \frac{1}{2} - \frac{\varepsilon}{2}\right)^2}, \text{ with } n = 0, 1, 2, \ldots\,. \tag{3.43}$$

Table 3.2 | Experimentally measured energies of surface states and comparison of theoretically calculated and experimentally measured energies of image potential states (all in eV): Both states origin from the s, p band gaps of Cu, Ag and Au. The energies of the Shockley states are given relative to the Fermi level E_F, whereas the binding energies of the image potential states are referred to the vacuum energy E_{Vac}.

plane	Cu		Ag		Au	
Shockley states ($E - E_F$ in eV)						
	Experiment		Experiment		Experiment	
$(111)\bar{\Gamma}$	−0.40 [113] −0.39 [116]		−0.12 [114] −0.08 [117]		−0.50 [115] −0.45 [118]	
$(001)\bar{\Gamma}$	1.15 [119] 1.10 [120] 0.80 [121]					
First image potential states, $n = 1$-solution ($E_{Vac} - E$ in eV)						
	Exp.	Theory	Exp.	Theory	Exp.	Theory
$(111)\bar{\Gamma}$	0.90 [122] 0.70 [128] 0.70 [131] 0.83 [133]	0.76 [123] 0.81 [129] 0.80 [127]	0.60 [124] 0.77 [130] 0.90 [132]	0.77 [125] 0.78 [123]	0.42 [126] 0.60 [127]	0.85 [127] 0.68 [129]
$(001)\bar{\Gamma}$	0.62 [121] 0.64 [128] 0.60 [136] 0.57 [133]	0.62 [127] 0.52 [123]	0.50 [124]	0.62 [121] 0.55 [135] 0.53 [123]	0.63 [128]	0.69 [134]
$(110)\bar{\Gamma}$	0.30 [131]		0.90 [137]		0.70 [138]	

As stated before, the value of Φ_C is determined by the relative position of the vacuum level E_{Vac} within the projected gap, which is expressed by the parameter ε:
Shockley states are located near the lower gap edge, where $\varepsilon \cong 0$ so that for $n = 0$

$$E_{Vac} - E_1 \cong 3.4\,\text{eV}.$$

This is a typical value for the binding energy of a 'normal' surface state with respect to the vacuum level [67].

For image potential states, E_{Vac} lies just above the top of the gap in the case of a copper (111) or a silver (111) surface, for example. Thus, the phase change Φ_C at the crystal surface is about $\Phi_C = \pi$ and ε is equal to one [67, 83]. For copper (001) and silver (001) faces, on the other hand, E_{Vac} is located in the middle of the gap and, consequentially, $\Phi_C = \pi/2$ and $\varepsilon = 1/2$ [67, 83]. The binding energies of the image potential state for $n = 1$ are then

$$E_{Vac} - E_1 = 0.55\,\text{eV} \text{ for } \varepsilon = \frac{1}{2}$$

and

$$E_{Vac} - E_1 = 0.85\,\text{eV} \text{ for } \varepsilon = 1.$$

Image potential states are loosely bound. Thus, their wave functions are located outside the crystal (see also Figure 3.3). Since between E_{Vac} and E_1 an infinite number of states with energies $\approx n^{-2}$ arises, these states are also called 'Rydberg-like' series. The experimental observation of such surface states with AR-IPES and ARPES for the low-index faces of copper (Cu), silver (Ag) and gold (Au) is listed in Table 3.2. The theoretically calculated binding energies of the image potential states are also summarised.

3.5. Technical Requirements

As derived in Section 3.1, the intensities of spectra measured with an IPE spectrometer are by several orders of magnitude lower than those gained in PES. This fact results in experimental requirements on the electron source as well as on the detector of an IPE spectrometer, which is discussed in the current section. Additionally, the low penetration depth of $l \lesssim (10 - 20)\,\text{Å}$ makes IPES a very surface sensitive technique[11], which therefore requires clean surfaces and proper vacuum conditions. Furthermore, the usage of low-energy electrons makes a shielding of the earth and other magnetic fields necessary in order to prevent influence on the electron trajectories. In the following, these aspects are discussed in detail:

Electron Gun

The Need for Low Energies

Since the cross section of states usually decays rapidly with increasing kinetic energy of the incident electrons, low-energy electrons are more suitable for studies of most materials such as inorganic compounds, molecules or semiconductors [139]. In addition, the usage of high energy electrons can cause damage to the surface of the investigated sample and, therefore, might change or even destroy the electronic structure under investigation. Moreover, according to Equation (3.20), the uncertainty of the momentum scales with the square root of the kinetic energy of the incident electrons. Thus, since angle resolved measurements require a defined momentum within a fraction of the Brillouin zone [139, 140], high-energy techniques are not suitable for AR-IPES. Summarising, an electron gun that supports electrons of low energies between $5\,\text{eV}$ and $30\,\text{eV}$ is required for IPES [27, 139].

The Need for High Current

The above mentioned small cross section, which leads to low intensities, calls an electron source capable for producing high brightness and a well-focused electron beam. However, space charge effects have to be considered for such low energies and, therefore define an upper limit on usable electron currents [141]. In order to minimise the space-charge effects at the cathode of the gun and, thereby gain high currents, the thermally emitted electrons have to be first accelerated and subsequently be refocused onto the sample [141, 142]. Although the electron beam spot size on the sample is also space-charge limited and varies with the kinetic energy of the electrons, the electron gun needs to provide a well-focused beam with a

[11] The same argument applies to PES.

small spot of $\sim 1\,\mathrm{mm}$ in diameter and a uniform high beam current in the microampere range over the whole energy range [27, 141].

The Need for Low Angular Spread

In order to measure the momentum dispersion relation $E(\vec{k})$ and, thus, to gain a high $\vec{k}$-resolution in IPES, a well-defined angle of incidence of the electrons in the excitation channel is required. This demands an electron beam with a small divergence [140]. As can be derived from Equation (3.20), the momentum resolution is directly dependent on the angular resolution $\Delta\Theta$ and the energy resolution ΔE_{kin} [143]:

$$\frac{\Delta k_{||}}{k_{||}} = \sqrt{\left(\frac{\Delta\Theta}{\tan\Theta}\right)^2 + \left(\frac{\Delta E_{\mathrm{kin}}}{2E_{\mathrm{kin}}}\right)^2}. \tag{3.44}$$

Thus, the higher the electron energy, the lower the angular resolution has to be in order to keep the same momentum resolution for AR-IPES. Summarising, a parallel electron beam in a low kinetic energy range with a high current and of high angular resolution ($< 5\,^\circ$) is required in order to obtain a high $\vec{k}$-resolution [27, 140].

Many IPES research groups have built custom made low-energy electron guns based on the design presented by *N. G. Stoffel* and *P. D. Johnson* in 1985 [142], on that of *P. W. Erdman* and *E. C. Zipf* presented in 1982 [144] or designs developed further which are based on those two [139, 141]. However, when *N. G. Stoffel* and *P. D. Johnson* or *P. W. Erdman* and *E. C. Zipf* built their gun, there were no commercial options available. Over the past three decades, surface science technologies have greatly developed and, thus electron sources meeting the requirements for the usage in an IPE spectrometer are commercially available nowadays. Therefore, the electron gun $ELG-2$ was purchased from *Kimball Physics Inc.* [145] for the IPE spectrometer of the I. Institute of Physics (IA) of the RWTH Aachen University.

Detector

Due to the low cross section, IPES suffers from very low count rates. Therefore, photon detectors used for IPE measurements in the ultraviolet region require a high sensitivity, i.e. a very high quantum efficiency. The requirements of such a detector, namely a good resolution and a high yield, are in general incompatible[12] with each other [146]. Thus, a compromise between intensity and energy resolution has to be found for every specific scientific question. The photon detectors employed in IPES can be classified into two categories [27, 28, 146]:

i. those that operate in spectroscopic mode, which allows the detection of different photon energies, and

ii. those that operate in the isochromatic or fixed photon energy mode.

[12] In order to gain a high intensity, normally, the resolution is reduced and vice versa.

Spectroscopic Mode

A monochromator either utilising a grating monochromator or the energy dispersive properties of a lithium fluoride (LiF) lens is used for spectroscopic measurements [147, 148]. Both detector types have the major advantages of a good energy resolution of about $100\,\mathrm{meV}$ and a large tunability [146, 149]. Furthermore, the grating monochromator can be operated either in the isochromatic mode or in the spectroscopic mode. Unfortunately, the intensity of those detectors is much lower compared to those detecting at a fixed energy [149]. In addition to that, both spectroscopic detectors are much more complex, larger in size and expensive to construct [147, 150].

Isochromatic Mode

The isochromatic mode is realised using detectors which combine the transmission cut-off of an entrance window with either the ionisation onset of a gas or the photoemission threshold of a solid photocathode [151, 152]. Although bandpass detectors do not gain the high energy resolution compared to spectroscopic detector, solid-state or gas-filled detectors in the isochromatic mode are used more commonly because of their cost-effectiveness and simplicity: in contrast to the gas-filled detectors, solid-state detectors have no sharp bandpass, since the photo-emissive threshold decays exponentially to low energies. This results in an asymmetric shape of the bandpass and, therefore can influence the shape of a measured peak in the spectrum. Another disadvantage is the poor sensitivity, which is critical for measuring reactive surfaces, or surfaces with surface states of low cross sections [153]. Additionally, solid-state detectors exhibit a higher noise level. Thus, a smoothing of the spectra is necessary and results in a lowering of the effective resolution [28, 153]. One advantage of solid-state detectors is, however, the large detection area, which enables higher count rates.
Since the gas detector yields more advantages in comparison to solid-state detectors and grating monochromators, it is chosen for the IPE spectrometer built at the I. Institute of Physics (IA) at RWTH Aachen University in the course of this thesis. It is purchased from *M. Donath's* group of the Westfälische Wilhelms University of Münster, who can draw on a great experience basis in measuring occupied and unoccupied states – especially on the spin-states of electrons in low d-systems [89, 154] – as well as on building gaseous radiation detectors for IPES [140, 149, 155].

Vacuum Requirements

Since IPES is performed using low-energy electrons with penetration depths in the order of angstroms, this technique is very sensitive to the quality of the sample's surface. Therefore, no contaminating particles should be present on the surface of the sample under investigation. Preparing a clean surface and performing meaningful measurements requires an optimal environment of ultra-high vacuum (UHV), in which the sample remains between sample preparation and analysis. In addition to that, proper vacuum conditions are required to minimise scattering of the electrons with gas molecules during the measurement.

Monolayer Formation Time

Table 3.3 | Monolayer formation times t_{ml} for building a monolayer of $\sim 10^{15}\,\mathrm{atoms/cm^2}$ at room temperature ($T \approx 300\,\mathrm{K}$) for different pressures p of air, water H_2O and hydrogen H_2 as residual gases. (The values are taken from [156] on pages 236f.)

t_{ml} \ p	1 mbar	10^{-3} mbar	10^{-7} mbar	10^{-9} mbar	10^{-11} mbar
air	$3.6 \cdot 10^{-6}\,\mathrm{s}$	$3.6 \cdot 10^{-3}\,\mathrm{s}$	36 s	1 h	100 h
H_2O	$2.8 \cdot 10^{-6}\,\mathrm{s}$	$2.8 \cdot 10^{-3}\,\mathrm{s}$	28 s	47 min	78 h
H_2	$9.3 \cdot 10^{-7}\,\mathrm{s}$	$9.3 \cdot 10^{-4}\,\mathrm{s}$	9.3 s	16 min	26 h

The average time needed to cover a surface with an adsorbate in vacuum is called monolayer formation time t_{ml}. Assuming that the adsorbate has a unity sticking coefficient[13], the time to complete a monolayer[14] at room temperature for air as residual gas of pressure p can be roughly estimated by [156]

$$t_{\mathrm{ml}} = \frac{3.6 \cdot 10^{-4}\,\mathrm{Pa}}{p}\mathrm{s}. \tag{3.45}$$

The resulting monolayer formation times for building such a monolayer at room temperature are given in Table 3.3 for different pressures of air, water and hydrogen [156].
Please note that this estimate is carried out for the worst-case scenario, in which every molecule that reaches the surface sticks to it. The timescale will be longer for a real material since the a monolayer is often larger than $10^{15}\,\mathrm{atoms/cm^2}$ and, more importantly the sticking coefficient is often very close to zero [156, 157]. As a result, the above mentioned time scales have to be corrected leading to sufficiently long time scales. Consequently, if the measurement is performed under proper UHV conditions, IPE measurements can be performed without a critical sample contamination.

Mean Free Path between Residual Gas Molecules

According to the kinetic theory of gases, the mean free path between two molecular collisions L_{coll} is given by

$$L_{\mathrm{coll}} = \frac{k_{\mathrm{B}}T}{1.414 \cdot p \cdot \sigma_{\mathrm{coll}}}\,\mathrm{m}, \tag{3.46}$$

where k_{B} is the Boltzmann constant, T expresses the absolute temperature and p represents the pressure given in Pa. σ_{coll} is the cross section of the collision[15] [158]. As a rule of thumb, the mean free path L_{coll} given in cm for air as residual gas at room temperature is

$$L_{\mathrm{coll}}(\mathrm{cm}) \approx \frac{0.01}{p(\mathrm{Torr})}. \tag{3.47}$$

Consequently, for a pressure $p \leq 5 \cdot 10^{-5}\,\mathrm{mbar}$ the mean free path between two molecules is about $L_{\mathrm{coll}} \geq 2\,\mathrm{m}$ and therefore large enough to avoid collisions of the electrons with the residual gas molecules [158].

[13] This means that every molecule which reaches the surface sticks to the surface without desorption.
[14] The monolayer is assumed to be of the size of $\sim 10^{15}\,\mathrm{atoms/cm^2}$.
[15] The cross section of the collision σ_{coll} is given by $d_{\mathrm{m}}^2\pi/4$ with d_{m} being the molecular diameter.

Shielding

An electron experiencing a magnetic force perpendicular to its direction of motion travels along a curved trajectory with radius r_{mag}. The magnitude of the magnetic force is given by the Lorentz equation

$$F_{\mathrm{mag}} = evB\sin(\theta) \tag{3.48}$$

with e being the elementary charge, v representing is the electron's speed, B expressing the magnitude of the magnetic field vector, and θ being the angle between $\vec{v}$ and $\vec{B}$. Consequently, r_{mag} can be given as a function of the kinetic energy of the electron E_{kin} in case of $\theta = 90\,^{\circ}$

$$r_{\mathrm{mag}} = \frac{\sqrt{2m_{\mathrm{e}}E_{\mathrm{kin}}}}{eB}. \tag{3.49}$$

The magnitude of the earth's magnetic field in the city of Aachen[16] is about $\sim 48\,\mu\mathrm{T}$ [159], which corresponds to a radius of about $r_{\mathrm{mag}} \approx 22\,\mathrm{cm}$ for an electron with the kinetic energy $E_{\mathrm{kin}} = 10\,\mathrm{eV}$. As a consequence, the presence of the earth's magnetic field clearly affects the direction of the beam. In particular, the uncertainty in the angle of incidence can approximately double, which causes a higher uncertainty of $\Delta k_{||}$. Therefore, the electrons have to be shielded against the earth's magnetic field and other stray fields, which is provided by a chamber made out of µ-metal[17] [143].

[16] This value was calculated by the IGRF Declination Calculator of the Helmholtz Centre Potsdam - GFZ German Research Centre for Geosciences for the city Aachen in January 2015 [159].

[17] µ-metal is an alloy with an especially high magnetic permeability that can be used for magnetic shielding. Most alloys are permalloys containing approximately $80\,\%$ of nickel (Ni), $20\,\%$ of iron (Fe) and small amounts of molybdenum (Mo) [160].

The Inverse Photoemission Spectrometer

4. Design of the IPE Spectrometer

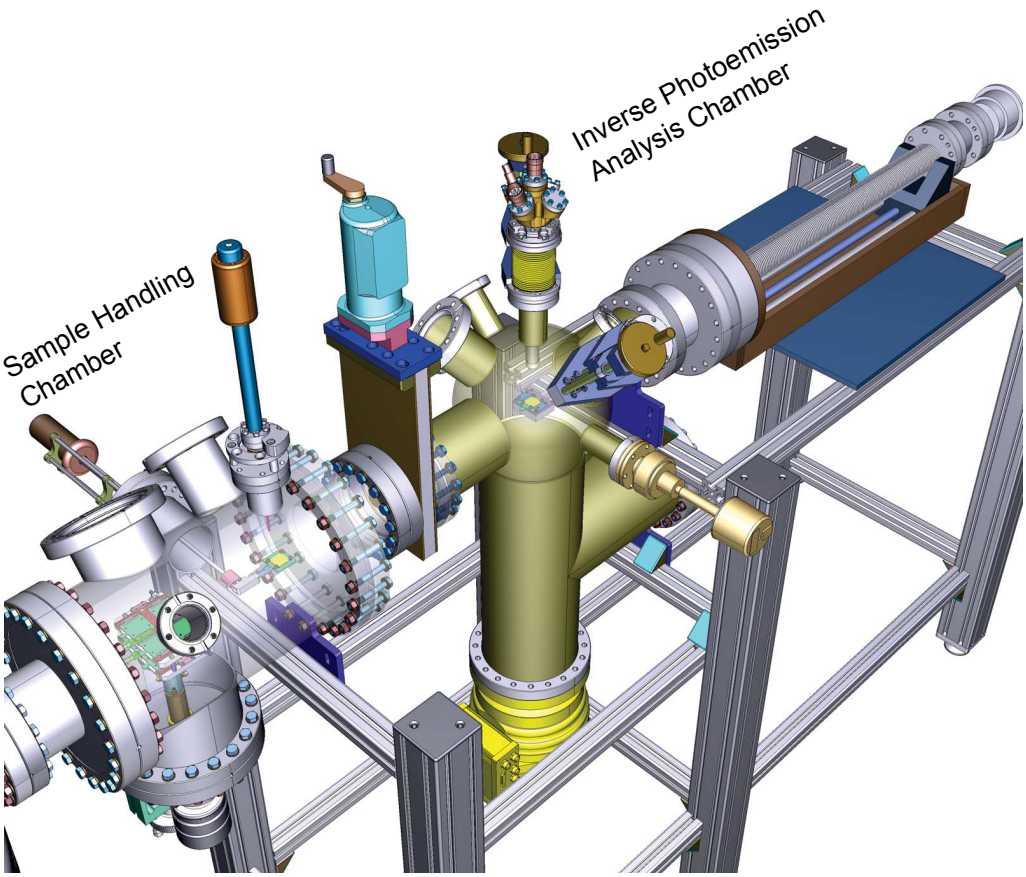

Figure 4.1 | 3D model of the IPE spectrometer: the analysis µ-metal UHV chamber of the spectrometer as well as the long sample manipulator can be seen on the right side of the sketch. The home-build UHV sample handling chamber, which serves as sample storage as well as transfer chamber, can be seen on the left. Both UHV chambers are custom designs. The analysis chamber is separated from the sample handling chamber by a gate valve. In order to additionally show the interior of each chamber, the walls are printed semi-transparent.

For a long time, complete solutions for inverse photoemission spectrometer were not commercially available. Therefore, many spectrometers, which are referred to in literature, and their technical surroundings are custom-designed and were built for a specific scientific purpose of the respective research group. Likewise, the IPE spectrometer of the I. Institute of Physics (IA) of the RWTH Aachen University was planned and built by the author in the course of this

thesis. On that score, a three-dimensional (3D) computer model of all components and the two chambers was created in cooperation with the engineering department of the I. Institute of Physics. Thereby, the compatibility to essential components of the existing UHV cluster tool ORPHEUS'[1] was taken into account. On the basis of technical drawings, the in-house workshop manufactured some parts of the tools and one of the two chambers.
A 3D model of the analysis µ-metal UHV chamber of the inverse photoemission spectrometer and the attached so-called sample handling chamber (SHC) is shown in Figure 4.1. The SHC, in turn, is connected to the sample transfer chamber called handler of the ORPHEUS cluster tool, which also holds an analysis chamber for ultra-violet photoelectron spectroscopy (UPS) and X-ray photoelectron spectroscopy (XPS). In this chapter the important design features of the new spectrometer, the custom-designed UHV-chambers and other components are presented. First, in the following chapter, the sample handling chamber, which includes a storage for eight samples as well as tools for sample movement and contacting, is introduced. Thereafter, the design of the µ-metal chamber and the inverse photoemission spectrometer are discussed in Section 4.2.

4.1. Sample Handling Chamber

The sample handling camber (SHC) was completely planned, drawn and fabricated in-house in the course of this thesis. The design of the sample handling chamber (SHC) is depicted in Figure 4.2. The diameter of the inner pipe of the SHC is about 204 mm and its length amounts to 351 mm measured between both DN 200 conflat (CF) flanges. In order to simplify the assembly process and to keep the compatibility to the UHV cluster ORPHEUS, each DN

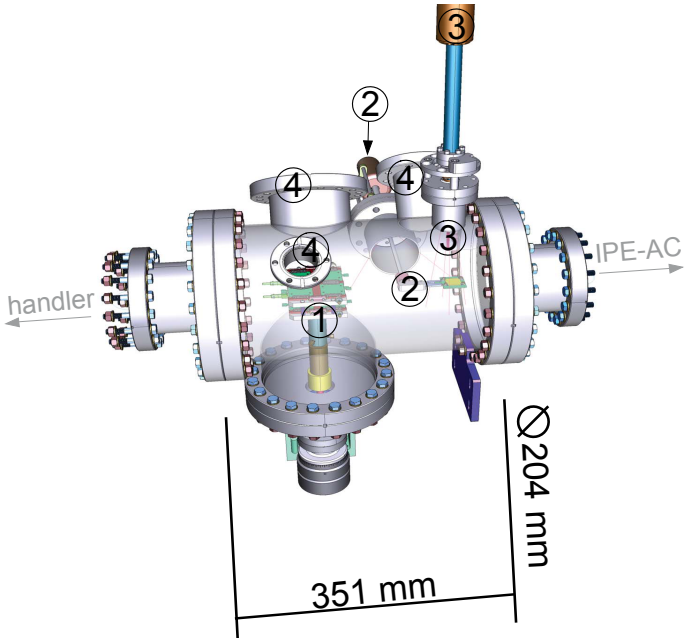

Figure 4.2 | 3D model of the sample handling camber: the sample handling camber is attached to the sample transfer chamber called handler' of the ORPHEUS cluster tool as well as the analysis chamber of the IPE spectrometer. It contains a sample storage (1), which is able to hold eight samples fixed on sample holders positioned at two trays each. With the help of the in-vacuum pincer (2), one sample holder can be placed on the manipulator (not shown). This sample holder can, thereafter be contacted with the help of the in-vacuum screwdriver (3). The sample movement can be monitored through the three view ports (4).

[1]The cluster 'organic photoemission ultra-high vacuum system' is shortened by ORPHEUS.

200 CF flange is reduced and equipped with a DN 100 CF rotary flange, which can be seen at both endings in the 3D model of Figure 4.2. The chamber wall consists of the corrosion resistant steel V4A – DIN1.4404, which stands for a chromium-nickel steel[2] with $(2.0 - 2.5)\,\%$ molybdenum added. Due to its low carbon content ($\leq 0.03\,\%$), the V4A steel is weldable without being susceptible to intergranular corrosion and is therefore highly suitable for vacuum applications [161, 162].

The sample handling camber is attached to the sample transfer chamber called handler of the ORPHEUS UHV cluster tool without separation by a gate valve. Thus, the turbo molecular pump, which is attached to the handler also evacuates the SHC. The handler reaches a base pressure of about $< 5 \cdot 10^{-10}\,\mathrm{mbar}$, so that the base pressure in the SHC is assumed to be in the same order of magnitude. In order to keep the wall of the chamber clean and to obtain good UHV conditions, a heating tape surrounds the chamber, which allows the heating of the complete chamber. Thereby, the temperature of the chamber wall is measured by a thermocouple. Additionally, it is regulated by a control unit, which also monitors the other chambers apart from the analysis chamber of the IPE spectrometer.
The opposite end of the SHC is connected to the analysis chamber of the IPE spectrometer. Both chambers are separated by a DN 100 CF hand wheel UHV gate valve, which was purchased from *VAT Vacuumvalves AG* [163]. The gate valve is bellows-sealed and its mechanism is free of lubricants, which makes it highly suitable for UHV applications [163].
In Figure 4.2, the wall of the chamber is displayed semi-transparent. Thereby, the sample storage (1), the in-vacuum pincer (2) and the screwdriver (3) become visible. The three view ports (4) give an inside view into the chamber. The view port, which can be seen on the left in the back, has the size of a DN 100 CF flange. The one positioned in the front a DN 40 CF flange and that one on the right side has the size of a DN 63 CF flange. A light-emitting diode (LED) lamp is positioned at the smallest view port in order to illuminate the chamber. The tools (sample storage, in-vacuum pincer and screwdriver) which are needed for the handling of the sample are discussed in the following:

Sample Handling

Within the UHV cluster tool ORPHEUS, samples are transferred and placed on so-called trays, which can carry four samples mounted on sample holders at the same time. Thus, in order to measure one single sample, it is necessary to store the tray and to be able to remove a single sample holder and put it onto the manipulator of the IPE spectrometer. These parts are briefly explained in the following.

Sample Storage

As displayed in Figure 4.3, two of these trays (1), i.e. eight sample holders (2) can be stored in the SHC. The sample storage was also designed and built in-house in the course of this

[2] The steel V4A – DIN1.4404 consists of $(16.5 - 18.5)\,\%$ chromium and $(10.0 - 13.0)\,\%$ nickel [161].

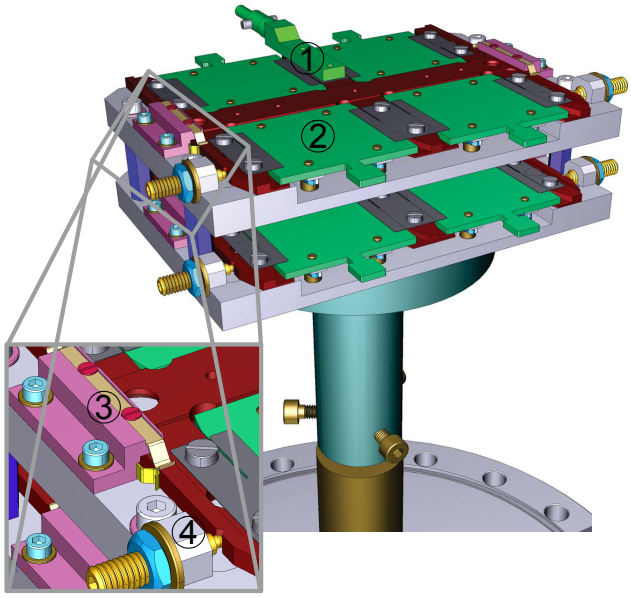

Figure 4.3 | 3D model of the sample storage: the sample storage is able to hold two trays (1), which can be equipped with up to eight sample holders (2) at the same time. Each tray is stabilised by a guide bar (3) and is hold by a pin (4) which pushes into a notch in the tray.

thesis. It is equipped with a rotary feedthrough (PD $40 - 50$ LD), which allows rotation of $360°$ around the vertical axis, and a linear translator (LD $40 - 50$) in order to move the sample storage about $\pm 25\,\mathrm{mm}$ along the vertical axis. Thus, each sample holder can be reached and grabbed with the pincer. The rotary feedthrough and the linear translator were both bought from *VAb Vakuum-Anlagenbau GmbH* [164].
When the tray is moved into the sample storage by the manipulator of the handler chamber, it is stabilised by a guide bar (3). Additionally, it is hold by a pin (4) which pushes into a notch on the long side of the tray. Thereby, the tray is fixed in position after the manipulator of the handler chamber is removed and does not move when a single sample holder is pulled out of the tray.

Sample Transfer

In Figure 4.4 a 3D model of the tools of the sample handling camber, which are needed to move a single sample holder (1), is shown. The SHC is equipped with a wobble stick[3] (MDWS-WZB 100), which was purchased from *VAb Vakuum-Anlagenbau GmbH* [164]. Its front end is assembled with a $90°$ angled pincer that is controlled by the handle on the atmospheric side (see Figure 4.2 (2) and Figure 4.4 (2)). With its help, samples can be handled inside the UHV chamber in order to move one single sample holder from the tray to the IPE manipulator. On the score of compatibility to the already existing sample holder design, the gripping device of the pincer is manufactured in that way that the pin of the sample holder, which is circled in grey Figure 4.4, is completely surrounded by the pincer. The maximum angle of movement is about $\pm 22°$ [164], which is indicated by the thin red lines in Figure 4.4. It is possible to reach both the sample storage as well as the position of the IPE manipulator below the screwdriver.

[3] A wobble stick is a manipulator, which is guided completely manually and which combines linear with angular movement.

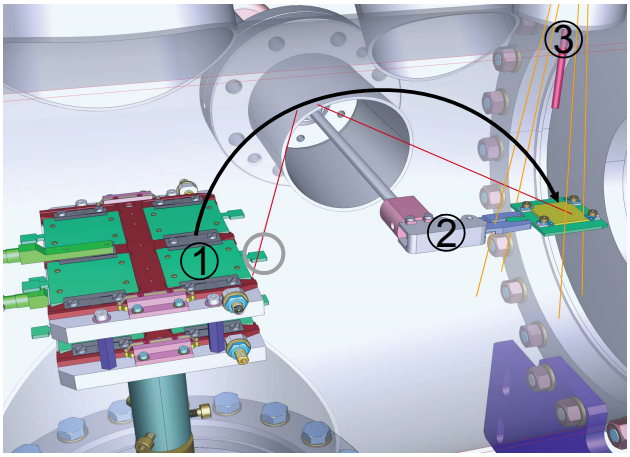

Figure 4.4 | 3D model of the tools used to move a single sample holder: a single sample holder (1) can be pulled out of the tray with the help of the pincer (2). For this purpose, the gripping device of the pincer is designed to completely surround the pin of the sample holder (grey circle). After the pincer is attached to the sample holder, it is turned by 180°, as depicted by the black arrow. Thereafter, the sample holder is inserted into the manipulator head of the IPE spectrometer, which is shown in Figure 4.5 in detail. With the help of the in-vacuum screwdriver (3), the sample holder is fixed on the manipulator and, thereby electrically connected.

After the sample holder is grabbed by the pincer, it is turned by 180° (black arrow) and afterwards inserted into the head of the manipulator of the IPE spectrometer, which is shown in Figure 4.5 in detail. With the help of the in-vacuum screwdriver (Figure 4.4 (3)), the position of the sample holder can be fixed by tightening the four Allen screws (golden), which force the two spring sheets (i) to push on the sample holder. At the same time, the sample holder is electrically connected[4] to the manipulator of the IPE spectrometer. In addition, also the sample surface can be electrically contacted with the help of the custom-designed and completely new developed ring washer (ii). This ring washer can be moved onto the sample surface by rotation of the respective Allen screw. The connection between the ring washer and the sample surface thus enables an in-vacuum bonding of the thin film, which for example, is deposited on insulating substrates. Since IPES is performed in the low-energy range, small magnetic fields effect the electron beam. Therefore, all components of the manipulator head and of the sample holder are manufactured out of titanium, which is not magnetisable.

The in-vacuum screwdriver (Figure 4.4 (3)) consists of a *UHV Design* wobble stick (WSLR-150-H), which is bought from *VACOM Vakuum Komponenten & Messtechnik GmbH* [165]. A robust bellows adapter allows to laterally move and at the same time to tilt the screwdriver. The maximal swivel range is about ±15°, which is indicated by the thin orange lines in Fig-

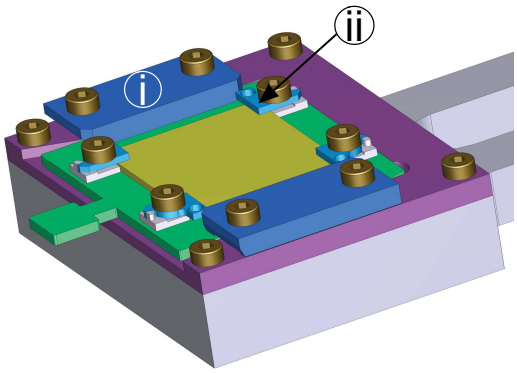

Figure 4.5 | 3D model of the manipulator head of the IPE spectrometer: a single sample holder (green) can be inserted into the manipulator head (violet). It is fixed and, thereby electrically connected by four Allen screws (golden), which force the two spring sheets (i) to push on the sample holder. The Allen screws can be tightened or loosened with the help of the in-vacuum screwdriver. In addition, the sample (yellow) can be electrically connected to the sample holder with the custom-designed ring washer (ii), which can be moved onto the sample surface by a rotation of the respective Allen screw.

[4]The electrical contact of the sample and the sample holder to the manipulator is needed to prevent charging when the electron beam hits the sample.

ure 4.4. In addition, a linear motion and a continuous rotation is possible with the help of a magnetic coupling[5]. The maximum torque that is transmitted is determined by the force that decouples the inner and outer magnets. It is about $0.45\,\mathrm{Nm}$ and the linear break-away force of the axis yields about $65\,\mathrm{N}$, which is sufficient for the intended utilisation. At the in-vacuum end of the *UHV Design* wobble stick an Allen key with a spherical head[6] is mounted.

4.2. Analysis Chamber for the Inverse Photoemission Spectrometer

The inverse photoemission analysis chamber (IPE-AC) was also designed by the engineering department of the I. Institute of Physics and was manufactured by *VG Scienta Ltd* [167] on the basis of the underlying technical drawings developed in the course of the thesis. Since it is fabricated out of µ-metal, in order to shield the interior of the IPE spectrometer from magnetic fields, special design aspects had to be considered: the high magnetic permeability of µ-metal provides a low reluctance of the magnetic flux. Thereby, the shielding effect is achieved by allocating a path for the magnetic field lines around the shielded area. Since the magnetic field lines are able to leave the µ-metal again at every edge or border, the area, which shall be field free, has to be located at a certain distance to the µ-metal chamber wall

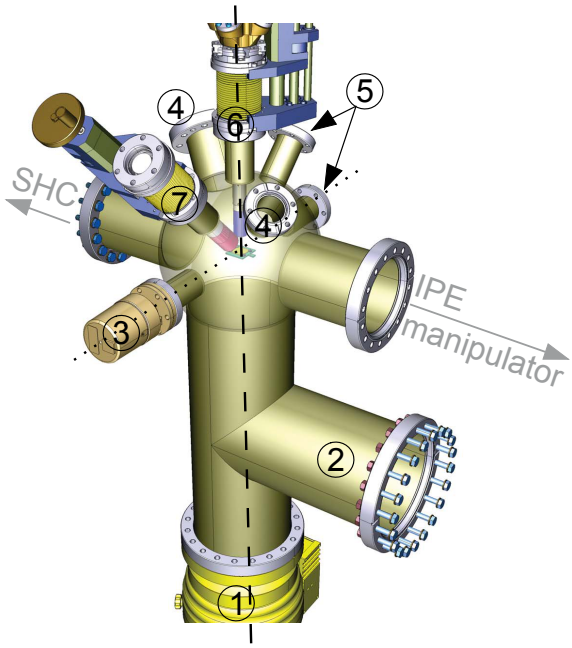

Figure 4.6 | 3D model of the analysis camber of the IPE spectrometer: the chamber is connected to the SHC as well as to the IPE manipulator, which moves a single sample holder from the SHC to measurement position. The UHV conditions of the inverse photoemission analysis chamber (IPE-AC) are provided by a turbo molecular pump (1) and a titanium sublimation pump (TSP) (2). The pressure of the chamber is measured by a cold cathode pressure gauge (3). The chamber's interior can be watched through two view ports (4). The basic design of the chamber is a sphere with two blind-flanged DN 40 CF flanges (5) and three filled DN 40 CF flanges, which are positioned on a 180° spherical line around the measurement position, respectively. The angle between each flange is about 45° . At one of these flanges the pressure gauge is installed, whereas the others are assembled with the electron gun (6) and the gaseous radiation detector (7), respectively. (The dotted line represents the horizontal axis of the chamber, whereas, the vertical axis is expressed by the dashed line.)

[5]The outer rotating ring magnetically couples through a stainless steel vacuum sheath to vacuum-side ring, which both have an identical number of strip magnets [166]. This eliminates the need for edge-welded bellows and reduces the risk of leaks [165].

[6]An Allen key with a spherical head allows turning the screw even if its axis is not aligned with that one of the screwdriver.

and especially to the edges or borders. In order to ensure, that the measurement position is free of magnetic fields, a spherical shape of the chamber is the best design choice. Secondly, the distance between every flange and the centre of the sphere have to be at least equal to the diameter of the inner tube of the flange [167, 168]. For these reasons, the IPE-AC is designed as a sphere with a diameter of about $232\,\mathrm{mm}$ and each flange is located at a distance to the outer wall of the sphere of more than a half of the diameter of its inner tube.

The IPE-AC is connected to the SHC as well as to the IPE manipulator, as it is depicted in Figure 4.6. As mentioned before, both chambers, IPE-AC and SHC, are separated by a *VAT* vacuum gate valve. In order to reach suitable UHV conditions, which are needed for the IPE experiment (see also Section 3.5), the IPE-AC is equipped with a turbo molecular pump (Figure 4.6 (1)) (HiPace®700) from *Pfeiffer Vacuum GmbH* [169]. The turbo pump is mounted on a DN 160 CF-F flange and has a pumping speed of up to $685\,\mathrm{l/s}$ for N_2 [169]. Its ultimate pressure according to *PNEUROP* [170] is lower than $5 \cdot 10^{-10}\,\mathrm{mbar}$ [169]. The turbo molecular pump of the IPE-AC is connected to a scroll pump via a second smaller booster turbo pump, which serves as a support pump for the whole UHV cluster. In order to further enhance the vacuum conditions, a titanium sublimation pump (TSP) (Figure 4.6 (2)) from *VACOM Vakuum Komponenten & Messtechnik GmbH* is also part of the chamber [171]. In a TSP, sublimed titanium is deposited on the surrounding surfaces, which forms a thin layer. Residual gas molecules then form a chemical compound with this layer, which results in a high pumping speed and a better vacuum. The TSP is connected to a liquid nitrogen cooling jacket of the size of a DN 160 CF flange. By cooling the surfaces with water or liquid nitrogen, the pumping speed can be further increased [171]. Additionally to the pump system, a custom-designed heating tent, which can be variably set up and be removed, was purchased from *HORST GmbH* [172]. This heating tent allows a homogenous heating of the chamber wall at $100\,^{\circ}\mathrm{C}$ in order to remove residual water from the walls of the UHV chamber. The chamber pressure is measured by a cold cathode pressure gauge (Figure 4.6 (3)) (IKR 270) from *Pfeiffer Vacuum GmbH* [173]. It is attached to the chamber at a DN 40 CF flange and monitors the pressure in the range of $5 \cdot 10^{-11}\,\mathrm{mbar}$ to $0.01\,\mathrm{mbar}$ with an accuracy of $\pm 30\,\%$ [173]. The base pressure that is reached in the IPE-AC after heating the analysis chamber and the IPE manipulator and after pumping with the titanium sublimation pump in combination with a continuously running turbo pump is lower than $5 \cdot 10^{-11}\,\mathrm{mbar}$. The lowest pressure, which can be reached, is about $(1.1 \pm 2.2) \cdot 10^{-11}\,\mathrm{mbar}$[7].

The interior of the IPE-AC can be monitored through two view ports (Figure 4.6 (4)) of the size of a DN 63 CF flange and of a DN 40 CF flange, respectively. Both windows are coated with a conductive In_2O_3:Sn[8] layer in order to prevent a charging of the glass during electron irradiation. They were purchased from *VAb Vakuum-Anlagenbau GmbH* [164]. The view ports are rotated through an angle of $55°$ regarding the horizontal axis (dotted line) and through an angle of $45°$ regarding the vertical axis (dashed line). An LED-lamp is positioned at the DN 40 CF view port in order to illuminate the chamber.

[7] Although, a minimum detectable pressure of $5 \cdot 10^{-11}\,\mathrm{mbar}$ is reported for the IKR270 pressure gauge [173], it is possible to measure lower values. The estimated error is then a factor of two [174].

[8] In2O3:Sn is called tin-doped indium oxide or indium tin oxide (ITO)

In addition, five DN 40 CF ports are positioned on a spherical line on the horizontal axis (dotted line) with an angle of 45° between each flange (see Figure 4.6). Two flanges are blind-flanged and can be used for the assembling of additional detectors, for example. The remaining ports are equipped with the pressure gauge (Figure 4.6 (3)), the electron gun (Figure 4.6 (6)), which is oriented parallel to the vertical axis (dashed line), and the photon band-pass detector (Figure 4.6 (7)). The electron gun as well as the detector are installed on a linear translator (type CLSM38-50-H-ES) with a lift of 50 mm, respectively, which was purchased from *VACOM Vakuum Komponenten & Messtechnik GmbH* [175]. Figure 4.7 shows a schematic drawing of the IPE spectrometer. In addition, the calculated lengths as well as the travels of the electron gun (ELG-2) (in violet) and the detector (in blue) are given in mm, respectively. In order to prevent collision damage during experiments, safety distances were considered during the planning phase. They are painted in red and are also given in mm. Consequently, the electron gun can be set to higher positions, when the sample has to be changed, for example. Thus, collision damage on the gun and the IPE manipulator is prevented, but the working distance of 20 mm between gun and sample can be restored after having exchanged the samples. Since the count rate increases with a higher solid angle of detection $\Omega_{\text{detection}}$ [176], the detector can be brought as close as possible to the sample, but the implemented design assures a minimum distance of 5 mm between the detector and the electron gun. Hence, damage due to a collision is also prevented. The resulting measurement position is located at a distance of 32 mm between the window face of the detector and the middle of the sample holder.
In the following, the main parts of the inverse photoemission analysis chamber, the electron gun, the detector and the sample manipulator, are discussed from a technical point of view.

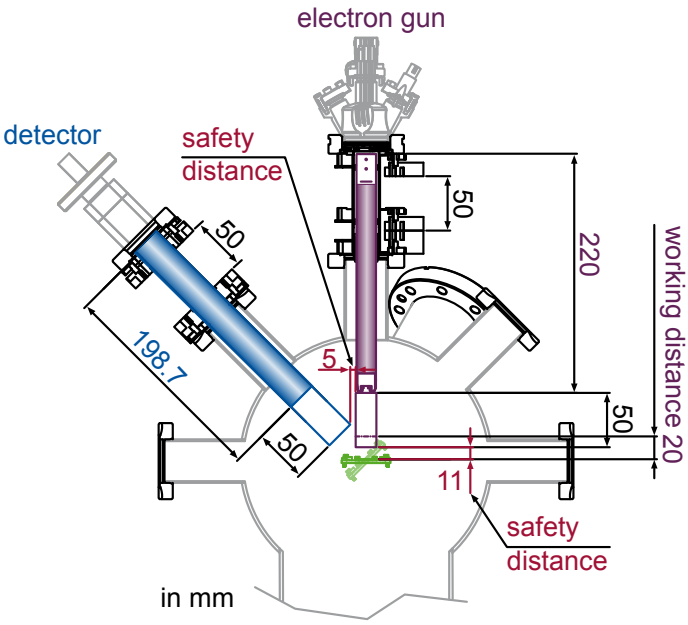

Figure 4.7 | Technical drawing of the length and safety distances: electron gun (printed in violet) and detector (in blue) are installed on a linear translator with a lift of 50 mm. In order to prevent collision damage upon experiments, safety distances (printed in red) as well as the working distance between the gun and the sample manipulator (in green) were considered during the planning phase. The resulting length of the ELG-2 and the detector are also drawn. All values are given in mm.

Electron Gun

The IPE spectrometer is equipped with an electron gun (ELG-2), which was purchased from *Kimball Physics Inc.* [145]. It provides a low energy, medium spot, electron beam [177]. The main components of the ELG-2, which are used to produce and control the electron beam, are: cathode, grid, anode, focus and deflection. These components are controlled by modular power supplies composited in the EGPS-1022 power supply. A 3D model of the electron gun in cross section is shown in Figure 4.8. As already mentioned, the ELG-2 is connected to a linear translator (lift of 50 mm) assembled on the IPE-AC via a DN 40 CF flange and a Copper

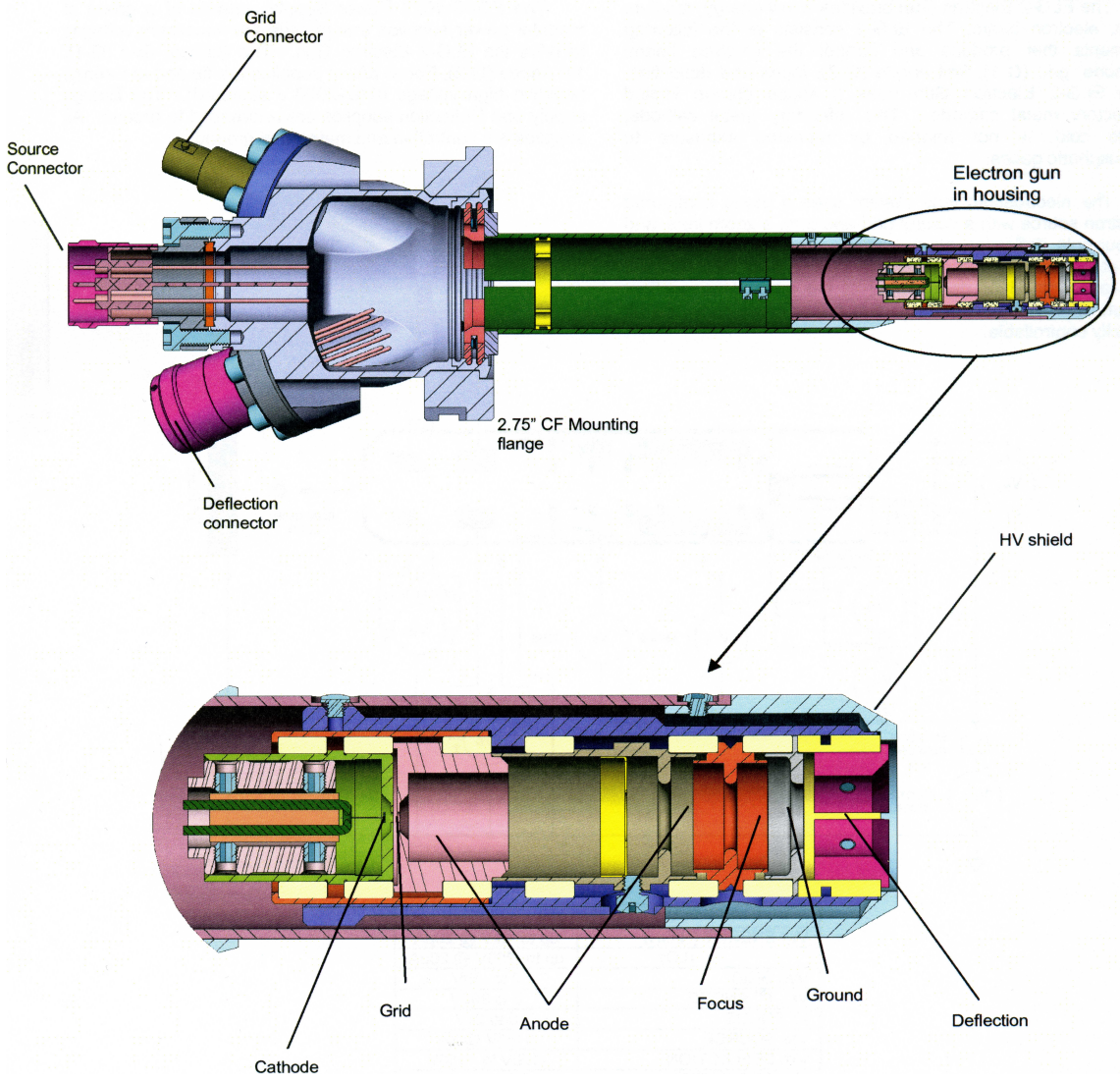

Figure 4.8 | 3Dmodel of the electron gun in cross section: the upper part of the figure shows the whole electron gun including the electrical connectors and the housing of the gun. The enlargement in the bottom depicts the major components needed to produce and control the electron beam: cathode, grid, anode, focus, ground and deflection. (Reprinted with kind permission from [177]. Copyright ©2013 by *Kimball Physics, Inc.* Wilton, N.H.)

gasket. In the upper part of Figure 4.8, the whole gun is displayed. The source connector supports the cathode, first anode and focus, whereas, grid and deflection are connected to the power supply by the grid connector and the deflection connector, respectively. Source, grid, anode and focus power supplies are floated at the energy of the beam. The energy supply and the supplies needed for the deflection of the beam are again referenced to the ground potential [177].
The enlargement of the electron gun displayed in the bottom of Figure 4.8 depicts the main part consisting of the cathode, grid, anode, focus and deflection. The emitted electrons are pre-accelerated in the gird/first anode part of the gun. Thereafter, the electron beam is accelerated or decelerated and focused in the focus/ground section. After having left the ground, the electrons can be deflected by a four-pole deflection plate system [177]. The y- and x-direction of the deflection are oriented parallel the horizontal axis of the IPE-AC and in the perpendicular direction, respectively. Strictly speaking, a deflection in the x-direction means a movement of the beam in the same direction as a motion of the IPE manipulator. A deflection in the y-direction, then, moves the beam on the dotted line of Figure 4.6.
As cathode a barium oxide (BaO)-coated disc cathode was chosen, which is characterised by low-light and low-temperature: compared to standard refractory metal cathodes, it has a lower heating current range and starts to emit electrons at lower temperatures [177]. Thus, a lower electron energy uncertainty[9] of $\Delta E_{EE} \lesssim 300\,\mathrm{meV}$ is achieved [141, 145]. In addition, longer lifetimes[10] are reached due to the lower heating current of the cathode [177].
The working principle and the characteristics of the electron gun are discussed in more detail in Section 5.1.

Photon Bandpass Detector

The photon bandpass detector was purchased from *M. Donath*'s research group at the Westfälische Wilhelms University of Münster, who can draw on a great pool of experience on building gaseous radiation detectors for IPES [140, 149, 155]. Its basic design is shown in Figure 4.9 [149, 178]: the detector is built as a modular system of a housing unit and an insertion unit. The housing unit is a stainless steel tube, which is weld on a DN 40 CF flange connected to a linear translator on the IPE analysis chamber. At its end, a transmission cut-off entrance CaF_2 window[11] from *Korth Kristalle GmbH* is mounted [179]. Outside the window a fine mesh of metal wires is placed in order to shield the fraction of the electrical field coming from inside the detector tube through the insulation glass [29, 176, 180]. Since an acetone-argon mixture is used as the counting gas, a Perlast O-ring[12] (G75H from *C. Otto*

[9] The electron energy uncertainty for a standard refractory metal cathode is about $\Delta E_{EE} \sim 500\,\mathrm{meV}$ [145].
[10] The lifetime of a cathode depends on the evaporation rate of the coating material, which, in turn, depends on the temperature at which the cathode is operated as well as on the vacuum conditions [177].
[11] The circular CaF_2 window has a diameter of $20\,\mathrm{mm}$ and a thickness of $2\,\mathrm{mm}$. It has VUV-quality and is laser-polished.
[12] A Viton gasket cannot be utilised here due to its solubility in acetone. However, at some point in time, Perlast gets permeable for argon, but it is never damaged or influenced by the acetone. The leakage of argon has to be considered when using the detector for longer measurements with just one gas filling. The change of the base pressure of the UHV chamber can be in the order of one magnitude when argon is diffusing through the perlast O-ring.

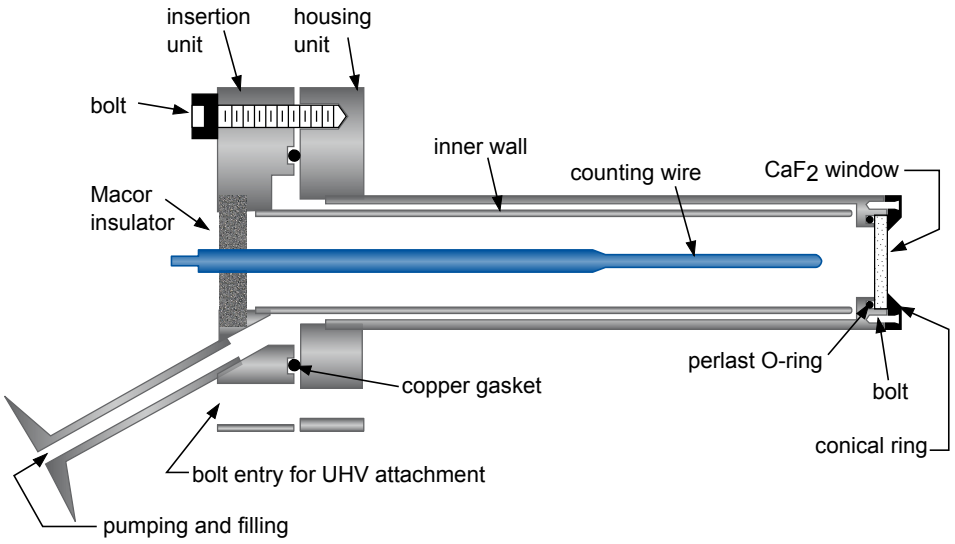

Figure 4.9 | Schematic drawing of the photon bandpass detector: the housing unit is closed at its end by a transmission cut-off entrance calcium fluoride (CaF_2) window. The insertion unit includes the inner wall and a small wire, which is placed in the middle of the tube and serves as the anode. The inner wall and the anode wire are the basis of a cylindrical capacitor. The detector can be filled with the counting gas or a gas mixture and can be pumped through a Swagelok port. (This picture is freely adapted from [178].)

Gehrckens GmbH & Co. KG Dichtungstechnik [181]) is chosen as gasket between the window and the stainless steel tube.

The insertion unit holds the inner parts of the detector (inner wall, counting wire and Macor insulator) and is connected to the housing unit with a DN 40 CF flange and a copper gasket. The inner wall and the counting wire serve as the cathode and the anode of a cylindrical capacitor, respectively. The cathode is at ground potential, while a high voltage is applied to the anode during the measurement. The Macor insulator holds the anode wire in the middle of the detector and electrically isolates the anode from the cathode.

The detector can be pumped and filled through a $6\,\mathrm{mm}$ metric Swagelok port. The gas filling system that is connected to this port is depicted in Figure 4.10. The detector and the gas pipelines are pumped by a turbo pumping station (HiCube®80 Eco) from *Pfeiffer Vacuum GmbH* [182]. It consists of a HiPace®80 turbo pump and an MVP 015 as backing pump. The pumping speed is about $67\,\mathrm{l/s}$ for N_2. The gas-fill pressures within the pipelines and the detector are measured by a gas-independent pressure capacitance manometer (type 627D) from *MKS instruments* [183]. The MKS pressure gauge measures the full range from $1000\,\mathrm{mbar}$ to $1 \cdot 10^{-1}\,\mathrm{mbar}$ with an accuracy of $0.12\,\%$ of reading plus or minus the zero stability of $0.002\,\%$ of the final value per centigrade [183]. The gas filling system is equipped with six flow valves, which can be used to mix the two gases (acetone and argon) and to fill the detector with the chosen gas mixture. Liquid, spectroscopy-grade acetone of the purity of $99.6\,\%$ becomes gaseous due to its high vapour pressure as soon as the flow valve is opened. It is allowed to leak into the detector until the pressure needed is reached. If desired, gaseous argon (degree of purity 5.0) can be added to the acetone by opening the respective flow valve. Since the

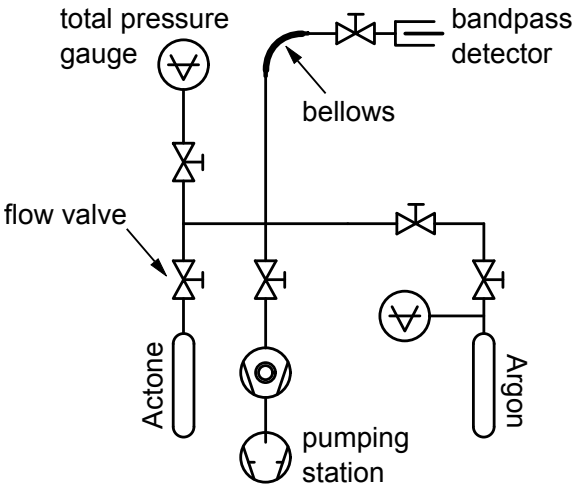

Figure 4.10 | Sketch of the filling system of the photon bandpass detector: the detector and the gas pipelines are evacuated by a turbo pumping station. The flow valves can be opened and closed in order to control the gas flow through the pipelines and the detector. A total pressure gauge is used to control the mixture of the gases. Since the detector is mounted on a linear translator, a bellows is inserted between the gas pipelines in order to keep the system flexible.

detector is mounted on a linear translator with a lift of $+50\,\mathrm{mm}$ from measurement position, a bellows is inserted between the gas pipelines in order to keep the gas filling system flexible. Due to the modular design of the detector, the insertion unit can be removed, so that the susceptible components (the inner wall and the counting wire) can be maintained without breaking the vacuum of the whole chamber.

As mentioned before, the count rate increases with the solid angle of detection $\Omega_{\mathrm{detection}}$. In case of a point source located along the axis of a circular cylindrical detector, $\Omega_{\mathrm{detection}}$ can be written as [143, 184]:

$$\Omega_{\mathrm{detection}} = 2\pi \left[1 - \left(\frac{d_{\mathrm{window}}}{\sqrt{d^2_{\mathrm{window}} + r^2_{\mathrm{window}}}} \right) \right]. \tag{4.1}$$

Here, d_{window} expresses the shortest distance from the middle of the sample to the window face and r_{window} is the radius of the used window. The radius of the CaF_2 window is about $r_{\mathrm{window}} = 10\,\mathrm{mm}$. With the distance between the sample's centre and the window face $d_{\mathrm{window}} = 32\,\mathrm{mm}$ (see Figure 4.7), $\Omega_{\mathrm{detection}}$ is about $\sim 4.6\,\%$ of total $2\pi\,\mathrm{sr}$, which is $\Omega_{\mathrm{detection}} \sim 16.6°$. This agrees very well with the range of the solid angles of detection reported in literature [143, 185, 186].

Sample Manipulator of the Inverse Photoemission Spectrometer

The interior of the inverse photoemission analysis chamber can be seen in detail in Figure 4.11. The travels of the detector (1) and the electron gun (2) are depicted in blue and violet, respectively. Here, the end of each coloured cylinder mark the respective measurement or working position.
The basis of the manipulator, i.e. the bellows and the x-, y- and z- movement, was recycled from an existing, un-used sample manipulator, while the complete head was newly designed and manufactured. The basic structure consists of titanium. The first part of the manipulator head (3), which holds a single sample holder, has already been described before (see

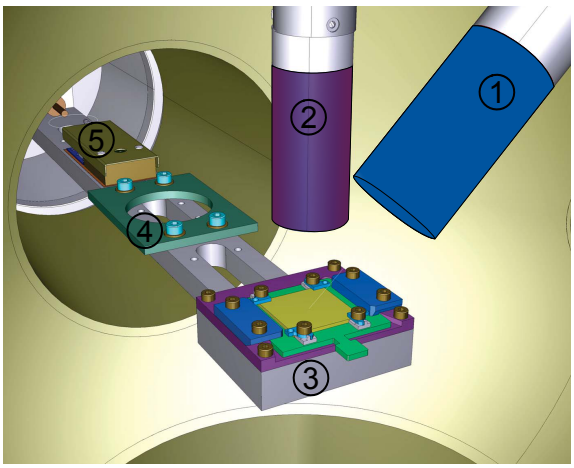

Figure 4.11 | 3D model of interior of the IPE-AC: the travels of the detector (1) and the electron gun (2) are depicted in blue and violet, respectively. Here, the end of each coloured cylinder mark the respective measurement or working position.
The first part of the head (3) is used to hold and electrically contact a single sample holder. In addition, it is equipped with a ZnO:Zn phosphor screen (4) and a faraday cup (5) with an aperture of $0.5\,\mathrm{mm}$ in order to view and measure the behaviour of the electron beam under different working conditions.

Figure 4.5). In addition, a phosphor screen (4) from *GIDS-GmbH–German Image Detector Systems* [187] consisting of a ZnO:Zn phosphor with an emission threshold of $2.2\,\mathrm{V}$ [188] is assembled on the manipulator. Consequently, the behaviour of the electron beam under different working conditions can be monitored also for low electron energies. In order to measure the beam divergence and the profile of the electron beam, the manipulator is furthermor equipped with a faraday cup (5) (FC-70) with a custom aperture of $0.5\,\mathrm{mm}$ from *Kimball Physics Inc.* [189].

5. Characterisation of the IPE Spectrometer

After the IPE spectrometer had been successfully mounted and assembled to the ORPHEUS cluster tool, the setup was characterised in the course of this thesis. First, the behaviour of the electron gun was characterised in order to find adequate operation parameters, which fit the conditions discussed in Section 3.5. The results are shortly summarised in the following. Thereafter, Section 5.2 first outlines the physical properties of the photon bandpass detector, before the characteristics of the implemented detector are described in case of the Geiger-Müller counter and afterwards in case of the proportional counter. In the last section, the total energy resolution of the IPE spectrometer is determined and the result is compared to other spectrometers found in literature.

5.1. Characterisation of the Electron Gun

The IPE spectrometer is equipped with an electron gun ELG-2 from *Kimball Physics, Inc.* Besides the electron energy E_{EE}, the voltages U_{ES}[1], U_{G}, U_{A}, U_{F} applied to the cathode, grid, anode and focus lenses, respectively, are important parameters to control the electron beam. In order to find the optimal operation parameters of the electron gun, for which the resulting electron beam meets the requirements of an IPE spectrometer (see Section 3.5), the electron gun was characterised in the course of the thesis. After the important operation voltages are briefly introduced, the results are discussed and explained in the following.

Figure 5.1 depicts the block diagram of the electron gun ELG-2 [177]. Free electrons are produced by thermionic emission. Therefore, the cathode is heated by increasing the cathode voltage U_{ES}. After the electron emission has been started, the beam is pre-accelerated in the grid and anode section of the gun. The voltage U_{G} applied at the grid is of negative potential and thus able to suppress the electrons that have left the cathode. The grid voltage can be used to totally cut off the electron beam when the sample has to be exchanged, for example. The anode voltage U_{A} is controlled by a positive voltage supply. It creates an electron extraction field between the cathode and anode in order to increase electron emission. Thus, the emitted electrons are pre-accelerated. After having left the anode section, the beam is

[1] The index 'ES' is the abbreviation for electron source.

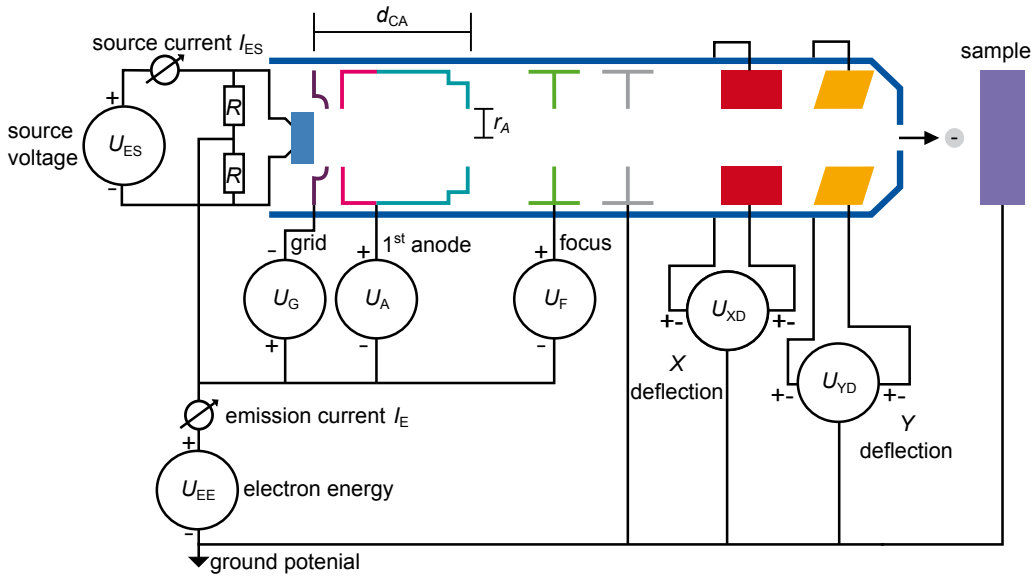

Figure 5.1 | Block diagram of the electron gun ELG-2: after electron emission of the cathode (U_{ES}) has been started, the electron beam is pre-accelerated in the grid (U_G) and anode (U_A) section and is then focused (U_F) and accelerated or decelerated (U_{EE}) in the zoom lens section. The beam can be directed in 2 dimensions by using a four-pole deflection plate system (U_{XD} and U_{YD}). (This picture is freely adapted from [177]. Copyright ©2013 by *Kimball Physics, Inc.* Wilton, N.H.)

focused or de-focused by applying U_F in the zoom lens section. Afterwards, it is accelerated or decelerated to the electron energy $E_{EE} = e \cdot U_{EE}$. Optionally, the beam can be deflected or a raster modus can be applied by using the four-pole deflection plate system and applying the voltages U_{XD} and U_{YD}. Hence, if desired, the measured sample can be scanned as it is the case in a scanning electron microscope (SEM), for example.

As mentioned before, source, grid, anode and focus are floating on the energy power supply U_{EE}, whereas the energy supply as well as the deflection supplies are referenced to ground potential. In order to prevent the electrons from an additional acceleration or deceleration after having left the gun, also the sample is electrically connected to ground potential. The voltage ranges of each power supply can be found in Table 5.1. In addition, the current ranges of the metered source current[2] I_{ES} and the emission current I_E are given [177].

[2]The source current is limited. This limit is set individually for each system during initial testing at *Kimball Physics, Inc.* For an ELG-2 with BaO cathode, this value is set between 1.15 A and 1.20 A. For the system used in the I. Institute of Physics (IA) at the RWTH Aachen University, it is set to 1.15 A [190].

Table 5.1 | Control and driving voltages of the electron gun. (If not stated differently, the respective value is taken from [177].)

power supply	voltage range
energy U_{EE}	High-energy-mode: up to $-2\,\mathrm{kV}$ Low-energy-mode: up to $-200\,\mathrm{V}$
source/cathode voltage U_{ES} (programmed and metered) current I_{ES} (only metered)	 $0\,\mathrm{V}$ to $+1.20\,\mathrm{V}$ for a BaO cathode $0\,\mathrm{A}$ to $+1.15\,\mathrm{A}$ [190]
Emission current I_E (only metered)	$0\,\mu\mathrm{A}$ to $+20\,\mu\mathrm{A}$
Grid U_G	$0\,\mathrm{V}$ to $-50\,\mathrm{V}$
1^{st} **Anode** U_A	$0\,\mathrm{V}$ to $+200\,\mathrm{V}$
Focus U_F	$0\,\mathrm{kV}$ to $+2\,\mathrm{kV}$
X**-Deflection** U_{XD}	$-150\,\mathrm{V}$ to $+150\,\mathrm{V}$
Y**-Deflection** U_{XD}	$-150\,\mathrm{V}$ to $+150\,\mathrm{V}$

Cathode and Anode

In general, the emission current I_E, i.e. the number of electrons leaving the electron gun per time, depends on

1. the temperature of the cathode, which is proportional to the voltage U_{ES} applied to the cathode, and

2. the voltage U_A applied to the anode.

The lifetime of the cathode is a decreasing function of the temperature, since the cathode material evaporates more quickly at higher temperatures. Thus, in order to ensure the maximum lifetime of the cathode, a low operation temperature of the cathode is required during experiments. Additionally, with regard to a minimum possible thermal uncertainty of the electron energy[3], also the temperature of the cathode has to be kept low and constant in experiments. By taking these aspects into consideration, the emission current only depends on the voltage applied to the anode. In Figure 5.2 the emission current I_E is plotted as a function of the anode voltage U_A for a cathode temperature T_{ES} of $1150\,\mathrm{K}$, which is the lowest stable operation temperature reached during experiments in the course of the current work. Here, the emission current I_E was metered with the electron gun power supply EGPS-1022 for decreasing anode voltages U_A starting at $U_A = 200\,\mathrm{V}$. The measurement was performed when the gun was operating in thermal equilibrium, which is the case approximately one hour after powering up the gun. The time between metering the emission current and the adjustment of the anode voltage was $10\,\mathrm{s}$. The energy of the electrons was set to $E_{EE} = 15\,\mathrm{eV}$, while focus and grid were held at $U_F = 240\,\mathrm{V}$ and $U_G = 0\,\mathrm{V}$, respectively. The base pressure of the chamber was below $5 \cdot 10^{-11}\,\mathrm{mbar}$.

[3]The thermal energy uncertainty of the electron gun is a random distribution. It is assumed by a Maxwellian distribution with a FWHM of $\Delta E_{EE} \sim 2.45 k_B T_{ES}$, where T_{ES} is the temperature of the cathode [191].

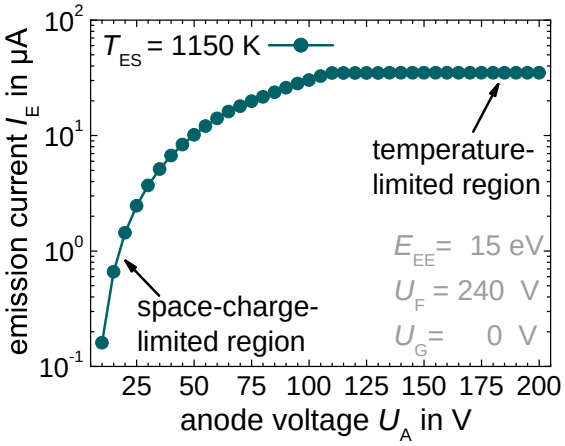

Figure 5.2 | Emission current of the electron gun as a function of the anode voltage: if the temperature of the cathode is held constant, at low anode voltages U_A the emission characteristic of the electron gun is determined by a space-charge-limited behaviour according to the *Langmuir-Child* law. At higher anode voltages, the gun is operating in a temperature-limited region, where the temperature of the cathode is too low to emit additional electrons. Consequently, the emission current is constant. (In the current work, the electron gun was operated with an electron energy of $E_{EE} = 15\,\mathrm{eV}$ and a focus voltage of $U_F = 240\,\mathrm{V}$, while the grid voltage was set to zero.)

For low voltages U_A of the anode, the emission current I_E increases with increasing anode voltage. This relation is described by the *Langmuir-Child* law [177, 192, 193]

$$J_{SCL} = \frac{K \cdot U_d^{3/2}}{d_{CA}^2}, \tag{5.1}$$

$$\Longrightarrow I_{SCL} = \pi r_A^2 \cdot J_{SCL} = 7.35 \left(\frac{r_A}{d_{CA}}\right)^2 U_d^{3/2}\,\mu\mathrm{A}. \tag{5.2}$$

Here, J_{SCL} is the emission current density in $\mathrm{A/cm^2}$ and the constant[4] K equals $2.335 \cdot 10^{-6}\,\mathrm{A/V^{-3/2}}$ in case of an electron. U_d expresses the difference between the voltage applied to the cathode and that one applied to the anode in V, and d_{CA} is the distance between the cathode and the anode in cm (see Figure 5.1). I_{SCL} is the emission current in µA and r_A expresses the radius of the aperture of the anode. The cathode is operating in the space-charge-limited mode, in which the emission current density as well as the emission current only depend on the difference between cathode and anode voltage. Consequently, if the temperature of the cathode is constant, the emission current only increases with increasing anode voltage (see Figure 5.2).

For higher anode voltages U_A, the emission current I_E reaches a constant value. The gun is then operating in a temperature-limited region, where the temperature of the cathode T_{ES} is too low to emit additional electrons. The value for the emission current limit is given by the *Richardson-Dushman* equation [22, 177]

$$J_{TL} = \frac{4\pi m_e e}{h^3} (k_B T_{ES})^2\, e^{-\Phi_{EC}/k_B T_{ES}}, \tag{5.3}$$

$$\Longrightarrow I_{TL} = \pi r_A^2 \cdot J_{TL} = \frac{4\pi^2 m_e r_A^2 e}{h^3} (k_B T_{ES})^2\, e^{-\Phi_{EC}/k_B T_{ES}}, \tag{5.4}$$

where J_{TL} is the emission current density, Φ_{EC} represents the work function of the cathode material, and I_{TL} is the emission current in the temperature-limited region.

[4] The constant $K = (4/9)\,\epsilon_0\,(-2q/m)^{1/2}$ depends on the vacuum permittivity ϵ_0 and the charge-to-mass ratio q/m of the particle.

From the results and the considerations presented above, the following parameter were chosen for the operation the electron gun during the measurement of the samples presented in this thesis:

- the cathode voltage U_{ES} was chosen to provide a constant cathode current of $I_{\mathrm{ES}} = 1.02\,\mathrm{A}$, which is equivalent to a cathode temperature of $T_{\mathrm{ES}} = 1150\,\mathrm{K}$. Thus, a thermal energy uncertainty of the electron gun of $\Delta E_{\mathrm{EE}} \sim 243\,\mathrm{meV}$ is expected, which meets the technical requirements (see Section 3.5).

- It is known from literature that the voltage of the anode has to be set between the space-charge-limited and the temperature-limited region in order to ensure stable electron beam conditions and long lifetimes [177]. Here, the voltage of the anode was chosen to be $U_{\mathrm{A}} = 50\,\mathrm{V}$. The resulting sample current, i.e. the current which is measured on a sample with a pico-ammeter (*Keithley* 6485/E), was always in the microampere range between $1.0\,\mu\mathrm{A}$ and $3.0\,\mu\mathrm{A}$. The achieved sample current also meets the technical requirements discussed before (see Section 3.5).

Beam Characteristics

Since a well-focused electron beam is important for IPE experiments (see Section 3.5), the focus voltage is chosen in a way that it forms an electron beam of small spot size and with a small angular divergence:

- First, the focus voltage was selected on the basis of the manual of the electron gun (see [177] on page 3-7 Fig. 3.5-2).

- Secondly, the shape, spot size and the divergence of the electron beam was measured and checked with the Faraday cup attached to the manipulator head of the IPE-AC manipulator. The aperture of the Faraday cup has a diameter of $0.5\,\mathrm{mm}$, which allows the measurement of the spot size and the shape of the electron beam. However, it was not possible to measure the beam profile or its shape for energies between $5\,\mathrm{eV}$ and $15\,\mathrm{eV}$, which are used in the IPE experiments, since the maximum power ($I_{\mathrm{E}} E_{\mathrm{EE}} < 0.24\,\mathrm{mW}$) of the electron beam achieved was too low for detection. Thus, the electron current was not measurable at the Faraday cup even with a pico-ammeter used for the measurements. Nevertheless, the beam profile and its shape were analysed for an electron energy of $E_{\mathrm{EE}} = 150\,\mathrm{eV}$, which was the minimum energy at which the characterisation could be performed. During the measurement, the gun has been providing a maximum emission current of $I_{\mathrm{E}} = 16\,\mu\mathrm{A} \longrightarrow I_{\mathrm{E}} E_{\mathrm{EE}} \sim 2.4\,\mathrm{mW}$[5] . The characterisation procedure is exemplarily presented and explained in the following. For the purpose of measuring the shape and the spot size of the electron beam, the gun was operated at an electron energy of $E_{\mathrm{EE}} = 150\,\mathrm{eV}$, at a focus voltage of $U_{\mathrm{F}} = 240\,\mathrm{V}$ and an anode voltage of $U_{\mathrm{A}} = 50\,\mathrm{V}$,

[5] The recommended maximum beam power at the Faraday cup is $100\,\mathrm{mW}$.

while the grid voltage was set to zero. The distance between the electron gun and the Faraday cup was about 20 mm, which is the working distance of the electron gun recommended for low energy applications [177]. For determination of the divergence of the electron beam, the distance between the Faraday cup and the electron gun was varied.

◇ Thirdly, after the characterisation of the beam at an electron energy of $E_{\mathrm{EE}} = 150\,\mathrm{eV}$ has been performed, the spot size was visually controlled on the phosphor screen attached to the manipulator head of the IPE-AC manipulator for energies between 5 eV and 15 eV.

In Figure 5.3 the beam profile of the electron beam in x-direction is exemplarily shown. Here, the current measured at the Faraday cup is plotted as a function of the relative x-position of the Faraday cup. The maximum sample current is centred at zero position. The beam profile is clearly Gaussian-like as expected. In order to measure the shape of the electron beam and its spot size, several beam profiles at varying positions in x- and y-direction were recorded. Figure 5.4 shows a two-dimensional (2D) colour plot of the beam size as a function of the current measured at the Faraday cup. The current is printed in colours from red to blue, in which red represents the highest sample current and blue the lowest. The beam is of elliptical shape and has a diameter of $(1.3 \pm 0.5)\,\mathrm{mm}$ in x-direction and $(0.7 \pm 0.1)\,\mathrm{mm}$ in y-direction. The elliptical shape can be explained by a mismatch in the thread which moves the manipulator head in x-direction. This mismatch leads to an inaccuracy in the determination of the exact x-position and, thus, gives rise to the measured widening of the electron beam in x-direction. For a focus voltage of $U_{\mathrm{F}} = 240\,\mathrm{V}$, a roundish shape of the beam was observed on the phosphor screen for a beam with an electron energy of $E_{\mathrm{EE}} = 150\,\mathrm{eV}$ and also for energies $E_{\mathrm{EE}} < 150\,\mathrm{eV}$. The measured spot size again meets the technical requirements (see Section 3.5).

In Figure 5.5, the determination of the beam divergence $\Delta\Theta$ of an electron gun with the help of the Faraday cup is schematically displayed. For this purpose, first, beam profiles are measured at different positions A, B, C with varying distance z from the electron gun. The experimental setup can be found in Figure 5.5 (a), while exemplary beam profiles are shown in Figure 5.3 and Figure 5.5 (b)). Thereby, changes in the beam profile as a function of the distance z give an indication of the beam divergence $\Delta\Theta$ when monitoring the shape of the electron beam waist (schematically shown in Figure 5.5 (c)). The beam divergence of the

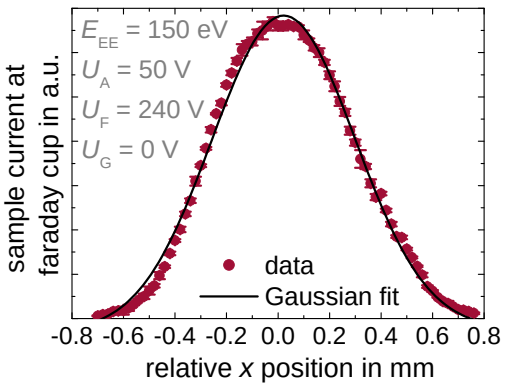

Figure 5.3 | Beam profile of the electron beam in *x*-direction: the sample current is plotted as a function of the relative x-position of the Faraday cup. A clear Gaussian shape of the beam profile can be seen. (The electron gun was operated at an electron energy of $E_{\mathrm{EE}} = 150\,\mathrm{eV}$, a focus voltage of $U_{\mathrm{F}} = 240\,\mathrm{V}$ and an anode voltage of $U_{\mathrm{A}} = 50\,\mathrm{V}$, while the grid voltage was set to zero. The distance between the electron gun and the Faraday cup was set to 20 mm, which is the working distance of the electron gun.)

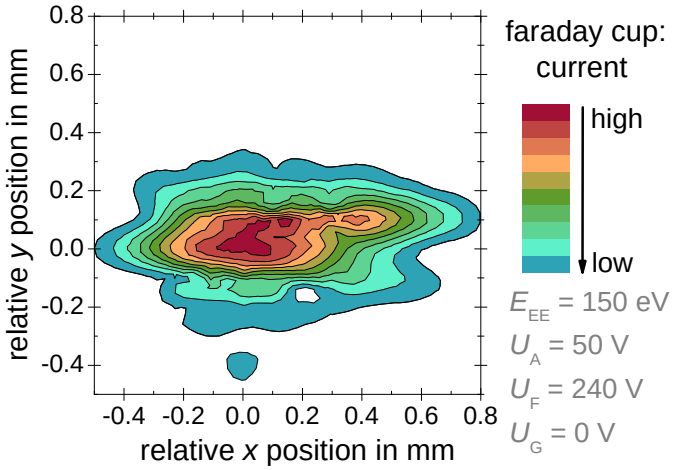

Figure 5.4 | 2D colour plot of the electron beam as a function of the sample current: the electron beam is plotted in two dimensions x and y. The sample current, which was measured by the Faraday cup, is printed in colours from red to blue. Here, red represents the highest sample current and blue the lowest. The beam is of elliptical shape and has a diameter of $(1.3 \pm 0.1)\,\mathrm{mm}$ in x-direction and $(0.7 \pm 0.1)\,\mathrm{mm}$ in y-direction. (The measurement conditions can be found in the caption of Figure 5.3.)

electron gun operated at an electron energy $E_{\mathrm{EE}} = 150\,\mathrm{eV}$, with a focus voltage $U_{\mathrm{F}} = 240\,\mathrm{V}$, an anode voltage $U_{\mathrm{A}} = 50\,\mathrm{V}$ and the grid voltage set to zero is $\Delta\Theta = 4.45° \pm 0.71°$. This value perfectly matches values found in literature [29, 140, 143, 176].

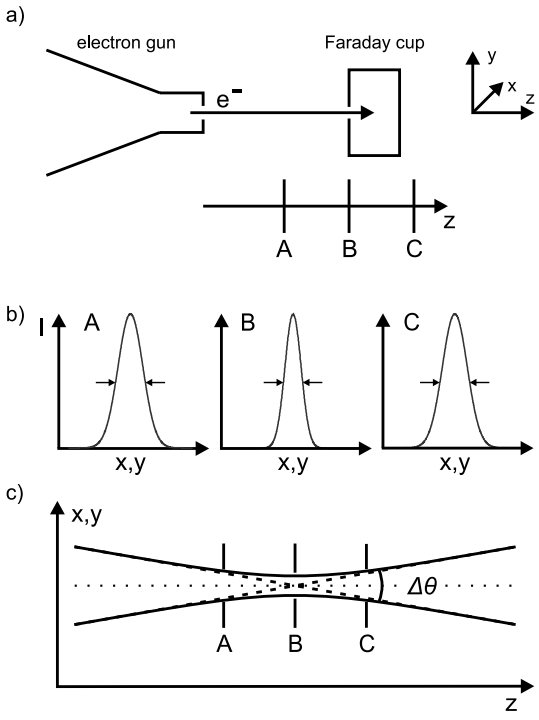

Figure 5.5 | Schematic drawing of the determination of the electron beam divergence: (a) In order to determine the beam divergence, beam profiles are measured as shown in Figure 5.3, but at different positions A, B, C with varying distance z from the electron gun. (b) The FWHM of the beam profiles are determined for the positions A, B, C. (c) The electron beam divergence is obtained from the opening angle $\Delta\Theta$ of the electron beam waist. (Reprinted with permission from [140]. Copyright ©2015, AIP Publishing LLC.)

As a short summary, the operation parameters for the electron gun were determined and the resulting beam has been characterised:

- ◇ During IPE measurements, the current of cathode has to be held constant at a value of $I_{\mathrm{ES}} = 1.02\,\mathrm{A}$, which is equivalent to a cathode temperature of $T_{\mathrm{ES}} = 1150\,\mathrm{K}$ and thus leads to small thermal energy uncertainty and longer lifetimes.

- ◇ The anode voltage is chosen to be $U_{\mathrm{A}} = 50\,\mathrm{V}$, which leads to an adequate sample current.

- ◇ The focus voltage should be set to $U_{\mathrm{F}} = 240\,\mathrm{V}$, which results in a well-focused beam with a roundish shape[6] observed on the phosphor screen.

- ◇ Finally, the beam divergence was determined to $\Delta\Theta = 4.45° \pm 0.71°$, which perfectly matches values reported in literature.

5.2. Characterisation of the Photon Bandpass Detector

> *'The Geiger counter has a long and continuing history of usefulness in a wide range of fields, both academic and applied. The art of the making and use of the Geiger counter remains just that: an art; one has learnt empirically how to construct counters that function in certain ways to perform certain tasks. But behind the pragmatic art there lies a science, albeit a science itself only semiquantitative and heuristic rather than prescriptive.'*
> D. H. Wilkinson, May 1992 [194].

As discussed in Section 3.5, the gaseous radiation detector is chosen for the IPE spectrometer built in the frame of this thesis since it yields more advantages in comparison to solid-state detectors and grating monochromators.

The Geiger-Müller counter was firstly introduced by *H. Geiger* and *W. Müller* in 1928, whereas the gas detector used as a proportional counter appeared in the late 1940s [184]. In 1977, *V. Dose* and co-workers used the gaseous ionisation Geiger-Müller-type counters, which were filled with iodine for inverse photoemission for the first time [77]. Iodine has a high ionisation, and in combination with a CaF_2 window a bandpass with a full width half maximum (FWHM) of $0.8\,\mathrm{eV}$ is reached [28]. However, the use of iodine has some disadvantages: firstly, the bandpass is wide, which results in a poor energy resolution. This poor resolution can be improved by adding an additional strontium fluoride (SrF_2) window in front of the detector, which however results in a decrease of intensity. Secondly, Iodine reacts chemically with the stainless-steel and aluminium of the apparatus. Additionally, the sensitivity strongly depends on the temperature by $8\,\%/°\mathrm{C}$ [153]. Therefore, in 1986, the acetone-filled

[6] An elliptically shaped beam with a diameter of $(1.3 \pm 0.5)\,\mathrm{mm}$ in x-direction and $(0.7 \pm 0.1)\,\mathrm{mm}$ in y-direction was measured with the Faraday cup. This shape was explained by a mismatch in the thread which moves the manipulator head in x-direction, which leads to an inaccuracy in the determination of the exact x-position.

counting tube was firstly introduced by *D. Funnemann* and *H. Merz* [186]. Acetone does not react chemically with the apparatus and the count rate of this detector is not temperature-dependent. In combination with a CaF_2 window, acetone vapour provides an optical resolution between $320\,\mathrm{meV}$ and $330\,\mathrm{meV}$ and has an energy-selective optical bandpass at a mean energy of $\sim 9.8\,\mathrm{eV}$ [29, 149].

The photon bandpass detector, which is installed in the IPE spectrometer, is operated either with a pure acetone or with an argon-acetone mixture. The physical properties of the photon bandpass detector are discussed in a general manner in the following section. Thereafter, the characterisation and the choice of the operation conditions is described first for the Geiger-Müller counter and afterwards for the proportional counter.

Physical Properties of the Photon Bandpass Detector

Although different types of gas detectors are existent, they all work according to the same principle of ionisation of gas particles and charge separation due to an applied electrical field. Based on the book of *G. F. Knoll* [184] and on the report of *F. Sauli* [195], this chapter will outline general properties of such gas-filled detectors.

Detector Geometry, Formation of a Current Pulse and Detection

The counting tube basically consists of a cylindrical capacitor realised by two coaxially aligned cylinders. The inner cylinder, which is most commonly used as the anode, is realised by a fine wire (radius a) as it is schematically sketched in Figure 5.6 on the left[7]. The anode is positioned along the middle axis of a large hollow tube (inner radius b), which serves mostly as the cathode. The space between the two cylinders is filled with the so-called counting gas. Additionally to that, a small amount of quench gas can be mixed to the counting gas in order to prevent multiple pulsing (see also section 'Choice of the Gas Filling' on page 71). One end of the counting tube is closed with a Macor insulator, which holds the thin anode wire in the middle of the cathode and, at the same time, isolates the two electrodes from each other. On the opposite side, the tube is closed by a transmitting window. Thus, a bandpass is created due to the combination of the transmission cut-off of the window and the minimal ionisation energy of the gas mixture inside the detector.

While the cathode is grounded, a positive high voltage U_{detector} is applied to the anode and an electrical field arises inside the capacitor

$$E(r) = \frac{C \cdot U_{\mathrm{detector}}}{2\pi\epsilon_0}\frac{1}{r} = \frac{U_{\mathrm{detector}}}{\ln(b/a)r}, \tag{5.5}$$

where r denotes the radial distance to the anode wire and $C = 2\pi\epsilon_0/\ln(b/a)$ is the capacitance. This electrical field has its maximum at the surface of the anode wire and decreases inversely proportional to r towards the cathode (see Figure 5.6 on the right side). In most areas of the

[7] A complete schematic drawing of the photon bandpass detector is also shown in Figure 4.9.

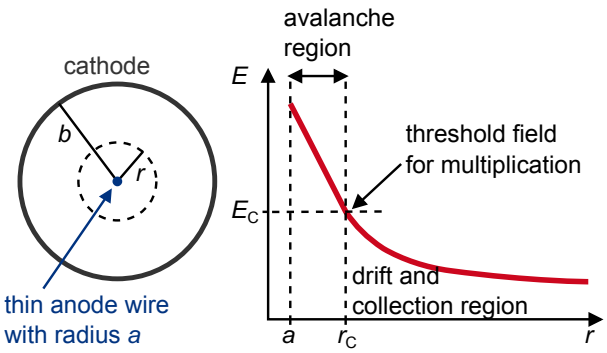

Figure 5.6 | Coaxial cylindrical counter and the shape of the applied electrical field: left: schematic drawing of the cylindrical counter displaying the cathode (radius b), the thin anode wire (radius a).
Right: the shape of the electrical field around the thin anode showing a rapid decrease in electric field strength with distance r from the anodes surface limiting the multiplication region to a small volume. (This picture is freely adapted from [184], [196].)

detector, the field causes the positive and negative charges created during primary radiation to drift in opposite directions to the cathode and anode, respectively. If then a charge Q is moved along the distance dr in a system with the total capacitance lC, where l denotes the length of the counter tube, the induced signal dU can be expressed by

$$\mathrm{d}U = \frac{Q}{lCU_{\text{detector}}} \frac{\mathrm{d}U}{\mathrm{d}r} \mathrm{d}r. \tag{5.6}$$

During the migration of these charges, many collisions with neutral gas molecules or atoms take place. Since the positively charged ions feature a low mobility, they achieve very little average energy between theses collisions. In contrast, the free electrons can easily be accelerated. Consequently, very close to the anode and in case a critical threshold E_C of the electrical field strength is reached, they may have an energy greater than the ionisation energy of the neutral gas molecules or atoms. The distance at which E_C is reached is denoted by r_C (see also Figure 5.6 on the right side). In case the electrons reach an energy greater than the ionisation energy of the neutral gas molecules or atoms, an additional ion pair can be created during collision. The electron created by this secondary ionisation process is also accelerated by the electrical field and, thus, can create an additional ionisation, and so on. The gas multiplication process has the form of a cascade. It is known as Townsend avalanche, in which each free electron created in such a collision can potentially create more free electrons by the same process. The avalanche multiplication amplifies the signal amplitude by several orders of magnitude, since more ion pairs and free electrons can contribute to the signal.

Since the electrons are produced very close to the anode wire, it is known from literature that their contribution to the signal is very small [195]. The positive ions, on the contrary, drift across the counter and generate most of the signal. It can be easily shown for typical counters that the electron contribution to the signal is about $1\,\%$ of the total. As a consequence, the time development of the signal can easily be calculated by assuming that the positively charged ions leaving the surface of the anode with constant mobility are the only contribution. After integration of Equation (5.6), the time-dependent signal $U(t_C)$ is given by

$$U(t_C) = -\frac{Q}{4\pi\epsilon_0 l} \ln\left(1 + \frac{t_C}{\tau}\right). \tag{5.7}$$

Here, t_C represents the charge collection time and τ is time constant which depends on the geometry of the detector and the measurement conditions. It can be seen that half of the

signal is developed after one thousandth of total time. After this fast increase, the signal grows much slower. Therefore, a resistance R is added into the measurement circuit in order to terminate the counter, such that the signal is differentiated with the time constant $\tau = RC$[8]. In Figure 5.7 the time development of the signal $U(t_C)$ over the charge collection time t_C is depicted for different time constants τ. The slowly increasing sector of signal development is cut off due to the differentiation with τ. Thus, a subsequent pulse can be detected. In order to preserve the fast increasing part of the signal, the time constant τ normally amounts a few microseconds.

Since the arrival of the radiation quantum is a random phenomenon, which is Poisson-distributed, the time intervals between these current pulses are statistically spread.

Modes of Detector Operation

As it is said before, radiation detectors produce an electrical signal after each interaction of a photon with the counting gas. The signal generated during such an irradiation has to pass through a series of electronic circuits in order to be amplified and measured. There are two fundamental ways of producing the signal by the circuitry: pulse mode ($\tau \ll t_C$[9] or $\tau \gg t_C$) and current mode or mean square voltage mode (MSV mode) (both $\tau \to 0$).

Pulse Mode

The pulse mode is the most commonly used mode of operation, in which each individual irradiation quantum that interacts with the counting gas generates a separate electrical pulse. This mode provides information about the properties of the each detected photon. Circuits with a large RC are commonly used in radiation spectroscopy systems, in which the distribution of the incident radiation is measured. In such a system, the measured pulse height U_{max} is directly proportional to the corresponding amount of charges N generated within the detector and thus to the deposited energy. In simpler approaches, all pulses above a low-level threshold are measured. This pulse counting is useful for applications, for example in Geiger-Müller tubes or proportional counters, in which only the intensity of radiation is of interest. A major disadvantage of this operation mode, especially for Geiger-Müller counters, is the

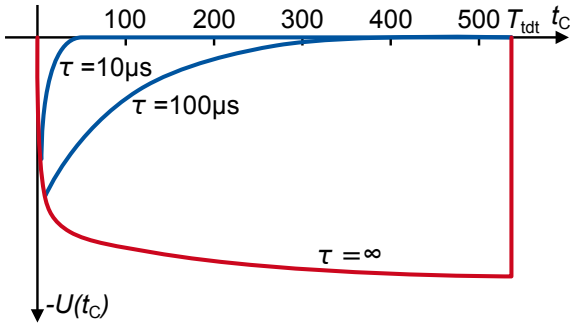

Figure 5.7 | Time development of the pulse in a gaseous ionisation detector: the pulse shape obtained with several different time constants τ over the charge collection time t_C is shown. At first the signal increases very fast in only a view hundred nanoseconds followed by a very slow increase. T_{tdt} means the total drift time of the positive ions from the anode to the cathode. (This picture is reprinted with permission from [195] ©1977 CERN.)

[8] Here, C represents the capacitance of the detector and the measurement circuit.
[9] Here, t_C still denotes the charge collection time.

so-called dead time, which is the time after each counting event during which the system is not able to record another one. If a second interaction occurs during this time interval, its signal will be lost. Furthermore, if it is close enough in time to the first interaction, it may even distort the signal from the first interaction. The fraction of counts lost from dead-time effects is smaller at low interaction rates and increases with increasing interaction rate and, thus, with the count rate.

Current Mode
If the time between events becomes too short to carry out an adequate analysis or if the current pulses from successive events begin to overlap in time, pulse mode becomes impractical or even impossible. In that case, a current metre is connected to the detector output and the signal can be measured in current mode or in MSV mode. Assuming that the current metre has a fixed response time T, then the recorded signal will be a time-dependent current. The response time T is usually longer compared to the average time between individual current pulses from the detector, so that an average current is recorded at a time t. This current depends again on the product of the interaction rate and the charge per interaction. Most ionisation chambers, including ion chamber survey metres and the dose calibrators used in nuclear medicine, are operated in current mode. Both modes – current mode or MSV mode – are also used for measurements in environments with mixed radiation. In current mode the measured current linearly reflects the charges contributed by each radiation type, while the MSV mode favours a type of radiation giving the larger average charge per event.

The achievable sensitivity is often much larger when using pulse mode in comparison to that when using current or MSV mode. Additional to that, each pulse amplitude carries information of the individual pulse, so that the pulse mode is more advantageous in comparison to the usage of one of the others. Consequently, the pulse mode is the most common choice for radiation detector application. The photon bandpass detector, which is used in inverse photoemission spectroscopy, is also operated in pulse mode, so that all following subsections will only be discussed for this mode.

Avalanche Formation and Gas Multiplication Factor

Gas multiplication is a consequence of the migration of free electrons in a strong electrical field. At low values of the field, charged particles (electrons and positive ions), which are created during radiation, simply move to their respective electrodes. During this movement they collide with neutral gas atoms or molecules of the counting gas. When the field strength is above $10^6\,\mathrm{V/m}$ for typical gases at normal pressure, the electrons gain enough energy between these collisions to initiate a secondary ionisation. These secondary electrons are also accelerated towards the anode. During their movement, they collide with neutral gas atoms as well, and additionally ionise the hit molecules. The growth of the amount of electrons is terminated when they reach the anode. This cascade-like production of electrons, which is triggered by a single free electron, is called Townsend avalanche.

In Figure 5.8 the time development of such an avalanche is shown. First a single electron drifts towards the anode and thereby, undergoes ionising collisions in regions of increasingly high fields. A drop-like avalanche develops in which the electrons are in front and the ions move behind. Shortly thereafter, the avalanche surrounds the wire, because of lateral diffusion and the small diameter of the anode. The electrons are collected within only a few nanoseconds and the positively charged ions migrate slowly towards of the cathode.

The total charge Q generated by n_0 original ion pairs can be expressed by

$$Q = n_0 e M, \tag{5.8}$$

where M is the average gas multiplication factor. The average gas multiplication factor is referred to as the ratio between primary and secondary generated electrons. M is a characteristic parameter of the counter and can be written as

$$\ln(M) = \int_a^{r_C} \alpha(r) \mathrm{d}r. \tag{5.9}$$

Here, $\alpha(r)$ denotes the first Townsend coefficient. The integration is carried out from the anode radius a to the critical radius r_C beyond which the field is not strong enough to support gas multiplication (see also Figure 5.6 on the right side). In general, the first Townsend coefficient is given by [197]

$$\frac{\alpha(r)}{p} = A \cdot \exp\left(-\frac{Bp}{E(r)}\right), \tag{5.10}$$

where A and B are gas-dependent parameters, p denotes the pressure and $E(r)$ represents the electrical field strength. Additionally, $\alpha(r)$ is also dependent on the ionisation path λ_i, i. e. the distance in field direction the electron has to travel to gain enough energy between

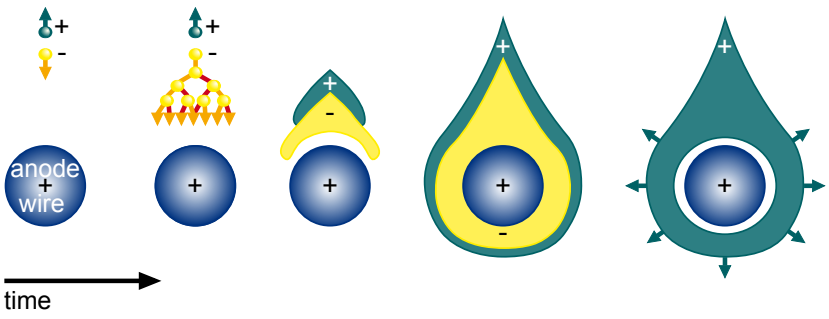

Figure 5.8 | Time evolution of a Townsend avalanche: the individual stages of the evolution of a Townsend avalanche are shown. First, the charges of the ion pair are separated. The electron and the positively charged ion are accelerated towards the wire and the cylindrical cathode, respectively. If a critical value of the field strength is reached, the electron starts an avalanche by multiple collisions with the gas atoms until the front reaches the anode wire. Shortly thereafter, the avalanche surrounds the wire, because of lateral diffusion and the small diameter of the anode. The ions are left behind in a characteristic drop shape. While the electrons are collected from the wire, the ions form a belt around the wire and drift slowly to the outside. (This picture is reprinted with permission from [195]©1977 CERN,[196] ©2011 CERN.)

two successive ionisations. λ_i in turn is dependent on the gas pressure and on the electrical field strength [197]. If λ_m[10] is the mean free path of an electron and $\lambda_m < \lambda_i$, the gas multiplication is small. The electron gains not enough energy for a successive ionisation and undergoes elastic collisions. If $\lambda_m \geq \lambda_i$, the distance between two collisions in the field direction becomes greater than the electron path required to gain enough energy to ionise atoms and gas amplification is initiated [197].
Equation (5.9) can be derived in two different ways:

◇ First, α can be calculated by using Equation (5.5) and assuming that the first Townsend coefficient is linearly dependent on the average energy of the electrons $\bar{E}$ ($\alpha = \bar{E}Nk$), with N being the number of molecules per unit volume and k being the constant of proportionality. If, furthermore, $1/\alpha$ is the mean free path for ionisation, the average energy $\bar{E}$, which is obtained by an electron from the electrical field between collisions, is $\bar{E}/\alpha$ with

$$\alpha(r) = \sqrt{\frac{kNCU_{\text{detector}}}{2\pi\epsilon_0}}\frac{1}{r}. \tag{5.11}$$

Inserting this into Equation (5.9) gives

$$\ln(M) = \sqrt{\frac{kNCU_{\text{detector}}}{2\pi\epsilon_0}}\int_a^{r_C}\frac{\mathrm{d}r}{\sqrt{r}}, \tag{5.12}$$

$$= 2\sqrt{\frac{kNCaU_{\text{detector}}}{2\pi\epsilon_0}}\left(\sqrt{\frac{r_C}{a}} - 1\right). \tag{5.13}$$

Together with $r_c/a = U_{\text{detector}}/U_T$, where U_T is the threshold voltage, Equation (5.13) can be written as

$$\ln(M) = 2\sqrt{\frac{kNCaU_{\text{detector}}}{2\pi\epsilon_0}}\left(\sqrt{\frac{U_{\text{detector}}}{U_T}} - 1\right). \tag{5.14}$$

For $U_{\text{detector}} \gg U_T$, the gas multiplication factor is exponentially dependent on the charge per unit length $Q = CU_{\text{detector}}$ and M can be written as

$$M = K \cdot \exp(CU_{\text{detector}}). \tag{5.15}$$

Thus, it increases exponentially with the applied voltage once the detector voltage is $U_{\text{detector}} \gg U_T$. Consequently, the voltage between cathode and anode has to be extremely stable to ensure a good energy resolution.

◇ The second, but more semi-empirical expression for the logarithm of the multiplication factor is attributable to *W. Diethorn* [198] under the assumption of linearity between α and $\bar{E}$:

$$\ln(M) = \frac{U_{\text{detector}}}{\ln(a/b)} \cdot \frac{\ln 2}{\Delta V}\left(\ln\frac{U_{\text{detector}}}{pa\ln(a/b)} - \ln K\right) \tag{5.16}$$

[10] The mean free path of an electron λ_m depends also on the gas pressure.

Thereby, ΔV expresses the difference in potential the electron is moving through between successive ionising events. K yields the minimum value of E/p below which multiplication cannot occur. Both parameters should be constant for any given gas mixture. Therefore, additionally to the dependency on the detector voltage U_{detector}, the gas multiplication factor M also depends on the gas pressure p. For the reason of a good energy resolution, the gas pressure has to be stable, as well. Thus, since the total amount of charge is directly proportional to gas multiplication factor M (see Equation 5.8), it can be controlled and be optimised by the applied voltage U_{detector} and the gas pressure p.

Choice of the Gas Filling

In principle it is possible to choose every kind of gas or gas mixture for the operation of the gaseous ionisation detector. However, the specific experimental requirements such as low working voltage, high gain operation, long lifetime, etc. lead to the need of a careful choice of them. In addition to that, gas multiplication critically depends on the movement of free electrons. Hence, a gas species which has no considerable electron attachment coefficient has to be chosen. Commonly, noble gases are selected and used in combination with polyatomic gases for better stability and quenching. Gas multiplication occurs in noble gases already at low field strength. Normally, argon gas is used as counting gas due to a high specific ionisation and also for economic reasons.

As mentioned before, gas multiplication is based on a secondary ionisation process caused by collisions between electrons and neutral gas atoms. Besides ionisation, excited argon atoms may also be produced during these collisions. Although these excited atoms do not contribute directly to the avalanche and thus to the signal, two effects can occur leading to the formation of a new avalanche elsewhere in the detector and creating spurious pulses, which are independent on the incident radiation:

- ◇ On the one hand, the excited gases can return to ground state via the emission of a photon with a minimum energy well above the ionisation potential of any metal constituting the cathode.
- ◇ On the other hand, argon ions can be neutralised at the wall of the cathode. In order to keep the balance of energy, either a photon is radiated or a secondary emission, i. e. the extraction of another electron from the metal surface, takes place. Photoelectrons can, therefore, be created at the metal surface of the cathode and, thereafter, are able to start a new Townsend avalanche.

Both processes are able to initiate a new avalanche. These spurious pulses can lead to multiple counting and are a potential cause of instabilities. However, they are often very small and can thus be eliminated by simple amplitude discrimination.

The addition of a small amount of polyatomic molecule gas, such as methane, suppresses the photo-induced effects due to their large amount of non-radiative states allowing the ab-

sorption of photons over a wide range. This gas component is often called quench gas. After absorption, the molecules dissipate the excess energy either by elastic collisions or by dissociation into simpler molecules or by polymerisation into lager complexes. The quenching efficiency of a polyatomic gas increases with the number of atoms in the molecule. Another advantage of more complex molecules is the lower probability for secondary emission. Even a small amount of a polyatomic quencher added to the noble gas changes the operation of a counter completely. It reduces instabilities and due to the lower ionisation potential results in a very effective charge exchange. Good photon absorption and the suppression of secondary emissions allow for gains of up to 10^6 electrons. The highest gains can be achieved by the addition of small quantities of electronegative gases, since they can additionally absorb electrons and thereby build negative ions.

However, the addition of a quench gas has also a significant disadvantage: the lifetime of the counter is reduced due to the dissociation of the polyatomic molecules. For example at a high flux of radiation and at a gain of 10^6, a typical detector changes its operation properties substantially after about 10^{10} counts. The polymers produced by molecular recombination are, furthermore, deposited on the cathode wall. This substantially modifies the operation conditions at an integral flux of around $\left(10^7 - 10^8\right)\ \mathrm{counts/cm^2}$ or higher. Since the polymeric thin film is isolating, the positively charged ions cannot be neutralised at the cathode and a dipole electrical field arises, which extracts electrons from the cathode and through the insulator (Malter effect [199]). A regime of permanent discharge is induced. Even if the original source of radiation is removed, the discharge will not stop until the applied detector voltage is lowered. After this incident, the detector stays damaged. Only a complete cleaning can regenerate the damaged detector.

Counting Curves and Pulse Height Distribution

When operating the radiation detector in pulse mode, normally the pulses provided by the detector are fed to a counting device which counts the incoming pulses as a function of the time. In order to be registered by such a counting device, signal pulses must exceed a given discrimination level U_{trigger} to avoid the counting of electrical noise and spurious pulses. When measuring the count rate, which is the number of pulses N arising during a fixed time interval Δt, as a function of the variation of the discrimination level, information about the amplitude distribution of the pulses is provided. This series of measurements is an experimental determination of the so-called integral pulse height distribution (integral PHD), which needs to be specified in order to find the operation point of the detector providing maximum stability over long periods of time. Depending on the operation region of the detector, less pulses will lie above the level U_{trigger} with increasing U_{trigger}. Consequently, the number of pulses always decreases monotonically with increasing discrimination level until it reaches zero. In the case of a Geiger-Müller counter, the count rate will stay constant over a wide range of U_{trigger}, since all pulses are of the same height[11]. At $U_{\mathrm{trigger}} = 0\,\mathrm{V}$, the measured value corresponds to the total number of pulses N_0 plus the height of the electrical noise. Regions of minimum

[11] For further information, see also the next section.

slope in the integral PHD are called counting plateaus and represent areas of operation in which the detector is minimum sensitive to drifts in discrimination level. In these regions stabile operation conditions are achieved.

Plateaus in the counting data can also be observed by applying a different procedure. In most detectors used for IPES, it is possible to vary the gain or the amplification factor for charges produced during radiation by the variation of the applied voltage U_{detector}. The number of pulses recorded as a function of the applied voltage U_{detector} is called counting curve and is similar to an integral PHD. Consequently, in order to find an operation point of maximum stability, again counting plateaus indicate optimal operation voltage regimes.

Regions of Detector Operation

The dependence of the count rate and, therefore of the amount of generated ion pairs versus the applied detector voltage U_{detector} is depicted in Figure 5.9.

I. At very low values of the detector voltage, the resulting electrical field is too weak to prevent recombination of the original ion pairs, which are created during radiation interaction. Consequently, the collected charge is less than the amount of charges produced by the original ion pairs.

II. **Ionisation Chamber**
As the voltage U_{detector} is raised, recombination is more and more suppressed until the collection of all charges produced by a direct ionisation begins. The counter is now operating in the *ionisation chamber* mode. Ionisation chambers are mostly used in current mode. The measured signal is directly proportional to the number of ion pairs and, hence, to the total radiation dose. However, if knowledge of the energy deposited by each individual radiation interaction is required, the ionisation chamber can also be operated in pulse mode. Since the applied voltage U_{detector} lies below the threshold voltage

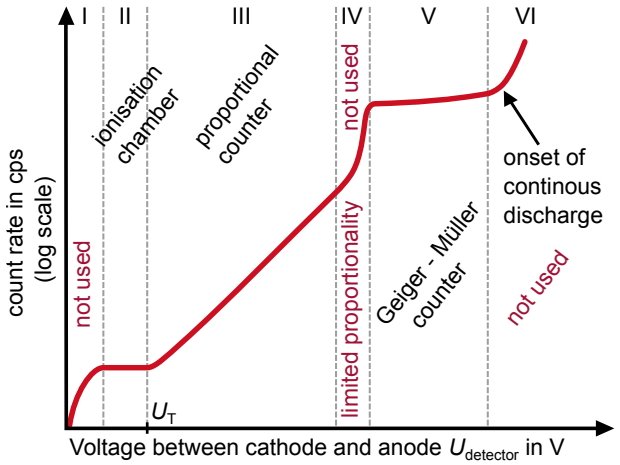

Figure 5.9 | Regions of detector operation: the measured count rate and, therefore of the amount of generated ion pairs is plotted versus the applied voltage U_{detector}, i. e. versus the electric field within the detector. The strength of the electric field between the electrodes determines the detector's response to ionising radiation and thus the operation conditions. The different regions of detector operation are discussed in detail in this section. (This picture is freely adapted from [184].)

U_T, at which gas multiplication starts, in ionisation chamber mode no gas multiplication occurs. As a consequence, the collection of ion pairs is effectively constant until the threshold voltage U_T is reached. The signal amplitude is very small.

III. **Proportional Counters**
When the voltage $U_{detector}$ is raised above the threshold voltage U_T, the electrical field near the anode surface is high enough to start gas multiplication and the observed pulse amplitude increases. Each ion pair produces a single discrete avalanche, which is formed in an axial position within the tube (see also Figure 5.10). One discrete avalanche is, therefore, basically independent of all the other avalanches, which are formed during other ionisation events. Since all avalanches are nearly identical, the collected charge is proportional to the number of original ions pairs created during radiation. As a result, the detected signal is proportional to the energy deposited during radiation. The detector is now operating in the region of true proportionality, which is used for conventional proportional counters. The proportional counter was first introduced as a type of gas-filled detectors in the late $1940s$. Gains up to 10^4 electrons per avalanche can be reached.

IV. At even higher values of $U_{detector}$, the proportionality is gradually lost: a higher electrical field strength introduces nonlinear effects due to the slow drifting of positive ions, which are created during secondary ionisation processes. If the concentration of these ions is high enough, they can be regarded as a space charge which counteracts to the electrical field within the detector. Since further gas multiplication depends on the electrical field strength, some nonlinearities can be observed. This region is called 'region of limited proportionality'. Here, the pulse amplitude still increases with increasing number of initial ions pairs, but not linearly. It is not used for detector operation.
There are two different categories of space charge effects:

- ◇ The so-called self-induced effects develop for sufficiently high gas gains. As a consequence, the positive ions, which are formed during a discrete avalanche, can reduce the field strength so that the number of electrons produced in further stages of the same avalanche is reduced. This effects clearly depends on the magnitude of the

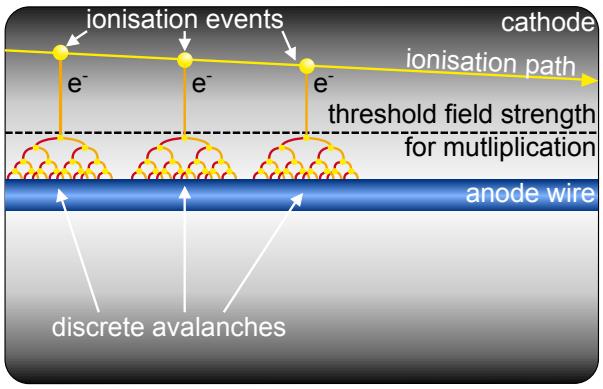

Figure 5.10 | Generation of discrete Townsend avalanches in a proportional counter: proportional counters operate in a region where the voltage between anode and cathode is high enough to allow the formation of discrete Townsend avalanches. Each ion pair produces a single avalanche so that the generated output current pulse is proportional to the deposited energy of the incoming ionisation particle. The avalanche is generated in a small volume around the anode wire (see Equation (5.5) and following), where the minimum electric field strength for avalanche formation is reached.

gas multiplication factor M and on the geometry of the counting tube, but does not depend on the pulse rate itself.

◇ The general space charge effect includes the cumulative effect of all positive ions created during many different avalanches. It becomes very important as the number of events within the counting tube increases and becomes visible even at lower values of gas multiplication.

V. **Geiger-Müller counter**

The region of limited proportionality merges into a region where each Townsend avalanche can trigger another secondary avalanche at a different position within the counting tube by itself. This secondary avalanche is a result of the reabsorption of a UV photon. Unlike the radiation photon, which starts the original avalanche, the second UV photon is emitted by an excited molecule, which has returned into its ground state and its origin is located in the first avalanche. On average, each new avalanche can create at least one more avalanche, which results in a self-propagating reaction chain. This chain leads to many avalanches, which initiate at random radial positions along the wire (see Figure 5.11). In principle, an exponentially growing number of avalanches can be created enveloping the entire anode wire within very short time intervals.

This so-called Geiger discharge is self-quenching when reaching a certain size, i. e. a certain amount of Townsend avalanches took place, since collective effects of all the individual avalanches come into play terminating the chain reaction. The space charge effect caused by the positively charged ions then becomes dominant. The produced space charge is large enough to suppress the electrical field strength below the point at which

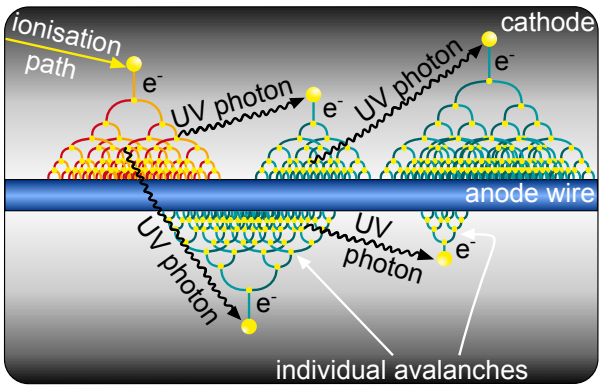

Figure 5.11 | The Geiger discharge in a Geiger-Müller tube: Geiger-Müller tubes operate in a region with a very high field strength that enhance the intensity of each Townsend avalanche (primary avalanche in red/orange). Additionally, this avalanche can trigger secondary avalanches (in colour petrol/turquoise), which are spread along the anode wire, by UV photons generated due to an emission-accompanied relaxation of an excited gas molecule. Once the Geiger discharge reaches a critical size, the large amount of slowly traveling ions reduces the electrical field strength around the anode wire so that the Geiger discharge is terminated. Consequently, all output current pulses are of the same height regardless of the number of original ions pairs that caused the process. (This picture is freely adapted from [184].)

additional gas multiplication can take place. This limiting point is always reached after the same number of avalanches had been created. Consequently, all pulses are of the same amplitude height and the detected signal is independent of the original ionising events. This is the region in which the Geiger-Müller counter operates. The production of multiple avalanches results in an amplification of $\left(10^9 - 10^{10}\right)$ electrons per discharge and, thus, produces a large output impulse which is typically in the order of volts.
As stated before, the large amount of positively charged ions build up a space charge, which terminates the Geiger discharge. Since this ions reduce the electrical field strength, a considerable time has to pass in which the ions move to the counter wall. Afterwards, second Geiger discharge can be generated in the tube. If the field is, however not fully restored, the new discharge will be less intense than before, since fewer positive ions are needed to shut down the discharge again. This pulse may or may not be detected by the counting system, depending on its sensitivity and the chosen discrimination level U_{trigger}. When all positive ions have moved to the cathode, the field strength will be the same as before, which is also true for the pulse height.
Because of the reduction of the electrical field strength below the value at which the Geiger discharge can be initiated, it is not possible to detect another ionising event. During that time interval the detector is 'dead' and any radiation interactions that occur in the tube during this period will be lost. In most Geiger-Müller counter, this 'dead' time is of the order of $50\,\mu\text{s}$ to $100\,\mu\text{s}$.
The operating detector voltage is normally chosen by recording a counting curve and finding the middle of the so-called Geiger counting plateau, as it is also depicted in Figure 5.9. In real cases, the counting plateau always shows some finite slope. This slope can be caused by many effects:

- ◇ Some regions near the end of the tube may have a slightly lower electrical field strength resulting in smaller discharges.
- ◇ Additionally, some small pulses can be counted during the 'recovery time'[12] of the counter.
- ◇ Furthermore, the occasional failure of the quenching mechanism would lead to a satellite or spurious pulse in addition to the primary Geiger discharge.

VI. The last region of operation is the continuous discharge. In this region, the applied voltage U_{detector} is higher than the breakdown voltage of the counting gas. As a consequence, an arc across the electrodes is formed. The detector should never be operated in this region since the electrodes can be severely damaged due to the sputtering processes which accompanies the electrical discharge.

[12] The 'recovery time' describes the time interval required to return into the detectors original state and to become capable for producing a second pulse of full amplitude. In practice, the terms 'dead time' and 'recovery time' are often used interchangeably and the term 'dead time' can also be used to describe both behaviours of the detector.

Since, the photon bandpass detector used for the inverse photoemission spectrometer at the I. Institute of Physics (IA) of the RWTH Aachen is in principle able to be operated as both, Geiger-Müller counter and proportional counter, the characteristics and optimal operation conditions are discussed in the two following sections. Thereafter on page 84 and the following, both detector types are compared and a recommendation on the use of the Geiger-Müller counter for the investigation of materials used in the course of the current work is given.

Geiger-Müller Counter

In order to find the optimal operation conditions for the Geiger-Müller counter, the detector was characterised for different argon-acetone gas mixtures with a total pressure of $p_{\mathrm{GM}} = 75\,\mathrm{mbar}$: for this purpose, the acetone partial pressure was varied and, thereafter, the detector was filled with argon gas up to a total pressure of $p_{\mathrm{GM}} = 75\,\mathrm{mbar}$. For each gas mixture, a counting curve, as it was discussed above, was measured.
In order to monitor the averaged normalised count rate as a function of the detector voltage U_{detector}, the amount of incoming counts was measured 400 times at each detector voltage for one second each. In all these measurements, $50\,\mathrm{nm}$ polycrystalline silver thin films freshly evaporated on a silicon (100) substrate, which had been covered with $5\,\mathrm{nm}$ of chromium as an adhesion layer before, were used. The energy of the electrons was kept constant at $E_{\mathrm{EE}} = 8.5\,\mathrm{eV}$, which is little above the Fermi level. In Figure 5.12, the normalised count rate[13] is plotted versus the number of repetitions for an exemplary gas mixture with an argon-acetone ratio of $70.7\,\mathrm{mbar}/4.3\,\mathrm{mbar}$ and a detector voltage of $U_{\mathrm{detector}} = 945\,\mathrm{V}$. The discrimination level was set to $U_{\mathrm{trigger}} = 200\,\mathrm{mV}$. The mean value of the normalised count rate[13] $\bar{N} = 26.8\,\#/\mu\mathrm{As}$ is marked by the red solid line. Its experimental standard deviation was determined to be $\sigma_{\mathrm{exp}} = 7.1\,\#/\mu\mathrm{As}$. Counting events follow the Poisson statistic with the standard deviation

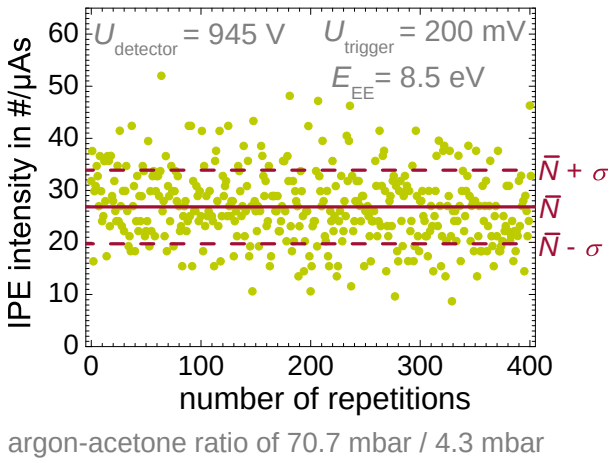

Figure 5.12 | Achieving one data point of a counting curve: the graph shows an exemplary measurement which serves for obtaining one data point of a counting curve. A gas mixture with an argon-acetone ratio of $70.7\,\mathrm{mbar}/4.3\,\mathrm{mbar}$ was used. The discrimination level was set to $U_{\mathrm{trigger}} = 200\,\mathrm{mV}$ and the detector voltage was about $U_{\mathrm{detector}} = 945\,\mathrm{V}$. During the measurement the energy of the electrons was kept constant at $E_{\mathrm{EE}} = 8.5\,\mathrm{eV}$. The normalised count rate[13] is plotted versus the quantity of repetitions. The mean value of the normalised count rate is marked by the red solid line, whereas the dashed red lines illustrate the interval $\bar{N}\pm\sigma$. $69.9\,\%$ of the data points lie within this interval, which is close to the expected value of $68.3\,\%$.

[13] Since in IPES the count rate critically depends on the sample current I_{S}, which varies with the electron energy and the time the electron gun is running, the count rate is normalised to I_{S} for every measurement presented in this thesis. The sample current is measured with the pico-ammeter *Keithley* 6485/E.

$\sigma = \sqrt{\bar{N}}$. Thus, in theory $68.3\,\%$ of the data points should lie within $\bar{N}\pm\sigma$, which is represented by the red dashed lines. Here, the experiment results in $69.9\,\%$ of all measured values being located within the interval $\bar{N}\pm\sigma$. The small discrepancy to the theoretically expected value of $68.3\,\%$ can be explained by the comparatively small statistic of 400 measurements per detector voltage U_{detector}. A higher amount of measurements would lead to a better statistic, but would also increase the measurement time for the whole characterisation.

By repeating this procedure in steps of $5\,\text{V}$ of the detector voltage, a counting curve can be gained by plotting the mean value of normalised count rate versus the detector voltage. It shall be noted that the increase of the voltage should be stopped before the region of continuous discharge is reached, since otherwise the detector might be damaged. Here, the abort criterion is defined by the standard deviation. If the theoretically expected standard deviation $\sigma = \sqrt{\bar{N}}$ is no longer equal to the experimental one within the range of error, it can be assumed that the detector is operating near the region of continuous discharge. Therefore, the experimental and the theoretically expected standard deviation were calculated and compared after each measurement before the detector voltage was increased and a new measurement was started.

The measured detector characteristic is exemplarily shown in Figure 5.13 for a gas mixture of an argon-acetone ratio of $70.7\,\text{mbar}/4.3\,\text{mbar}$. The averaged normalised count rate is plotted in logarithmic scale versus the detector voltage U_{detector}. The dashed grey lines are inserted in order to illustrate the different regions of detector operation (from the left to the right): I, II: the ionisation chamber region, III+IV: the proportional regions and V: the Geiger-Müller region. Additionally, the voltage of operation U_{OP} is marked by a petrol-coloured star. The shape of the curve is discussed in more detail in the following:

the voltage, at which the first counts are measured, is often called starting voltage. When the detector is filled with a gas mixture of an argon-acetone ratio of $70.7\,\text{mbar}/4.3\,\text{mbar}$, the starting voltage is about $U_{\text{SV}} = 850\,\text{V}$[14]. With increasing detector voltage the counting curve

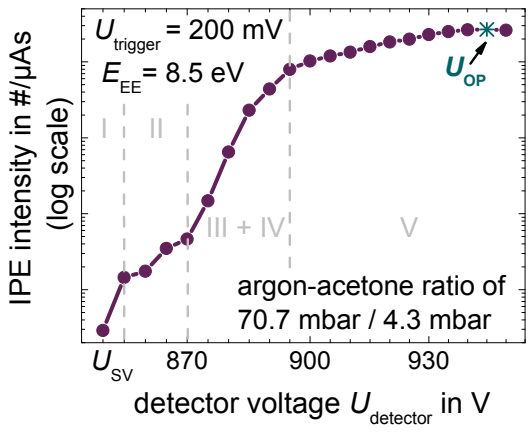

Figure 5.13 | Exemplary plot of a detector characteristic: the graph shows an exemplary for a counting curve. A gas mixture with an argon-acetone ratio of $70.7\,\text{mbar}/4.3\,\text{mbar}$ was used. The discrimination level was set to $U_{\text{trigger}} = 200\,\text{mV}$. During the measurement the energy of the electrons was kept constant at $E_{\text{EE}} = 8.5\,\text{eV}$. The averaged, normalised count rate is plotted in logarithmic scale versus the detector voltage. The detector starts to count at $U_{\text{SV}} = 850\,\text{V}$. The voltage of operation $U_{\text{OP}} = 945\,\text{V}$ is marked by a petrol-coloured star. The dashed grey lines are inserted in order to illustrate the different regions of detector operation: I, II: the ionisation chamber region, III+IV: the proportional regions and V: the Geiger-Müller region (from left to right).

[14] It is possible that the value of the starting voltage slightly shifts, if the gas mixture of the detector was renewed. Small changes in temperature or a small amount residual gas molecules, for example, can change the exact pressure in the detector. During the experiments performed in the course of this thesis, staring voltages between $U_{\text{SV}} = 850\,\text{V}$ and $U_{\text{SV}} = 880\,\text{V}$ were observed.

shows three different slopes. The first can be seen in the interval between $855\,\mathrm{V}$ and $865\,\mathrm{V}$. Since the count rate stays nearly constant, this interval can be attributed to the ionisation region. In the second interval ($865\,\mathrm{V}$ to $895\,\mathrm{V}$), the slope of the counting curve is steepest. The detector is now operating in the proportional region. Thereafter, the Geiger plateau can be seen between $895\,\mathrm{V}$ and $950\,\mathrm{V}$. As mentioned before, the Geiger plateau shows a finite slope which might be owed to slightly lower electrical fields at the ends of the tube or smaller pulses during recovery time, for example [184]. In principle, any voltage in the Geiger-Müller region ensures stable operation conditions and thus can be chosen as voltage of operation U_{OP}. However, in order to prevent the detector from reaching the discharge region during operation[15], an operation voltage slightly larger than the voltage at the transition point but far away from the continuous discharge is chosen in experiments [184]. For a detector filled with a gas mixture of an argon-acetone ratio of $70.7\,\mathrm{mbar}/4.3\,\mathrm{mbar}$, the operation voltage was usually set to a value between $U_{\mathrm{OP}} = 945\,\mathrm{V}$ and $U_{\mathrm{OP}} = 970\,\mathrm{V}$.

In order to find not only stable measurement conditions, but also conditions at which the maximum possible count rate is achieved, the partial pressure of acetone was varied. All measured detector characteristics of different argon-acetone ratios are summarised in Figure 5.14. The figure shows the IPE intensity as a function of the acetone pressure[16] and the detector voltage in a colour plot. Here, red areas represent high intensity and blue areas indicate nearly zero intensity. Every single detector characteristic was gained in the same way as explained before and under the same conditions.
It can be seen that the starting voltage increases with increasing partial pressure of acetone as it was also predicted by *J. Craggs* and co-workers and by *D. H. Wilkinson* [201, 202]. Additionally, the counting curves broaden and the regions of high intensity shift to higher voltages with increasing partial pressure of acetone. This behaviour can be explained by the decreasing mean free path λ_{m} of the electrons with increasing pressure: in order to still fulfil the condition $\lambda_{\mathrm{m}} \geq \lambda_{\mathrm{i}}$, where λ_{i} is the distance in field direction the electron has to travel to gain enough energy between two successive ionisations, it is necessary to also decrease λ_{i}. Consequently, in order to start the avalanche process, the detector voltage U_{detector} needs to be higher with increasing partial pressure of acetone.
The colour plot of Figure 5.14 can be separated in two different parts where the highest achieved IPE intensity marks the reversal point (black rectangle:): a filling with an argon-acetone ratio of $70.7\,\mathrm{mbar}/4.3\,\mathrm{mbar}$ and an operation voltage of $U_{\mathrm{detector}} \approx 945\,\mathrm{V}$. For lower partial pressures of acetone, the maximum gained intensities are lower than that achieved for $4.3\,\mathrm{mbar}$ of acetone and the region of continuous discharge is reached at smaller voltages. For higher partial pressures of acetone, maximum gained intensities slightly decrease again.

The increase of the maximum gained intensities with increasing pressures of acetone can

[15] Since the acetone molecules dissociate into simpler molecules or polymerise into lager complexes during the counting process [195, 200], the detector characteristic shifts towards smaller voltages. Thus, after a long period of measurements, the chosen operation voltage can be too high and the continuous discharge is reached. In order to prevent this scenario, the operation voltage should be decreased after some time, or the gas mixture should be renewed.

[16] After the desired partial pressure of acetone was filled in the detector, the tube was filled with argon up to a total pressure of $75\,\mathrm{mbar}$.

be explained by the multiplication factor, which is not only proportional to the detector voltage, but also to the pressure (see Equation (5.16)). An increased multiplication factor entails larger pulses. Larger pulses in turn increase the count rate, since more pulses can overcome the chosen discrimination level U_{trigger}. Nevertheless, for the region $p_{\text{GM-acetone}} < 4.3\,\text{mbar}$, the partial pressure of acetone seems to be too low for an effective quenching, since the continuous discharge is reached at smaller voltages.
The slight decrease of the maximum gained intensities at higher partial pressures of acetone $p_{\text{GM-acetone}} > 4.3\,\text{mbar}$ can be explained by an increasing amount of electronegative molecules. These molecules are generated by the capture of an electron or the charge exchange between a positive ion and a neutral molecule. During these processes and also by interaction with a photon of an energy of $h\nu = 10.52\,\text{eV}$, the acetone molecules (CH_3COCH_3) dissociate into CH_3CO^+, CH_3 and an electron [200, 203]. In addition, acetone can fragment into H_2, CH_4, CO and C_2H_6 [204]. The capture of a secondary electron or the charge exchange between a positive ion and a neutral molecule quenches the avalanche process within the counting tube [184, 202] and results in smaller pulse heights, which cannot overcome the discrimination level U_{trigger}. Furthermore, the development of a Townsend avalanche can be prevented if the primary electron is captured by the electronegative gas, which also results in smaller count rates.

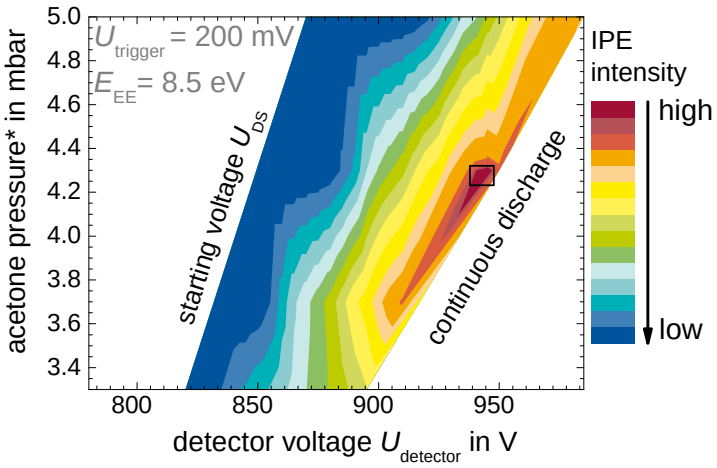

*Note: The detector is operated in Geiger-Müller mode.
↳ The total pressure is set to 75 mbar by adding the sufficient amount of argon.

Figure 5.14 | Overview of all measured counting curves for the Geiger-Müller counter: the discrimination level was set to $U_{\text{trigger}} = 200\,\text{mV}$ and the energy of the electron beam was kept by $E_{\text{ebeam}} = 8.5\,\text{eV}$ during all measurements. The IPE intensity is plotted as a function of the acetone partial pressure* and the detector voltage in a colour plot. More reddish regions mark high intensities, whereas more bluish ones mark low intensity regions. The region of continuous discharge is also marked. In order to achieve the optimal operation conditions and maximum count rate, a gas mixture and the corresponding operation voltage should be in the reddish region, which is marked by the black rectangle: an argon-acetone ratio of $70.7\,\text{mbar}/4.3\,\text{mbar}$ and an operation voltage of $U_{\text{OP}} \approx 945\,\text{V}$ can be chosen.

In order to achieve the optimal operation conditions and maximum count rate, the chosen gas

mixture and the corresponding operation voltage should lie within the reddish region of the graph in Figure 5.14: thus, for all measurements presented in the following, an argon-acetone ratio of $70.7\,\mathrm{mbar}/4.3\,\mathrm{mbar}$ and an operation voltage between $940\,\mathrm{V}$ and $965\,\mathrm{V}$ was used.

Since IPE measurements can take some hours, it is important to verify that the chosen gas mixture in combination with the selected operation voltage provides a stable count rate over the measurement time. Therefore, the normalised count rate for the above mentioned mixture of an argon-acetone ratio of $70.7\,\mathrm{mbar}/4.3\,\mathrm{mbar}$ and an operation voltage of $U_{\mathrm{detector}} = 940\,\mathrm{V}$ was measured for a time period of $2\,\mathrm{h}$, which is shown in Figure 5.15. During this period, the operation voltage of the detector, the discrimination level $U_{\mathrm{trigger}} = 200\,\mathrm{mV}$ and all driving parameters of the electron gun were kept constant. Again, a beam with an electron energy of $E_{\mathrm{EE}} = 8.5\,\mathrm{eV}$ was hitting the surface of a polycrystalline silver thin film, which was produced in the same way as mentioned above.
In Figure 5.15, the green solid line marks the mean value of the measured normalised intensity, which amounts $\overline{N} = 20.8\,\#/\mu\mathrm{As}$. The green line also illustrates a linear fit of the data. The count rate stays nearly constant for at least 2 hours, which is important for the utilisation of such a detector system in an IPE spectrometer. Just a slight increase with a slope of $(5.9 \pm 3.1)\,10^{-5}\,\#/\mu\mathrm{Ash}$ can be observed. This increase is probably caused by the change of the gas mixture over time. The green dashed lines again mark the interval $\overline{N} \pm \sigma$ with $\sigma = 5.4\,\#/\mu\mathrm{As}$. Here, as expected $68.7\,\%$ of the data points lie within this interval.

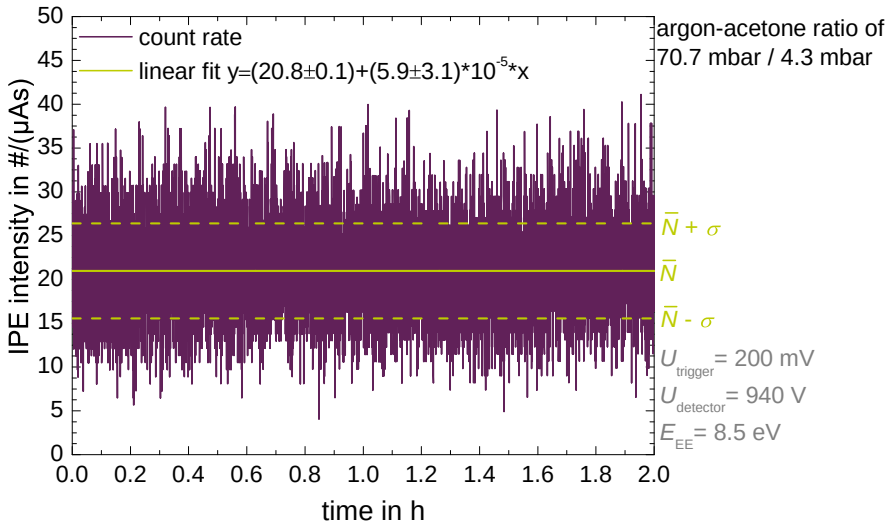

Figure 5.15 | Stability test of the Geiger-Müller counter: the graph shows the normalised IPE intensity in dependence of the time in hours. A gas mixture with an argon-acetone ratio of $70.7\,\mathrm{mbar}/4.3\,\mathrm{mbar}$ was used. The discrimination level was set to $U_{\mathrm{trigger}} = 200\,\mathrm{mV}$ and the detector voltage was about $U_{\mathrm{detector}} = 940\,\mathrm{V}$. During the measurement the energy of the electrons was kept constant at $E_{\mathrm{EE}} = 8.5\,\mathrm{eV}$. The mean value $\overline{N} = 20.8\,\#/\mu\mathrm{As}$ is marked by the green solid line, whereas the dashed green lines mark the interval $\overline{N} \pm \sigma$ with $\sigma = 5.4\,\#/\mu\mathrm{As}$. As expected $68.7\,\%$ of the data points lie within this interval. The count rate stays nearly constant over the time. Just a slight increase with a slope of $(5.9 \pm 3.1)\,10^{-5}\,\#/\mu\mathrm{Ash}$ is observed.

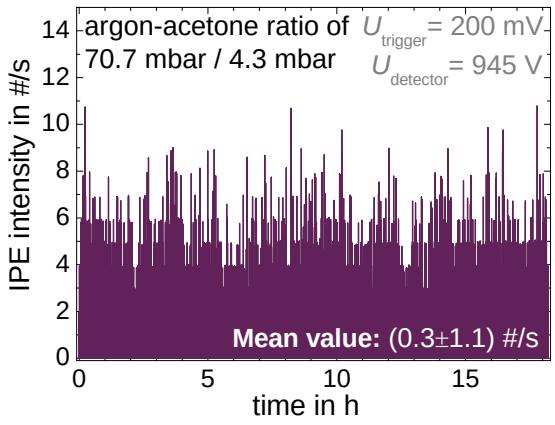

Figure 5.16 | Dark count measurement: the graph shows the IPE intensity that is produced only by interferences of the surrounding, as a function of the measurement time in hours. A gas mixture of an argon-acetone ratio of $70.7\,\mathrm{mbar}/4.3\,\mathrm{mbar}$ was used. The discrimination level was set to $U_{\mathrm{trigger}} = 200\,\mathrm{mV}$ and the detector voltage was about $U_{\mathrm{detector}} = 945\,\mathrm{V}$. During the measurement the electron gun and the pressure control system were turned off. The mean dark IPE intensity is about $(0.3 \pm 1.1)\,\#/\mathrm{s}$.

Additionally, background measurements were performed in a very similar way: the dark counts, meaning the mean count rate produced only when the electron gun is turned off, were measured for a period of $18.3\,\mathrm{h}$. Figure 5.16 shows the count rate that is caused just by interferences of the surrounding, over the measurement time for a Geiger-Müller counter with an argon-acetone ratio of $70.7\,\mathrm{mbar}/4.3\,\mathrm{mbar}$ and a discrimination level set to $U_{\mathrm{Trigger}} = 200\,\mathrm{mV}$. The operation voltage amounted $U_{\mathrm{Detector}} = 945\,\mathrm{V}$. The mean dark IPE intensity is about $(0.3 \pm 1.1)\ \#/\mathrm{s}$, which is comparable to values gained in *M. Donath's* research group at the Westfälische Wilhelms University of Münster [205, 206].
It is important to mention that the pressure gauge was turned off during the measurement of the background. It has been found out that the pressure gauge in its on-state also causes background counts, which leads to an up to ten times larger dark count rate. Therefore, it is recommended to turn off the pressure gauge during IPE measurements. Otherwise the signal-to-noise ratio is highly increased in the spectrum gained. All spectra, which are presented in the following, are measured with the pressure gauge turned to its off-state.

Proportional Counter

In addition to the utilisation as Geiger-Müller counter, the photon bandpass detector can also be used as proportional counter. For this purpose, the detector is only filled with acetone. In order to find the optimal conditions for this counter type, the pressure of acetone was varied from $4\,\mathrm{mbar}$ to $9\,\mathrm{mbar}$ in steps of $1\,\mathrm{mbar}$ Thereby, for each pressure step a counting curve was measured under the same conditions and in the same way as already explained for the Geiger-Müller counter. An exemplary detector characteristic of the proportional counter can be found in Figure 5.17 for an acetone pressure of $p_{\mathrm{Prop}} = 8\,\mathrm{mbar}$ and the discrimination level set to $U_{\mathrm{trigger}} = 80\,\mathrm{mV}$. The averaged normalised count rate is plotted in logarithmic scale versus the detector voltage U_{detector}. The dashed grey line separated the different regions of detector operation (from the left to the right): I+II: ionisation chamber region and III: proportional region.
The first counts are measured at a starting voltage of $U_{\mathrm{SV}} = 850\,\mathrm{V}$. The maximum achieved count rate is $12\,\#/\mu\mathrm{As}$. At detector voltages higher than $U_{\mathrm{detector}} > 970\,\mathrm{V}$, the count rate starts

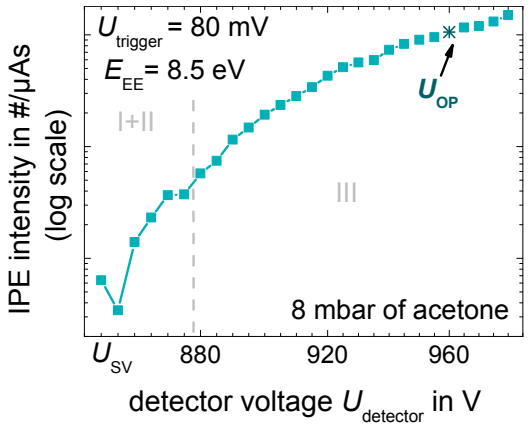

Figure 5.17 I Exemplary plot of a detector characteristic: the detector was filled up to $p_{\mathrm{Prop}} = 8\,\mathrm{mbar}$ with acetone gas. The discrimination level was set to $U_{\mathrm{trigger}} = 80\,\mathrm{mV}$. During the measurement the energy of the electrons was kept constant at $E_{\mathrm{EE}} = 8.5\,\mathrm{eV}$. The averaged normalised count rate is plotted in logarithmic scale versus the detector voltage. The detector starts to count at a starting voltage of $U_{\mathrm{SV}} = 850\,\mathrm{V}$. The voltage of operation $U_{\mathrm{OP}} = 960\,\mathrm{V}$ is marked by a star. The dashed grey line marks the different regions of detector operation: I+II: ionisation chamber region and III: proportional region (from left to right). This type of counter does not cross the Geiger-Müller regime before reaching the region of Geiger discharge [200].

to increase in larger steps and the experimental standard deviation significantly exceeds the theoretically expected standard deviation $\sigma = \sqrt{\overline{N}}$. This is an indication for the counter being close to the region of continuous discharge.
It has been shown by *S. Banik* and his co-workers that a counter which is filled only with acetone vapour is a proportional counter which does not operate in the Geiger-Müller regime before reaching the region of continuous discharge [200]. Here, the above mentioned fragmentation of acetone might account for this behaviour. This fragmentation might lead to the formation of electronegative gas particles, which are able to catch electrons and thus prevent the formation of secondary avalanches or provide even smaller avalanches.
The voltage of operation U_{OP} is set to a value, which gains a high count rate, but is not too close to the region of continuous discharge. In Figure 5.17, the voltage of operation of $U_{\mathrm{OP}} = 960\,\mathrm{V}$ is marked by a petrol-coloured star.

All measured detector characteristics are summarised in Figure 5.18 measured with a discrimination level set to $U_{\mathrm{trigger}} = 80\,\mathrm{mV}$. The figure shows the IPE intensity as a function of the acetone pressure and the detector voltage in a colour plot. Here, red areas indicate high intensity and blue areas represent nearly zero intensity.
In analogy to the Geiger-Müller counter, also starting voltage increases with increasing acetone pressure in case of the proportional counter which had not been predicted before. However, the model of *J. Craggs* and co-workers and by *D. H. Wilkinson* [201, 202] has already been successfully applied in case of the proportional counter by *M. Donath's* research group at the Westfälische Wilhelms University of Münster [205, 206].
For $p_{\mathrm{Prop}} \leq 5\,\mathrm{mbar}$, the quenching mechanism of acetone seems again be too ineffective, so that the region of continuous discharge is reached at smaller voltages. With increasing acetone pressure ($p_{\mathrm{Prop}} \leq 8\,\mathrm{mbar}$), the counting curves broaden and the regions of high intensity shift

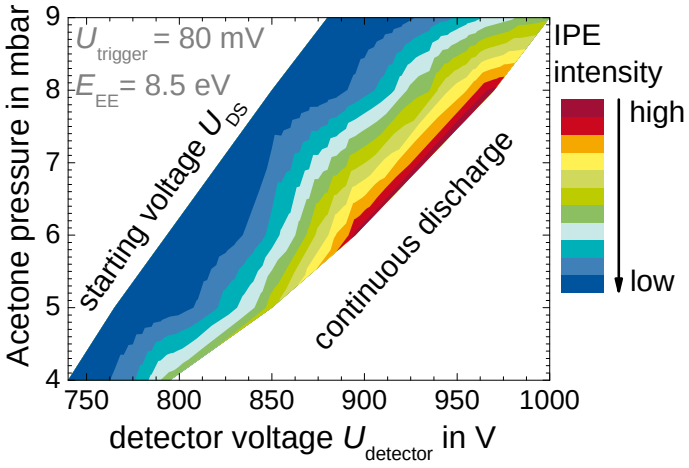

Figure 5.18 | Overview of all measured counting curves for the proportional counter: the discrimination level was set to $U_{\text{trigger}} = 80\,\text{mV}$ and the energy of the electron beam was kept constant at $E_{\text{EE}} = 8.5\,\text{eV}$ during all measurements. The IPE intensity is plotted as a function of the acetone pressure and the detector voltage in a colour plot. More reddish regions mark high intensities, whereas more bluish ones indicate low intensity regions. The region of continuous discharge is also marked. In order to achieve the optimal operation conditions and maximum count rate, the chosen acetone pressure and the corresponding operation voltage should be in the reddish region: the acetone pressure can be set between $6\,\text{mbar}$ and $8\,\text{mbar}$ entailing an operation voltage interval of $(895 - 970)\ \text{V}$, which depends on the chosen acetone pressure.

to higher voltages. For higher acetone pressures ($p_{\text{Prop}} > 8\,\text{mbar}$), maximum gained intensities decrease again. These observations are analogous to those observed for the Geiger-Müller counter (see page 80).
In order to achieve the optimal operation conditions and maximum count rate, an acetone pressure and the corresponding operation voltage should lie within the reddish region of Figure 5.18: thus, the acetone pressure can be set between $6\,\text{mbar}$ and $8\,\text{mbar}$ entailing an operation voltage interval of $(895 - 970)\ \text{V}$, which depends on the chosen acetone pressure.

A stability test over $2.4\,\text{h}$ for the proportional counter with $7\,\text{mbar}$ of acetone, which lies in the reddish region of Figure 5.18, can be found in Figure A.1 in the Appendix on page III. The count rate stays constant over the whole period of measurement.
If the detector is operated with $7\,\text{mbar}$ of acetone at a detector voltage of $U_{\text{OP}} = 940\,\text{V}$ and a discrimination level at $U_{\text{trigger}} = 80\,\text{mV}$, the dark count rate, which is produced only by interferences of the surrounding, amounts to $(0.5 \pm 1.1)\,\#/\text{s}$. The corresponding view graph can be found in the Appendix on page IV. This value is near to those gained in *M. Donath's* research group at the Westfälische Wilhelms University of Münster [205, 206].

Comparison of the Proportional Counter and the Geiger-Müller Counter

Up to now, the operation parameter found for the Geiger-Müller counter and the proportional counter have been discussed without paying attention on the discrimination level U_{trigger}. As a short reminder, the discrimination level is the voltage height the signal pulses must exceed

in order to be detected by the counting device. Consequently, if the discrimination level is set too low, electrical noise or spurious pulses are also counted by the counting device resulting in a larger and less meaningful count rate. Therefore, the optimal discrimination level has to be found in order to avoid counting of electrical noise or spurious pulses but also to ensure the counting of every meaningful signal pulse. For this purpose, the normalised integral pulse height distribution was measured by varying the discrimination level from $20\,\mathrm{mV}$[17] to $2500\,\mathrm{mV}$ and measuring the respective averaged normalised count rate. Here, the count rate is not only normalised to the sample current, but also to its maximum at $U_{\mathrm{trigger}} \geq 20\,\mathrm{mV}$ for better comparison. For the Geiger-Müller detector, a gas mixture with an argon-acetone ratio of $70.7\,\mathrm{mbar}/4.3\,\mathrm{mbar}$ and an operation voltage set to $U_{\mathrm{OP}} = 945\,\mathrm{V}$ was used. For the proportional counter, the detector was filled with $7\,\mathrm{mbar}$ of acetone vapour and the operation voltage was set to $U_{\mathrm{OP}} = 940\,\mathrm{V}$. The operation conditions of the electron gun were kept constant during the measurements with an electron energy again set to $E_{\mathrm{EE}} = 8.5\,\mathrm{eV}$. The measured sample was analogously produced to those mentioned before. In order to gain the averaged count rate for any chosen discrimination level, the amount of incoming counts was measured for 400 repetitions for each discrimination level for one second each(analogously to the procedure described before). The resulting normalised integral pulse height distribution is shown in Figure 5.19. Here, the violet dots represent the measurement of the Geiger-Müller counter, while the turquoise triangles indicate that of the proportional counter:

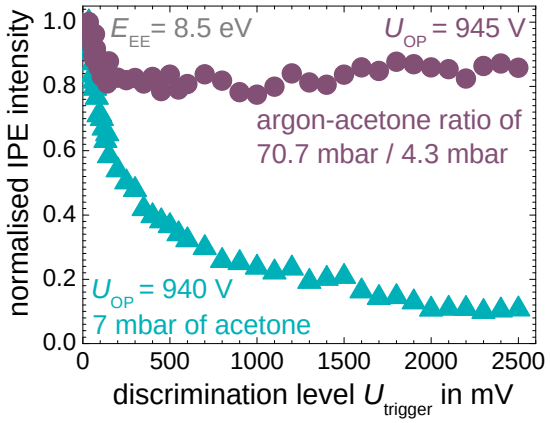

Figure 5.19 | Normalised integral pulse height distribution integral PHD: the averaged normalised count rate is shown as a function of the discrimination level U_{trigger}. For the Geiger-Müller detector, a gas mixture with an argon-acetone ratio of $70.7\,\mathrm{mbar}/4.3\,\mathrm{mbar}$ and an operation voltage of $U_{\mathrm{OP}} = 945\,\mathrm{V}$ was used. For the proportional counter, the detector was filled with $7\,\mathrm{mbar}$ of acetone vapour and the operation voltage was set to $U_{\mathrm{OP}} = 940\,\mathrm{V}$. The energy of the electron beam was kept constant at $E_{\mathrm{EE}} = 8.5\,\mathrm{eV}$ during the measurements. The violet dots represent the measurement for the Geiger-Müller counter, while the turquoise triangles indicate that for the proportional counter. In case of the Geiger-Müller counter the intensity decreases first very rapidly for very small voltages U_{trigger}. Since all pulses are of equal height, the intensity stays nearly constant for higher voltages. In case of the proportional counter the intensity decreases exponentially with increasing U_{trigger}.

[17] It was found that the count rate caused by the electrical noise is zero for a discrimination level $U_{\mathrm{trigger}} \geq 20\,\mathrm{mV}$.

- ◇ GEIGER-MÜLLER COUNTER (violet dots): for small voltages $U_{\text{trigger}} < 150\,\text{mV}$, the averaged normalised count rate decreases rapidly. In this region, the discrimination level is too small. Thus, also secondary pulses, which are of low voltage, can overcome U_{trigger} and contribute to the count rate. These pulses are caused by satellite or spurious pulses, for example [184]. For $U_{\text{trigger}} \geq 150\,\text{mV}$, the averaged, normalised count rate stays nearly constant at $80\,\%$ of the highest achieved count rate, as all pulses that originate from Geiger discharges are of the same height and can overcome the discrimination level [184]. The voltage U_{trigger} should be chosen to lie within this plateau. It was set to $U_{\text{trigger}} = 200\,\text{mV}$ for all measurements presented in this thesis.

- ◇ PROPORTIONAL COUNTER (turquoise triangles): the averaged normalised count rate decreases nearly exponentially with increasing discrimination level, because the pulses for the proportional counter are all of different height [184]. Consequently, less pulses are able to exceed U_{trigger} with increasing discrimination level. For this counter, the voltage U_{trigger} should be chosen in a way that as many secondary pulses as possible are blocked from overcoming the discrimination level, but at the same time the overall count rate does not become too small. Thus, the recommended discrimination level lies between $50\,\text{mV}$ and $100\,\text{mV}$, which results in an decrease of the maximum count rate of $(90 - 70)\,\%$.

The operation conditions found for the Geiger-Müller counter and the proportional counter are summarised in Table 5.2. But still the question stands, which counter type to choose for the IPE spectrometer: the advantage of a proportional counter is the small dead time[18] of $4\,\mu\text{s}$ [200]. However, the small or hardly existing Geiger-Müller plateau is a great disadvantage. When operating the detector as a proportional counter, the operation voltage should be chosen as high as possible since the intensity increases linearly with on the voltage, as explained before. The acetone, however, dissociates during the counting process. Consequently, the gas pressure and gas condition change. After a long period of operation at a fixed operation voltage U_{OP}, the detector automatically drifts into continuous discharge, which destroys the detector. Additionally, the maximum gained count rate of $\sim 12\,\#/\mu\text{As}$[19] (see Figure 5.17) is lower in comparison to that obtained with the detector operating in the Geiger-Müller region (see Figure 5.13).
In most Geiger tubes, the dead time is of the order of several hundred µs [153, 184]. The maximum IPE intensity achieved during the measurements was about $(20 - 30)\,\#/\mu\text{As}$[19] meaning that $(30 - 45)\,\#/\text{s}$ were detected at an average sample current of $\sim 1.5\,\mu\text{A}$ during experiments. Thus, every $\sim 22\,\text{ms}$ one primary impulse is counted. Consequently, the average time between the appearance of two subsequent pulses is much larger than the time needed to restore the detector. This means that no dead time correction has to be taken into account for the detector presented here. Additionally, the operation on a large Geiger plateau reduces

[18] As a short reminder, the dead time is defined as the period between the initial pulse and the time at which a second pulse can be detected.
[19] This count rate was measured on a $50\,\text{nm}$ polycrystalline silver thin film freshly evaporated on a silicon (100) substrate, which had been covered with $5\,\text{nm}$ of chromium as an adhesion layer before. The electron energy was $E_{\text{EE}} = 8.5\,\text{eV}$.

Table 5.2 | Optimal operation parameters found for the Geiger-Müller and the proportional counter.

parameter \ counter type	Geiger-Müller counter	proportional counter
gas mixture	argon/acetone	pure acetone
partial pressure	$70.7\,\mathrm{mbar}/4.3\,\mathrm{mbar}$	$(6-8)\,\mathrm{mbar}$
starting voltage U_{SV}	$(850-880)\,\mathrm{V}$	$(800-850)\,\mathrm{V}$
operation voltage U_{OP}	$(945-970)\,\mathrm{V}$	$(890-965)\,\mathrm{V}$
discrimination level U_{trigger}	$(0.2-0.5)\,\mathrm{V}$	$0.08\,\mathrm{V}$

the probability to reach the region of continuous discharge after a long period of operation. For that reason the Geiger-Müller counter has been used for all measurements shown in the next part of this thesis.

5.3. Apparatus Function and Total Energy Resolution

In this section, the apparatus function and the total energy resolution of the IPE spectrometer is determined: the total energy resolution of an IPE spectrometer is given by the convolution of the optical bandpass of the detector and the variance of the electron energy distribution. The variance σ_{tot} of the total energy resolution is given by [149]

$$\sigma_{\mathrm{tot}}^2 = \sigma_{\mathrm{opt}}^2 + \sigma_{\mathrm{el}}^2, \tag{5.17}$$

with σ_{opt} representing the variance of the optical bandpass of the detector and σ_{el} being the variance of the electron energy distribution. In the case of a Gaussian FWHM, Equation (5.17) can be written as

$$\mathrm{FWHM} = 2\sigma_{\mathrm{tot}}\sqrt{2\ln 2}. \tag{5.18}$$

As mentioned before, during experiments the temperature of the cathode of the electron gun was kept constant at $T_{\mathrm{ES}} = 1150\,\mathrm{K}$, which results in a thermal energy uncertainty of the electron gun of $\Delta E_{\mathrm{EE}} \sim 243\,\mathrm{meV}$ in FWHM [191]. Regarding the detector, the combination of an argon-acetone gas mixture with the CaF_2 window provides an optical resolution of $320\,\mathrm{meV}$ to $330\,\mathrm{meV}$ in FWHM [29, 149]. According to Equation (5.17) and (5.18), the theoretically expected energy resolution is in the region between $\Delta E_{\mathrm{IPES}} \sim 402\,\mathrm{meV}$ and $\Delta E_{\mathrm{IPES}} \sim 410\,\mathrm{meV}$ in FWHM.

In order to confirm this value, the Fermi edge of a $50\,\mathrm{nm}$ polycrystalline silver thin film freshly evaporated on a silicon (100) substrate, which had been covered with $5\,\mathrm{nm}$ of chromium as an adhesion layer before, was measured. For this purpose, the electron energy was varied from $7\,\mathrm{eV}$ to $8\,\mathrm{eV}$ in steps of $100\,\mathrm{meV}$ while the count rate was measured for every energy step. This

procedure has been repeated 29 times. Thereafter, all spectra were added and averaged[20]. The resulting IPE spectrum can be found in Figure 5.20 (a). Here, the energy is plotted with respect to the Fermi energy. The black dots represent measured data. The relative position of the Fermi energy[21] was determined by a Gaussian fit of the derivative of the spectrum in Figure 5.20 (a). The peak position of the Gaussian equals the relative position[22] of the Fermi edge of the IPE spectrometer to which the energy axis is referred to. This position was found to be at $(7.46 \pm 0.05)\,\mathrm{eV}$ for the IPE spectrometer presented here.

M. Budke et al. assumed that the intrinsic signal $I(E)$ can be described by [149]

$$I(E) = (a + bE) \cdot [1 - F(E)], \tag{5.19}$$

where $F(E)$ is the Fermi function at room temperature, b is the slope of a linear increasing background and a is a constant offset. By convoluting the intrinsic signal with Gaussians of different FWHMs, the experimental data is fitted. The FWHM of the Gaussian which fits best the experimental data equals the total energy resolution of the IPE spectrometer and gives a good estimate of the overall apparatus function [149]. This fit is represented by the red dashed line in Figure 5.20 (a). The total experimental resolution was determined to be $\Delta E_{\mathrm{IPES}} = (400 \pm 2)\,\mathrm{meV}$, which fits the theoretically expected value. This resolution is in good agreement with those reported in literature, which vary from $400\,\mathrm{meV}$ to $550\,\mathrm{meV}$ for comparable spectrometers [29, 62, 176, 200, 207, 208].

Since the term 'resolution' is not well-defined, in addition to the FWHM, the shape of the Fermi edge is also crucial for the comparison of different spectrometers [149]. The rise of the IPE signal at the Femi edge from $10\,\%$ to $90\,\%$ of the total intensity is, for this reason, also a strong criterion for the resolution. In Figure 5.20 (b), the relation between this $10\,\%$ to $90\,\%$ criterion and the FWHM is shown for theoretical apparatus functions. In order to obtain values for the theoretical $10\,\%$ to $90\,\%$ width of the Fermi edge, the Fermi distribution functions for temperatures of $T = 0\,\mathrm{K}$ (light grey line), $T = 100\,\mathrm{K}$ (grey line) and $T = 300\,\mathrm{K}$ (black line) are convoluted with a Gaussian shape of given FWHMs. If the data point of a given experimental determined apparatus function lies above these lines, it has a longer tail than a Gaussian function. Otherwise, apparatus functions are narrower than a Gaussian [149].
For the IPE spectrometer built in the course of this thesis, the $10\,\%$ to $90\,\%$ width of the Fermi edge is $\Delta E_{\text{10-90}} = (426 \pm 10)\,\mathrm{meV}$, which is represented in relation to the FWHM determined above by the red dot in Figure 5.20 (b). Within the errors, it can be seen that this red data point lies on the theoretical 'Gaussian line' for $T = 300\,\mathrm{K}$. Thus, the apparatus function of the IPE spectrometer built in the course of this thesis is symmetric with the consequence that all spectral features including the Fermi level onset will have a symmetric Gaussian shape with a minimum FWHM of $\Delta E_{\mathrm{IPES}} = (400 \pm 2)\,\mathrm{meV}$.
In order to compare this result with similar spectrometers found in literature, six data points

[20] This measurement procedure results in an IPE spectrum which can automatically be measured with the IPE programme. This programme was completely developed by the author in the course of this thesis.
[21] As a short reminder, the energy axis of an IPE spectrum is mostly referred to the Fermi level as it is also the case for UPS spectra.
[22] For the energetics of IPES see also Section 3.2.

(black dots) are shown in Figure 5.20 (b), which are taken from *M. Budke*, *M. Donath* and coworkers [149] and illustrate the results for various operation conditions of their spectrometer. In addition, the results of four different experiments found in the literature are marked by open squares ((a) Ref. [209], (b) Ref. [91], (c) Ref. [210], (d) Ref. [211]), secondary source [149]). Three data points lie above significantly, while all the others including that of the spectrometer presented here are positioned on top of the theoretical line. Thus, the resolution of the presented IPE spectrometer is not only in good agreement with those reported in literature, but also fits the stronger $10\,\%$ to $90\,\%$ criterion, which is not always the case for those found in literature.

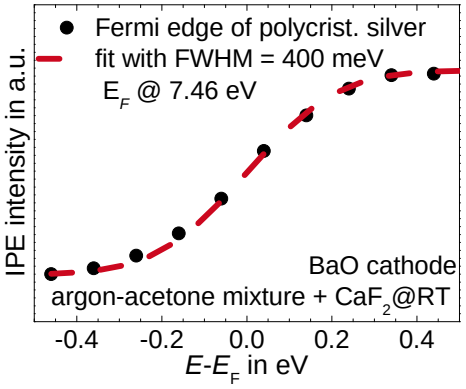

(a) | Fermi edge of a polycrystalline silver sample including a fit of the data in order to obtain the apparatus function.

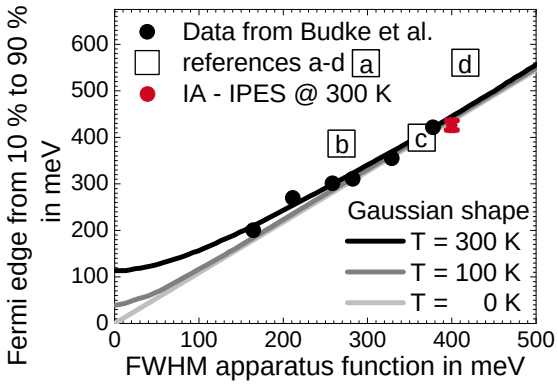

(b) | Relation between the rise of the IPE signal from $10\,\%$ to $90\,\%$ of the achieved intensity at the Fermi edge and the FWHM of the apparatus function ((a) Ref. [209], (b) Ref. [91], (c) Ref. [210], (d) Ref. [211]). (This figure is adapted from [149]. Copyright ©2007, AIP Publishing LLC.)

Figure 5.20 | Determination of the resolution of the IPE spectrometer: the Fermi edge of a polycrystalline silver thin film of $50\,\mathrm{nm}$ in thickness was measured. In (a), the IPE intensity is plotted against the energy $E - E_\mathrm{F}$. The data is represented by the black dots, while the red dashed line shows the fit of the measured data. The relative position of the Fermi edge is determined to be at $(7.46 \pm 0.05)\,\mathrm{eV}$. The fit which matches the measured data best was obtained by the convolution of the intrinsic signal of Equation (5.19) with a Gaussians with a FWHM of $(400 \pm 2)\,\mathrm{meV}$, as it was expected. In (b), the relation between the rise of the IPE signal at the Fermi edge from $10\,\%$ to $90\,\%$ of the achieved intensity and the FWHM of the apparatus function is depicted. The grey and black lines belong to calculations for Fermi distributions at different temperatures, which are convoluted with a Gaussian shaped apparatus functions. The black dots represent the data points taken from the work of *M. Budke* and coworkers [149]. For additional comparison, the results of four different experiments taken from literature are marked by open squares ((a) Ref. [209], (b) Ref. [91], (c) Ref. [210], (d) Ref. [211]), secondary source [149]). The red dot represents the result for the presented IPE spectrometer. Within the errors it lies on the black line, which illustrates the Fermi distribution at $300\,\mathrm{K}$ convoluted with a Gaussian shaped apparatus function. Thus, the IPE spectrometer build in the course of this thesis has a symmetric the apparatus function with the consequence that the spectral features including the Fermi level onset are of symmetric shape, too.

The Interface between Metals and Organic Semiconductors

6. Electronic Structure of Noble Metals

The occurrence and the behaviour of the *Shockley*-type crystal-induced surface states (SS) as well as of the image potential states of copper, silver and gold have been intensively studied before [67, 83, 126, 127, 212–214]. Thus, IPE measurements of gold and copper thin films serve as reference systems to approve a proper working condition of the IPE spectrometer built in the frame of this thesis. Furthermore, since one of the aims of the current thesis is to understand the electronic structure at organic-metal interfaces, it is essential to provide a basis in terms of the electronic states of pure metal surfaces. Therefore, this chapter presents the electronic structure of (111) oriented gold and copper thin films investigated with ultraviolet and inverse photoemission spectroscopy.

The thin films presented in the following are produced on freshly cleaved MICA[1] substrates in a UHV thermal evaporation chamber with a base pressure of less than $5 \cdot 10^{-8}\,\mathrm{mbar}$. The process steps were described by *D. Meyer* [16], *T. Schäfer* [215] and *B. Lüssem* and coworkers [216] in detail. All films are $200\,\mathrm{nm}$ thick.
The IPE spectra were measured by varying the electron energy from $6\,\mathrm{eV}$ to $16\,\mathrm{eV}$ in steps of $100\,\mathrm{meV}$ with a measurement time of $15\,\mu\mathrm{As}$ per step. Each spectrum is averaged over 17 full scans resulting in a total time per spectrum of approximately $6\,\mathrm{h}$[2]. The base pressure in the chamber was kept below $5 \cdot 10^{-11}\,\mathrm{mbar}$.
In order to confirm the high crystal quality of the films, the samples were additionally analysed with X-ray diffraction in *Bragg-Brentano*-geometry[3] (Θ2Θ) by *C. Jodocy* using the Bruker D8 Discover X-ray setup at the research group at the I. Institute of Physics (IA).
The UPS spectra $(h\nu = 21.22\,\mathrm{eV})$ of comparable samples were recorded by *D. Meyer* at the research group at the I. Institute of Physics (IA). They are printed with kind permission.

[1] MICA (high quality Muskovit (KAl_2 (OH, F)$_2$ ($AlSi_3O_10$)) substrates were ordered from *Plano GmbH*, Germany.
[2] The comparably long measurement time has been chosen in order to gain a very good signal-to-noise ratio. Adequate spectra can also be recorded under similar condition with averaging over $(4-5)$ full spectra in shorter time scales of approx. $1.5\,\mathrm{h}$.
[3] The corresponding spectra are shown on page V and following in the Appendix.

Gold

The UPS and IPE spectra of a well-ordered and highly textured gold (111) thin film are shown in Figure 6.1: the intensity is plotted as a function of the energy with respect to the Fermi energy E_F.

The left graph shows the ionisation threshold of the secondary electrons, which is directly connected to the work function Φ of the surface. The energy position E_cutoff of the secondary electron cutoff (SEC) is given by the point of intersection of a linear fit on the secondary electron cutoff and the background (marked by the two black solid lines). It is used to determine Φ via $\Phi = h\nu - E_\mathrm{cutoff} = (5.3 \pm 0.1)\,\mathrm{eV}$, which is in good agreement with literature [67].

The valence band region (VBR) is displayed in the middle of Figure 6.1. The spectrum consists of a number of well-defined peaks featuring the density of occupied states of gold. The major contribution to the peaks located in the interval between $(-7 \pm 0.1)\,\mathrm{eV}$ and $(-2 \pm 0.1)\,\mathrm{eV}$ can be attributed to the Au 5d states [67] (see also Figure 6.2). When comparing the VBR-spectrum of Figure 6.1 with the projected density of states (PDOS) plotted in Figure 6.2[4], a difference in the shapes of the peaks attributed to the 5d states can be observed. This can be explained as following: the PDOS projects an average of the band structure over the total k-space, whereas the UPS measurement is just able to average over a small part of the reciprocal space ($\Delta k_{||} = \pm 7\%$) [215]. On the one hand, the d bands of noble metals are comparably flat, as can be seen in Figure 6.3 showing the 3D bandstructure of gold. Consequently, only a little difference is expected for their projection when comparing DFT calculations with UPS spectra. The p and s bands, on the other hand, are highly dependent on the wave vector. Additionally, their contribution to the PDOS is distributed over the entire energy scale in Figure 6.2. Therefore, a difference in their shape is possible, when PDOS and UPS spectra are compared [215].
The lower edge of the sp gap labelled L_2' in single group notation is slightly visible at $(-1 \pm 0.1)\,\mathrm{eV}$, which fits the predictions made by theory (see the 3D bandstructure of gold in Figure 6.3) as well as the values given in literature [127, 218]. As a short reminder, the $L_2' \rightarrow L_1$ gap is '*Shockley* inverted', meaning that the more p-like L_2' level lies below the more s-like L_1 level (see also the three dimensional band structure of Au in Figure 6.3) [219]. Since the corresponding bands are highly dependent on the wave vector, their contribution to the density of states is expected to be small, which explains the low intensity observed for the L_2' feature in the valence band region (VBR) spectrum of Figure 6.1.
Near the Fermi level in the same spectrum in Figure 6.1, another peak can be observed, which is the well-known *Shockley*-type crystal-induced surface state (SS) [67, 83, 126, 127, 212–214]. This type of surface state is located at the $\overline{\Gamma}$ point of the surface Brillouin zone (SBZ) within the nearly parabolic shaped sp inverted gap at the L point of the 3D Brillouin zone [26] (see Figure 6.3 and also Section 3.4). The SS has a reported band minimum at a binding energy of $E_\mathrm{B} = -0.49\,\mathrm{eV}$ with respect to E_F [212], which fits the measured value of

[4]The energy scale of Figure 6.2 is shifted by $0.5\,\mathrm{eV}$, which is necessary to gain a better comparability to the experimental data. It can be explained by the fact that DFT just calculates states which are in the ground state. As the states measured by UPS and IPES are in principle excited states, the measured DOS does not exactly equal the single-particle approach of DFT calculations [215].

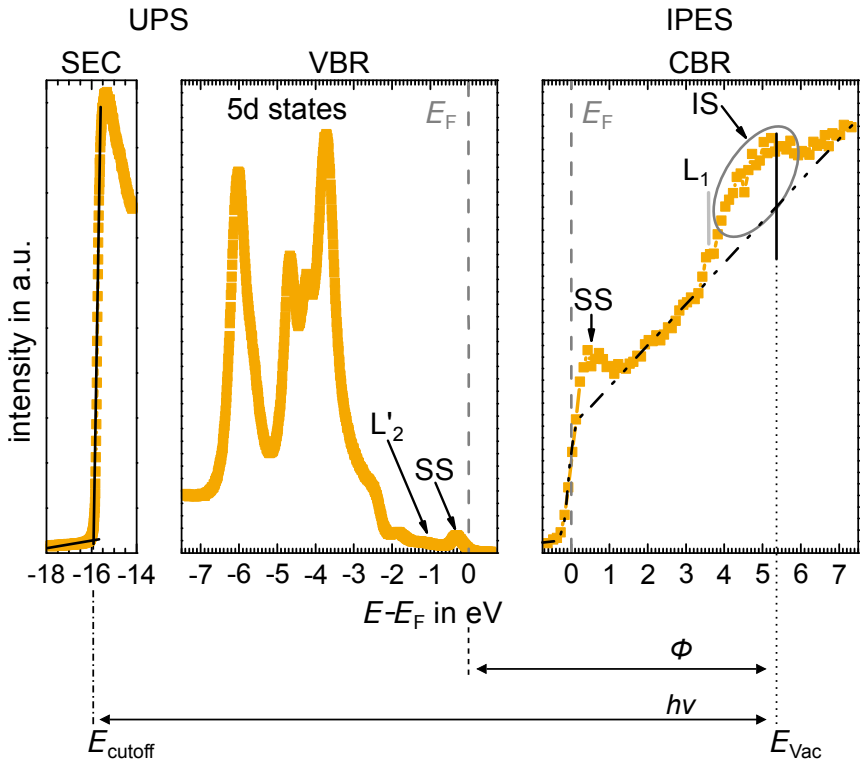

Figure 6.1 | Combined UPS and IPE spectra showing the electronic structure of a well-ordered and highly textured gold (111) thin film: in the left graph, the secondary electron cutoff (SEC) featuring the threshold for photoionisation is used to gain the work function via $\Phi = h\nu - E_{\text{cutoff}} = (5.3 \pm 0.1)\,\text{eV}$. The UPS spectrum in the middle displays the valence band region (VBR), while the frontier unoccupied electronic states are shown in the IPE spectrum in the right graph. In all graphs, the intensity is plotted as a function of the energy with respect to the Fermi energy E_F. The position of the Fermi level is marked by the grey dashed lines in both frontier state spectra. Furthermore, the vacuum level is marked by a short black line named E_{Vac}.
In the valence band region, four peak maxima can be distinguished in the interval between $(-7 \pm 0.1)\,\text{eV}$ and $(-2 \pm 0.1)\,\text{eV}$, which correspond to the typical d-band structure of Au with favoured (111)-direction. The *Shockley*-type crystal-induced surface state (SS) can be observed near the Fermi level. Amongst, a peak caused by the L'_2 band edge is slightly visible at $(-1 \pm 0.1)\,\text{eV}$.
The Shockley-type crystal-induced surface state can also be identified in the conduction band region (CBR) at $(+0.5 \pm 0.2)\,\text{eV}$. The L_1 band-edge feature can be observed at $(+3.6 \pm 0.2)\,\text{eV}$, which is marked by a light grey line. Additionally, image potential states (IS) are located at $(+4.6 \pm 0.5)\,\text{eV}$ relative to E_F. They are highlighted by a dark grey circle. The vacuum level E_{Vac} is marked by a short black line at $(+5.3 \pm 0.1)\,\text{eV}$. The black dashed-dotted line represents a simulation of the background used to determine peak positions. (The UPS spectra, which were recorded on a comparable sample, are provided by *D. Meyer* [16]. They are printed with kind permission.)

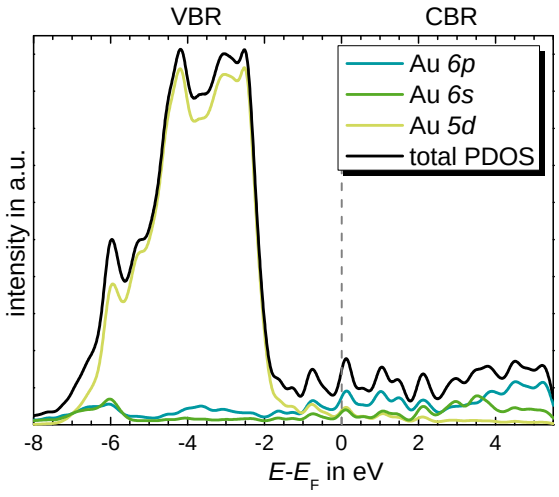

Figure 6.2 | Projected density of states: the intensity is plotted as a function of the energy with respect to the Fermi energy. The energy scale is shifted by $0.5\,\mathrm{eV}$ [215]. Au $6s$ (green), Au $6p$ (turquoise) and Au $5d$ (light green) states contribute to the total projected density of states (PDOS).
In the interval between $-7\,\mathrm{eV}$ and $-2\,\mathrm{eV}$, the PDOS can mainly be attributed to Au $5d$ states. The contributions from the $6s$ band as well as that of the Au $6p$ electrons are approximately constant over the entire energy scale. (DFT calculations were performed by *T. Schäfer* at the research group at the I. Institute of Physics (IA). For the computational details see [215, 217]. Data are printed with kind permission.)

$(0.4 \pm 0.1)\,\mathrm{meV}$. Since this surface states appears just at a certain wave vector, its contribution to the PDOS is comparably small. Hence, such a state is not expected to be observable in the PDOS in Figure 6.2. This explains the difference of the peak shape near the Fermi energy when comparing the PDOS spectrum with the measured data plotted in the VBR spectrum in Figure 6.1.

In addition to the UPS spectrum in Figure 6.1, also the IPE spectrum features the *Shockley*-type crystal-induced surface state at an energy of $(+0.5 \pm 0.2)\,\mathrm{eV}$. However, the surface state of gold is fully occupied when measured under normal incidence. Its band crosses the Fermi level at $k_{||Au} = (0.167/0.192)\,\mathrm{\AA}^{-1}$ [212]. Consequently, the SS should not be visible in the IPE spectrum. Admittedly, since the electron beam has always a certain angular divergence, the *Shockley*-type crystal-induced surface state is visible in all IPE spectra published so far [126, 127]. Because of this angular divergence of the electron beam, every state which is occupied but located right at Fermi level is also visible in the IPE spectrum.
At higher energies, the L_1 band-edge feature of the sp inverted band gap can be observed at $(+3.6 \pm 0.2)\,\mathrm{eV}$. Its position agrees well with the values reported in literature and is marked by a light grey line in the conduction band region (CBR) spectrum in Figure 6.1 [127, 218, 224]. DFT calculations of unoccupied states have to be treated with great care, since DFT is just based on ground state calculations and therefore, can hardly predict unoccupied states. However, the L_1 band edge is slightly visible in Figure 6.2 and its s-like character is also predicted.
At an energy of $(+4.6 \pm 0.5)\,\mathrm{eV}$ the image potential state (IS), which is introduced in Section 3.4, can be identified. In comparison to the *Shockley*-type crystal-induced surface state, image potential states do not arise from bulk states or from breaking the symmetry at the surface [26, 67]: electrons, which arrive at the surface, are screened by the conducting electrons of the metal. This screening can be described by a positive image charge inside the metal at the same distance from the surface as the real charge. Thus, the arriving electron is positively attracted by its image potential located inside the metal, which leads to the development of bound states in a region up to several Å above the surface (see also Figure 3.3).

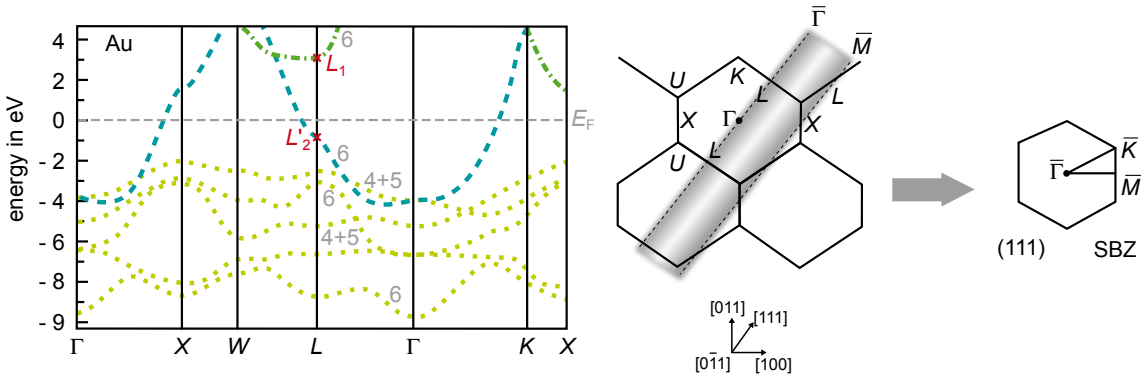

Figure 6.3 | Band structure of gold: the band structure of Au along high symmetry directions of the three dimensional Brillouin zone is shown as computed in [220–222]. Symmetry labels are given in double group notation for the ΓL line (grey numbers). The band edge features L'_2 and L_1 are marked by a red cross each. For better illustration the colour code is similar to that used in Figure 6.2. The fully occupied $5d$ bands lie below the Fermi energy and are drawn in light green. The Fermi energy crosses the middle of a band wherein s and p states hybridise. In [219], it was shown by *B. Yan* and co-workers that this band is more p-like (turquoise), whereas the sp band above is of s character (green) up to an energy of $E_F + 5\,\mathrm{eV}$. On the right side, the ΓLUX plane of the three dimensional Brillouin zone is drawn. The grey shaded emission plane contains the symmetry points Γ, L, U and X of Au (111). Since only the (111) surface Brillouin zone (SBZ) is accessible when using photoemission [67], it is also illustrated. Its symmetry points $\bar{\Gamma}$ and $\overline{M}$ are associated with the lines in the grey shaded emission plane in the ΓLUX plane of the three dimensional Brillouin zone. (This picture was inspired by the data found in [220–223].)

In literature, image potential states are often referenced to the vacuum level instead of to the Fermi energy [26], which in the case of gold was determined to $E_{\mathrm{Vac}} = (+5.3 \pm 0.1)\,\mathrm{eV}$. In order to gain a better comparability, the position of the observed image potential state is determined to $(+0.7 \pm 0.2)\,\mathrm{eV}$ relative to E_{Vac}. It matches the theoretically expected values [127] (see also Table 3.2).

Finally, a short discussion on the background of the IPE spectrum, which is observable Figure 6.1 is given: all peaks considered so far are superimposed on a steadily increasing background. This background originates from incident electrons losing their kinetic energy prior to photon emission due to inelastic scattering inside the sample. In this case, the initial state energy of the radiative transition equals no longer the energy of the incident electron beam. The resulting background gets higher with increasing electron energy, because a larger number of unoccupied states is existent, in which the electrons can be inelastically scattered before a photon is emitted [225].
The energy and the FWHM of the spectral features of an IPE spectrum can be determined directly from the measured spectrum or alternatively after subtraction of the background. Both approaches are reported in literature [225]. However, in most of the studies the IPES spectra are analysed with the background present, which is only advantageous if intensive, sharp features are present at low electron energies where the background is typically small [225, 226]. However, a uniform background model is still not available for IPE spectra in literature [225–227]. So far, several functions have been applied reaching from a linear or cubic polynomial function to quite complex approaches using scattering theory or EELS spectra in order to

adequately describe the IPE background [149, 225, 228, 229]. In the presented thesis, the background was only subtracted for analytic purposes if the peaks could hardly be identified in the raw data. The background was simulated as following (see also Section 5.3): again, the intrinsic signal $I(E)$ is described by [149]

$$I(E) = (a + bE) \cdot [1 - F(E)], \tag{6.1}$$

where $F(E)$ is the Fermi function at room temperature, b is the slope of a linear increasing background and a is a constant offset. By convoluting the intrinsic signal with Gaussians of different FWHMs, the experimental data is fitted near the Fermi level. At higher energies the background is described by a linear curve[5]. Such a background is represented by the dashed dotted line in the CBR spectrum in Figure 6.1.

Copper

The UPS and IPE spectra of a well-ordered and highly textured copper (111) thin film are shown in Figure 6.4: the intensity is plotted as a function of the energy with respect to the Fermi energy E_F. The analysis of these spectra can be performed in analogy to that discussed before.

As for gold, also for copper the energy position E_cutoff of the secondary electron cutoff is used to determine the work function Φ via $\Phi = h\nu - E_\mathrm{cutoff} = (4.9 \pm 0.1)\,\mathrm{eV}$, which is in good agreement with literature [67].
The UPS spectrum of the VBR reveal four well-defined peaks. Two of them can be attributed to the flat $3d$ bands. They are located between $(-4 \pm 0.1)\,\mathrm{eV}$ and $(-2 \pm 0.1)\,\mathrm{eV}$. At an energy of $(-0.8 \pm 0.1)\,\mathrm{eV}$, the peak caused by the L_2' band edge is observable. Its peak position is in good agreement with values found in literature [230, 231] and fits also the PDOS and the $3D$ band structure shown in Figure 6.5. The *Shockley*-type crystal-induced surface state (SS) caused by the sp-inverted gap can be observed at the Fermi level of the VBR spectrum in Figure 6.4. When comparing Figure 6.4 with the projected density of states of Figure 6.5 (a) calculated with DFT, again some deviations can be observed, which can be similarly explained as done already for gold.
Again, the IPE spectrum of Figure 6.4 also exhibits the SS at $(0.4 \pm 0.2)\,\mathrm{eV}$ with respect to E_F, which is due to the angular divergence of the electron beam. At a higher energy of $(+4.4 \pm 0.5)\,\mathrm{eV}$, a superposition of the image potential state (IS) and the L_1 band edge feature can be seen (see Figure 6.4).

In order to demonstrate that the spectrometer is also working well when angle-resolved inverse photoemission is performed, $k_{||}$ was varied. As a short reminder, only the parallel component of the electron wave vector is conserved during traversing the vacuum-solid interface [80] (see Section 3.3). All $k_{||}$ dependent spectra are plotted in Figure B.4 on page VII in the Appendix. Thereof, the energetic positions of the peak centre of the *Shockley*-type

[5] The background of the UPS spectra in the VBR is fitted in a similar way. Therein, it is described by an exponential increase at higher energies.

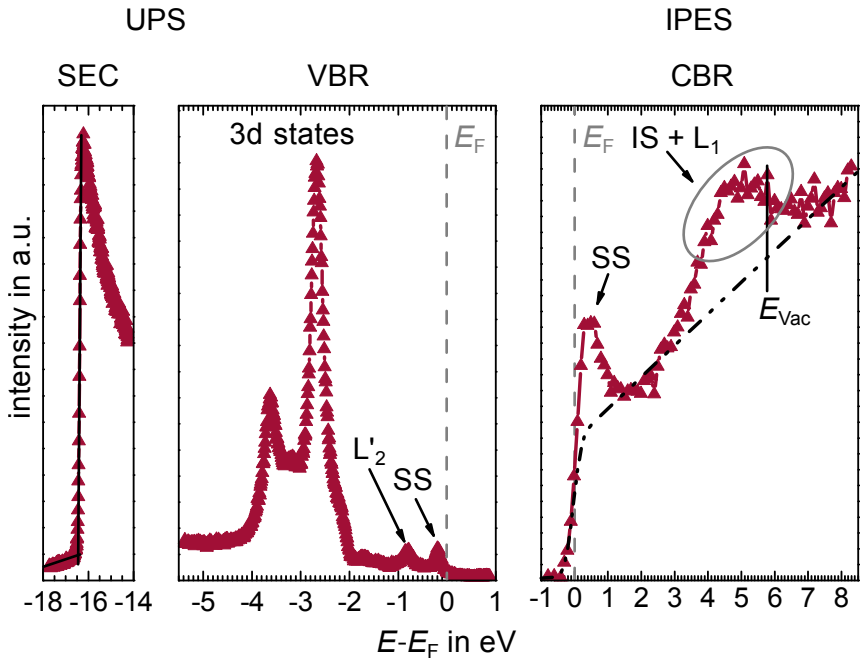

Figure 6.4 | Combined UPS and IPE spectra showing the electronic structure of a well-ordered and highly textured copper (111) thin film: in the left graph, the secondary electron cutoff (SEC) featuring the threshold for photoionisation is used to gain the work function via $\Phi = h\nu - E_{\text{cutoff}} = (4.9 \pm 0.1)\,\text{eV}$. The UPS spectrum in the middle displays the valence band region (VBR), while the conduction band region (CBR) is shown in the IPE spectrum in the right graph. In all graphs the intensity is plotted as a function of the energy with respect to the Fermi energy E_F. The position of the Fermi level is marked by the grey dashed lines in both frontier state spectra. In addition, the vacuum level is marked by a short black line named E_{Vac}.
In the valence band region, two intense peak maxima can be distinguished in the interval between $(-4 \pm 0.1)\,\text{eV}$ and $(-2 \pm 0.1)\,\text{eV}$, which corresponds to the typical d-band structure of Cu with favoured (111)-direction. The *Shockley*-type crystal-induced surface state (SS) can be observed at the Fermi level. The peak caused by the L'_2 band edge is observable at $(-0.8 \pm 0.1)\,\text{eV}$.
At $(+0.5 \pm 0.2)\,\text{eV}$, the SS can again be identified. At a higher energy of $(+4.4 \pm 0.5)\,\text{eV}$, a superposition of the image potential state (IS) and the L_1 band edge feature can be seen. They are highlighted by a dark grey circle. The vacuum level E_{Vac} is marked by a short black line at $(+4.9 \pm 0.1)\,\text{eV}$. The black dashed-dotted line represents a simulation of the background used to determine peak positions. (The UPS spectra, which were recorded on a comparable sample, are provided by *D. Meyer*. They are printed with kind permission.)

crystal-induced surface state of copper (111) are obtained via a peak fit after a careful background subtraction was performed. The background was fitted as explained above and is exemplarily plotted with a black dashed dotted line in Figure 6.4. The peak positions gained are summarised in the energy dispersion $E(k_{||})$ plotted in Figure 6.6. The plot in Figure 6.6 only contains results gained with IPES measurements.
For copper (111), the surface state has its band minimum at a binding energy of $E_B = -0.44\,\text{eV}$ with respect to E_F [212]. It crosses the Fermi level at $k_{||Cu} = 0.215\,\text{Å}^{-1}$ [212]. In Figure 6.6 the nearly free-electron-like dispersion of this state was simulated with the tight-binding model of *L. Bürgi* et al. [232] and is represented by the dashed black line. According to this, the surface state should not be visible in IPE spectra for $k_{||} < 0.215\,\text{Å}^{-1}$. However, the

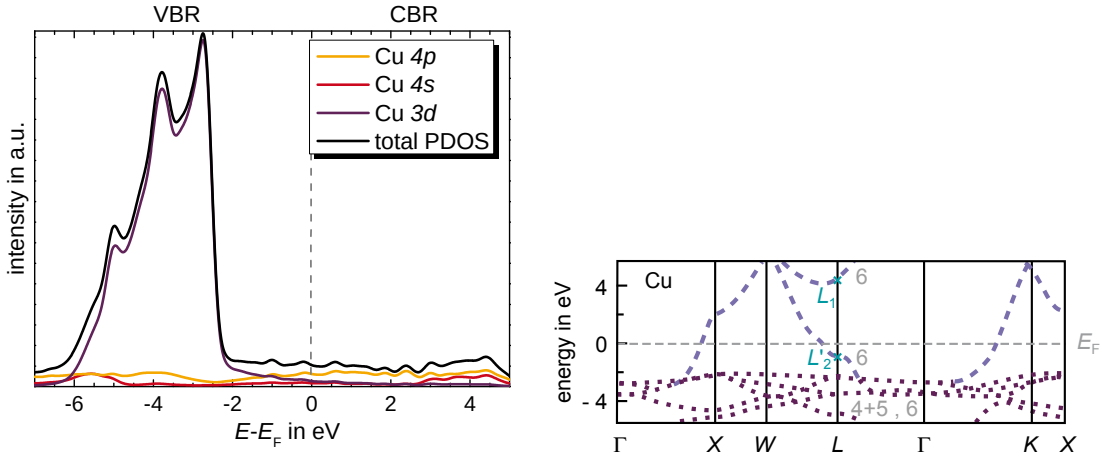

(a) | Projected density of states (PDOS) of copper

(b) | Band structure of copper

Figure 6.5 | Projected density of states: (a) the intensity is plotted as a function of the energy with respect to the Fermi energy. The energy scale is shifted by $0.7\,\mathrm{eV}$ [215]. Cu $4s$ (red), Cu $4p$ (orange) and Cu $3d$ (violet) states contribute to the total projected density of states (PDOS) (black).
In the interval between $-6\,\mathrm{eV}$ and $-2\,\mathrm{eV}$, the PDOS can mainly be attributed to Cu $3d$ states. The contribution from the $4s$ bands as well as that of the Cu $4p$ electrons are located over the entire energy scale. (DFT calculations were performed by *T. Schäfer* at our research group at the I. Institute of Physics (IA). For the computational details see [215, 217]. Data are printed with kind permission.)
Band structure of copper: (b) the band structure of Cu along high symmetry directions of the three dimensional Brillouin zone is shown as computed in [221, 223]. Symmetry labels are given in double group notation for the ΓL line (grey numbers). The band edge features L_2' and L_1 are marked both by a turquoise cross. For better illustration, the colour code is as followed: the fully occupied $3d$ bands lie below the Fermi energy and are drawn in violet just as in Figure 6.5 (a). The Fermi energy crosses the middle of a band wherein s and p states hybridise to sp bands coloured in purple. (This picture is inspired by the data found in [221, 223].)

surface state is also visible in the IPE spectrum due to the angular divergence of the electron beam as discussed above (see also Section 5.1).
As can be seen in Figure 6.6, the position of the surface state stays nearly constant within the experimental error ($\Delta E_{\mathrm{exp}} = \pm 0.2$) for $k_{||} < 0.1\,\mathrm{Å}^{-1}$. Thereafter, the peak position shifts to higher energies for larger $k_{||}$. While leaving the grey area, the surface state seems to disperse as expected within the experimental errors. Here, the grey area represents a region in which the measured peak positions may appreciably differ from their 'true' values due to their vicinity to E_{F} [214, 233]. This can be explained by a combined effect of the temperature-dependent Fermi function, the intrinsic line width of the feature, the inelastic background and the experimental broadening of the peak [214]. Thus, peak positions closer to the Fermi level than the experimental resolution convoluted with the temperature-dependent line width of the Fermi function do not represent the energy of the electronic state under consideration [213, 233]. It was shown by *M. Budke* and co-workers that an improved energy resolution also improves the reliability of the determined state energies near the Fermi level [213]. Apart from the de-

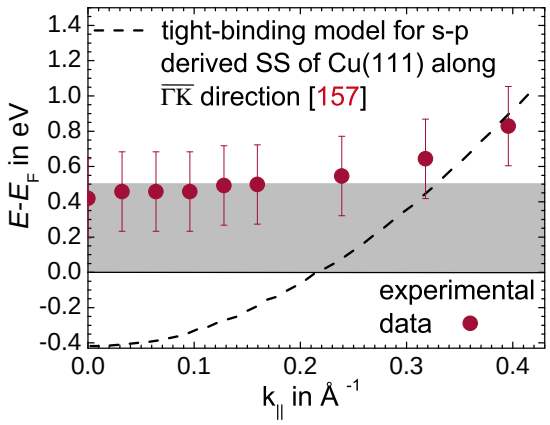

Figure 6.6 | Energy dispersion $E(k_{||})$ of the *Shockley*-type crystal-induced surface state of copper (111): the energetic positions of the peak centre of the *Shockley*-type crystal-induced surface state (SS) are represented by the filled red dots and are plotted in dependence of the reciprocal space vector $k_{||}$. The energy scale is given with respect to the Fermi energy E_F.
The expected dispersion of the surface state was simulated with the tight-binding model of *L. Bürgi* et al. [232]. It is represented by the dashed black line. The difference between the tight-binding model of *L. Bürgi* and the measured data can be explained by the following: Since this plot only shows results gained with IPES, its occupied part located below E_F does not contain any data point. As known from literature the surface state disperses into the unoccupied region for reciprocal lattice vectors of $k_{||} \geq 0.215\,\text{Å}^{-1}$ [212]. Thus, it should not be visible for values $k_{||} < 0.215\,\text{Å}^{-1}$. However, the SS can also be observed with IPES because of the angular divergence of the electron beam as explained before. For that reason, it is not surprising that the peak position stays constant within the experimental error up to a reciprocal lattice vector $k_{||} = 0.2\,\text{Å}^{-1}$. For $k_{||} \geq 0.2\,\text{Å}^{-1}$, while leaving the grey area representing the area of the experimental resolution convoluted with the temperature-dependent line width of the Fermi function [213, 214], the surface state seems to disperse as it is expected within the experimental errors.

scribed and explained deviations, the IPE data seem to follow the predicted dispersion within the experimental errors. However, it has to be mentioned, that this statement is based on only two data points. Therefore, it is suggested to repeat the measurement in future studies on a comparable sample by applying larger angles of incidence.

Summary

In this chapter the electronic structure of well-ordered and highly textured gold and copper (111) thin films is discussed. Therefore, UPS and IPES measurements were applied and the results are compared to DFT calculations as well as to the band structure along high symmetry directions of the three dimensional Brillouin zone.
The work function is determined from the secondary electron cutoff via $\Phi_{\text{Au}} = h\nu - E_{\text{cutoff}} = (5.3 \pm 0.1)\,\text{eV}$ for gold and $\Phi_{\text{Cu}} = (4.9 \pm 0.1)\,\text{eV}$ for copper. They fit the values given in literature [67].
The valence band spectra of both metals reveal well-defined peaks: the most prominent ones can be attributed to the flat d bands. Furthermore, the L_2' band edge feature is identified

in the UPS spectra. The *Shockley*-type crystal-induced surface state, which located at the $\overline{\Gamma}$ point of the surface Brillouin zone (SBZ) within the nearly parabolic shaped sp inverted gap at the L point of the 3D Brillouin zone, is not only visible near the Fermi edge in the UPS spectra but also in the IPE spectra. As discussed above, this type of surface state is fully occupied when measuring under normal incidence. Consequently, the SS should not be visible in IPE spectra. However, since the electron beam has always a certain angular divergence, the *Shockley*-type crystal-induced surface state is visible in all IPE spectra published so far [126, 127] and also in those reported in this thesis. Moreover, the IPE spectra exhibit the L_1 band edge feature as well as the image potential states, in which electrons are bound in their positive Coulombic image potential above the sample surface.
All peaks are identified not only for the UPS spectra but also for the IPE spectra. The position of their peak centres fit the values reported in literature. Thus, it can be concluded that the IPE spectrometer, which was built in the course of this thesis, is properly working and provides reliable results[6].
For the copper (111) thin film, also results gained from angle-resolved inverse photoemission are presented. Here, the focus is on the energy dispersion of the *Shockley*-type crystal-induced surface state which is compared to a simulation applying the tight-binding model as performed by *L. Bürgi* et al. [232]. The behaviour of the experimental data are explained and the IPE data seem to follow the predicted dispersion within the experimental errors.

[6] An IPE spectrum of a well-ordered silver (111) thin film can be found on page VIII Figure B.5 in the Appendix.

7. Electronic Structure of Organic Semiconductors - Bulk-like Thin Films

Before interface effects at organic-metal surfaces can be understood, the electronic structure of organic semiconductors has to be discussed in a more general way. Therefore, this chapter first briefly introduces to the basics of the electronic structure of aromatic molecules. Thereafter, the combined UPS and IPE spectra of DiMe-PTCDI are presented in Section 7.2. Therein, also the data analysis used to gain the values for the transport band gap, the ionisation energy IE, the electron affinity EA as well as the position of highest occupied molecular orbital (HOMO) and its counterpart, the lowest unoccupied molecular orbital (LUMO) are explained. In addition, a discussion of ways to determine the transport gap is given. In the last section, the electronic structure of perylene and its derivatives PTCDA, DiMe-PTCDI and PTCDI-C_8 are compared and discussed in order to gain a first understanding of the impact of derivatisation, i.e. adding an electron-withdrawing group to the perylene core.

7.1. The Electronic Structure of Aromatic Molecules

A free carbon atom exhibits the electronic configuration $1s^2 2s^2 2p^2$ in its ground state as it is shown in Figure 7.1 a). Thus, two valence electrons are available for the formation of chemical bonds in general. However, under certain circumstances the formation of hybrid orbitals is favourable: in planar, aromatic molecules, which are usually utilised in (opto-) electronics, sp^2 hybridisation takes place. Here, three sp^2 orbitals are built by a superposition of the atomic s

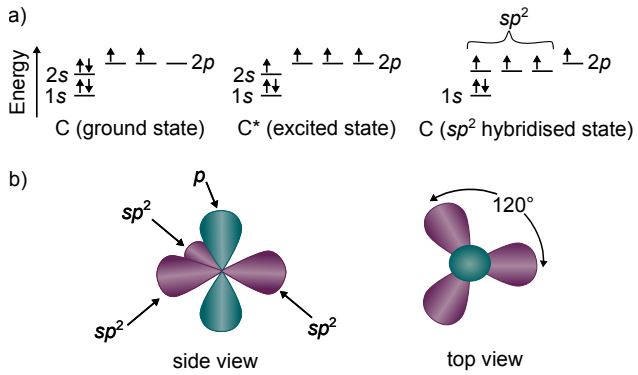

Figure 7.1 | Schematic sketch qualitatively explaining the sp^2 hybridisation in the case of carbon:
a) Schematic of the energy diagram of the sp^2 hybridisation in the case of carbon.
b) Illustration of the sp^2-hybrid orbitals of a carbon atom in side view and top view.

orbital with the two p orbitals p_x and p_y (see Figure 7.1 a)). As illustrated in Figure 7.1 b), the three sp^2 orbitals coloured in violet are coplanar and oriented at $120°$ relative to each other. Chemical bonds, which are formed by these orbitals, are called σ bonds. The fourth valence electron remains in its atomic orbital p_z (petrol-coloured), which is directed perpendicular to the plane of the sp^2-orbitals (see Figure 7.1 b)) [18].

The most simple aromatic molecule is benzene (C_6H_6), which is shown in Figure 7.2 a). It exhibits a hexagonal shape, where the carbon atoms are oriented in the σ bonds at bond angles of $120°$. Here, three of the four valence electrons of each carbon atom contribute to the σ bonds (see Figure 7.2 b)). The remaining electrons are located in the atomic p_z orbitals (see Figure 7.2 c)). They overlap and build three additional bonds, which are called π bonds.
Alternating single and double bonds are distributed along the benzene ring. Such a bonding type is commonly called conjugated, which can as well occur in linear molecules. Due to the overlap of the atomic p_z orbitals and the two degenerate possibilities of $p_z \cdot\cdot p_z$ interactions along the benzene ring, it is no longer possible to attribute the former p_z electrons to distinct positions in the molecule. Hence, the six π electrons are delocalised in clouds slightly above and beneath the carbon nuclei, which is shown in Figure 7.2 d). Such a planar, cyclic molecule that consists of conjugated double bonds as it is the case for benzene is called aromatic [18, 234].

A schematic sketch of the electronic structure of a single molecule is shown in Figure 7.3 a). The uppermost part of the potential well represents the vacuum level E_{Vac}, which an electron has to overcome to escape from the molecule to the vacuum. The electrons are represented by arrows with spin up and down.
When forming a molecule, the overlap of two σ orbitals leads to an energy splitting in which the new σ bonding level is occupied with electrons, while the anti-bonding state σ^* is unoccupied (see Figure 7.3 on the left side, all σ states are coloured in violet). In analogy, there is also a splitting in the p_z system forming to the π levels and the anti-bonding counterpart π^*. The energy levels of the π system are drawn by petrol-coloured lines and each bonding level is occupied with two electrons in spin up and down, respectively. Because of the weakness of the

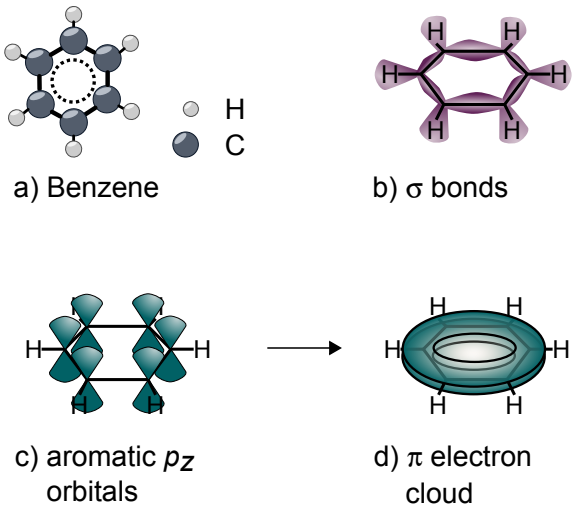

Figure 7.2 | Schematic sketch qualitatively illustrating the electronic system of the benzene ring:
a) Chemical structure of benzene (C_6H_6), which exhibits a hexagonal shape. The carbon atoms are oriented at $120°$.
b) The sp^2 orbitals are covalently bonded. The σ electron system is formed by three of the four valence electrons.
c) The fourth valence electron remains in its atomic p_z orbital, which is directed perpendicular to the plane of the sp^2 orbitals.
d) Due to the overlap of the atomic p_z orbitals, the six electrons in these orbitals form π clouds slightly above and beneath the carbon nuclei. These electrons are relatively delocalised over the benzene ring.

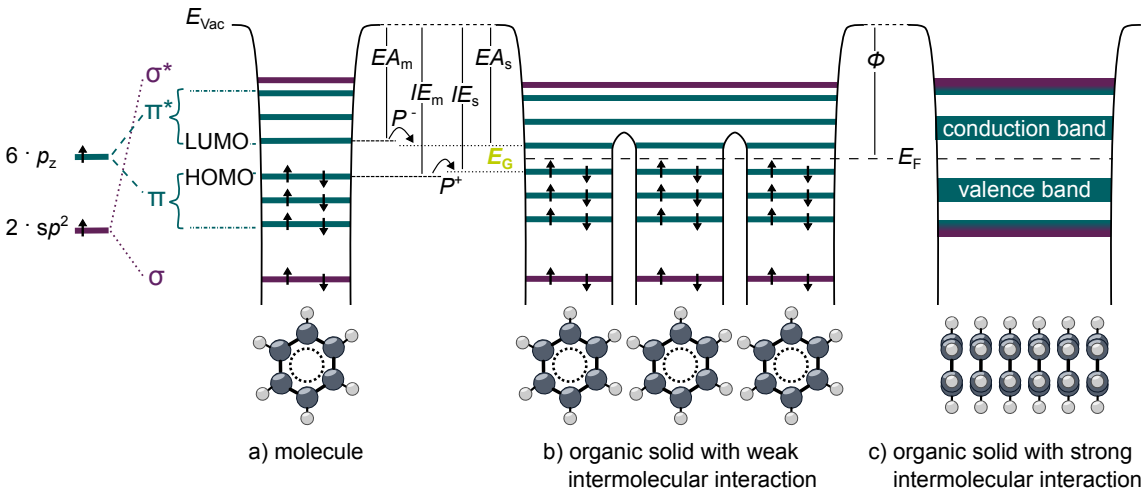

Figure 7.3 | Schematic sketch, qualitatively illustrating the evolution of the electronic structure from a single molecule to an organic solid:
a) The electronic structure of a single molecule.
b) The electronic structure of an organic solid with only weak interaction between adjacent molecules.
c) The electronic structure of an organic solid with strong intermolecular interaction.
A detailed discussion of this picture is given in the text. (This picture is freely adapted from [36, 235].)

π bonds and the weak localisation of their electrons, the splitting is much smaller compared to that of the σ system.

As illustrated in Figure 7.3 a), the outermost molecular orbital (MO), which is occupied, features electrons only of the π-system. It is called highest occupied molecular orbital (HOMO) and its counterpart, the lowest unoccupied molecular orbital (LUMO), is also a π state. The energy difference between the positions of HOMO or LUMO and E_{Vac} are defined as the ionisation energy IE_{m} or the electron affinity EA_{m} of the molecule, respectively. The ionisation energy is the minimal energy necessary for the removal of an electron from the molecule and its transfer to infinity with its kinetic energy equal to zero. The electron affinity is defined as the amount of energy released or spent when an electron is added to a neutral molecule to form a negative ion. The positions of HOMO and LUMO relative to the Fermi level E_{F} define the hole injection barrier (HIB) and the electron injection barrier (EIB), respectively, and the energy difference between HOMO and LUMO is defined as band gap E_{G}.

If the intermolecular interaction is weak like van der Waals interactions, while the molecules gather together to form an organic solid, the wave functions of the occupied and the lower unoccupied bands are mainly localised on each molecule (see Figure 7.3 b)). Their bandwidths thereby stay smaller than $\sim 400\,\mathrm{meV}$ [235]. Consequently, the electronic structure of the molecule is almost preserved in the organic solid. Thus, organic solids can carry characteristics of both, a solid state material and a single molecule [235]. With increasing strength of the intermolecular interaction, the relevant MOs of neighbouring molecules have a larger overlap. This leads to the formation of occupied valence and unoccupied conduction bands as already known from non-organic systems [18, 236, 237] (see Figure 7.3 c)). The bandwidth is

related to the spatial spread of the MO as well as to the intermolecular distance [36, 238]. Independent on the strength of the intermolecular interaction, the absolute values of the energy levels of an organic solid shift with respect to the E_{Vac} and with respect to the MOs of a single molecule because of the change in the polarisation of their surroundings. This leads to a decrease of the band gap E_{G} between HOMO and LUMO, to an increase of the electron affinity EA_{s} and to a lowering of the ionisation energy IE_{s}:

$$IE_{\mathrm{s}} = IE_{\mathrm{m}} - P^{+} \tag{7.1}$$

$$EA_{\mathrm{s}} = EA_{\mathrm{m}} + P^{-}. \tag{7.2}$$

Here, P^{+} represents the polarisation energy for a hole, while P^{-} is that for an electron. The polarisation energies P^{+} and P^{-} can differ from each other [207, 239, 240].
If charge transport in organic solids takes place, an additional charge has to be present on the molecule of an organic thin film. This may either be an additional electron which is hosted in an anti-bonding orbital, or an electron that is removed from a bonding orbital. Consequently, the molecule is no longer in the ground state but in a charged excited state. This leads to a change of the relative positions of the molecular orbitals with respect to the vacuum level E_{Vac}. Moreover, if an electron is removed from a π orbital or added to a π^{*} orbital, the spatial distribution of electrons in the more strongly bound σ orbitals is changed resulting in different bond lengths of the molecule. The energy associated with this change is known as geometric reorganisation energy and does also contribute to P^{+} and P^{-} [235, 241]. The charge in combination with the geometric distortion of the molecular atoms is referred to as a polaron [241].

In order to measure the electronic structure of organic thin films, usually ultra-violet photoelectron spectroscopy and inverse photoemission spectroscopy are applied. Since both methods lead to ionisation of the molecules in the solid thin film, in principle only energy levels of the charged, excited molecular states can be measured. As explained before, theses states are referred to polarons, which shift the energy levels on the order of a few $100\,\mathrm{meV}$ compared to the neutral molecule energy level [17]. As these polaron levels are directly derived from the respective HOMO and LUMO levels of the neutral molecule, the terms of HIB, EIB, IE, EA and HOMO and LUMO are used for the ground state as well as for the charged, excited state [17].

It is useful to shortly revise the difference between the transport gap E_{t} and the optical gap E_{opt} in semiconductors: the energy which is necessary to create spatially well-separated electrons and holes is called transport gap E_{t}. In the case of organic semiconductors, this energy is equal to the energy necessary for an excitation of an electron from the HOMO of one molecule and relaxation of it directly into the LUMO of another molecule. The optical gap E_{opt}, on the other hand, is defined as the energy needed for the formation of a correlated electron-hole pair, which is called exciton. For most inorganic semiconductors, this exciton is known as the *Wannier* exciton. Its binding energy is only about a few meV because of the small polarisation and good carrier screening efficiency in inorganic semiconductors. Therefore, the exciton binding energy, or charge separation energy $E_{\mathrm{t}} - E_{\mathrm{opt}}$ is usually negligible

for most inorganic semiconductors. Thus, the band gap is often obtained from the onset of the optical absorption spectra and E_t equals approximately E_{opt} [229].
In the case of an organic semiconductor, the formation of an electron-hole pair on the same molecule called *Frenkel* exciton or of a change transfer (CT) exciton with the electron and the hole on two adjacent molecules is equated to the optical gab E_{opt}. While, the exciton binding energy is small ($\sim 200\,\mathrm{meV}$) in conjugated polymers, it can be larger than $1.5\,\mathrm{eV}$ in small molecules like C_{60} [229].

7.2. Perylene and Perylene Derivatives – An Example: DiMe-PTCDI

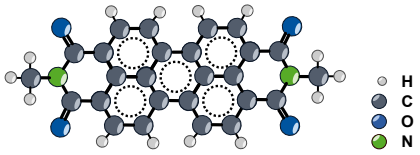

DiMe-PTCDI

On the left side of Figure 7.4, UPS spectra (secondary electron cutoff (SEC) and the occupied frontier states) of a $30\,\mathrm{nm}$, bulk-like DiMe-PTCDI[1] layer grown on a silver thin film[2] are shown, while the right side of the same figure shows the IPE spectra of the same sample. The intensity is plotted as a function of the binding energy with respect to the Fermi level for each spectrum. The spectra consist of a number of well-defined peaks featuring the density of occupied and unoccupied states of DiMe-PTCDI as well as a low-energy secondary electron cutoff (SEC) peak resulting from inelastically scattered electrons.
The SEC marks the threshold for photoionisation and is used to determine the work function via $\Phi = h\nu - E_{cutoff} = (4.2 \pm 0.1)\,\mathrm{eV}$. The work function Φ also gives the energy position of the vacuum level E_{Vac} with respect to the Fermi level, which is marked by a black solid line in the IPE spectrum on the right side of Figure 7.4.
The UPS spectrum of the plot in the middle of Figure 7.4 shows the occupied frontier electronic states of DiMe-PTCDI. At an energy of $E_{HOMO} = (-2.0 \pm 0.2)\,\mathrm{eV}$, the HOMO starts to rise. The onset position is determined from the extrapolation of the leading peak edge and the background. The energy difference between this onset and the vacuum level is the ionisation energy $IE = E_{Vac} - E_{HOMO} = (6.2 \pm 0.2)\,\mathrm{eV}$ [242]. The HOMO becomes maximal at $E = (-2.6 \pm 0.1)\,\mathrm{eV}$ [229]. As can be seen from density functional theory (DFT) calculations in [229], it is mainly located over the perylene core and partly on the oxygen atoms. Its character is purely π. The second peak in the UPS spectrum can be identified as a superposition of π as well as σ states of the molecule, where the contribution of the π state is stronger [208, 229, 243]. Its maximum is observable at $E = (-4.5 \pm 0.1)\,\mathrm{eV}$.
The LUMO starts to rise at an energy of $E_{LUMO} = (+0.6 \pm 0.3)\,\mathrm{eV}$, which can be seen in the IPE spectrum on the right side of Figure 7.4. The energy difference between E_{LUMO} and the

[1] The DiMe-PTCDI thin film was prepared at room temperature at a rate of $0.1\,\text{Å/s}$ by organic molecular beam deposition (OMBD). OMBD is a common method for thin film preparation of small molecule organic semiconductors via evaporation of the molecules in an ultra-high vacuum chamber.
[2] In contrast to the discussion in Chapter 6, the silver thin film is now of polycrystalline structure. It was thermally evaporated at a deposition rate of $1\,\text{Å/s}$ on a freshly cleaved MICA substrate.

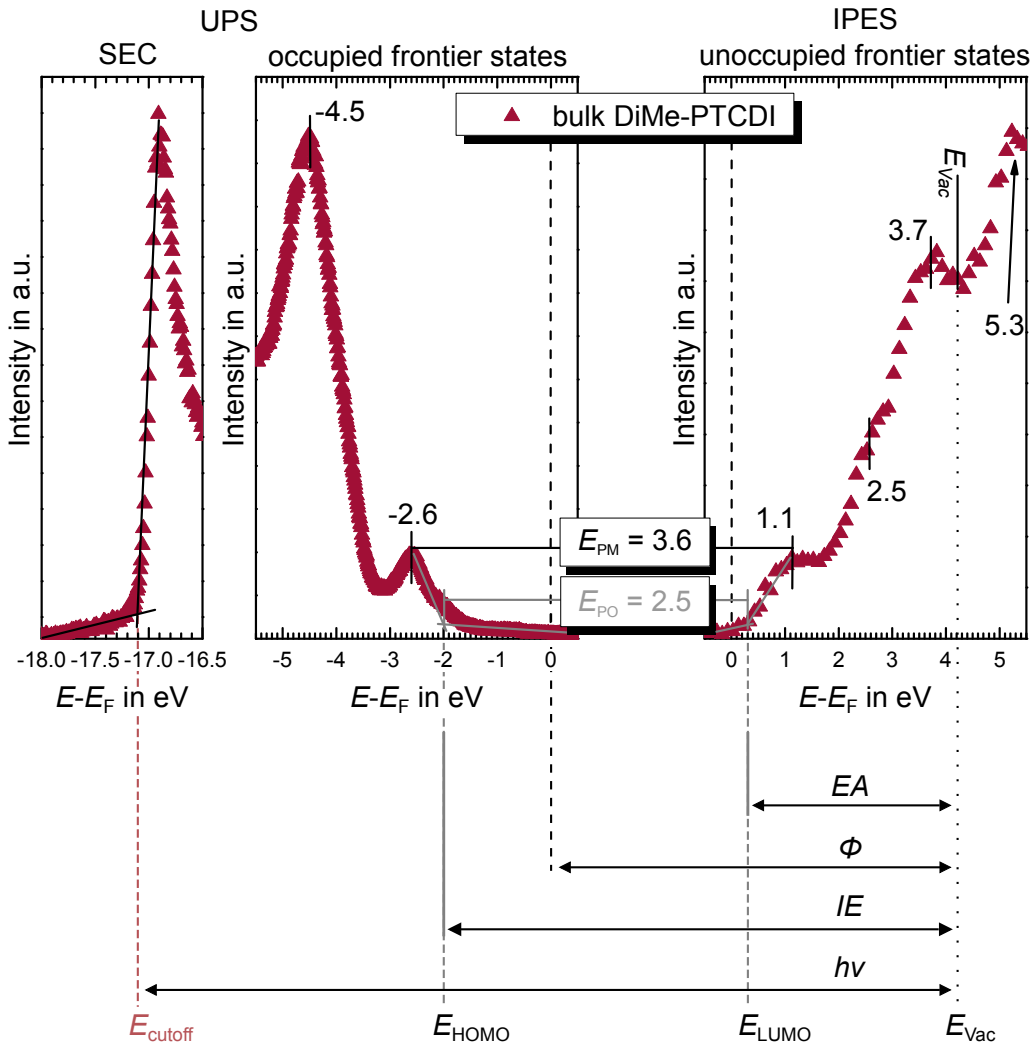

Figure 7.4 | Combined UPS and IPE spectra showing the electronic structure of bulk-like DiMe-PTCDI: all spectra were recorded on a 30 nm, bulk-like DiMe-PTCDI layer grown on a silver film. In the left graph, the secondary electron cutoff (SEC) featuring the threshold for photoionisation is used to determine the work function via $\Phi = h\nu - E_{\text{cutoff}}$. The UPS spectrum in the middle displays the occupied frontier states, whereas the unoccupied electronic states are shown in the IPE spectrum in the right graph. In all graphs, the intensity is plotted as a function of the energy, where the energy scale is referenced to the Fermi level E_F. The position of the Fermi level is marked by the black dashed lines in both frontier state spectra. In addition, the vacuum level is marked by a short black line labelled E_{Vac}.
The HOMO of DiMe-PTCDI starts to rise at an energy of $E_{\text{HOMO}} = (-2.0 \pm 0.2)\,\text{eV}$ and has its maximum at $E = (-2.6 \pm 0.1)\,\text{eV}$ [229]. The ionisation energy IE yielding the energy difference from the rise of the HOMO to the vacuum level ($IE = E_{\text{Vac}} - E_{\text{HOMO}}$) is determined to be $(6.2 \pm 0.2)\,\text{eV}$ [242]. The second peak in the UPS spectrum can be identified as a superposition of π as well as σ states of the molecule, whereby, the contribution of the π state is stronger [208, 229, 243]. It is centred at $E = (-4.5 \pm 0.1)\,\text{eV}$. In the IPE spectrum, the LUMO starts to rise at an energy of $E_{\text{LUMO}} = (+0.6 \pm 0.3)\,\text{eV}$. The electron affinity $EA = E_{\text{Vac}} - E_{\text{LUMO}}$ is $(3.7 \pm 0.3)\,\text{eV}$. The LUMO reaches its maximum at $E = (+1.0 \pm 0.2)\,\text{eV}$ [229]. Moreover, three additional peaks are positioned at $E = (+2.6 \pm 0.2)\,\text{eV}$, $E = (+3.7 \pm 0.2)\,\text{eV}$ and $E = (+5.2 \pm 0.2)\,\text{eV}$.
In addition, the distance between the peak onsets (grey lines) of HOMO and the LUMO and the distance between the their maxima (black lines) are indicated by horizontal lines, where the corresponding energy values $E_{\text{PM}} = (3.6 \pm 0.2)\,\text{eV}$ and $E_{\text{PO}} = (2.5 \pm 0.3)\,\text{eV}$ are noted.

vacuum level gives the electron affinity $EA = E_{\mathrm{Vac}} - E_{\mathrm{LUMO}} = (3.7 \pm 0.3)\,\mathrm{eV}$. The LUMO reaches its maximum at $E = (+1.0 \pm 0.2)\,\mathrm{eV}$ [229]. DFT calculations of [229] verify the pure π character of the LUMO level, which is delocalised over the perylene core of DiMe-PTCDI. Three additional states can be found at $E = (+2.6 \pm 0.2)\,\mathrm{eV}$, $E = (+3.7 \pm 0.2)\,\mathrm{eV}$ and $E = (+5.2 \pm 0.2)\,\mathrm{eV}$.

Data Analysis

At this point it is important to shortly explain and discuss the analytical approaches used to evaluate the measured data.
As a short reminder, the energy position of the secondary electron cutoff E_{cutoff} is given by the point of intersection of a linear fit on the secondary electron cutoff crossing the linear fit to the background (see the left graph in Figure 7.4).
For identification of the peak maxima, the background of the frontier state UPS and IPE spectra was subtracted by fitting an exponential function. Thereafter, the spectra were reproduced by a multi peak fit procedure giving the energy position of the peak maximum.
In order to determine the peak onsets correctly, the energy resolution of each spectroscopy has to be considered: at room temperature, the energy resolution of a UPS measurement is $100\,\mathrm{meV}$ if using the He I discharge lamp. Therefore, no deconvolution of the instrumental broadening is necessary since the instrumental resolution is much smaller than the width of the spectral features (FWHM $\geq 500\,\mathrm{meV}$). However, a deconvolution of the peaks has to be performed in the case of IPE data because of the comparably poor instrumental resolution of the IPES ($\Delta E_{\mathrm{IPES}} = 400\,\mathrm{meV}$). On that score, the FWHM of the IPE peaks was corrected by

$$\mathrm{FWHM}_{\mathrm{corrected}}[\mathrm{meV}] = \sqrt{\mathrm{FWHM}^2_{\mathrm{exp}}[\mathrm{meV}] - (0.4\,\mathrm{meV})^2}. \tag{7.3}$$

The peak onsets are then determined by the intercept of two linear extrapolations and after a proper deconvolution of the IPES spectra. One extrapolation describes the background. For the second one, a tangent is placed to the peak band edge in the inflection point [229].

Transport Gap

The questions about how to determine the transport gap E_{t} with UPS and IPES and, thus the exciton binding energy are controversially discussed for organic as well as inorganic semiconductors in literature [62, 207, 208, 244, 245]. In principle there are at least two ways possible. One is to determine the transport band gap E_{t} between the peak maxima E_{PM} of HOMO and LUMO. The other method defines the energy difference between the onsets E_{PO} of HOMO and LUMO as E_{t}. The values derived from these methods can differ by more than $1\,\mathrm{eV}$ [62, 207]. Thus, the question arises which method is physically correct and yields the accurate transport gap.
For DiMe-PTCDI, the transport gap is determined to $E_{\mathrm{PM}} = (3.6 \pm 0.2)\,\mathrm{eV}$ for the peak maximum method and $E_{\mathrm{PO}} = (2.5 \pm 0.3)\,\mathrm{eV}$ for the onset method (see Figure 7.4). These, values differ by $(1.1 \pm 0.2)\,\mathrm{eV}$. Although there is still no established and commonly accepted

approach, arguments can be pointed out that verify the onset method as physically correct [62, 229, 245, 246]. *S. Krause* and co-workers have recently shown that – in contrast to the peak maximum method – the peak onset method leads to a very good agreement of values derived from direct and inverse photoemission with those from optical measurements for representative inorganic semiconductors, i.e., II-VI, III-V, and elemental semiconductors as well as for organic semiconductors [62, 245]. From an experimental point of view, the reason is addressed to a certain probability of a state measured by photoemission not being the completely relaxed, i.e. fully screened final state. Meaning, if for example a hole is created in a solid by a photoionisation process, the electronic system is changed until the total energy is minimised. For this purpose, the charges are rearranged. If this relaxation process takes place on the same timescale as the photoionisation process, kinetic energy of the emitted electron corresponds to the binding energy of the relaxed system. However, in the case of localised orbitals it is possible that the positive charge essentially remains localised during the photoemission process apart from small rearrangements in the immediate vicinity. As a consequence, the emitted electron has a lower kinetic energy in comparison to the fully relaxed final state [245]. However, only the binding energy of the completely relaxed state is relevant for the determination of the transport level.
Furthermore, the peak widths are observed to be very similar for of all measured states of DiMe-PTCDI ($\overline{\mathrm{FWHM}} = (0.7 \pm 0.2)\,\mathrm{eV}$). Moreover, they are much larger than expected on the basis of the instrumental resolution at least in the UPS spectrum. This behaviour can be attributed to lifetime broadening under the assumption that the relaxation process occurs on the same timescale as the photoemission process. As a consequence, the measured peak positions do not equate to the fully relaxed final state. It was found that this lifetime broadening is in the order of eV for strongly coupled semiconductor-like systems [245, 247].
Other effects which can also influence the peaks are of no or minor importance. As already discussed above, the energy resolution in IPE spectra is on the same order of magnitude as the width of the spectral features. Therefore, a deconvolution of the peaks has to be performed for the IPE data in order to gain correct values of the peak onsets. The energy difference caused by this correction is about $\sim 100\,\mathrm{meV}$, which is also observed in literature [245]. Additionally, a surface effect like band bending can arise due to partially or completely filled surface states in the gap. However, this effect is known to usually extend over several hundred nm and is equal for all bands. Therefore, it can be neglected in the context of the determination of the transport band gap. Last but not least, the influence of the surface on the transport gap can also be neglected. It was shown, that the first layer contributes to $35\,\%$ and to $15\,\%$ to the electron spectra at $\sim 20\,\mathrm{eV}$ (He I) and at $\sim 10\,\mathrm{eV}$(Ar I), respectively. Thus, the major proportion of the spectrum comes from bulk states [62, 67, 245].
For these reasons, the peak onsets give the correct values of band extrema and, hence the correct transport gap.

7.3. Perylene and Perylene Derivatives – A Comparison

The data analysis discussed before was also performed for bulk-like thin films of perylene, PTCDA and PTCDI-C_8. For this purpose, a $100\,\mathrm{nm}$ thick perylene thin film was grown on ITO and $15\,\mathrm{nm}$ PTCDA and PTCDI-C_8 were deposited both on a silicon substrate[3]. In Figure 7.5, the results of the data analysis on the photoemission spectra of perylene and its derivatives are summarised and compared. For better comparison, the binding energy is now given with respect to the vacuum energy. The position of the Fermi level E_F with respect to the vacuum level is given by a grey line for each molecule. Different colours represent the different molecules: perylene (orange), PTCDA (violet), DiMe-PTCDI (red) and PTCDI-C_8 (turquoise). The analysed peaks are illustrated by one thicker line and two thinner ones and an underlying colour box. The thicker line represents the peak centre, while the thinner ones illustrate $\pm\mathrm{FWHM}/2$. As explained before, the FWHM of peaks in the IPE spectra are corrected by the FWHM of the apparatus function $\left(\mathrm{FWHM}_{\mathrm{corrected}} = \sqrt{\mathrm{FWHM}^2_{\mathrm{exp}} - 0.4^2}\right)$ [229, 245]. In Addition, the onset of the respective HOMO and LUMO is also plotted by thick lines in a lighter colour. The chemical structure of each molecule is also depicted. The measured work functions as well as the values for EA, IE, E_t are summarised in Table 7.1. In addition, the optical gaps found in literature [243, 244, 248] as well as the thereof derived exciton binding energy ($E_{B;ex}$), which is the difference between the optical and the transport gap, are also given.

Table 7.1 | Comparison the work functions Φ, the ionisation energies (IE) and the electron affinities (EA) of all investigated thin films of perylene and its derivatives. Additionally, the transport gaps (E_t) determined from the peak onset are compared to optical gaps (E_{opt}), which are reported in [244] in the case of perylene, in [243] in the case of PTCDA and DiMe-PTCDI and in [248] in the case von PTCDI-C_8. The deviation of the optical from the transport gap is the exciton binding energy ($E_{B;ex}$), which is also given.

	perylene	PTCDA	DiMe-PTCDI	PTCDI-C_8
Φ ±0.1 eV	4.4 eV	4.5 eV	4.2 eV	4.2 eV
IE ±0.2 eV	5.2 eV	6.6 eV	6.2 eV	6.1 eV
EA ±0.3 eV	1.7 eV	4.0 eV	3.7 eV	3.7 eV
E_t ±0.3 eV	3.5 eV	2.6 eV	2.5 eV	2.4 eV
E_{opt}	2.83 eV	2.22 eV	2.16 eV	2.20 eV
$E_{B;ex}$ ±0.1 eV	0.7 eV	0.4 eV	0.3 eV	0.2 eV

Perylene[4]

As a short reminder, all values are now given with respect to E_{Vac}. At an energy of $E_{HOMO} = (-5.2 \pm 0.1)\,\mathrm{eV}$, the HOMO starts to rise, which yields also the ionisation energy IE [244]. The HOMO is centred at $E = (-5.8 \pm 0.1)\,\mathrm{eV}$. The second peak is centred at $(-7.5 \pm 0.1)\,\mathrm{eV}$.
The LUMO starts to rise at an energy of $E_{LUMO} = (-1.7 \pm 0.3)\,\mathrm{eV}$ also representing the electron affinity EA. The LUMO is centred at $E = (-1.1 \pm 0.2)\,\mathrm{eV}$. Due to the high-lying LUMO

[3] The deposition rate was 2 Å/s for the perylene sample and 0.2 Å/s for the PTCDA and PTCDI-C_8 samples. All samples were produced at room temperature.

[4] The combined UPS and IPE spectrum is shown in Figure C.1 in the appendix on page IX.

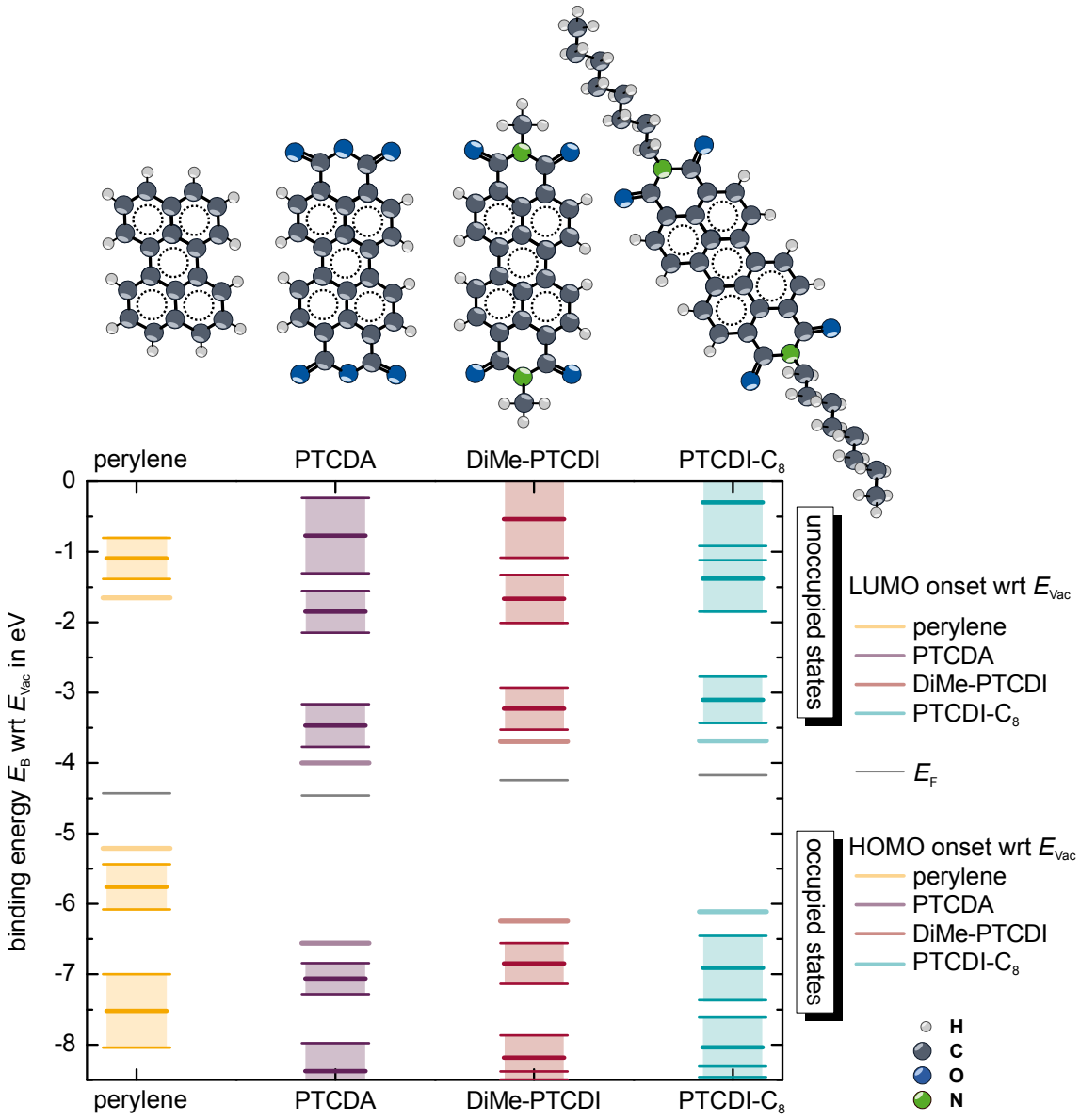

Figure 7.5 | Comparison of the electronic structure of perylene, substituted perylenes: the occupied and unoccupied electronic states of bulk-like thin films of perylene (orange), PTCDA (violet), DiMe-PTCDI (red) and PTCDI-C_8 (turquoise) are measured using UPS and IPES, respectively. In order to improve the comparability, the states are illustrated by one thicker line and two thinner ones and an underlying colour box. The thicker line represents the peak centre, while the thinner ones illustrate $\pm$FWHM$/2$. As explained before, the FWHM of peaks in the IPE spectra are corrected by the FWHM of the apparatus function $\left(\mathrm{FWHM}_{\mathrm{corrected}} = \sqrt{\mathrm{FWHM}^2_{\mathrm{exp}} - 0.4^2}\right)$ [229]. In Addition, the onset of the respective HOMO and LUMO is also plotted by thick lines in a lighter colour. All energies are referenced to the vacuum level E_{Vac}. The position of the Fermi level E_{F} with respect to the vacuum level is given by a grey line for each molecule. The resulting ionisation energies (IE) and the electron affinities (EA) as well as the measured transport gaps are summarised in Table 7.1.
The figure is discussed in detail in the text.

with respect to E_F, the injection barrier for electrons from metal electrodes is very high resulting in a mainly p-type electrical transport, which is also observed in [51, 249].

The molecules 3,4,9,10-perylene-tetracarboxylic acid dianhydride (PTCDA) and N,N'-substituted perylene-3,4,9,10-perylene dicarboximide (PTCDIs) are the most prominent substituted perylenes. As can be seen in Figure 7.5, the substitution of perylene with electron-withdrawing anhydride or imide groups significantly lowers the molecular orbitals with respect to the vacuum level. It has recently been shown that molecules containing elements with a relatively high ionisation energy, like N ($IE = 14.5\,\mathrm{eV}$), O ($IE = 13.6\,\mathrm{eV}$) or F ($IE = 17.4\,\mathrm{eV}$), tend to increase their IE, too [242, 250]. This can also be observed for PTCDA and the PTCDIs when comparing their IE to that of perylene (see Table 7.1). Moreover, the LUMO seems to be more affected by the placement of a functional group to the perylene core than the HOMO, which results in a stronger increase of EA and thus in a lowering of the optical and the transport gap (see Table 7.1).

PTCDA[5]

At an energy of $IE = (-6.6 \pm 0.2)\,\mathrm{eV}$, the HOMO starts to rise. The HOMO is centred at $E = (-7.1 \pm 0.1)\,\mathrm{eV}$ [208, 229, 242]. A second peak is centred at $(-8.4 \pm 0.1)\,\mathrm{eV}$.
The LUMO starts to rise at an energy of $EA = (-4.0 \pm 0.3)\,\mathrm{eV}$. The LUMO is centred at $E = (-3.7 \pm 0.2)\,\mathrm{eV}$ [62, 208, 229]. A second peak can be observed at $E = (-1.9 \pm 0.2)\,\mathrm{eV}$ and a third at $E = (-0.8 \pm 0.2)\,\mathrm{eV}$. Due to the low-lying LUMO with respect to E_F, the injection barrier for electrons from metal electrodes is very low resulting in a mainly n-type electrical transport.

When comparing the results gained for PTCDA with those for DiMe-PTCDI discussed in Section 7.2, the replacement of the oxygen atom in the anhydride group of PTCDA by the less polar methylimide group in the case of DiMe-PTCDI results in a small increase of the molecular orbitals with respect to the vacuum level as a consequence of the higher electronegativity of oxygen compared to N-CH_3. This results in a slightly smaller electron affinity as well as in a decreased ionisation energy in the case of DiMe-PTCDI (see Table 7.1). Therefore, it can be concluded, that also the placement of the elements is important for the discussion of the electronic structure of molecules [242].

PTCDI-C_8[6]

At an energy of $IE = (-6.1 \pm 0.2)\,\mathrm{eV}$, the HOMO starts to rise. The HOMO is centred at $E = (-6.9 \pm 0.1)\,\mathrm{eV}$. A second peak and a third peak is centred at $(-8.0 \pm 0.1)\,\mathrm{eV}$ and $(-8.7 \pm 0.1)\,\mathrm{eV}$, respectively.
The LUMO starts to rise at an energy of $EA = (-3.7 \pm 0.3)\,\mathrm{eV}$. The LUMO is centred at $E = (-3.1 \pm 0.2)\,\mathrm{eV}$. A second peak can be observed at $E = (-1.4 \pm 0.2)\,\mathrm{eV}$ and a third at $E = (-0.3 \pm 0.2)\,\mathrm{eV}$. PTCDI-C8 is also n-type semiconductor, due to the low-lying LUMO with respect to E_F.

[5] The combined UPS and IPE spectrum is shown in Figure C.2 in the appendix on page X.
[6] The combined UPS and IPE spectrum is shown in Figure C.3 in the appendix on page XI.

The lengthening of the alkyl chain, on the other hand, when going from DiMe-PTCDI (PTCDI-C_1) to PTCDI-C_8, has only a minor impact on the electronic structure: similar to PTCDA or DiMe-PTCDI, LUMO and HOMO are mainly located on the perylene core of PTCDI-C_8 and are not pinpointed on the alkyl chain [251]. Furthermore, the lengthening of the alkyl chain leads to an electrical screening, which results in less pronounced peaks in the UPS and IPE spectra but not in a significant shift of the peaks. However, it leads to an increase of the molecular diffusivity on the substrate and, thus, longer alkyl chains support an efficient ordering within the solid state [252]. This increased ordering of PTCDI-C_8 in comparison to that of DiMe-PTCDI can be a potential explanation for the small changes in the electronic structure observable in Figure 7.5 because crystal order and also the orientation of the molecules in a solid film influence the electronic structure [17, 36].

Comparison of electronic and optical properties of perylene and substituted Perylenes

In Figure 7.6, the optical gap is plotted versus the transport gap E_t (for the values see Table 7.1). The colour code representing the molecules is the same as used before: perylene (orange), PTCDA (violet), DiMe-PTCDI (red) and PTCDI-C_8 (turquoise). A linear fit to the data gives a slope and an intercept of (1.6 ± 0.2) and $(-0.9 \pm 0.4)\,\mathrm{eV}$, respectively. It is represented by the black dashed-dotted line. With increasing optical band gap, also the transport gap increases. Thus, the exciton binding energy $E_{B;ex} = E_t - E_{opt}$ increases with increasing transport gap energy E_t. This behaviour is already known from inorganic semiconductors [244]. In this case, the polarisability and hence permittivity ε of the material decrease with increasing transport gap. Thus, for organic semiconductors, the exciton binding energy is expected to increase linearly with the transport gap since its binding energy is inversely proportional to ε [244]. However, the charge density and distribution, which depend on the molecular size, also influence the exciton binding energy [244]. This is a potential explanation, for PTCDI-C_8 featuring a slightly smaller exciton binding energy than DiMe-PTCDI.

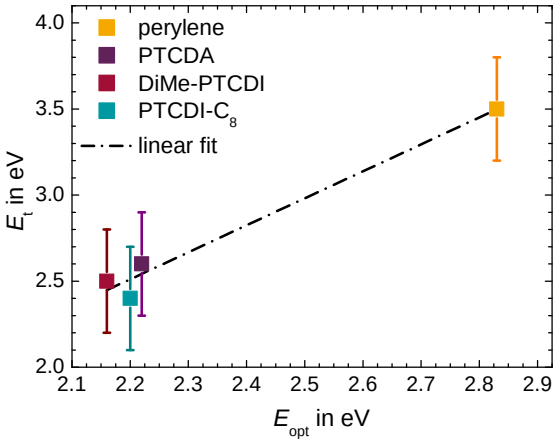

Figure 7.6 | Comparison of electronic and optical gab of perylene and substituted perylenes: the optical gap E_{opt} [243, 244, 248] is plotted versus the transport gap E_t. All values are referenced to the vacuum level E_{Vac}. The linear fit to the data gives a slope and an intercept of (1.6 ± 0.2) and $(-0.9 \pm 0.4)\,\mathrm{eV}$, respectively. Concluding, the exciton binding energy $E_{B;ex}$ increases with increasing transport gap energy E_t. This behaviour is also known from inorganic semiconductors. Thus, the material polarisability decreases with increasing band gab, since the binding energy is inversely proportional to the permittivity [244].

7.4. Summary

This chapter focused on the electronic structure of bulk-like organic thin films: in this context first the results gained for DiMe-PTCDI were discussed in detail. Thereafter, they were compared to the electronic structure of perylene, PTCDA and PTCDI-C_8 in order to investigate the influence of the substitution with elements of a relatively high ionisation energy as well as the influence of the alkyl chain length when comparing PTCDI-C_8 with DiMe-PTCDI.
For DiMe-PTCDI, the work function was determined via $\Phi = h\nu - E_{\text{cutoff}} = (4.2 \pm 0.1)\,\text{eV}$. The UPS spectrum showed the occupied frontier electronic states of DiMe-PTCDI: at an energy of $E_{\text{HOMO}} = (-2.0 \pm 0.2)\,\text{eV}$, the HOMO starts to rise. The energy difference between this onset and the vacuum level is the ionisation energy $IE = E_{\text{Vac}} - E_{\text{HOMO}} = (6.2 \pm 0.2)\,\text{eV}$ [242]. The HOMO is centred at $E = (-2.6 \pm 0.1)\,\text{eV}$ [208, 229]. As can be seen from density functional theory (DFT) calculations in [229], it is mainly located over the perylene core and partly spread on the oxygen atoms. Its character is purely π. The second peak in the UPS spectrum can be identified as a superposition of π as well as σ states of the molecule, whereby the contribution of the π state is stronger [208, 229, 243]. It is centred at $E = (-3.9 \pm 0.1)\,\text{eV}$.
The LUMO starts to rise at an energy of $E_{\text{LUMO}} = (+0.6 \pm 0.3)\,\text{eV}$. The energy difference between E_{LUMO} and the vacuum level yields the electron affinity $EA = E_{\text{Vac}} - E_{\text{LUMO}} = (3.7 \pm 0.3)\,\text{eV}$. The LUMO is centred at $E = (+1.0 \pm 0.2)\,\text{eV}$ [208, 229]. Again DFT calculations of [229] verify the pure π character of the LUMO level, which is delocalised over the perylene core of DiMe-PTCDI. Three additional states can be seen at $E = (+2.6 \pm 0.2)\,\text{eV}$, $E = (+3.7 \pm 0.2)\,\text{eV}$ and $E = (+5.2 \pm 0.2)\,\text{eV}$.
As discussed above, the transport band gap differs from the optical band gap by the comparably large binding energy of the *Frenkel* excitons. There are at least two ways used in literature to determine the transport gap: the energy difference between the peak maxima of HOMO and LUMO E_{PM} or that between the onsets of HOMO and LUMO E_{PO}. Since the peak onsets yield the binding energy of the completely relaxed state, the difference between E_{PO} yields the correct transport band gap.
The comparison of the electronic structure of perylene with its derivatives PTCDA, DiMe-PTCDI and PTCDI-C_8 manifests that the substitution of perylene with functional groups containing elements with a relatively high ionisation energy leads to a lowering of the molecular orbitals with respect to the vacuum level. The impact of the electron-withdrawing groups on the perylene core is stronger for the LUMO than for the HOMO, which results in a lowered gap. Furthermore, the shift of the molecular orbitals results in a change of the transport properties. While perylene clearly shows p-type electrical transport, its derivatives are n-type semiconductors because of the low-lying LUMO yielding a low injection barrier for electrons.
When comparing the results gained for PTCDA with those for DiMe-PTCDI, the exchange of the bridging oxygen of the anhydride side group of PTCDA with a nitrogen atom in the case of DiMe-PTCDI results in a small increase of the molecular orbitals with respect to the vacuum level. This results in a slightly smaller electron affinity as well as in a decreased ionisation energy in the case of DiMe-PTCDI. Therefore, it is concluded that also the placement of the elements is important for the discussion of the electronic structure of molecules [242]. The

lengthening of the alkyl chain, on the other hand, when going from DiMe-PTCDI (PTCDI-C_1) to PTCDI-C_8, has only a minor impact on the electronic structure: similar to PTCDA or DiMe-PTCDI, LUMO and HOMO are mainly located on the perylene core of PTCDI-C_8 and are not pinpointed on the alkyl chain [251]. Moreover, it is shown that the exciton binding energy $E_{\mathrm{B;ex}} = E_{\mathrm{t}} - E_{\mathrm{opt}}$ increases with increasing transport gap energy E_{t}, which is already known from inorganic semiconductors [244].

8. Interface Formation between DiMe-PTCDI Molecules and a Noble Metal Surface

The interaction taking place at an organic-metal interface may cause a charge exchange or polarisation. This, in turn, would influence the direction and size of the interface dipole and the position of the molecular orbitals relative to those of the isolated molecule as well as relative to each other. These parameters then determine the charge injection properties into an organic layer from an inorganic contact electrode [63]. Therefore, the energy level alignment (ELA) at such interfaces has to be known in order to ensure an effective charge transfer and thus, to enhance the performance of (opto-) electronic devices [17, 19, 20]. However, the ELA is not only interesting in the context of the technological progress, but also from a fundamental point of view: at such an interface two different scientific fields – solid-state physics and molecular science – come together [21, 22].

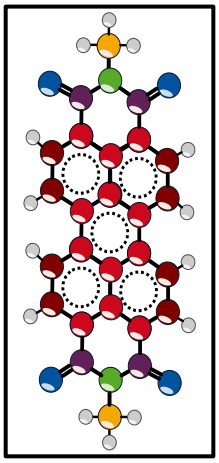

DiMe-PTCDI

This chapter focuses on the chemical and electronic interaction between silver and copper thin film with thin layers of DiMe-PTCDI deposited on top. In contrast to the discussion in Chapter 6, for the following evaluation, the metallic substrates are now of polycrystalline structure. They were thermally evaporated at a deposition rate of $1\,$Å/s on a freshly cleaved MICA substrate and have a nominal film thickness of $30\,\mathrm{nm}$. Subsequently and without breaking the vacuum, various organic layers were prepared with different film thickness ($4\,$Å - $32\,$Å and $300\,$Å, which equals a coverage of 0.6 monolayers (ML) - $4.8\,$ML and $45.5\,$ML) at a rate of $0.1\,$Å/s by organic molecular beam deposition. All samples were produced at room temperature. Thereafter, the samples have been characterised in-situ with XPS, UPS and IPES in order to gain information about the chemical and electronic interaction. Additionally, the morphology of the thin DiMe-PTCDI layers was monitored ex-situ with atomic force microscopy[1] (AFM).

[1] Atomic force microscopy (AFM) is applied to investigate the morphology of thin films. In AFM, a sharp tip scans across the sample in order to probe the surface. It is connected to a cantilever. When the tip approaches the surface, at a certain distance, it will interact with the surface. This interaction induces a mechanical bending of the tip cantilever due to attracting or repulsing forces. The mechanical bending is measured by the change in the reflection of a laser beam pointed on the cantilever and detected by a photo detector. All AFM images presented in this thesis were taken with the AFM Nanoscope III a from Digital Instruments used in tapping mode. The lateral resolution of the images depends on the chosen scan size, because the size of the images is limited to a maximum of 512 pixel x 512 pixel.

The results for DiMe-PTCDI grown on a silver substrate are discussed in the first section, while, those gained with copper as substrate are shown in Section 8.2. Each section, first presents the results in a purely descriptive way. Thereafter, these results are discussed in combination and an explanation is given.
It should be noted that the measurements presented below were recorded in cooperation with the master student *G. Huang*, who was supervised during the course of this thesis.

8.1. The Interface between DiMe-PTCDI and Silver

Growth of DiMe-PTCDI on Silver in the (Sub-)Monolayer Regime

In Figure 8.1, AFM images of DiMe-PTCDI thin films grown on a silver surface are displayed. Each picture with a scan size of $(2 \times 2)\,\mu m^2$ represents the morphology of the respective film in a colour-coded image: the corresponding height can be inferred from the colour scale on the right side.
The sample shown in Figure 8.1a) displays the pristine silver surface, which is used as substrate. The morphology can be divided into two different regions: smooth, large areas (green square) with an average island size of $(875 \pm 22)\,nm$ cover the substrate by $(24 \pm 2)\,\%$, while $(76 \pm 6)\,\%$ feature a grainy surface (blue square) with small islands with a size of $(61 \pm 5)\,nm$. At a film thickness of 0.6 ML of DiMe-PTCDI (Figure 8.1b)), the molecules cluster in large islands of the size of $(104 \pm 18)\,nm$ on the smooth, large areas of the silver substrate (green square). The smooth area is covered by $(20 \pm 4)\,\%$ with DiMe-PTCDI islands. A less amount of DiMe-PTCDI islands $((5 \pm 1)\,\%)$ forms smaller islands with an average island size of $(22 \pm 5)\,nm$ on the grainy area (blue square). With increasing thickness up to 1.8 ML (Figure 8.1b) - Figure 8.1d)), the islands located on the smooth, large areas of the silver substrate (green square) grow in size and in the coverage (see Figure 8.2 a) an b)). The smaller islands stay constant in their size, which can be also seen in Figure 8.2 a) showing the average island size as a function of the number of monolayers. After an increase in the average island coverage between a DiMe-PTCDI layer thickness of 0.6 ML and 1.2 ML, the average DiMe-PTCDI island coverage on the grainy silver area (blue) stays constant up to $\Theta_n = 3.6$ ML (see Figure 8.2 b)). Between a coverage of 2.4 ML and 3.6 ML, the growth of the smaller islands becomes dominant (blue square). First, they tend to overgrow the larger islands, which results in an 'decrease' in their average island size (see Figure 8.2 a) green plot). Thereafter, the larger islands are no more observable and the size as well as the coverage of the smaller islands increases (see Figure 8.2 a) and b) as well as Figure 8.1e) and f)). The morphology of the 3.6 ML thick DiMe-PTCDI thin film is similar to that of the samples covered with 4.8 ML and 45.5 ML of DiMe-PTCDI (see Figure D.1 on XIII in the appendix).
Up to $\Theta_n = 2.4$ ML, the RMS roughness increases, which can be seen in Figure 8.2 c) displaying the RMS roughness as a function of the number of monolayers. For $\Theta_n > 2.4$ ML, where the growth of smaller islands dominates, the RMS roughness first stays constant. Thereafter ($\Theta_n = 4.8$ M), it is decreased due to the increasing coverage with smaller DiMe-PTCDI

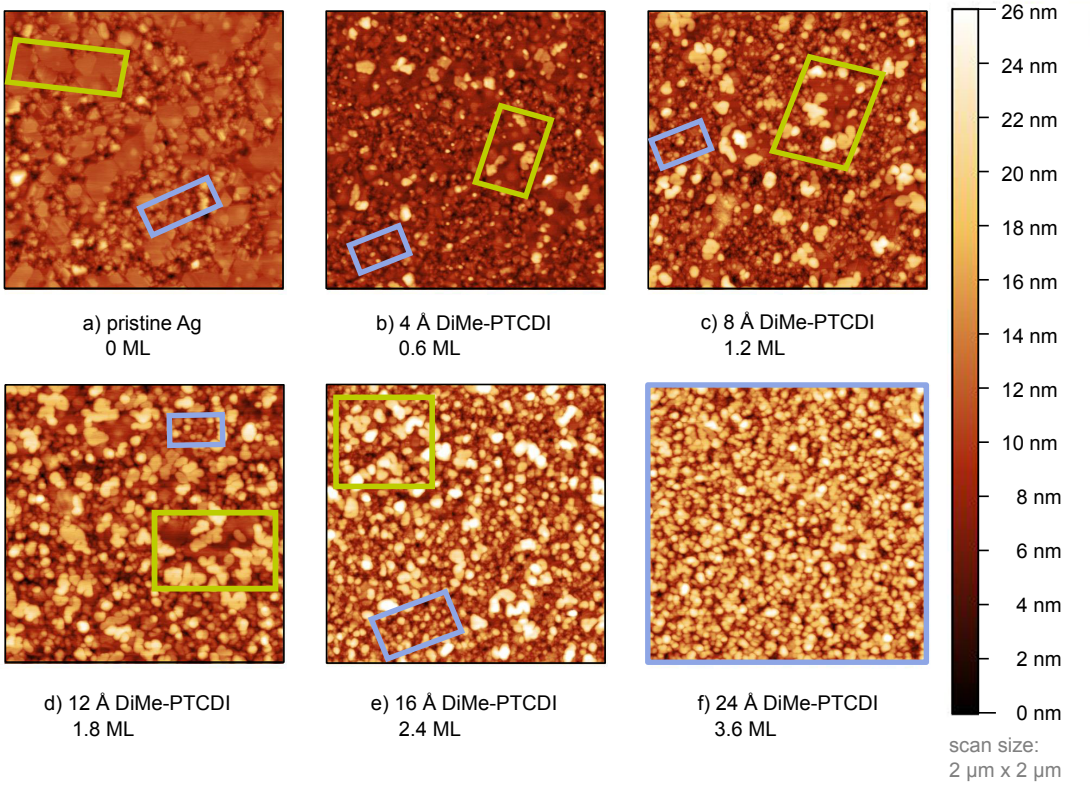

Figure 8.1 | AFM images of the DiMe-PTCDI thickness series grown on silver: a) - f) The scan of the size $(2 \times 2)\,\mu m^2$ shows the morphology of each sample surface in a colour coded image: the respective height can be inferred from the colour scale on the right side. The sample shown in a) displays the morphology of the pristine silver surface used as substrate. On top of this substrate, DiMe-PTCDI thin films are grown with a coverage of b) 0.6 monolayers (ML), c) 1.2 ML, d) 1.8 ML, e) 2.4 ML and f) 3.6 ML. The light green and light blue squares mark different regions of the samples. A detailed description is given in the text. Images of DiMe-PTCDI thin films with larger film thickness can be found in Figure D.1 on XIII in the appendix.

islands. The bulk-like DiMe-PTCDI features an RMS roughness of $(5.4 \pm 0.2)\,nm$.

It has been highlighted in Section 2.1, how X-ray photoelectron spectroscopy is a surface sensitive technique. Thereby, the detected electrons may have penetrated a certain amount of the material before they leave the surface of the metal or the molecule. Thus, the special origin of the emitting atom defines the penetration length that the electrons have to traverse to reach the surface. Consequently, irrespective of the binding energy of the electrons, the observed intensity I is a function of the mean-free path λ of these electrons and of the amount of matter they moved through. During the growth of several monolayers of the organic material on a metal substrate, the signal intensity of both, the molecule as well as of the metal, changes with the number of monolayers Θ_n [26]. The decay of intensity due to the adsorbate thickness z can be expressed analogous to the case of the absorption of electromagnetic light [26]. For the simplest case of layer by layer growth (*Frank-van der Merve* growth) and

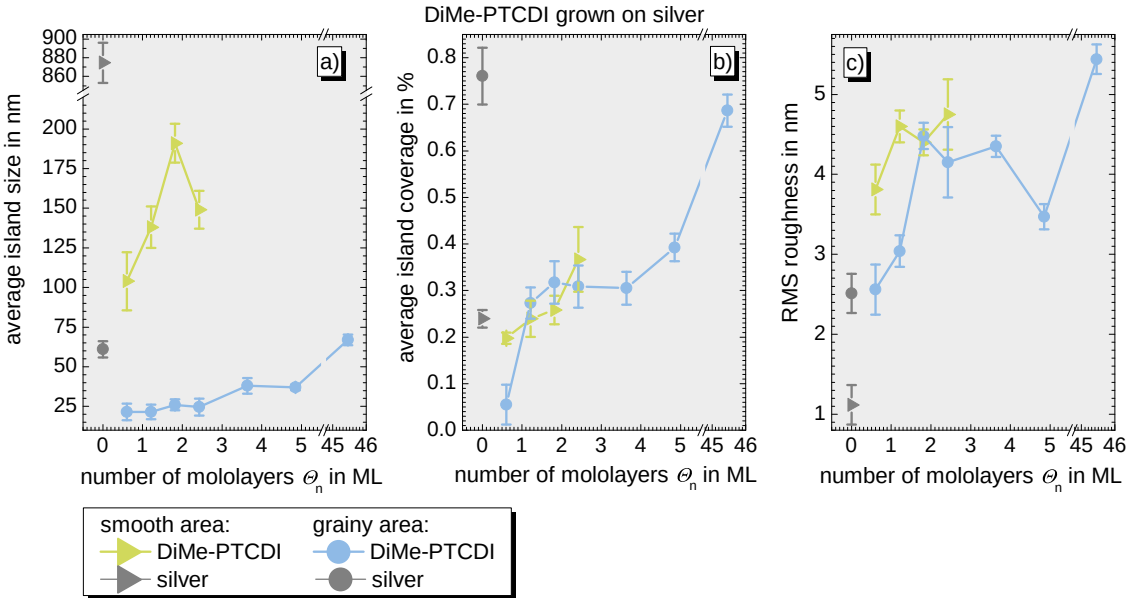

Figure 8.2 | AFM statistics of the DiMe-PTCDI thickness series grown on silver: a) The average island size is plotted as a function of the number of DiMe-PTCDI monolayers for both silver substrate areas (smooth and grainy).
b) The average island coverage is displayed as a function of the number of monolayers for the smooth and grainy silver substrate area, respectively.
c) The RMS roughness is depicted as a function of the number of monolayers for both areas.

under the assumption of a simple continuum-type description the change of the XPS emission line intensity dI is proportional to the change of film thickness dz

$$\frac{\mathrm{d}I}{I} = -\frac{\mathrm{d}z}{\lambda}. \tag{8.1}$$

If an organic thin film is prepared on a metal substrate, the increase of the XPS emission line intensity I^{F} due to the adsorbate thickness z can be expressed by:

$$\frac{I^{\mathrm{F}}}{I^{\mathrm{F}}_{\infty}} = 1 - e^{-z/\lambda} = 1 - e^{-\Theta_{\mathrm{n}} d/\lambda}. \tag{8.2}$$

Here, I^{F}_{∞} is the emission line intensity of the bulk-like film and Θ_{n} represents the number of the monolayers of the thickness d. The decay of the emission line intensity I^{S} which originates from the substrate atoms after a coverage with Θ_{n} monolayers of the film is then given by

$$\frac{I^{\mathrm{S}}}{I^{\mathrm{S}}_{0}} = e^{-\Theta_{\mathrm{n}} d/\lambda}, \tag{8.3}$$

where I^{S}_{0} is the intensity of the clean metal substrate.
The behaviour of the XPS emission line intensity as a function of the number of the monolayers Θ_{n} of the thickness d is schematically depicted in Figure 8.3. Here, the red line represents the intensity ratio of the deposited material, while the grey one illustrates the intensity de-

cay of the substrate XPS emission line. Figure 8.3 a) illustrates the case of layer by layer growth (*Frank-van der Merve* growth), b) island growth (*Volmer-Weber* growth) and c) layer plus island growth (*Stranski-Krastanov* growth). As introduced before, layer by layer growth can be described by an exponential function. For island growth, however, the intensity versus coverage dependence $I(\Theta_n)$ is different. During film growth, large areas of the substrate are not covered with the deposited material. In contrast to the case of layer-by-layer growth with complete over layers, the substrate signal is less suppressed [26]. Consequently, only a slow increase and decrease of the film and of the substrate signal, respectively, is observed with increasing number of monolayers Θ_n (see Figure 8.3 b)). Layer plus island growth is characterised by a change in the slope of the linear increase or decrease (see Figure 8.3 c)). While the first few monolayers grow layer by layer, the slope is steeper as compared to the subsequent following island growth. The slope after the island formation becomes dominant is dependent on the density and the shape of the islands as well as on the mean-free path of the particular electrons [26].

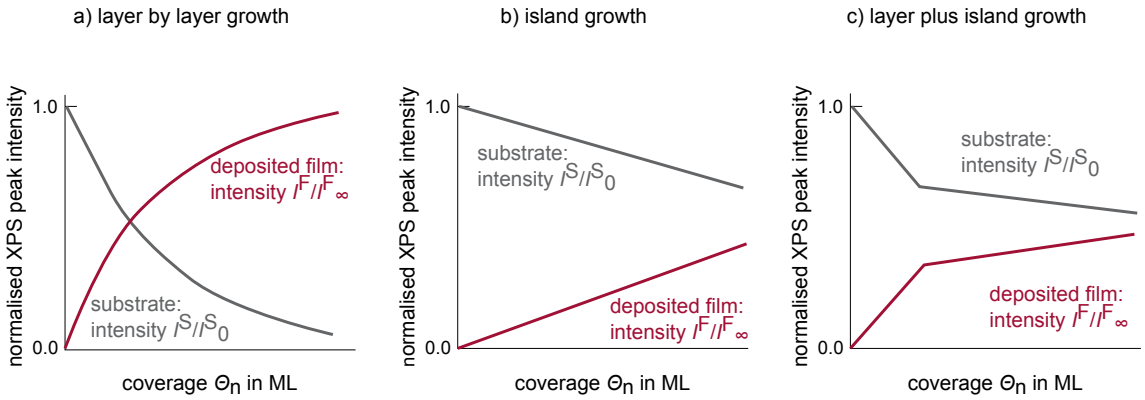

Figure 8.3 | Schematic representing the behaviour of the XPS line intensities of the deposited thin film and the substrate as a function of the number of the monolayers Θ_n of the thickness d: in the case of a) layer by layer growth (*Frank-van der Merve* growth), b) island growth (*Volmer-Weber* growth) and c) layer plus island growth (*Stranski-Krastanov* growth). (This schematic is freely adapted from [26].)

In Figure 8.4 a), the normalised XPS peak intensity is plotted as a function of the number of DiMe-PTCDI monolayers Θ_n. Here, the grey triangles represent the normalised intensity $\left(I^{Ag}/I^{Ag}_{pristine}\right)$ of the Ag $3d$ XPS emission peaks, while the red circles are the normalised data $\left(I^C/I^C_{bulk}\right)$ gained from the C $1s$ peak.

For $\Theta \leq 2.4$ ML, the curve representing the silver substrate decreases with increasing coverage, while that for DiMe-PTCDI increases. The curves cross each other at a coverage of 3.4 monolayers which equals a film thickness of 22.4 Å. With further increasing number of DiMe-PTCDI monolayers Θ_n, the silver curve seems to stay. The red curve, on the other hand, increases further. However, its slope is much lower as for $\Theta_n \leq 2.4$ ML. The change of the slope of each curve can be explained with the before observed change in the growth behaviour. Up to a thickness of $\Theta_n = 2.4$ ML, large DiMe-PTCDI islands cover the smooth surface area of the silver substrate. The grainy part of the silver surface, however, is covered

with less and smaller islands. Between $\Theta_n = 2.4\,\text{ML}$ and $\Theta_n = 3.6\,\text{ML}$, the growth of the smaller islands starts to become dominant. Furthermore, the smaller islands seem to overgrowth and to cover the larger islands. Consequently, the silver signal stays constant as the average island coverage does. Since the amount on deposited molecules increases also the intensity of the XPS C $1s$ further increases. However, the slope of the C $1s$ curve changes, since it is dependent on the density and the shape of the islands [26]. In Figure 8.4 b), the schematic representing the behaviour of XPS line intensities for the case of island growth is extended for the case of the overgrowth and coverage with smaller islands. Here, $\Theta_n = m$ represents the point of the change in the growth behaviour. It is assumed that with further increasing island density the film and the substrate signal increase and decrease again, respectively. This behaviour could not be proven in the course of the presented thesis. Therefore, it is proposed for future studies to analyse the XPS emission intensities of films which are thicker than $\Theta_n = 4.8\,\text{ML}$.

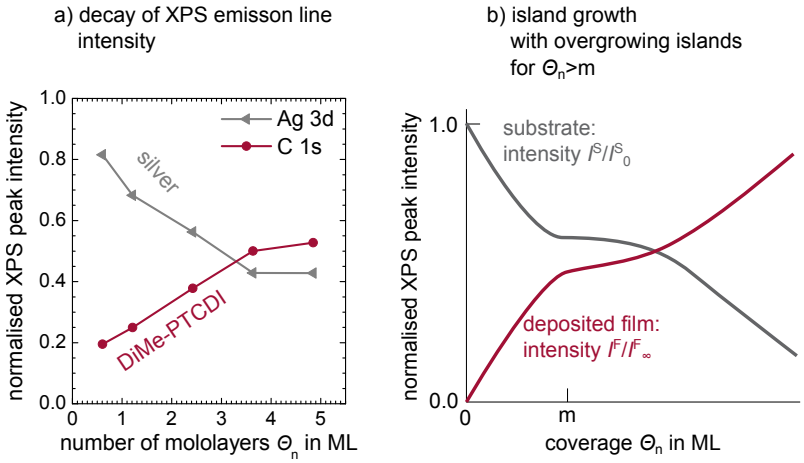

Figure 8.4 | Normalised XPS peak intensity as a function of the number of DiMe-PTCDI monolayers: a) the plot shows the normalised XPS peak intensity $\left(I^{\text{Ag}}/I^{\text{Ag}}_{\text{pristine}}\right)$ of the Ag $3d$ substrate peak (grey) and $\left(I^{\text{C}}/I^{\text{C}}_{\text{bulk}}\right)$ the C $1s$ peak of DiMe-PTCDI (red) as a function of the amount of deposited material (number of DiMe-PTCDI monolayers Θ_n).
b) Schematic representing the behaviour of XPS line intensities extended for the case of island growth with overgrowing smaller islands starting at $\Theta_n = m$.

In summary, DiMe-PTCDI grows in islands (*Volmer-Weber* growth) on a silver substrate. Up to a coverage of 2.4 monolayers, the silver substrate seems to influence the growth of the islands in the way that larger islands of DiMe-PTCDI form on the smooth and large areas of the silver substrate. In contrast, very small and less islands grow on the grainy part of the silver surface. This behaviour is reflected in Figure 8.4, which shows the normalised XPS peak intensity as a function of the coverage. Both curves strongly decrease or increase in the case of silver, respectively DiMe-PTCDI indicating a fast coverage of the substrate. For $\Theta_n \geq 3.6\,\text{ML}$, the silver curve seems to stay constant. The curve representing the DiMe-PTCDI thin film, on the other hand, further increases. However, its slope is much lower as for $\Theta_n \leq 2.4$ monolayers. Here, the growth of small islands becomes dominant, which first tend to overgrow and cover the lager islands. The question if, the underlying silver substrate

influences the chemical surrounding of DiMe-PTCDI is answered in the following.

XPS Investigation of the Molecular Core Level

X-ray photoelectron spectroscopy was performed in order to investigate the interaction between DiMe-PTCDI and silver from a chemical point of view. In Figure 8.5, an overview of the core level spectra of a $300\,\text{Å}$ bulk-like DiMe-PTCDI thin film ($45.5\,\text{ML}$) grown on a silver surface is illustrated. In all spectra, the intensity is plotted as a function of the electron binding energy. The survey spectrum, which is plotted in Figure 8.5 a), displays the presence of all expected elements. Here, only photoemission peaks of carbon, nitrogen and oxygen are observed. However, a high resolution scan of the Ag $3d$ core level revealed that the XPS emission peaks are still visible but are of very low intensity (see the inlay in Figure 8.5 a)). This can be explained by the before discussed island growth of DiMe-PTCDI on a silver substrate. Since DiMe-PTCDI tends to grow in islands, photoelectrons originating from the silver substrate still reach the vacuum at a DiMe-PTCDI film thickness of $300\,\text{Å}$.
Since the cross section of hydrogen atoms is too small to be detected in XPS, the H atoms of DiMe-PTCDI are not visible. The elemental composition of DiMe-PTCDI ($C_{26}H_{14}N_2O_4$) is determined from the high resolution scans of the O $1s$, N $1s$ and C $1s$ core levels [16, 253]: $(82 \pm 2)\,\%$ carbon, $(12 \pm 2)\,\%$ oxygen and $(7 \pm 2)\,\%$ nitrogen. This result fits the theoretically expected elemental composition of $81\,\%$ carbon, $13\,\%$ oxygen and $6\,\%$ nitrogen. Consequently, it can be concluded that the measured volume contains just DiMe-PTCDI molecules.

In Figure 8.5 b) - d), high resolution scans of the O $1s$, N $1s$ and C $1s$ core levels are depicted. In order to distinguish and assign the contributing peaks as well as the satellite structures and to evaluate their energetic positions, a peak fit analysis[2] was performed. A coloured molecule structure of DiMe-PTCDI is given as inlay in Figure 8.5 a), which helps to identify the different bindings of the elements of the molecule. The same colour code is used to visualise the fitted peaks.
The high resolution scan of the O $1s$ photoelectron peak displayed in Figure 8.5 b) only exhibits the carboxylic contribution and a shake-up satellite: The most intense peak represents the doubly bound oxygen (O=C) and is centred at $E_\text{B} = (531.8 \pm 0.1)\,\text{eV}$ [229]. The second peak is centred at $E_\text{B} = (533.5 \pm 0.1)\,\text{eV}$ and results from an intramolecular charge transfer (shakeup process) from the aromatic part of the molecule acting like a donor to the accepting functional groups ($\pi \rightarrow \pi*_{\text{O=C}}$) [229].
The N $1s$ core level emission appears at a binding energy of $E_\text{B} = (400.8 \pm 0.1)\,\text{eV}$, which can be attributed to the C-N bonds in DiMe-PTCDI (see Figure 8.5 c)) [229]. Furthermore, the peak of the $\pi \rightarrow \pi*_{\text{N=C}}$ shakeup process is identified at $E_\text{B} = (402.6 \pm 0.1)\,\text{eV}$ [229].

[2]The peak fit analysis was performed with the programme CasaXPS [254]. The line shape of each component was described by a convolution of Gaussian and Lorentzian contributions. The O $1s$ and C $1s$ background was fitted by a Shirley background, while a linear background is used for the N $1s$ peak in the case of DiMe-PTCDI grown on silver. Since the N $1s$ core level is located directly on top of a satellite peak of the Ag $3d$ level, standard background subtractions cannot be used especially for very thin organic films. Therefore, a scan of this satellite peak of a clean silver surface was subtracted from the N $1s$ scan. Thereafter, the linear background was used for the fit routine. For DiMe-PTCDI grown on Copper, the N $1s$ Spectrum is fitted by a Shirley background.

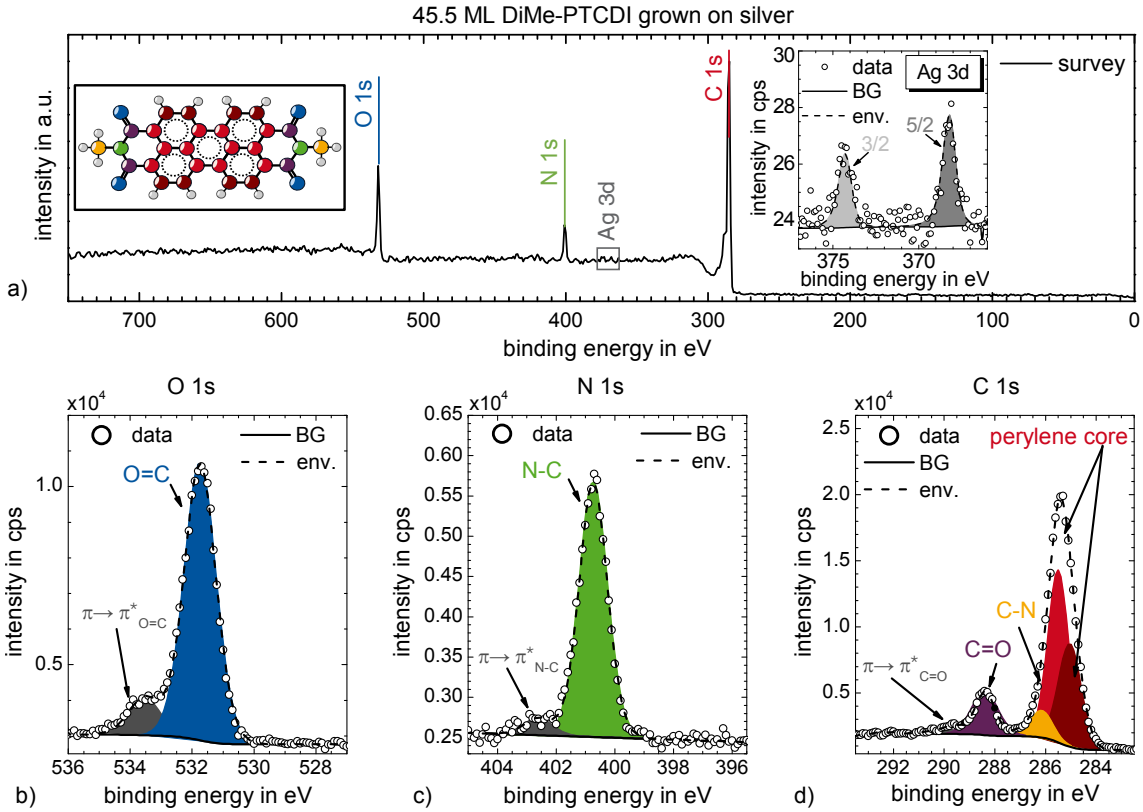

Figure 8.5 | XPS spectra of bulk-like DiMe-PTCDI on a silver surface: a) - d) The intensity is plotted in dependence of the binding energy for every spectrum.
a) The survey spectrum confirms the presence of all expected elements. Only photoemission peaks of carbon, nitrogen and oxygen are observed. However, a high resolution scan of the Ag $3d$ core level revealed that the XPS emission peaks are still visible but are of very low intensity (see inlay on the right side). The inlay on the left shows the molecular structure of DiMe-PTCDI. Here, the individual binding components for O $1s$ (blue), N $1s$ (green) and especially C $1s$ (red) of the molecule are assigned according to the colour coding which is used in the following.
b) - d) High resolution scans of the O $1s$, N $1s$ and C $1s$ core levels:
b) The O $1s$ spectrum is fitted with two peaks. The first represents the oxygen doubly bound to the aromatic ring (O=C) and is centred at $E_B = (531.8 \pm 0.1)\,\mathrm{eV}$. The second peak is centred at $E_B = (533.5 \pm 0.1)\,\mathrm{eV}$ and results from an intramolecular charge transfer (shakeup process) from the aromatic part of the molecule acting like a donor to the accepting functional groups ($\pi \rightarrow \pi*_{O=C}$) [229].
c) The nitrogen bound in the methylimide group (N-C) is represented by a peak centred at $E_B = (400.8 \pm 0.1)\,\mathrm{eV}$ in the N $1s$ spectrum. Additionally, the peak of the $\pi \rightarrow \pi*_{N=C}$ shakeup process is identified at $E_B = (402.6 \pm 0.1)\,\mathrm{eV}$ [229].
d) In principal, the C $1s$ spectrum consists of two well-separated features. The main feature is centred at $(285.4 \pm 0.1)\,\mathrm{eV}$. It originates from the different carbon atoms of the aromatic part (perylene core $E_B = (284.9 \pm 0.2)\,\mathrm{eV}$ and $E_B = (285.4 \pm 0.2)\,\mathrm{eV}$) and the carbon atoms involved in the C-N bond ($E_B = (286.0 \pm 0.3)\,\mathrm{eV}$). The carbon atoms of the C=O bonds contribute to the second peak at $(288.4 \pm 0.1)\,\mathrm{eV}$. In addition, a peak resulting from the shakeup process $\pi \rightarrow \pi*_{C=O}$ is centred at $E_B = (289.6 \pm 0.1)\,\mathrm{eV}$ [229].

The core level emission of C $1s$ has a more complex peak structure (see Figure 8.5 d)). Therefore, in order to facilitate the allocation of the different bonding contributions, each atom depicted in the inlay of Figure 8.5 a) is painted in the same colour code as used in Figure 8.5 d). In principal, the C $1s$ spectrum consists of two well-separated features. The main feature is peak centred at $(285.4 \pm 0.1)\,\mathrm{eV}$. It originates from the different carbon atoms of the perylene core ($E_\mathrm{B} = (284.9 \pm 0.2)\,\mathrm{eV}$ and $E_\mathrm{B} = (285.4 \pm 0.2)\,\mathrm{eV}$) and the carbon atoms involved in the C-N bond ($E_\mathrm{B} = (286.0 \pm 0.3)\,\mathrm{eV}$) [229]. The carbon atoms of the C=O bonds contribute to the second peak at $(288.4 \pm 0.1)\,\mathrm{eV}$ [229]. The highly electronegative O and N atoms in the functional group withdraw electrons. Thus, the charge density particularly on the covalently bond carbon atoms of the functional group is reduced. Therefore, the binding energies of the carbon atoms in the C-N and C=O bonds are higher as those of the C atoms in the perylene core [229, 255]. Furthermore, the peak resulting from the shakeup process $\pi \rightarrow \pi*_{\mathrm{C=O}}$ is centred at $E_\mathrm{B} = (289.6 \pm 0.1)\,\mathrm{eV}$ [229].

In order to investigate a possible chemical interaction between DiMe-PTCDI and the silver surface, very thin films of DiMe-PTCDI were grown on silver and subsequently measured with XPS. The measurement of such films in the (sub-)monolayer regime enables the investigation of a possible molecule-metal interaction. Therefore, the results are compared to those gained from the bulk-like film.
As an example, an overview of the core level spectra of $0.6\,\mathrm{ML}$ of DiMe-PTCDI grown on silver is displayed in Figure 8.6. Since the silver surface is just slightly covered with DiMe-PTCDI islands at 0.6 monolayers, the survey spectrum in Figure 8.6 a) is dominated by XPS emission lines originating from silver. The elemental composition of the DiMe-PTCDI layer is determined to $(80 \pm 4)\,\%$ carbon, $(10 \pm 4)\,\%$ oxygen and $(10 \pm 5)\,\%$ nitrogen, which fits the theoretically expected ratio for DiMe-PTCDI of $81\,\%$ carbon, $13\,\%$ oxygen and $6\,\%$ nitrogen within the experimental error. Consequently, the organic layer just contains DiMe-PTCDI molecules and is free of impurities.

The high resolution XPS scans of the O $1s$, N $1s$ and C $1s$ core levels are plotted in Figure 8.6 b) - d). The O $1s$ core level emission in Figure 8.6 b) reveals the C=O main peak centred at $E_\mathrm{B} = (531.6 \pm 0.2)\,\mathrm{eV}$ [229]. When comparing its position to that of bulk-like DiMe-PTCDI film shown in Figure 8.5, it can be seen that the $(\mathrm{O{=}C})_{0.6\,\mathrm{ML}}$ peak is shifted to smaller binding energies. The peak, which is located at $E_\mathrm{B} = (533.6 \pm 0.2)\,\mathrm{eV}$, results from the $\pi \rightarrow \pi*_{\mathrm{O=C}}$ shakeup process [229]. Furthermore, a third peak is needed to adequately describe the O $1s$ spectrum of the $0.6\,\mathrm{ML}$ DiMe-PTCDI thin film. This newly-observed peak is centred at $E_\mathrm{B} = (529.5 \pm 0.2)\,\mathrm{eV}$. Since the elemental composition matches the theoretically expected values, this new peak has to be caused by the oxygen atom of the functional group of DiMe-PTCDI. Thus, an oxidised silver surface during the sample production can be excluded as origin of the new peak. As it is known for similar molecules, like PTCDA grown on silver, this peak is a clear indication for a strong chemical interaction with the underlying substrate, which is discussed at the end of this chapter [32, 41, 45, 246].
In Figure 8.6 c), the N $1s$ high resolution XPS spectrum is shown. Here, standard background subtractions cannot be used especially for very thin organic films, since the N $1s$ core level is located directly on top of a satellite peak of the Ag $3d$ level. Therefore, a scan of this

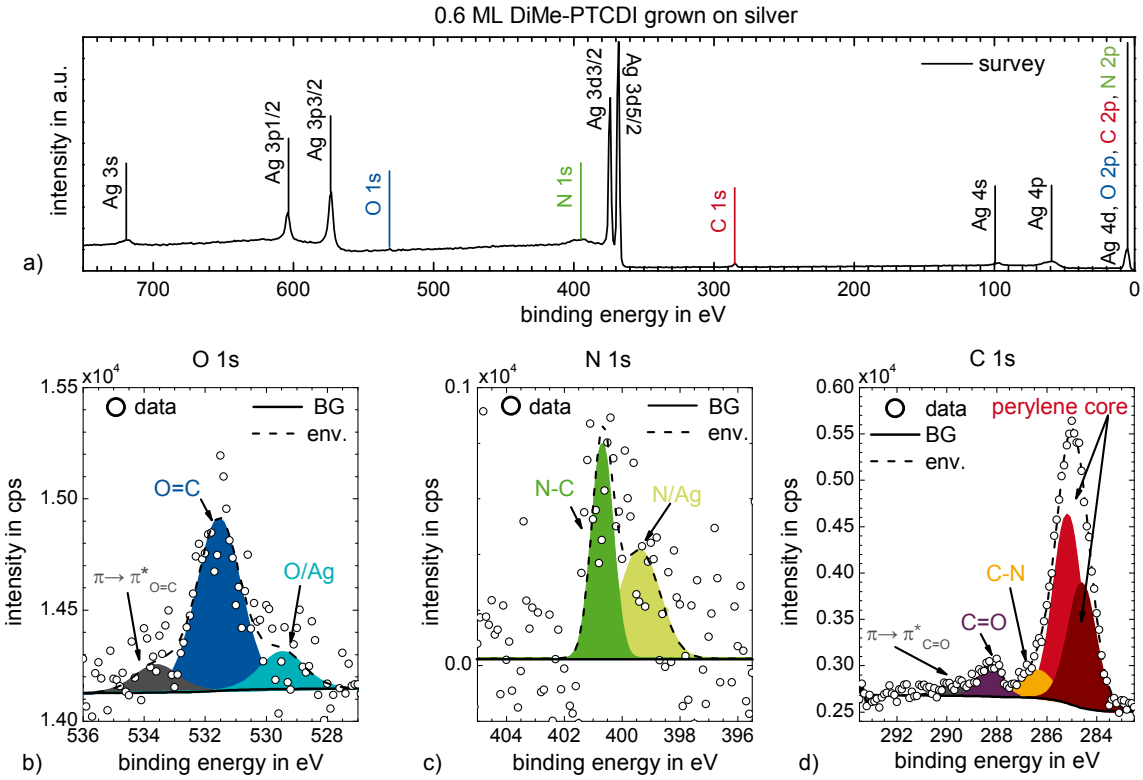

Figure 8.6 | XPS spectra of 0.6 ML of DiMe-PTCDI on a silver surface: a) - d) The intensity is plotted in dependence of the binding energy for every spectrum.
a) The survey spectrum confirms the presence of all expected elements as well as the absence of impurities. Only photoemission peaks of silver, carbon, nitrogen and oxygen are observed.
b) - d) High resolution scans of the O 1s, N 1s and C 1s core levels:
b) The O 1s spectrum is fitted with three peaks. The first is centred at $E_B = (531.6 \pm 0.2)$ eV, which represents the oxygen doubly bound to the aromatic ring (O=C). The second peak is centred at $E_B = (533.6 \pm \pm 0.2)$ eV and results from the $\pi \rightarrow \pi*_{O=C}$ shakeup process [229]. The third peak, which is needed to describe the O 1s spectrum, is centred at $E_B = (529.5 \pm 0.2)$ eV.
c) The N 1s spectrum is fitted with two peaks. The first is centred at $E_B = (400.4 \pm 0.2)$ eV, which represents the nitrogen bound in the methylimide group (N-C) [229]. Additionally, a second peak is needed to describe the N 1s core level spectrum centred at $E_B = (398.9 \pm 0.2)$ eV.
d) The carbon spectrum reveals different contributions originating from different chemical environments: the perylene core ($E_B = (284.6 \pm 0.3)$ eV and $E_B = (285.1 \pm 0.3)$ eV), the C-N bonds ($E_B = (285.9 \pm 0.3)$ eV) and the C=O bonds ($E_B = (288.3 \pm 0.2)$ eV). In addition, the peak of the $\pi \rightarrow \pi*_{C=O}$ shakeup process is identified at $E_B = (289.7 \pm 0.2)$ eV [229].

satellite peak of a clean silver surface was subtracted from the N 1s scan. Thereafter, a linear background was used for the fit routine. The main peak (N-C) is centred at $E_B = (400.4 \pm 0.2)$ eV [229]. Again, a comparison with the bulk-like film reveals a peak shift to smaller binding energies. Moreover, an additional peak at the low energy side is needed to describe the spectrum. This peak is located at $E_B = (398.9 \pm 0.2)$ eV. As in the case of the O 1s spectrum, this peak can be addressed to a chemical interaction of the nitrogen atoms with the underlying silver surface (N/Ag) [32, 246, 256]. A discussion about this interaction is given together with the discussion of the results gained from UPS/IPES measurements, which are shown in the next section. The peak of the shakeup process is not observable, because of the

very low intensity of the N $1s$ spectrum.
In comparison to the bulk-like film, almost all contributions to the C $1s$ spectrum are shifted to smaller binding energies: $E_B = (284.6 \pm 0.3)\,\mathrm{eV}$ and $E_B = (285.1 \pm 0.3)\,\mathrm{eV}$ for the bonds in the perylene core and $E_B = (288.3 \pm 0.2)\,\mathrm{eV}$ for the C=O bonds. The peak representing the C-N bonds is located at $E_B = (286.3 \pm 0.3)\,\mathrm{eV}$. Additionally, the peak of the $\pi \rightarrow \pi*_{C=O}$ shakeup process is identified at $E_B = (289.7 \pm 0.2)\,\mathrm{eV}$ [229].
An overview of all measured high resolution core level spectra of DiMe-PTCDI grown on silver as well as the determined elemental composition of these films are depicted in Figure D.2 and Table D.1, respectively, on page XIV in the Appendix. Within the experimental error, the elemental composition matches the theoretically expected one for all films. Therefore, it can be concluded that all films are free of impurities and each organic thin film consists just of DiMe-PTCDI molecules.

The peak positons of all fitted core level spectra of DiMe-PTCDI grown on silver are plotted as a function of the number of DiMe-PTCDI monolayers Θ_n in Figure 8.7 a) - c). As above, a greenish colour is used to mark the components of the N $1s$ spectrum, a bluish one for O $1s$ and reddish for the carbon components.
Starting at a coverage of $0.6\,\mathrm{ML}$, the binding energy of every component increases with increasing film thickness. The maximum peak shift $\Delta_{45.5\,\mathrm{ML}-0.6\,\mathrm{ML}}$ is $400\,\mathrm{meV}$ for the N-C bonds (see Figure 8.7 a)). The N/Ag peak shifts by $\Delta_{2.4\,\mathrm{ML}-0.6\,\mathrm{ML}} = 200\,\mathrm{meV}$. As can be seen in Figure 8.7 b), the bonding energy of the O=C bonds shifts by $\Delta_{45.5\,\mathrm{ML}-0.6\,\mathrm{ML}} = 200\,\mathrm{meV}$, while, the O/Ag peak shifts by $\Delta_{2.4\,\mathrm{ML}-0.6\,\mathrm{ML}} = 1100\,\mathrm{meV}$. The peak representing the carbon component of the C=O bonds shifts by $\Delta_{45.5\,\mathrm{ML}-0.6\,\mathrm{ML}} = 100\,\mathrm{meV}$. The peaks representing the perylene core shift both by $\Delta_{45.5\,\mathrm{ML}-0.6\,\mathrm{ML}} = 300\,\mathrm{meV}$. The contribution of the C-N bonds shifts from smaller to higher binding energies as well, but the peak positions itself are located at higher binding energies when compared to the emission of the bulk-like film. The maximum shift is $\Delta_{45.5\,\mathrm{ML}-2.4\,\mathrm{ML}} = -900\,\mathrm{meV}$ (see Figure 8.7 c)). The components, which indicate an interaction of oxygen and nitrogen with the silver substrate, are no more observable for a coverage of $\Theta_n > 2.4\,\mathrm{ML}$. Moreover, for $\Theta_n > 2.4\,\mathrm{ML}$, almost all peak positions match those of the bulk-like film within the experimental error. As it is known form the growth behaviour, which is discussed above, the growth of smaller islands becomes dominant between $\Theta_n = 2.4\,\mathrm{ML}$ and $\Theta_n = 3.6\,\mathrm{ML}$. Thereby, these smaller islands tend to overgrow und thus to cover the underlying islands. Therefore, it is concluded, that films with a film thickness of $\Theta_n \geq 3.6\,\mathrm{ML}$ are too thick for the investigation of the interaction between DiMe-PTCDI and silver [41]. Thus, the influence of the substrate on the chemical nature of DiMe-PTCDI is no more measureable.

The fact that the $0.6\,\mathrm{ML}$ DiMe-PTCDI/Ag spectra (see Figure 8.6) look very different to their bulk-like counterparts in Figure 8.5 is a clear indication that the molecules strongly interact with the substrate [63]. Especially, the peaks found at the low energy side of the N $1s$ and O $1s$ emission peaks in combination with the observed peak shift marks these components as a different chemical species [32]. The shift of the carbon peaks indicate that this change in the chemical surrounding of the functional group affects the carbon atoms located on the perylene core, as well [32]. Therefore, it can be concluded that the DiMe-PTCDI molecules are strongly bound and, thus, chemisorbed to the silver substrate [41, 63, 246, 256, 257]. The

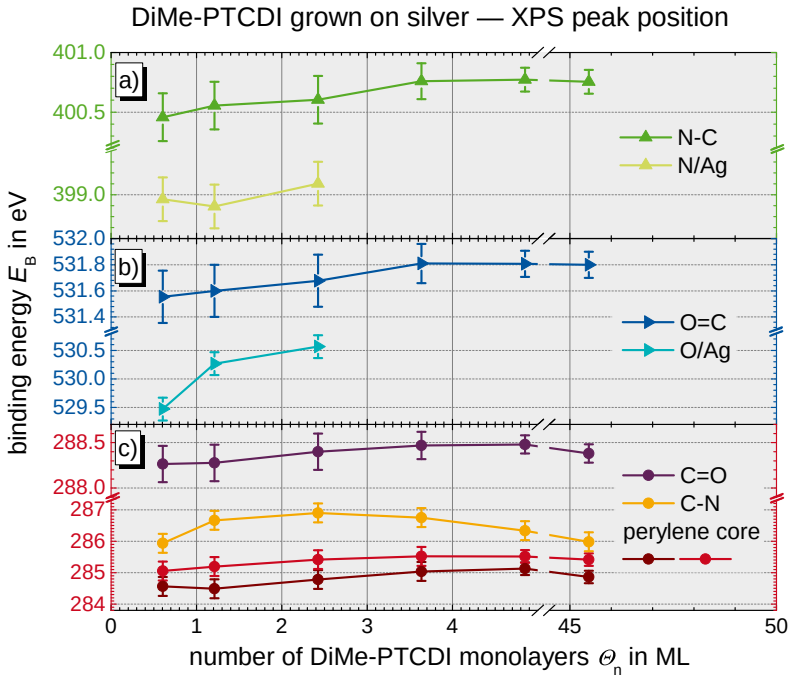

Figure 8.7 | Core level emission peak positions of DiMe-PTCDI grown on a silver surface: a) - c) The positions of the peak centres are plotted as a function of the number of DiMe-PTCDI monolayers Θ_n. The colour code is the same as already used to describe these peaks in Figure 8.5 and Figure 8.6. It has to be called attention to the axes. The x-axis as well as the y-axis are interrupted and the scaling is different in front of and behind each interruption for presentation purposes.
When comparing the smallest coverage of $0.6\,\mathrm{ML}$ with the bulk-like film, it can be clearly be seen that all peaks shift from lower to higher binding energies. At a coverage of $\Theta_n > 2.4\,\mathrm{ML}$, the peak positions of every component equal those of the bulk-like film within the experimental error. Moreover, the peaks indicating the interaction of the nitrogen or oxygen atoms with the underlying silver surface (N/Ag or O/Ag) are no more visible for $\Theta_n > 2.4\,\mathrm{ML}$. An explanation is given in the text.
a) The maximum shift $\Delta_{45.5\,\mathrm{ML}-0.6\,\mathrm{ML}}$ is $400\,\mathrm{meV}$ for the N-C bonds. The N/Ag peak shifts by $\Delta_{2.4\,\mathrm{ML}-0.6\,\mathrm{ML}} = 300\,\mathrm{meV}$. b) The bonding energy of the O=C bonds shifts by $\Delta_{45.5\,\mathrm{ML}-0.6\,\mathrm{ML}} = 200\,\mathrm{meV}$, whereas, the O/Ag peak shifts by $\Delta_{2.4\,\mathrm{ML}-0.6\,\mathrm{ML}}$ is $1100\,\mathrm{meV}$. c) The peak representing the C=O bonds is clearly separated from the other components. It shifts by $\Delta_{45.5\,\mathrm{ML}-0.6\,\mathrm{ML}} = 100\,\mathrm{meV}$. The peaks representing the perylene core shift both by $\Delta_{45.5\,\mathrm{ML}-0.6\,\mathrm{ML}} = 300\,\mathrm{meV}$. The contribution of the C-N bonds shifts from smaller to higher binding energies as well, but the peak positions itself are located at higher binding energies when compared to the emission of the bulk-like film. The maximum shift is $\Delta_{45.5\,\mathrm{ML}-2.4\,\mathrm{ML}} = -900\,\mathrm{meV}$.

impact of the observed chemical interaction on the electronic structure of DiMe-PTCDI grown on silver substrate is presented in the following. Thereafter, all results are discussed and an explanation is given.

Interface Electronic Structure

Figure 8.8 depicts the combined UPS and IPE spectra of a sub-monolayer DiMe-PTCDI ($0.6\,\mathrm{ML}$, open circles) grown on silver in comparison to the spectra of the bulk-like film (red

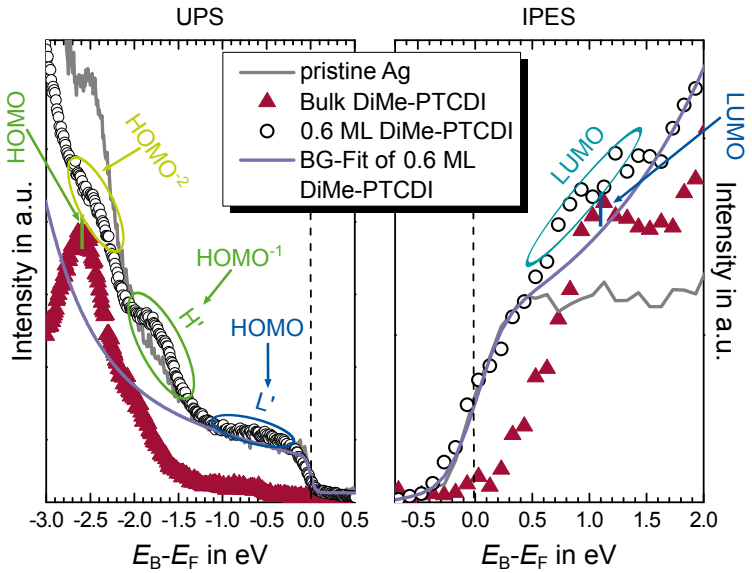

Figure 8.8 | UPS/IPES spectra of a sub-monolayer in comparison with bulk-like DiMe-PTCDI: the intensity is plotted as a function of the binding energy with respect to the Fermi level E_F. The UPS and IPE spectrum of 0.6 ML of DiMe-PTCDI are represented by the open circles. The violet solid line shows the fitted background. For better comparison, the spectra of the pristine silver substrate are drawn with the grey solid lines. The red triangles illustrate the UPS and IPE spectrum of the bulk-like DiMe-PTCDI film, which is discussed in Chapter 7 Figure 7.4. A detailed description is given in the text.

triangles) and a pristine silver surface (grey solid line). The electronic states of the bulk-like thin film are discussed in Chapter 7 (see Figure 7.4). In Figure 8.8, the intensity is plotted as a function of the binding energy with respect to the Fermi level E_F (black dashed line). For visualisation issues, the background[3] fitted to the spectra of the 0.6 ML thick thin film is represented by the violet solid line.

The UPS spectrum of 0.6 ML DiMe-PTCDI reveals three peaks: adjacent to the Fermi level, the HOMO starts to rise at $E_B = (-0.1 \pm 0.1)\,\mathrm{eV}$ and reaches its maximum at $E_B = (-0.5 \pm 0.1)\,\mathrm{eV}$. A second peak (HOMO^{-1}) is centred at $E_B = (-1.7 \pm 0.1)\,\mathrm{eV}$ and the HOMO^{-2} get maximal at $E_B = (-2.4 \pm 0.1)\,\mathrm{eV}$. Furthermore, the LUMO starts to rise at $E_B = (+0.3 \pm 0.2)\,\mathrm{eV}$ and is centred at $E_B = (+0.8 \pm 0.2)\,\mathrm{eV}$ in the IPE spectrum (see Figure 8.8 on the right side). As a short reminder: At an energy of $E_{HOMO} = (-2.0 \pm 0.2)\,\mathrm{eV}$, the HOMO starts to rise for the bulk-like DiMe-PTCDI film (red triangles). The HOMO becomes maximal at $E = (-2.6 \pm 0.1)\,\mathrm{eV}$ [229]. As can be seen in from density functional theory (DFT) calculations in [229], it is mainly located over the perylene core and partly on the oxygen atoms. Its character is purely π. The LUMO starts to rise at an energy of $E_{LUMO} = (+0.6 \pm 0.3)\,\mathrm{eV}$ and reaches its maximum at $E = (+1.0 \pm 0.2)\,\mathrm{eV}$. DFT calculations of [229] verify the pure π character of the LUMO level, which is delocalised over the perylene core of DiMe-PTCDI.
Thus, when comparing the spectra of 0.6 ML DiMe-PTCDI with that of the bulk-like film, a striking shift of the occupied states of several eV is observable, while the LUMO is shifted by

[3] The background is fitted as it is described in Chapter 6.

$300\,\mathrm{meV}$. A similar behaviour has already been observed for the well-studied electron acceptor molecule PTCDA[4] grown on metal substrates like Ag or Cu. Here, the peaks appearing near the Fermi edge can be assigned to hybrid states of the Ag $4d$ bands and the frontier molecular orbitals of the isolated molecule [32, 41]. Thereby, the LUMO of the isolated molecule becomes occupied when the molecule is attaching the silver surface. Consequently, this LUMO derived hybrid state, which can be found close to the Fermi level, becomes the new HOMO of the thin film [32, 41]. It is denoted by L' in order to express its origin. The HOMO^{-1} originates from the hybridisation of the HOMO of the isolated molecule with the Ag $4d$ bands. Therefore, it is marked with H'. Moreover, the remaining states of the isolated molecule relax towards E_F. Thus, the LUMO of the thin film originates from the molecular orbital LUMO^{+1} of the isolated molecule. The HOMO^{-2} of the thin film has its origin in the HOMO^{-1} of the isolated molecule and so on.
PTCDA has a very similar chemical structure to DiMe-PTCDI, but the nitrogen of DiMe-PTCDI is replaced by an oxygen atom. Furthermore, no alkyl chain is attached to PTCDA. However, DFT calculations of the frontier molecular orbitals revealed a similar distribution: HOMO and LUMO are mainly located over the perylene core and partly on the oxygen atoms for both molecule [229]. The similarity of the electronic structure of PTCDA and DiMe-PTCDI has also been demonstrated in Figure 7.5 in Chapter 7. Consequently, it is assumed, that the explanations found for PTCDA can also be applied to DiMe-PTCDI grown on silver. Nevertheless, scanning tunnelling microscopy (STM) could be performed on comparable thin films in future studies in order to further investigate the electronic origin of L' and H'.
The first monolayer of PTCDA grown on silver shows a metallic behaviour [41]. Although, the experimental error on the determination of the onsets of HOMO and LUMO is quite large, no indication is found for an metallic behaviour of DiMe-PTCDI, since both representing peaks clearly end in front of E_F. Consequently, the molecular layer DiMe-PTCDI is still semiconducting but possesses a lower transport band gap[5] of $E_\mathrm{t} = (0.4 \pm 0.2)\,\mathrm{eV}$ instead of $E_\mathrm{t} = (2.5 \pm 0.3)\,\mathrm{eV}$ for the bulk-like film.

The evolution of the electronic structure of DiMe-PTCDI grown on silver is illustrated in Figure 8.9. The intensity is plotted as a function of the binding energy, which is given with respect to the Fermi level E_F (black dashed line). The grey line represents the spectrum of the pristine silver substrate.
For $\Theta_\mathrm{n} \leq 2.4\,\mathrm{ML}$ (violet, red, orange), the before described chemical interaction of DiMe-PTCDI with the silver substrate results in a decrease of the ionisation energy (see Table 8.1). Hence, adjacent to the Fermi level, the LUMO derived new HOMO (L') starts to rise. Its intensity decreases with increasing film thickness. The same behaviour is revealed for the peak (H') originating from the hybridisation of the HOMO of the isolated molecule with the Ag $4d$ bands. The energy position ($E_\mathrm{B} = (-2.4 \pm 0.1)\,\mathrm{eV}$) of HOMO^{-2} nearly equals that of the HOMO of the bulk-like film at $E_\mathrm{B} = (-2.6 \pm 0.1)\,\mathrm{eV}$. All three peaks shift to higher binding energies with increasing film thickness. Furthermore, L' and H' are no more visible for $\Theta_\mathrm{n} > 2.4\,\mathrm{ML}$ (light and dark green). Here, the spectra show bulk-like behaviour (turquoise). As

[4] Its structure is based on a perylene core, to which two electron withdrawing anhydride side groups are added. The chemical structure is depicted in Figure 7.5 in Chapter 7
[5] The transport gap is determined as described in Chapter 7.

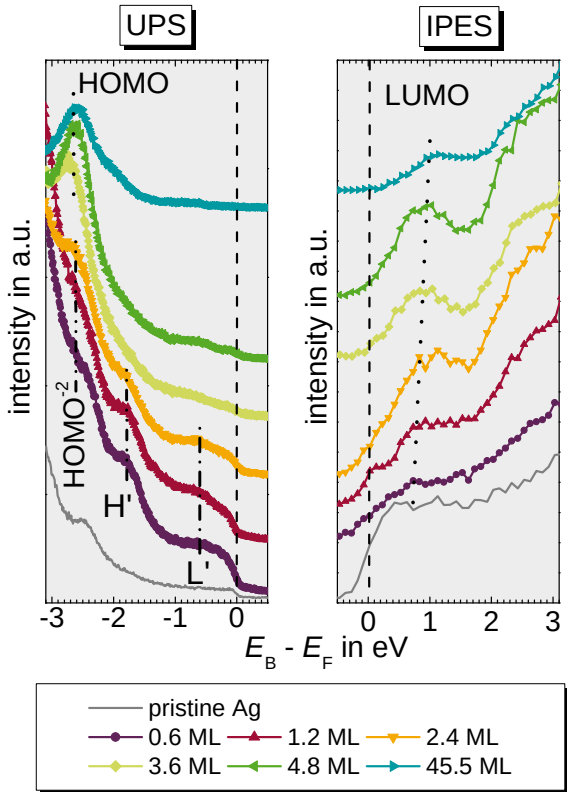

Figure 8.9 | Thickness-dependent UPS and IPE spectra of DiMe-PTCDI grown on silver: the intensity is plotted as a function of the binding energy with respect to E_F. The grey line represents the spectrum of the pristine silver substrate.
Occupied states: for $\Theta_n \leq 2.4\,\text{ML}$ (violet, red, orange), the spectra are quite similar to that of $0.6\,\text{ML}$ DiMe-PTCDI shown in Figure 8.8. Adjacent to the Fermi level, the LUMO derived new HOMO (L') starts to rise. Its intensity decreases with increasing film thickness. The same behaviour is observable for the peak (H') originating from the hybridisation of the HOMO of the isolated molecule with the Ag $4d$ bands. A third peak (HOMO^{-2}) is also observable. All three peaks shift to higher binding energies with increasing film thickness. Furthermore, L' and H' are no more visible for $\Theta_n > 2.4\,\text{ML}$ (light and dark green). Here, the spectra show bulk-like behaviour (turquoise).
Unoccupied states: the binding energy of LUMO slightly increases with increasing film thickness.
The dashed line marks the position of the Fermi energy.

already concluded from the presented XPS measurements, a film thickness of $\Theta_n \geq 3.6\,\text{ML}$ is too thick for the investigation of the interaction between DiMe-PTCDI and silver.
The binding energy of LUMO slightly increases with increasing film thickness. In contrast to IE, the electron affinity stays nearly constant within the range of the experimental error at $EA = (3.8 \pm 0.3)\,\text{eV}$, as can be seen in Table 8.1. However, the transport gap is significantly reduced to $\overline{E}_t = (0.5 \pm 0.3)\,\text{eV}$ instead of $E_t = (2.5 \pm 0.3)\,\text{eV}$ for the bulk-like film. For $\Theta_n > 2.4\,\text{ML}$, the energy positions of the occupied and unoccupied electronic states and, thus IE, EA and the transport band gap equal those of the bulk-like DiMe-PTCDI film.

Table 8.1 | Comparison of the ionisation energies (IE) and the electron affinities (EA) of DiMe-PTCDI thin films in dependence of film thickness. Furthermore, the transport gaps (E_t) determined from the peak onset are also given.

Θ_n	0.6 ML	1.2 ML	2.4 ML	3.6 ML	4.8 ML	45.5 ML
IE ±0.2 eV	4.3 eV	4.4 eV	4.4 eV	6.3 eV	6.3 eV	6.2 eV
EA ±0.3 eV	3.9 eV	3.7 eV	3.8 eV	3.8 eV	3.7 eV	3.7 eV
E_t ±0.3 eV	0.4 eV	0.7 eV	0.6 eV	2.5 eV	2.6 eV	2.5 eV

The evolution of the work function Φ of DiMe-PTCDI grown on silver is plotted as function of the number of monolayers Θ_n in Figure 8.10. The work function of the pristine silver substrate amounts to $\Phi_{Ag}(4.2 \pm 0.1)\,\text{eV}$. As a short reminder, the thin films used as substrates are of polycrystalline structure. Since the work function is different for every crystal facet, polycrystalline surfaces have a different work function compared to those measured for sin-

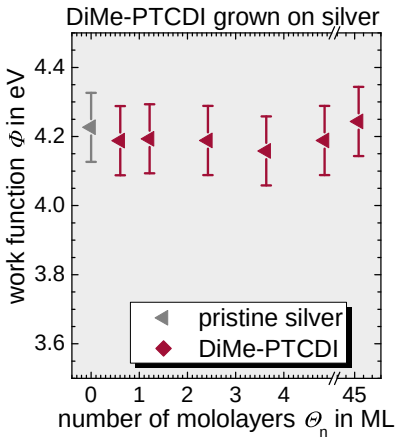

Figure 8.10 | Evolution of the work function of DiMe-PTCDI with increasing number of monolayers: the work function Φ of DiMe-PTCDI is plotted as function of the number of monolayers Θ_n. The work function of the pristine silver substrate amounts to $\Phi_{Ag} = (4.2 \pm 0.1)\,eV$. With increasing coverage, the work function of DiMe-PTCDI grown on a silver substrate stays constant within the experimental error.

gle crystals. With increasing coverage, the work function of DiMe-PTCDI grown on a silver substrate stays constant within the experimental error. Thereof, it can be concluded that no dipole is established at the DiMe-PTCDI-silver interface [63, 258]. This observation seems to be contradictory to the UPS/IPE spectra, which show a significant charge transfer from the substrate into the LUMO of DiMe-PTCDI [246]. In a simplified picture, this LUMO filling should result in a negatively charged DiMe-PTCDI monolayer, which in turn should cause a significant reduction of the work function. The finding, however that the work function stays constant reveals that just a little amount of charge is transferred onto the molecule. Thus, the question about origin of the electrons, which fill the LUMO, arises. Here, the so-called 'surface-induced aromatic stabilisation' (SIAS), which was recently introduced by *G. Heimel* and co-workers [32], can give an explanation. The shift of HOMO, $HOMO^{-1}$ and $LUMO^{+1}$ of the isolated molecule to the position of H', $HOMO^{-2}$ and LUMO, respectively, give the answer [63]. In addition to the donation from the metal, there is also a back-donation from these molecular orbitals to the metal [63]. Furthermore, the observed strong shift of these orbitals proves a strong interaction with the Ag $4d$ metal states and thus indicate a covalent chemical boning [63]. This is substantiated by the observation of the new peaks O/Ag and N/Ag and the resulting core-level shifts in the XPS spectra (see Figure 8.6). Thus, the formation of the bond leads to a charge transfer (back-donation) from the molecule into the metal, which balances the electron transfer from the metal to the LUMO of the isolated molecule but influences the frontier electronic system of DiMe-PTCDI [32, 63]. It is shown for similar molecules, that the change in the electronic structure in combination with the covalent bonding of the molecule to the metal substrate, bends the atoms in the functional group towards the metal surface [32, 41, 45]. Furthermore, the filling of the LUMO below the Fermi level of the metal weakens and lengthens, for example, the C=O bond towards a C-O single bond. This results in an re-hybridisation of the oxygen atoms and in an shift of the O $1s$ as well as the C $1s$ core level spectrum to smaller binding energies, as it is observed for DiMe-PTCDI grown on silver (see Figure 8.7). The re-hybridisation of O, in turn, favours the formation of a covalent bond with the underlying metal surface. Furthermore, it leads to a resonance structure, which exhibits a significantly extended π-electron system. The π-conjugation, then, extends from the perylene core over the functional group into the metal leading to strong coupling of the

molecular orbitals to the metal states. This, in turn, reduces the molecular gap of the isolated molecule, as it is observed for DiMe-PTCDI grown on silver. The reduction of the band gap shifts the LUMO of the isolated molecule down in energy. Thereby, more electrons move onto the molecule until E_F finally lies within the formerly unoccupied molecular DOS [32].
In order to investigate a possible bending of DiMe-PTCDI molecules, X-ray standing wave (XSW) experiments on comparable samples could be performed in future studies. In combination with profound DFT calculations on the bonding mechanism, this would complete the picture drawn for the effects occurring at the DiMe-PTCDI-silver interface.

8.2. The Interface between DiMe-PTCDI and Copper

Growth of DiMe-PTCDI on Copper in the (Sub-)Monolayer Regime

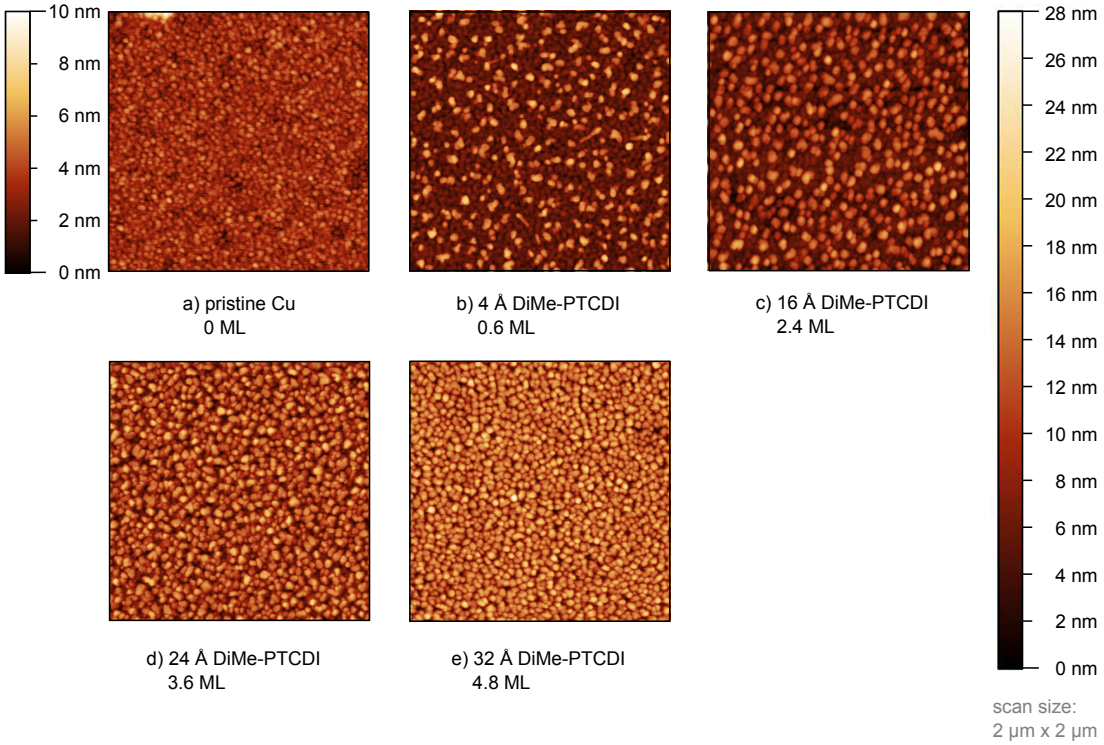

Figure 8.11 | AFM images of the DiMe-PTCDI thickness series grown on copper: a) - d) The scan of the size $(2 \times 2)\,\mu m^2$ shows the morphology of each sample surface in a colour coded image: the representing height can be inferred from the colour scale on the right side for the DiMe-PTCDI samples and on the left side of a) for the pristine copper surface. On top of this substrate, DiMe-PTCDI thin films are grown with a thickness of b) 0.6 ML, c) 2.4 ML, d) 3.6 ML and e) 4.8 ML.

In Figure 8.11, AFM images of the DiMe-PTCDI grown on copper is displayed for several film thicknesses. Each picture with a scan size of $(2 \times 2)\,\mu m^2$ represents the morphology of the respective film in a colour coded image: the representing height can be inferred from the

colour scale on the right side for the DiMe-PTCDI samples and on the left side of Figure 8.11 a) for the pristine copper surface.

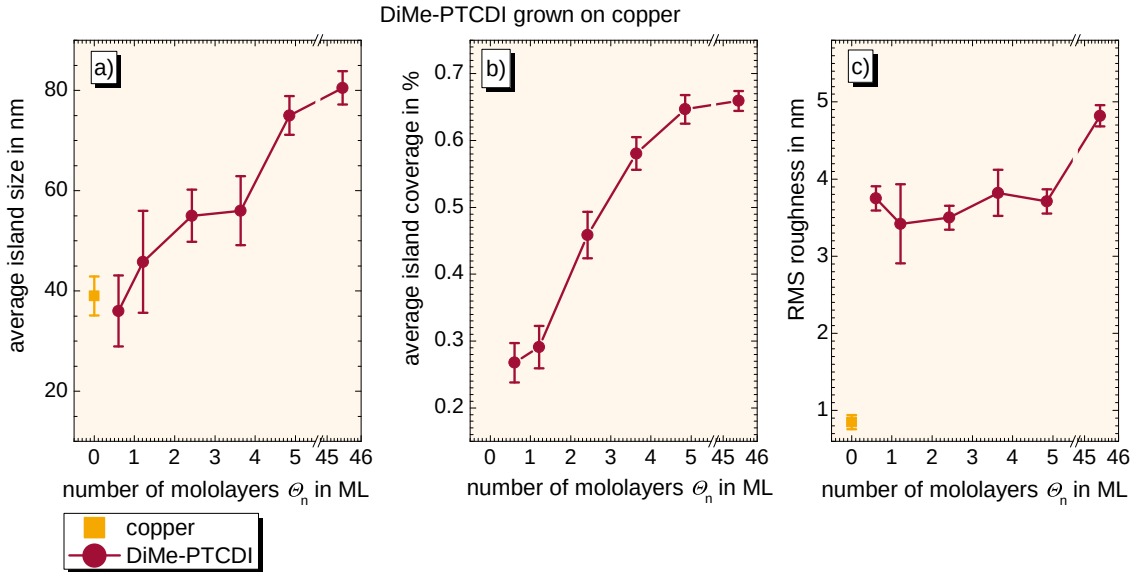

Figure 8.12 | AFM statistics of the DiMe-PTCDI thickness series grown on copper: a) The average island size is plotted as a function of the number of DiMe-PTCDI monolayers. b) The average island coverage is displayed as a function of Θ_n. c) The RMS roughness is depicted as a function of the number of monolayers.

In Figure 8.11 a), the morphology of the pristine copper surface is displayed. Its morphology is a very flat, grainy surface with an RMS roughness of $(0.8 \pm 0.1)\,\mathrm{nm}$. At a film thickness of $0.6\,\mathrm{ML}$ (see Figure 8.11 b)), the molecules initially cluster in small islands, which is also called *Volmer-Weber* growth. As can be seen in Figure 8.12 a), the islands, which form on copper, are as small as those, which cluster on the grainy part of the silver substrate (see Figure 8.2 a)). Their distribution, however, is more homogeneous than compared to DiMe-PTCDI grown on silver (see Figure 8.1 b)). Furthermore, the average island coverage is larger when DiMe-PTCDI is grown on a copper sample (see Figure 8.12 b)). Thus, the question is raised if DiMe-PTCDI grown on atomically flat silver surfaces shows a different growth behaviour, which could be in the focus of future studies.

With increasing film thickness (c) - e)), the average island size as well as the coverage increase (see Figure 8.12 a) and b)). The island height stays nearly constant with increasing film thickness, which results in a constant RMS roughness displayed in Figure 8.12 c). The surface of the bulk-like film shows a grainy morphology, which is similar to that of Figure 8.11 e) (see Figure E.1 on XV in the Appendix). A change in the growth is not observable for the investigated samples.

The *Volmer-Weber* growth is also confirmed by the evolution of the normalised XPS intensity, which is similar to the behaviour predicted in Figure 8.3 b) (see Figure E.2 on page XVI in the Appendix) [26]. The question about a possible chemical interaction of DiMe-PTCDI with the copper surface is given in the next section.

XPS Investigation of the Molecular Core Level

In order to investigate the samples of DiMe-PTCDI grown on copper from a chemical point of view, XPS measurements were performed. Thereafter, the results are compared to those gained from the bulk-like film, which matches the results of a bulk-like film grown on silver (see Figure 8.5 and Figure E.3 on page XVII in the Appendix). As an example[6], an overview of the core level spectra of $0.6\,\mathrm{ML}$ of DiMe-PTCDI grown on copper is displayed in Figure 8.13. The survey spectrum in Figure 8.13 a) displays all expected species, including these of the copper substrate.
The elemental composition of the $0.6\,\mathrm{ML}$ DiMe-PTCDI layer is determined from the high resolution scans of the O $1s$, N $1s$ and C $1s$ core levels to $(81 \pm 4)\,\%$ carbon, $(11 \pm 4)\,\%$ oxygen and $(8 \pm 5)\,\%$ nitrogen. They fit the theoretically expected ratio for DiMe-PTCDI of $81\,\%$ carbon, $13\,\%$ oxygen and $6\,\%$ nitrogen. Consequently, the organic layer just contains DiMe-PTCDI molecules and is free of impurities.

The high resolution XPS scans of the O $1s$, N $1s$ and C $1s$ core levels are plotted in Figure 8.13 b) - d). The O $1s$ core level emission in Figure 8.13 b) reveals that, within the experimental error, the O=C main peak is slightly shifted to smaller binding energies ($E_\mathrm{B} = (531.6 \pm 0.3)\,\mathrm{eV}$) at a film thickness of $\Theta_\mathrm{n} = 0.6\,\mathrm{ML}$ [229]. With increasing film thickness, the C=O peak stays constant at the same position as its counterpart of the bulk-like film at $\overline{E}_\mathrm{B} = (531.8 \pm 0.2)\,\mathrm{eV}$. A second peak is centred at $E_\mathrm{B} = (533.6 \pm 0.3)\,\mathrm{eV}$ and results from the $\pi \rightarrow \pi*_{\mathrm{O=C}}$ shakeup process [229]. However, a third peak, which indicates an interaction of the oxygen with the substrate similar to DiMe-PTCDI grown silver (see Figure 8.6 b)), is not visible on copper. This observation is consistent to the constant peak position of the O=C peak, which is depicted as a function of the number of monolayers in Figure 8.14 b).
In Figure 8.13 c), the N $1s$ high resolution XPS spectrum is shown. The main peak (N-C) is centred at $E_\mathrm{B} = (400.5 \pm 0.3)\,\mathrm{eV}$ [229]. A comparison with the bulk-like film reveals a peak shift of $\Delta_{45.5\,\mathrm{ML}-0.6\,\mathrm{ML}} = 500\,\mathrm{meV}$ to smaller binding energies, which is only observable for $0.6\,\mathrm{ML}$ DiMe-PTCDI grown on copper. With increasing film thickness, the peak position stays constant at $\overline{E}_\mathrm{B} = (400.8 \pm 0.2)\,\mathrm{eV}$ (see Figure 8.14 a)). However, an additional peak is needed to describe the spectrum indicating an interaction of the nitrogen atom with the underlying copper surface (N/Cu) [32, 256]. This peak is located at $E_\mathrm{B} = (398.9 \pm 0.3)\,\mathrm{eV}$ and shifts to higher binding energies with increasing film thickness. Nevertheless, when compared to the peak shifts of the N $1s$ and O $1s$ peaks and the respective peak intensities of the N/Ag and O/Ag peaks on silver, the results presented in this section reveal a much weaker interaction between DiMe-PTCDI and the underlying copper atoms. Only in the submonolayer regime, the nitrogen atoms of the functional group show a strong interaction with copper. The N/Cu peak is, however, observable up to a film thickness of $4.8\,\mathrm{ML}$, which can be explained by the island growth behaviour discussed in the section before.

[6] An overview of all measured high resolution core level spectra of DiMe-PTCDI grown on copper as well as the determined elemental composition of these films are depicted in Figure E.4 and Table E.1, respectively, on page XVIII in the Appendix. Within the experimental error, the elemental composition matches the theoretically expected one for all films. Therefore, it can be concluded that all films are free of impurities and each organic thin film consists just of DiMe-PTCDI molecules.

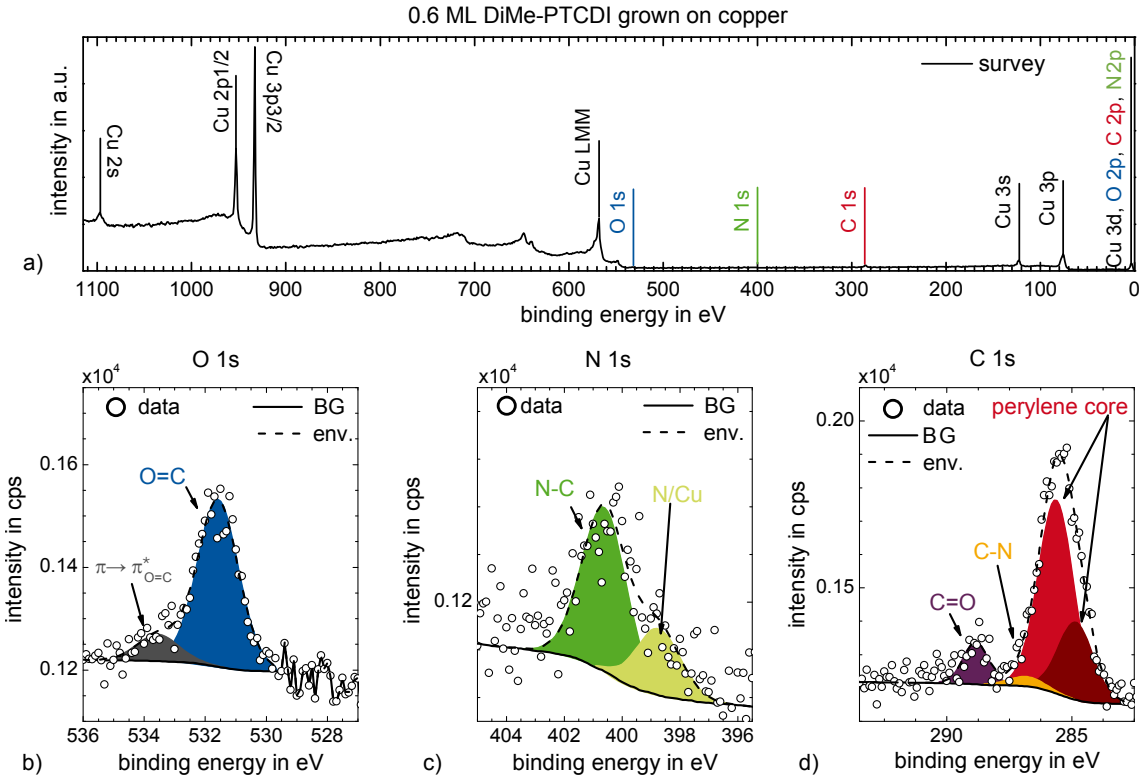

Figure 8.13 | XPS spectra of 0.6 ML of DiMe-PTCDI grown on a copper surface: a) - d) the intensity is plotted in dependence of the binding energy for every spectrum.
a) The survey spectrum confirms the presence of all expected elements as well as the absence of impurities. Only photoemission peaks of copper, carbon, nitrogen and oxygen are observed.
b) - d) High resolution scans of the O $1s$, N $1s$ and C $1s$ core levels:
b) The O $1s$ spectrum is fitted with two peaks. The first is centred at $E_B = (531.6 \pm 0.3)\,\mathrm{eV}$, which represents the oxygen doubly bound to the aromatic ring (O=C) [229]. The second peak is centred at $E_B = (533.6 \pm 0.3)\,\mathrm{eV}$ and results from the $\pi \rightarrow \pi*_{O=C}$ shakeup process [229]. A third peak, which indicates an interaction of the oxygen with the substrate similar to DiMe-PTCDI grown silver (see Figure 8.6b)), is not observable for the copper series.
c) Similar to Figure 8.6c), the N $1s$ spectrum has to be fitted with two peaks. The first is centred at $E_B = (400.4 \pm 0.3)\,\mathrm{eV}$, which represents the nitrogen bound in the methylimide group (N-C) [229]. Additionally, a second peak is needed to describe the N $1s$ spectrum. This second peak is centred at $E_B = (398.9 \pm 0.3)\,\mathrm{eV}$ indicating an interaction of the nitrogen atom with the underlying copper surface (N/Cu).
d) The carbon spectrum reveals different contributions originating from different chemical environments: the perylene core ($E_B = (284.8 \pm 0.3)\,\mathrm{eV}$ and $E_B = (285.6 \pm 0.3)\,\mathrm{eV}$), the C-N bonds ($E_B = (286.8 \pm 0.3)\,\mathrm{eV}$) and the C=O bonds ($E_B = (288.8 \pm 0.2)\,\mathrm{eV}$) [229].

The observation about the weaker interaction is consistent to the behaviour of the peaks in the C $1s$ core level spectrum in Figure 8.13 d) and Figure 8.14 c). Here, the peak position of the peaks representing the perylene core stay constant at $\overline{E}_B = (285.0 \pm 0.2)\,\mathrm{eV}$ and $\overline{E}_B = (285.6 \pm 0.2)\,\mathrm{eV}$. For the peak representing the C-N bond of the functional group, a shift to higher binding energies is observed. It is centred at $\overline{E}_B = (286.8 \pm 0.2)\,\mathrm{eV}$ and stays constant up to a thickness of 4.8 ML. The same behaviour is observed for carbon in the C=O bond. It stays constant at $\overline{E}_B = (288.76 \pm 0.2)\,\mathrm{eV}$ up to a thickness of 4.8 ML.

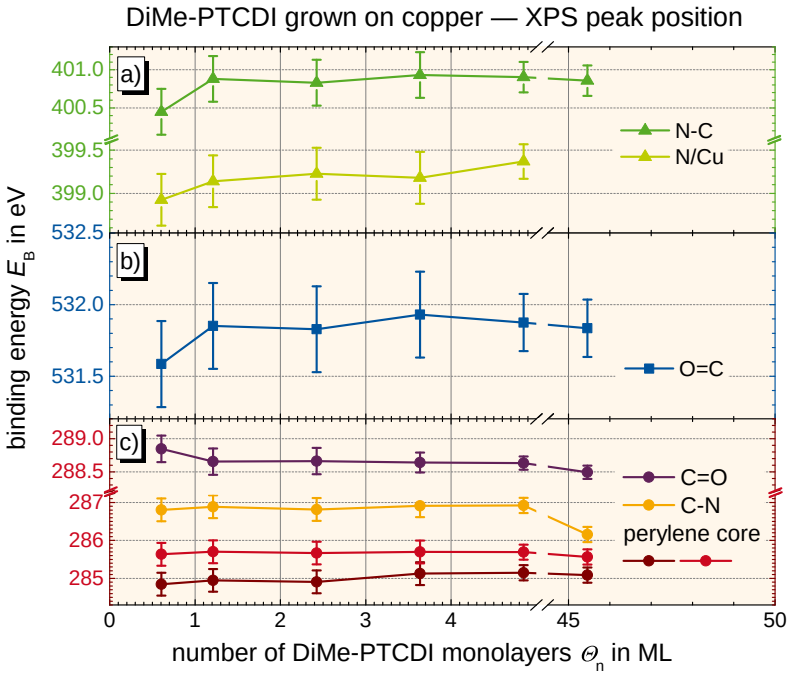

Figure 8.14 | Core level emission peak positions of DiMe-PTCDI grown on a copper surface: a) - c) the positions of the peak centres are plotted as a function of the number of DiMe-PTCDI monolayers Θ_n. The colour code is the same as already used to describe these peaks in Figure 8.13. It has to be called attention to the axes. Both x-axis and y-axis are interrupted and the scaling is different in front of and behind each interruption for presentation purposes.
a) A comparison with the bulk-like film reveals a peak shift of $\Delta_{45.5\,\mathrm{ML}-0.6\,\mathrm{ML}} = 500\,\mathrm{meV}$ to smaller binding energies, which is only observable for $0.6\,\mathrm{ML}$ DiMe-PTCDI grown on copper. With increasing film thickness, the peak position stays constant at $\overline{E}_B = (400.8 \pm 0.2)\,\mathrm{eV}$. The N/Cu peak constantly shifts from lower to higher binding energies by $\Delta_{4.8\,\mathrm{ML}-0.6\,\mathrm{ML}} = 400\,\mathrm{meV}$. b) Within the experimental error, the C=O peak shows a minor shift to smaller binding energies for $\Theta_n = 0.6\,\mathrm{ML}$. With increasing film thickness, the bonding energy of the C=O bonds stays constant at the same position as the bulk-like film at $\overline{E}_B = (531.8 \pm 0.2)\,\mathrm{eV}$. c) The peaks representing the perylene core stay constant at $\overline{E}_B = (285.0 \pm 0.2)\,\mathrm{eV}$ and $\overline{E}_B = (285.6 \pm 0.2)\,\mathrm{eV}$. For the peak representing the C-N bond of the functional group, a shift to higher binding energies is observed. It is centred at $\overline{E}_B = (286.8 \pm 0.2)\,\mathrm{eV}$ and stays constant up to a thickness of $4.8\,\mathrm{ML}$. The peak representing the C=O bond shifts to a constant higher binding energy of $\overline{E}_B = (288.7 \pm 0.2)\,\mathrm{eV}$ up to a thickness of $4.8\,\mathrm{ML}$.

The impact of the observed weak chemical interaction between nitrogen and copper, which from a chemical point of view, slightly influences the functional group of DiMe-PTCDI but not its perylene core, on the electronic structure of DiMe-PTCDI is presented in the following. Thereafter, the results are discussed together.

Interface Electronic Structure

The evolution of the electronic structure of DiMe-PTCDI grown on copper is illustrated in Figure 8.15. The intensity is plotted as a function of the binding energy, which is given with

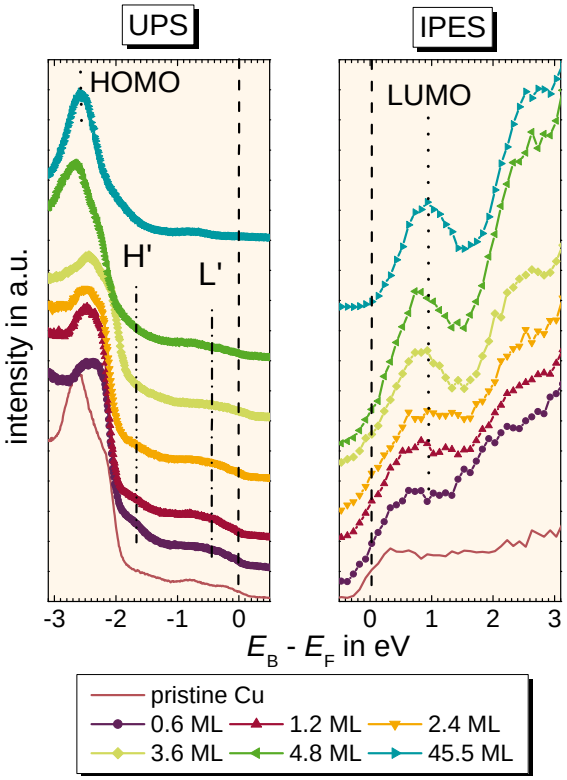

Figure 8.15 | Thickness-dependent UPS and IPE spectra of DiMe-PTCDI grown on copper: the intensity is plotted as a function of the binding energy with respect to E_F. The light red line represents the spectrum of the pristine copper substrate.
Occupied states: adjacent to the Fermi level, the LUMO derived new HOMO (L') starts to rise. Its intensity stays nearly constant with increasing film thickness. The same behaviour is observable for the peak (H') originating from the hybridisation of the HOMO of the isolated molecule with the Cu $3d$ bands. Both peaks stay constant with increasing film thickness. Neither L' nor H' are observable in the bulk-like spectrum (turquoise). Here, the HOMO is centred at $E_B = (-2.6 \pm 0.1)\,\mathrm{eV}$, which fits the value on silver.
Unoccupied states: the binding energy of LUMO stays constant $E_B = (+0.8 \pm 0.2)\,\mathrm{eV}$ with increasing film thickness.
The dashed line marks the position of the Fermi energy.

respect to the Fermi level E_F (black dashed line). The light red line represents the spectrum of the pristine copper substrate.

Within the experimental errors, the electronic structure of the bulk-like thin film of DiMe-PTCDI grown on copper (turquoise graph) equals that grown on silver (see Figure 7.4). Thus, it can be concluded that a film thickness of $45.5\,\mathrm{ML}$ is sufficient to measure the electronic states of DiMe-PTCDI without any influence forced by the substrates. For bulk-like DiMe-PTCDI grown on copper, the HOMO starts to rise at an energy of $E_{\mathrm{HOMO}} = (-2.1 \pm 0.2)\,\mathrm{eV}$ leading to an ionisation energy of $IE = (6.4 \pm 0.2)\,\mathrm{eV}$. Furthermore, the HOMO is centred at $E = (-2.6 \pm 0.1)\,\mathrm{eV}$. The LUMO starts to rise at an energy of $E_{\mathrm{LUMO}} = (+0.4 \pm 0.3)\,\mathrm{eV}$ resulting in an electron affinity of $EA = (4.0 \pm 0.3)\,\mathrm{eV}$. It is centred at $E = (+0.8 \pm 0.2)\,\mathrm{eV}$ [229].

As can be seen in the UPS spectra of Figure 8.15, for $\Theta_n \leq 4.8\,\mathrm{ML}$, adjacent to the Fermi level at $E_B = (-0.1 \pm 0.1)\,\mathrm{eV}$, the HOMO starts to rise, which is centred at $\overline{E}_B = (-0.4 \pm 0.2)\,\mathrm{eV}$. In comparison to DiMe-PTCDI grown on silver, this peak is positioned closer to E_F. This observation fits the statement drawn from XPS that the interaction between DiMe-PTCDI and copper is weaker than on silver [63]. A second peak has its maximum at $\overline{E}_B = (-1.8 \pm 0.2)\,\mathrm{eV}$. Both peaks stay constant in intensity and peak position up to a film thickness of $4.8\,\mathrm{ML}$. In comparison to the bulk-like film, the ionisation energy is decreased to a constant value of $\overline{IE} = (4.0 \pm 0.2)\,\mathrm{eV}$ up to an film thickness of $\Theta_n \leq 4.8\,\mathrm{ML}$ (see Table 8.2). The broad peak observed between $E_B = -1.8\,\mathrm{eV}$ and $E_B = -3.1\,\mathrm{eV}$ is a superposition of the a third peak arising from the organic layer and the Cu $3d$ bands.
Although the chemical interaction between DiMe-PTCDI and copper appears to be less strong

Table 8.2 | Comparison of the ionisation energies (IE) and the electron affinities (EA) of DiMe-PTCDI thin films in dependence of film thickness. Furthermore, the transport gaps (E_t) determined from the peak onset are also given.

Θ_n	0.6 ML	1.2 ML	2.4 ML	3.6 ML	4.8 ML	45.5 ML
IE ±0.2 eV	3.8 eV	4.0 eV	3.9 eV	4.1 eV	4.2 eV	6.4 eV
EA ±0.3 eV	3.4 eV	3.6 eV	3.5 eV	3.6 eV	3.6 eV	4.0 eV
E_t ±0.3 eV	0.4 eV	0.4 eV	0.5 eV	0.5 eV	0.6 eV	2.5 eV

than on silver and is mainly located on the nitrogen atom of the functional group, the observation of the interface states close to the Fermi level is an indication that the LUMO becomes occupied, when DiMe-PTCDI adsorbes on copper [32, 41, 256]. Therefore, it is concluded that HOMO and HOMO^{-1} originate from a hybridisation of LUMO and HOMO of the isolated molecule and the Cu $3d$ bands, respectively. Hence, they are again denoted as L' and H' in order to mark their origin.

As in the case of DiMe-PTCDI grown on silver, for copper, the organic layer stays semiconducting. Although the LUMO derived HOMO starts to rise at $E_B = (-0.1 \pm 0.1)\,\mathrm{eV}$, the LUMO starts to rise at $\overline{E}_B = (+0.4 \pm 0.2)\,\mathrm{eV}$. Consequently, both states are clearly separated. For all investigated film thicknesses, the peak centre of the LUMO stays constant at $\overline{E}_B = (+0.8 \pm 0.2)\,\mathrm{eV}$ within the experimental error. The electron affinity stays nearly constant, as can be seen in Table 8.2. However, in combination with the decrease of IE, the transport band gap is decreased to $\overline{E}_t = (0.5 \pm 0.3)\,\mathrm{eV}$ for $\Theta_n \leq 4.8\,\mathrm{ML}$ (see Table 8.2). Up to a film thickness of $4.8\,\mathrm{ML}$, the LUMO has its origin in the LUMO^{+1} of the isolated molecule, which relaxes towards the Fermi level caused by the filling of the LUMO [32, 41, 256].

Following the discussion above, the filling of the LUMO takes place on the first monolayer or in the submonolayer regime and is just observable for larger thicknesses because of the island growth of DiMe-PTCDI. Thereby, the island height stays constant up to $\Theta_n = 4.8\,\mathrm{ML}$. The observation, that L' and H' stay constant in intensity and peak position supports this statement. Nevertheless, scanning tunnelling microscopy (STM) could be performed on comparable thin films in future studies in order to further investigate the electronic origin of L' and H' and the extent of the chemical interaction.

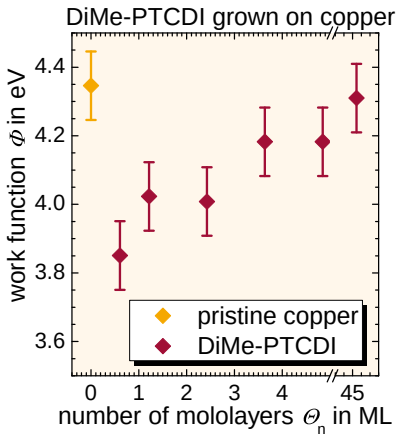

Figure 8.16 | Evolution of the work function of DiMe-PTCDI with increasing number of monolayers: the work function Φ of DiMe-PTCDI is plotted as function of the number of monolayers Θ_n. The work function of the pristine copper substrate amounts to $(\Phi_{Cu} = 4.4 \pm 0.1)\,\mathrm{eV}$. For a film of $0.6\,\mathrm{ML}$ DiMe-PTCDI, Φ is decreased by $0.5\,\mathrm{eV}$. Thereafter, the work function increases with increasing coverage. The determined work functions of both bulk-like films are equal.

The evolution of the work function Φ of DiMe-PTCDI grown on copper is plotted as function of the number of monolayers Θ_{n} in Figure 8.10. The work function of the pristine copper substrate amounts to $(\Phi_{\mathrm{Cu}} = 4.4 \pm 0.1)\,\mathrm{eV}$. As a short reminder, the thin films used as substrates are of polycrystalline structure. Since the work function is different for every crystal facet, polycrystalline surfaces have a different work function compared to those measured for single crystals. For DiMe-PTDI grown on copper, Φ is decreased by $0.5\,\mathrm{eV}$ for a film of $0.6\,\mathrm{ML}$. The reduction of the work function can be addressed to an arising interface dipole which pushes back the electrons of the metal surface that partially spill out into vacuum and thus decreases the pristine metal surface dipole [16, 256, 258, 259]. This so called 'push-back' effect is often the main reason for work function reductions in the range up to $1.0\,\mathrm{eV}$ [256, 260]. However, the observed interface states reveal a charge transfer, which commonly counter acts the 'push-back' effect [256, 258]. Furthermore, the shift of HOMO and LUMO^{+1} of the isolated molecule to the position of H' and LUMO, respectively, reveals that for DiMe-PTCDI grown on copper, also a back-donation from these molecular orbitals to the underlying metal takes place [63]. The observed shift of these orbitals proves the interaction with the Cu $2p$ metal states and thus indicate a chemical boning (chemisorption) [63]. This is substantiated by the observation of the new peak N/Cu. However, the observed core-level shifts in the XPS spectra indicate that the change in the electronic structure has only a small impact on the oxygen atoms of the functional group (see Figure 8.6). Moreover, the effect seems not to extend on the perylene core. Nevertheless, the formation of the bond leads to a charge transfer (back-donation) from the molecule into the metal, which balances the electron transfer from the metal to the LUMO of the isolated molecule but influences the frontier electronic system of DiMe-PTCDI [32, 63]. However, the observed interaction is much stronger for DiMe-PTCDI grown on silver than on copper. At this point, it has to be stated that the bonding mechanism between the nitrogen atoms of the functional group and copper or silver cannot be explained. A possible scenario, which is to cut off the alky chain, can be excluded because the elemental composition fits the theoretically expected values for each investigated thin films. Therefore, this question could be an interesting topic for future DFT investigations.

As can be seen in Figure 8.16, the work function increases with increasing coverage. In combination with the observation, that the XPS peak shifts are only noticeable for the $0.6\,\mathrm{ML}$ thin film, it is concluded that the interaction between DiMe-PTCDI and copper just happens in the first monolayer. However, the effect of LUMO filling is visible up to a film thickness of $4.8\,\mathrm{ML}$, which can be explained by the nearly constant height of the DiMe-PTCDI islands. For $\Theta_{\mathrm{n}} > 2.4\,\mathrm{ML}$, Φ equals those determined for DiMe-PTCDI grown on silver. Moreover, the work functions of both bulk-like films are equal, which again shows that a thickness of $45.5\,\mathrm{ML}$ is sufficient to measure the electronic states of DiMe-PTDI without any influence forced by the substrates.

It is stated above, that comparable molecules like PTCDA are bend when brought in contact to silver or copper [32, 41, 45]. Thus, in order to investigate a possible bending of DiMe-PTCDI molecules grown on copper and to further complete the picture drawn for the effects occurring at the DiMe-PTCDI-copper interface, X-ray standing wave (XSW) experiments on comparable samples could be performed in future studies.

Conclusion

9. Summary and Outlook

The comprehension of effects occurring at the interface between a metal electrode and an organic semiconductor is crucial for an enhanced performance of (opto-) electronic devices. This last chapter presents a brief summary and an outlook of the highlights of the interface physics discussed in this thesis, which is aimed at two goals: first, the **construction of an inverse photoemission spectrometer**, which enables the investigation of the unoccupied part of the density of states, and second, the **understanding of the electronic structure of metals**[1]**, organic semiconductors and organic-metal interfaces**.

Goal I – The Inverse Photoemission Spectrometer

Prior to this thesis, all studies carried out at the I. Institute of Physics (IA) of the RWTH Aachen University regarding the energetics at the interface between an organic semiconductor and a contact electrode were based on direct photoelectron spectroscopy (PES). Consequently, the impact on the electron injection barrier could only be measured indirectly. Furthermore, the precise position of the LUMO stayed completely unknown, which prevented making solid statements about the energy level alignment in device applications. Therefore, the **inverse photoemission spectrometer**, which is presented in Part II, was newly constructed and **successfully set up into operation** within the scope of the presented thesis. In Chapter 4, the various design choices of the spectrometer and its components are presented. Since inverse photoemission spectroscopy (IPES) is performed using low-energy electrons with penetration depths in the order of Angstroms, this technique is very sensitive to the quality of the sample's surface. Therefore, no contaminating particles should be present on the surface of the sample under investigation. Hence, preparing clean surfaces and performing meaningful measurements require an optimal environment of ultra-high vacuum (UHV). In addition to that, proper vacuum conditions are also required to minimise scattering of the electrons with gas molecules during the measurement. Furthermore, the presence of the earth's magnetic field would deflect the electron beam. For that reason, the inverse photoemission analysis chamber (IPE-AC), which holds the IPE spectrometer, was designed as a UHV µ-metal chamber shielding the electrons against the earth's magnetic field and other stray fields. The IPE-AC reaches a base pressure lower than $5{\cdot}10^{-11}\,\mathrm{mbar}$. At these pressures,

[1] Since the electronic structure of noble metals is already well-understood in literature. The measurement of their electronic structure serves as prove that IPE spectrometer built in the frame of this thesis is working well and that the measured results are reliable.

high-quality IPE measurements can be performed without a critical sample contamination at sufficient timescales. The spectrometer itself is equipped with an **electron gun (ELG-2)** purchased from *Kimball Physics Inc.* and a **gaseous (argon/acetone) photon bandpass detector** which was built by the research group of *M. Donath* at the Westfälische Wilhelms University of Münster [145, 180].
Besides the IPE-AC, a second UHV chamber was constructed, which includes a storage for eight samples as well as tools for sample movement and bonding. The so-called sample handling chamber (SHC), in turn, is connected to the sample transfer chamber called handler of the ORPHEUS cluster tool, which also holds an analysis chamber for ultra-violet photoelectron spectroscopy (UPS) and X-ray photoelectron spectroscopy (XPS) and deposition chambers. Thus, direct and inverse photoemission spectroscopy can be performed in-situ on the same sample, which is also produced in-situ.

After the IPE spectrometer had been successfully mounted and assembled to the ORPHEUS cluster tool, the setup was characterised in the course of this thesis. The results are presented in Chapter 5. The behaviour of the electron gun was characterised in order to find adequate operation parameters, which are summarised in Table 9.1. When applying these parameters, the beam divergence was determined to $\Delta\Theta = 4.45° \pm 0.71°$, which perfectly matches values reported in literature [29, 140, 143, 176].
The photon bandpass detector can be operated either with a pure acetone or with an argon/acetone mixture. The detector is characterised and its behaviour is discussed for both conditions. As explained in Section 5.2, it is recommended to utilise the detector as **Geiger-Müller counter** with an argon/acetone gas mixture of $70.7\,\mathrm{mbar}$ to $4.3\,\mathrm{mbar}$ at an operation voltage between $U_{\mathrm{OP}} = 945\,\mathrm{V}$ and $970\,\mathrm{V}$ and with a discrimination level between $200\,\mathrm{mV}$ and $500\,\mathrm{mV}$.
Finally, the total energy resolution and the apparatus function of the IPE spectrometer is determined to $\Delta E_{\mathrm{IPES}} = (400 \pm 2)\,\mathrm{meV}$, which is in **good agreement** with those reported in literature for comparable spectrometers [29, 62, 176, 200, 207, 208]. Furthermore, it is shown, that the IPE spectrometer also **fits the stronger** 10% **to** 90% **criterion**[2], which is not always the case for comparable spectrometers found in literature [149]. As a consequence, the apparatus function of the IPE spectrometer built in the course of this thesis is symmetric resulting in a **symmetric Gaussian shape** of all spectral features including the Fermi level onset.

The IPE spectra of the highly textured (111) noble metal thin films presented in Chapter 6 in Part III serve as reference systems to verify a proper working condition of the IPE spectrometer. The *Shockley*-type crystal-induced surface state (SS) is not only visible near the Fermi edge in the UPS spectra but also in the IPE spectra. It is located at the $\overline{\Gamma}$ point of the surface Brillouin zone (SBZ) within the nearly parabolic shaped sp inverted gap at the L point of the 3D Brillouin zone. This type of surface state is fully occupied when measuring under normal incidence. Consequently, the SS should not be visible in IPE spectra. However, since the electron beam has always a certain angular divergence, the *Shockley*-type crystal-

[2]The rise of the IPE signal at the Fermi edge from 10% to 90% of the total intensity is also a strong criterion for the resolution, since it gives an evidence on the shape of the Fermi edge and on that of the spectral features.

Table 9.1 | Operation parameters of the electron gun

cathode current I_{ES}	1^{st} **Anode** U_A	**Focus** U_F
$I_{ES} = 1.02\,\text{A}$= const. $\rightarrow$ low cathode temperature $\Rightarrow$ small thermal energy uncertainty and longer lifetime	$U_A = 50\,\text{V}$ $\rightarrow$ high sample current between $1.0\,\mu\text{A}$ and $3.0\,\mu\text{A}$ $\Rightarrow$ short measurement times	$U_F = 240\,\text{V}$ $\Rightarrow$ roundish, well-focused beam with $\varnothing \approx 1\,\text{mm}$

induced surface state is visible in all IPE spectra published so far [126, 127] and also in those reported in this thesis. Moreover, the IPE spectra exhibit the L_1 band edge feature as well as the image potential states, in which electrons are bound in their positive Coulombic image potential above the sample surface.
For the copper (111) thin film, results gained from angle-resolved inverse photoemission are also presented. Here, the focus is on the energy dispersion of the *Shockley*-type crystal-induced surface state which is compared to a simulation applying the tight-binding model. The behaviour of the experimental data is explained and the IPE data seem to follow the predicted dispersion within the experimental errors.
All peaks are identified not only for the UPS spectra but also for the IPE spectra. The position of their peak centres **fit the values reported in literature**. Thus, it can be concluded that the IPE spectrometer, which was built in the course of this thesis, is **properly working and obtains reliable results**.

Goal II – The Electronic Structure of Metals, Organic Semiconductors and Organic-Metal Interfaces

The photoemission spectra of the highly textured (111) noble metal thin films presented in Chapter 6 in Part III serve not only as reference systems for a proper working IPE spectrometer but shall also help to understand the organic-metal interfaces. The valence band spectra of all metals reveal well-defined peaks, whereby, the most prominent ones can be attributed to the **flat d bands** of the respective metal.

The electronic structure of organic semiconductors needs to be understood, before the effects occurring at the interface between organic semiconductors and metals can be explained. Therefore, the electronic structure is discussed in a more general way in Chapter 7. In this context, first the results obtained for DiMe-PTCDI, which is the molecule of interest, are presented in detail in Section 7.2.
Thereafter, these results are compared to the electronic structure of perylene and its derivatives PTCDA and PTCDI-C_8 (see Figure 7.5). The substitution of perylene with functional groups containing elements with a relatively high ionisation energy leads to a **lowering**

of the molecular orbitals with respect to the vacuum level. The impact of the electron-withdrawing groups on the perylene core is stronger for the LUMO than for the HOMO, which results in a **lowered transport band gap** E_t (see Table 7.1). Furthermore, the shift of the molecular orbitals results in a change of the transport properties. While perylene clearly shows p-type electrical transport, its derivatives are n-type semiconductors because of the low-lying LUMO yielding a low injection barrier for electrons. When comparing the results gained for PTCDA with those for DiMe-PTCDI, the exchange of the bridging oxygen of the anhydride side group of PTCDA with a nitrogen atom in the case of DiMe-PTCDI results in a small increase of the molecular energy level with respect to the vacuum level. This results in a slightly smaller electron affinity as well as in a decreased ionisation energy in the case of DiMe-PTCDI. Therefore, it is concluded, that also the **placement of the elements is important** for the discussion of the electronic structure of molecules [242]. The **extension of the alkyl chain**, on the other hand, when going from DiMe-PTCDI (PTCDI-C_1) to PTCDI-C_8, has only a **minor impact on the electronic structure**: similar to PTCDA or DiMe-PTCDI, LUMO and HOMO are mainly located on the perylene core of PTCDI-C_8 and are not pinpointed on the alkyl chain [251]. Consequently, the length of the alkyl chain should not influence the electronic structure. Moreover, it is shown that the exciton binding energy $E_{B;ex} = E_t - E_{opt}$ increases with increasing transport gap energy E_t, which is already known from inorganic semiconductors [244].

The last chapter of Part III focuses on the chemical and electronic interaction between a silver or copper thin film[3] and thin layers of DiMe-PTCDI deposited on top with varying film thickness.

Silver

DiMe-PTCDI grows in islands (***Volmer-Weber* growth**) on a silver substrate. Up to a coverage of 2.4 ML, the silver substrate seems to influence the growth of the islands in the way that larger islands of DiMe-PTCDI form on the smooth and large areas of the silver substrate. In contrast, very small islands grow on the grainy part of the silver surface. Between a coverage of 2.4 ML and 3.6 ML, the growth of the smaller DiMe-PTCDI islands becomes dominant, regardless of the nature of the underlying silver area (smooth vs. grainy). First, they tend to overgrow the larger islands. Thereafter, the larger islands are no more observable and the size as well as the coverage of the smaller islands increases.
XPS measurements reveal a **chemical interaction** of the oxygen and the nitrogen atoms of the functional group of DiMe-PTCDI with the underlying silver atoms. This interaction is accompanied by a shift of the C $1s$, N $1s$ and O $1s$ core level peaks from lower to higher binding energies with increasing coverage. In combination, both results indicate a strong chemisorption of the DiMe-PTCDI molecules on the silver substrate. For larger film thicknesses ($\Theta_n > 2.4$ ML), almost all peak positions of the core level spectra match those of the bulk-like film within the experimental error. Since the growth of small island becomes dominant in this thickness region, a film thickness of $\Theta_n > 2.4$ ML is too thick for the investigation

[3] In contrast to the metal films discussed in Chapter 6, the metal thin films, which are used as substrates, are now of polycrystalline structure.

of the interaction between DiMe-PTCDI and silver [41]. Thus, the influence of the substrate on the chemical nature of DiMe-PTCDI is no more measureable.
For $\Theta_n \leq 2.4$ ML, the described chemical interaction of DiMe-PTCDI with the silver substrate results in a decrease of the ionisation energy. Hence, adjacent to the Fermi level, a peak starts to rise, which is assigned to a **hybrid state** originating from the hybridisation of the LUMO of the isolated molecule with the Ag $4d$ bands. This hybridisation leads to a filling of the LUMO of the isolated molecule [32, 41, 63]. Its intensity decreases with increasing film thickness. The same behaviour is revealed for the peak (H') originating from the hybridisation of the HOMO of the isolated molecule with the Ag $4d$ bands. The binding energy of LUMO slightly increases with increasing film thickness. For $\Theta_n \leq 2.4$ ML, the LUMO^{+1} of the molecule relaxes towards E_F and becomes the LUMO of the thin film. In contrast to IE, the electron affinity stays nearly constant within the range of the experimental error. The **transport gap is significantly reduced** to $\overline{E}_t = (0.5 \pm 0.3)$ eV instead of $E_t = (2.5 \pm 0.3)$ eV for the bulk-like film. For $\Theta_n \geq 3.6$ ML, the energy positions of the occupied and unoccupied electronic states and, thus IE, EA and the transport band gap equal those of the bulk-like DiMe-PTCDI film. As already concluded from the presented XPS measurements, a film thickness of $\Theta_n \geq 3.6$ ML is too thick for the investigation of the interaction between DiMe-PTCDI and silver.
Within the experimental error, the work function of DiMe-PTCDI stays constant with increasing coverage. Thereof, it can be concluded that no dipole is established at the DiMe-PTCDI-silver interface [63, 258]. This observation seems to be contradictory to the UPS/IPE spectra, which show a significant charge transfer from the substrate into the LUMO of DiMe-PTCDI [246]. This LUMO filling, however, should result in a negatively charged DiMe-PTCDI monolayer, which in turn should cause a significant reduction of the work function. The finding that the work function stays constant reveals that just a little amount of charge is transferred onto the molecule. Thus, the question about origin of the electrons, which fill the LUMO, arises. This effect is explained with the help of SIAS recently introduced by G. Heimel and co-workers [32]. It is assumed that HOMO as well as LUMO^{+1} of the isolated molecule shift to the position of H' and LUMO, respectively [63]. In addition to the donation from the metal, there is also a back-donation from these molecular orbitals to the metal [63]. Furthermore, the observed strong shift of these orbitals proves a strong interaction with the Ag $4d$ metal states and thus indicate a **covalent chemical boning** [63]. This is substantiated by the observation of the new peaks O/Ag and N/Ag and the resulting core-level shifts in the XPS spectra. Thus, the formation of the bond leads to a charge transfer (back-donation) from the molecule into the metal, which balances the electron transfer from the metal to the LUMO of the isolated molecule but influences the frontier electronic system of DiMe-PTCDI [32, 63].
It is shown for similar molecules, that the change in the electronic structure in combination with the covalent bonding of the molecule to the metal substrate, bends the atoms in the functional group towards the metal surface [32, 41, 45]. Furthermore, the filling of the LUMO below the Fermi level of the metal weakens and lengthens, for example, the C=O bond towards a C-O single bond. This results in an re-hybridisation of the oxygen atoms and in an shift of the O $1s$ as well as the C $1s$ core level spectrum to smaller binding energies, as it is observed for DiMe-PTCDI grown on silver. The re-hybridisation of oxygen atoms, in turn,

favours the formation of a covalent bond with the underlying metal surface. Furthermore, it leads to a resonance structure, which exhibits a significantly extended π-electron system [32]. The π-conjugation, then, extends from the perylene core over the functional group into the metal leading to strong coupling of the molecular orbitals to the metal states. This, in turn, reduces the molecular gap of the isolated molecule as it is observed for DiMe-PTCDI grown on silver. The reduction of the band gap shifts the LUMO of the isolated molecule down in energy. Thereby, more electrons move onto the molecule until E_{F} finally lies within the formerly unoccupied molecular DOS [32].
In order to investigate a possible bending of DiMe-PTCDI molecules, *X-ray standing wave (XSW)* experiments on comparable samples could be performed in future studies. In combination with profound *DFT calculations* on the bonding mechanism, this would complete the picture drawn for the effects occurring at the DiMe-PTCDI-silver interface. Furthermore, *scanning tunnelling microscopy (STM)* could be performed on comparable thin films in future studies in order to further investigate the electronic origin of L' and H'.

Copper

DiMe-PTCDI shows ***Volmer-Weber* growth** when grown on a copper substrate: at a film thickness of $0.6\,\mathrm{ML}$, the molecules cluster in small islands. Their distribution is more homogeneous than compared to DiMe-PTCDI grown on silver. Furthermore, the average island coverage is larger when DiMe-PTCDI is grown on a copper sample. With increasing film thickness, the average island size as well as the coverage increase. The island height stays nearly constant with increasing film thickness, which results in a constant RMS roughness. A change in the growth is not observable for the investigated samples.
In order to investigate the samples of DiMe-PTCDI grown on copper from a chemical point of view, XPS measurements were performed. The results indicate a **weaker chemisorption of DiMe-PTCDI on copper** as on silver. A comparison with the bulk-like film reveals a peak shift of the N-C peak to smaller binding energies, which is only observable for $0.6\,\mathrm{ML}$ DiMe-PTCDI grown on copper. With increasing film thickness, the peak stays constant at the same position as its bulk-like counterpart. Similar to DiMe-PTCDI grown on silver, a peak indication an interaction of the nitrogen atoms with the underlying copper is visible. The N/Cu peak constantly shifts from lower to higher binding energies. Within the experimental error, the C=O peak shows a minor shift to smaller binding energies for $\Theta_{\mathrm{n}} = 0.6\,\mathrm{ML}$. With increasing film thickness, the bonding energy of the C=O bonds stays constant at the same position as the bulk-like film. For the oxygen atoms, no interaction with the copper atoms is observed. The peaks representing the perylene core are not influenced by the chemical interaction and thus stay constant at bulk-like position. For the peak representing the C-N bond of the functional group, a shift to higher binding energies is observed, where it stays constant up to a thickness of $4.8\,\mathrm{ML}$. The peak representing the C=O bond shifts also to a constant higher binding energy up to a thickness of $4.8\,\mathrm{ML}$.
Although the results obtained from the XPS spectra indicate a weaker chemisorption, similar to DiMe-PTCDI grown on silver, LUMO filling is also observed for DiMe-PTCDI grown on copper. The work function is decreased by $0.5\,\mathrm{eV}$ for a film of $0.6\,\mathrm{ML}$. The reduction of the work function can be addressed to an arising **interface dipole** which pushes back the electrons of

the metal surface that partially spill out into vacuum and thus decreases the pristine metal surface dipole [16, 256, 258, 259]. This so called 'push-back' effect is often the main reason for work function reductions in the range up to $1.0\,\mathrm{eV}$ [256, 260]. However, the observed interface states reveal a charge transfer, which commonly counter acts the 'push-back' effect [256, 258]. Furthermore, the shift of HOMO and LUMO^{+1} of the isolated molecule to the position of H' and LUMO, respectively, reveals that for DiMe-PTCDI grown on copper also a back-donation from these molecular orbitals to the underlying metal takes place [63]. The observed shift of these orbitals proves the interaction with the Cu $2p$ metal states and thus indicate a chemical boning (**chemisorption**) [63]. This is substantiated by the observation of the new peak N/Cu. However, the observed core-level shifts in the XPS spectra indicate that the change in the electronic structure has only a small impact on the oxygen atoms of the functional group. Moreover, the effect seems not to extend on the perylene core. Nevertheless, the formation of the bond leads to a charge transfer (back-donation) from the molecule into the metal, which balances the **electron transfer from the metal to the LUMO of the isolated molecule** but influences the frontier electronic system of DiMe-PTCDI [32, 63]. However, the observed interaction is much stronger for DiMe-PTCDI grown on silver than on copper.
The bonding mechanism between the nitrogen atoms of the functional group and copper or silver cannot be explained. A possible scenario, which is to cut off the alky chain, can be excluded because the elemental composition fits the theoretically expected values for each investigated thin films. Therefore, this question could be an interesting topic for future *DFT investigations*.
With increasing coverage, the work function of DiMe-PTCDI grown on copper increases. In combination with the observation, that the XPS peak shifts are only noticeable for the $0.6\,\mathrm{ML}$ thin film, it is concluded that the interaction between DiMe-PTCDI and copper just happens in the first monolayer. However, the effect of LUMO filling is visible up to a film thickness of $4.8\,\mathrm{ML}$, which can be explained by the nearly constant height of the DiMe-PTCDI islands. For $\Theta_\mathrm{n} > 2.4\,\mathrm{ML}$, the work function equals those determined for DiMe-PTCDI grown on silver. Moreover, the work functions of both bulk-like films are equal, which shows that a thickness of $45.5\,\mathrm{ML}$ is sufficient to measure the electronic states of DiMe-PTDI without any influence forced by the substrates.
As it is stated above, that comparable molecules like PTCDA bend when brought in contact to silver or copper [32, 41, 45]. Thus, in order to investigate a possible bending of DiMe-PTCDI molecules grown on copper and to further complete the picture drawn for the effects occurring at the DiMe-PTCDI-copper interface, *X-ray standing wave (XSW)* experiments on comparable samples could be performed in future studies.

Outlook

Besides the suggested experiments, the investigation of *DiMe-PTCDI thin films of various thicknesses grown on gold* would be worthwhile. For other acceptor molecules like PTCDA, only a weak physisorption and no LUMO filling are observed if the film is grown on gold [41]. Combined with the results obtained for silver and copper, such a thickness series on gold

would allow for drawing a comprehensive picture of the interface electronics between the organic molecule DiMe-PTCDI and noble metal surfaces. In the case of DiMe-PTCDI grown on noble metal surfaces, such data has not been published so far.
As a final goal the charge transport across the DiMe-PTCDI/metal interface is of high interest. Thus, *electronic transport measurements* on DiMe-PTCDI should be performed. These measurements would depict the next big step for the *correlation of the chemical and electronic properties* of the interfaces described in this study *with the device functionality*. Subsequently, the application of the institutes knowledge on self-assembled monolayers (SAM) on the different contact metals can be envisioned in order to control and tailor the metal-molecule interaction and the charge carrier injection into the DiMe-PTCDI layer [261]. The impact of the SAM onto to the electronic structure of DiMe-PTCDI would be of great interest.

Appendix

A. Supporting Information on the Gaseous Radiation Detector

Proportional counter

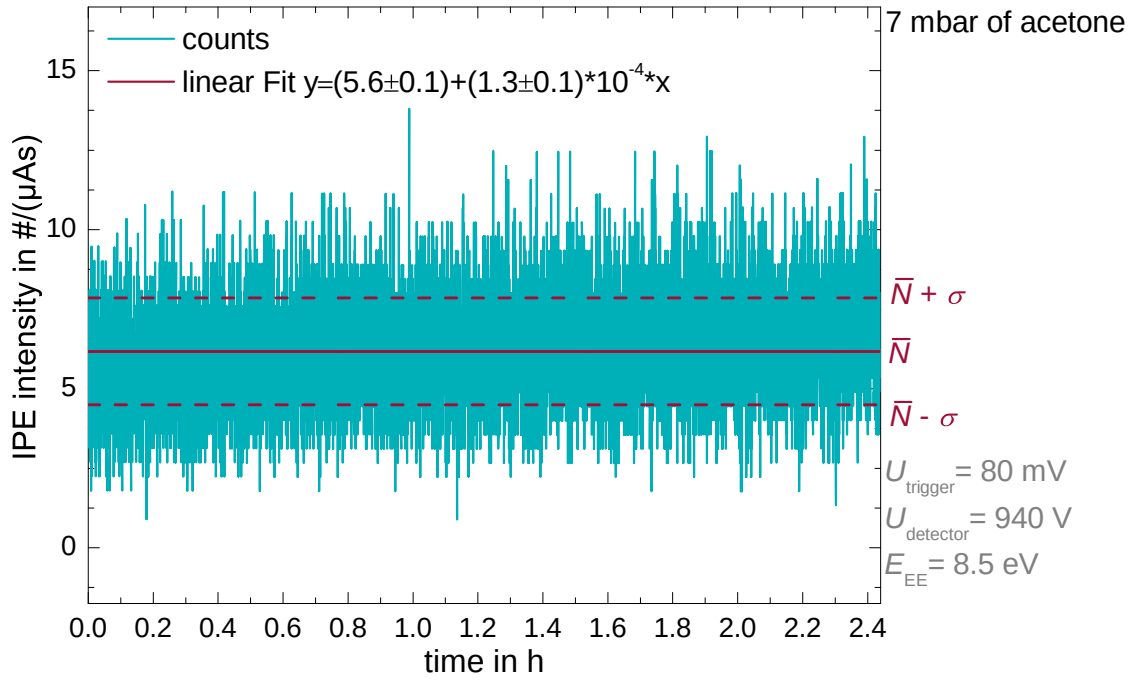

Figure A.1 | Stability test of the proportional counter: the graph shows the normalised IPE intensity in dependence of the time in hours. A pure acetone gas mixture of $7\,\mathrm{mbar}$ was used. The discrimination level was set to $U_{\mathrm{trigger}} = 80\,\mathrm{mV}$ and the detector voltage was about $U_{\mathrm{detector}} = 940\,\mathrm{V}$. During the measurement the energy of the electrons was kept constant at $E_{\mathrm{EE}} = 8.5\,\mathrm{eV}$. The mean value $\bar{N} = 5.6\,\#/\mu\mathrm{As}$ is marked by the red solid line, whereas the dashed red lines illustrate the interval $\bar{N} \pm \sigma$ with $\sigma = 1.7\,\#/\mu\mathrm{As}$. As expected $65.2\,\%$ of the data points lie within this interval. The count rate stays nearly constant over the time. Just a slight increase with a slope of $(1.3 \pm 0.1)\,10^{-4}\,\#/\mu\mathrm{Ash}$ is observed.

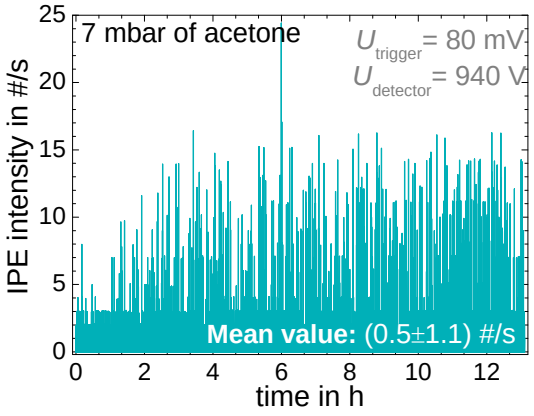

Figure A.2 | Dark count measurement: the graph shows the IPE intensity that is produced only by interferences of the surrounding, as a function of the measurement time in hours. A pure acetone gas mixture of $7\,\mathrm{mbar}$ was used. The discrimination level was set to $U_{\mathrm{trigger}} = 80\,\mathrm{mV}$ and the detector voltage was about $U_{\mathrm{detector}} = 940\,\mathrm{V}$. During the measurement the electron gun and the pressure control system were not operated. The mean dark IPE intensity is about $(0.5 \pm 1.1)\,\#/\mathrm{s}$.

B. Supporting Information on the Crystal and Electronic Structure of Noble Metal Surfaces

Θ2Θ-XRD Pattern of a Well-Ordered and Highly Textured 200 nm Noble Metal Thin Film

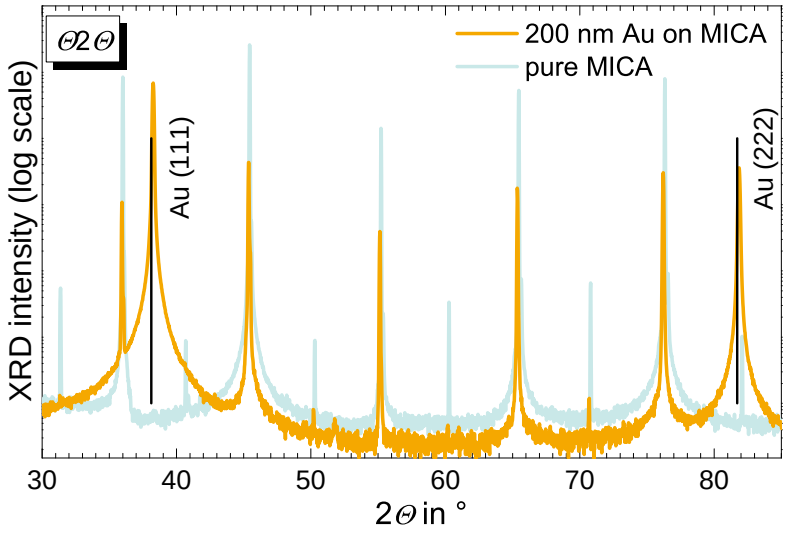

Figure B.1 | $\Theta 2\Theta$-XRD pattern of a well-ordered and highly textured 200 nm gold thin film: The graph shows the XRD intensity in a logarithmic scale in dependence of the angle 2Θ. Therein, the orange pattern represents the measured data. The positions of all gold peaks are marked by the black lines. All peaks, which are not marked, correspond to the MICA substrate, which is represented by the light blue pattern. Only peaks of the family with (111) orientation are observed, which means that only these lattice planes are oriented parallel to the sample surface. Consequently, only the (111) orientation contributes to the IPE signal, when measuring the sample angle-integrated under normal condition.

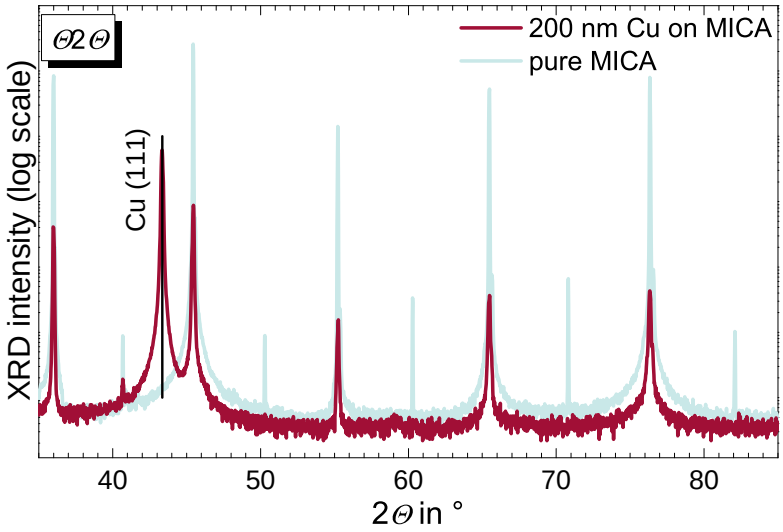

Figure B.2 | $\Theta 2\Theta$-XRD pattern of a well-ordered and highly textured 200 nm copper thin film: The graph shows the XRD intensity in a logarithmic scale in dependence of the angle 2Θ. Therein, the red pattern represents the measured data. The positions of all copper peaks are marked by the black lines. All peaks, which are not marked, correspond to the MICA substrate, which is represented by the light blue pattern. Only a peak which corresponds to the (111) orientation is observed, which means that only these lattice planes are oriented parallel to the sample surface. Consequently, only the (111) orientation contributes to the IPE signal, when measuring the sample angle-integrated under normal condition.

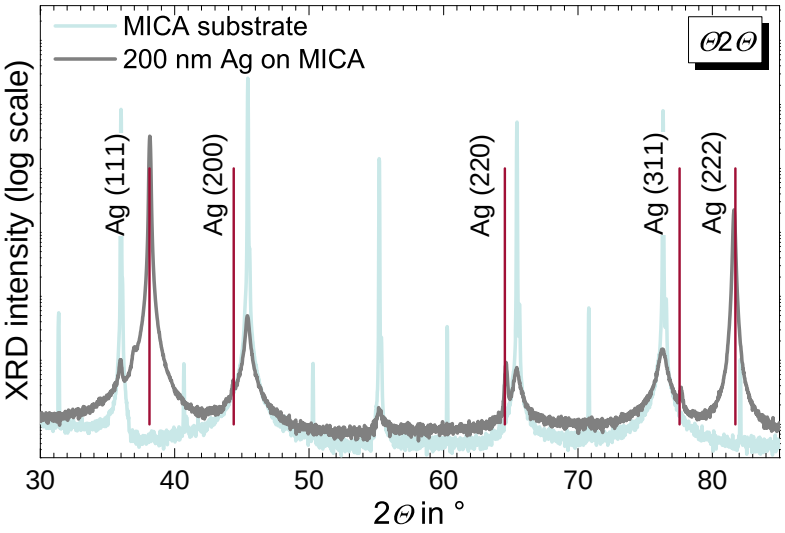

Figure B.3 | $\Theta 2\Theta$-XRD pattern of a well-ordered and highly textured 200 nm silver thin film: The graph shows the XRD intensity in a logarithmic scale in dependence of the angle 2Θ. Therein, the grey pattern represents the measured data. The positions of all silver peaks are marked by the red lines. All peaks, which are not marked, correspond to the MICA substrate. Here, not only peaky of the family with (111) orientation but also peaks which correspond to the (200), (220) and (311) orientation are observed. Consequently, all these lattice orientations contribute to the IPE signal, when measuring the sample angle-integrated under normal condition.

Angle Resolved IPE Spectra of a Highly Textured 200 nm Copper Thin Film

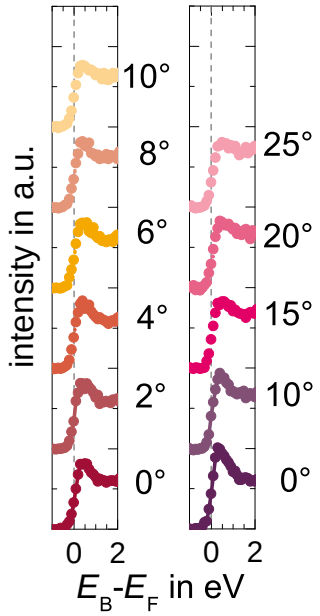

Figure B.4 | AR-IPE spectra of a well-ordered and highly textured copper (111) thin film as a function of the electron incidence angle Θ: The intensity is plotted in dependence of the binding energy. Again, the energy scale is given with respect to the Fermi energy E_F. At an electron incidence angle of $\Theta = 4\,^\circ$, the *Shockley*-type crystal-induced surface state (SS) starts to extend in intensity and FHWM. Thereafter $(\Theta \geq 10\,^\circ)$ it's intensity decreases and the state starts to shift to higher energies. The angle dependent behaviour of the *Shockley*-type crystal-induced surface state of Copper (111) is summarised in Figure 6.6. (The spectra shown on the left side are recorded on the same sample. All spectra displayed on the right side are also taken from the same sample, which was not the same as that on the left side. Nevertheless, the $\Theta 2\Theta$-XRD pattern of both samples verified a well-ordered and highly textured (111) orientation.)

Silver

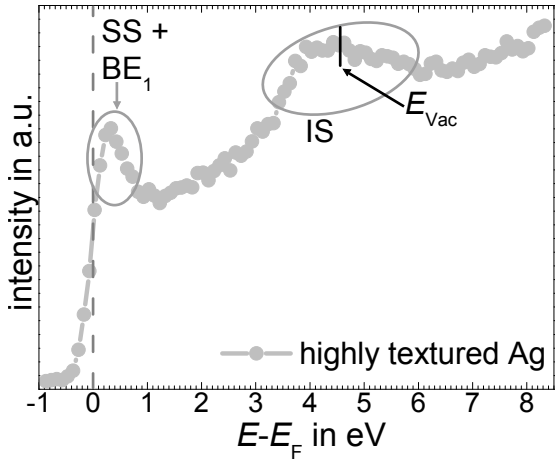

Figure B.5 | IPE spectrum of a well-ordered and highly textured silver thin film with preferred direction in (111): the intensity is plotted in dependence of the energy. Again, the energy scale is given with respect to the Fermi energy E_F. Its position is marked by a grey dashed line.
Besides an orientation of the (111) lattice plane parallel to the sample surface, $\Theta 2\Theta$-XRD pattern revealed also (200), (220) and (311) oriented lattice planes. (For more information see Figure B.3 on page VI in the Appendix.) Thus, it is not possible to clearly term the state at $(0.2 \pm 0.3)\,\mathrm{eV}$. Most likely, this peak yields overlap of the bulk direct transitions (BE_1) in (100) and the *Shockley*-type crystal-induced surface states (SS) originating from the electronic structure in these different directions. At higher energies, the image potential states (IS) of all lattice orientations can be seen, which is most probably superimposed by bulk features of the other lattice planes. The vacuum level is marked by a short black line.

C. Supporting Information on the Electronic Structure of Organic Semiconductors - Bulk-like Thin Films a Comparison

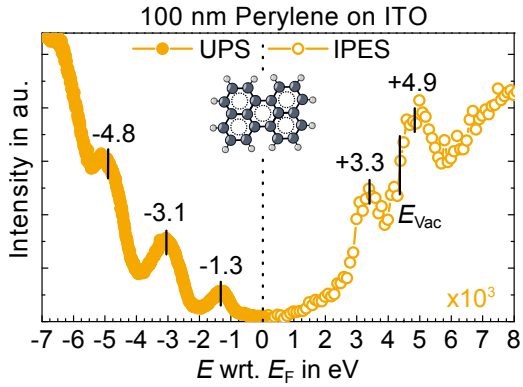

Figure C.1 | Combined UPS and IPE spectra showing the electronic structure of bulk-like Perylene: the occupied and unoccupied electronic states of a bulk-like Perylene thin film are measured with UPS and IPES, respectively. All spectra were recorded on a $100\,\mathrm{nm}$ Perylene layer grown on ITO. The intensity is plotted in dependence of the energy, whereas, the energy scale is referenced to the Fermi level E_F. In order to gain a better comparison, the intensity of the IPE spectrum was increased by a factor of 10^3. The position of the Fermi level is marked by a black dotted line. In addition, the vacuum level is marked by a short black line at $E_\mathrm{Vac} = (4.4 \pm 0.1)\,\mathrm{eV}$.
At an energy of $E_\mathrm{HOMO} = (-0.8 \pm 0.2)\,\mathrm{eV}$, the HOMO starts to rise. The energy difference between this onset and the vacuum level is the ionisation energy $IE = (5.2 \pm 0.2)\,\mathrm{eV}$ [244]. The HOMO is centred at $E = (-1.3 \pm 0.1)\,\mathrm{eV}$. The second and third features are centred at $(-3.1 \pm 0.1)\,\mathrm{eV}$ and $(-4.8 \pm 0.1)\,\mathrm{eV}$, respectively.
The LUMO starts to rise at an energy of $E_\mathrm{LUMO} = (+2.8 \pm 0.3)\,\mathrm{eV}$. The energy difference between E_LUMO and the vacuum level yields the electron affinity $EA = (1.7 \pm 0.3)\,\mathrm{eV}$. The LUMO is centred at $E = (+3.3 \pm 0.2)\,\mathrm{eV}$.

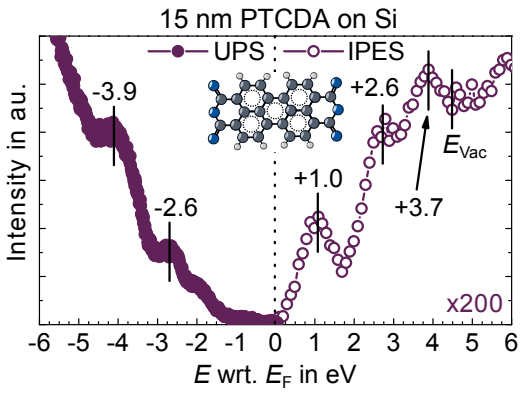

Figure C.2 | Combined UPS and IPE spectra showing the electronic structure of bulk-like PTCDA: the occupied and unoccupied electronic states of a bulk-like PTCDA thin film are measured with UPS and IPES, respectively. All spectra were recorded on a $15\,\mathrm{nm}$ PTCDA layer grown on a silicon substrate. The intensity is plotted in dependence of the energy, whereas, the energy scale is referenced to the Fermi level E_F. In order to gain a better comparison, the intensity of the IPE spectrum was increased by a factor of 200. The position of the Fermi level is marked by a black dotted line. In addition, the vacuum level is marked by a short black line at $E_\mathrm{Vac} = (4.5 \pm 0.1)\,\mathrm{eV}$.
At an energy of $E_\mathrm{HOMO} = (-2.1 \pm 0.2)\,\mathrm{eV}$, the HOMO starts to rise. The ionisation energy is determined to $IE = (6.6 \pm 0.2)\,\mathrm{eV}$. The HOMO is centred at $E = (-2.6 \pm 0.1)\,\mathrm{eV}$. The second and third features are centred at $(-3.9 \pm 0.1)\,\mathrm{eV}$ and $(-5.8 \pm 0.1)\,\mathrm{eV}$, respectively [208, 229, 242].
The LUMO starts to rise at an energy of $E_\mathrm{LUMO} = (+0.5 \pm 0.3)\,\mathrm{eV}$. The electron affinity is about $EA = (4.0 \pm 0.3)\,\mathrm{eV}$. The LUMO is centred at $E = (+1.0 \pm 0.2)\,\mathrm{eV}$. A second peak can be observed at $E = (+2.6 \pm 0.2)\,\mathrm{eV}$ [208, 229].

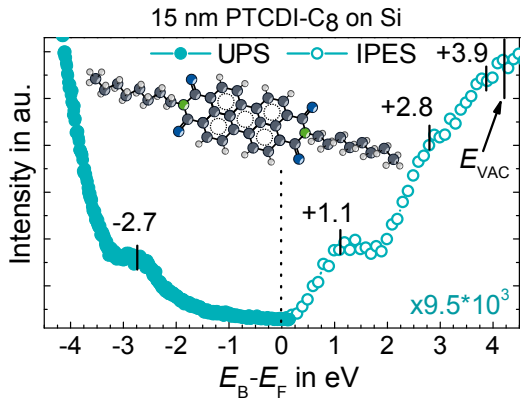

Figure C.3 | Combined UPS and IPE spectra showing the electronic structure of bulk-like PTCDI-C_8: the occupied and unoccupied electronic states of a bulk-like PTCDI-C_8 thin film are measured with UPS and IPES, respectively. All spectra were recorded on a $15\,\mathrm{nm}$ PTCDI-C_8 layer grown on a silicon substrate. The intensity is plotted in dependence of the energy, whereas, the energy scale is referenced to the Fermi level E_F. In order to gain a better comparison, the intensity of the IPE spectrum was increased by a factor of $9.5 * 10^3$. The position of the Fermi level is marked by a black dotted line. In addition, the vacuum level is marked by a short black line at $E_\mathrm{Vac} = (4.2 \pm 0.1)\,\mathrm{eV}$.
At an energy of $E_\mathrm{HOMO} = (-1.9 \pm 0.1)\,\mathrm{eV}$, the HOMO starts to rise. The ionisation energy is determined to $IE = (6.1 \pm 0.2)\,\mathrm{eV}$. The HOMO is centred at $E = (-2.7 \pm 0.1)\,\mathrm{eV}$. The second and third features are centred at $(-3.9 \pm 0.1)\,\mathrm{eV}$ and $(-4.5 \pm 0.1)\,\mathrm{eV}$, respectively.
The LUMO starts to rise at an energy of $E_\mathrm{LUMO} = (+0.5 \pm 0.3)\,\mathrm{eV}$. The electron affinity is about $EA = (3.7 \pm 0.3)\,\mathrm{eV}$. The LUMO is centred at $E = (+1.0 \pm 0.2)\,\mathrm{eV}$. A second peak can be observed at $E = (+2.8 \pm 0.2)\,\mathrm{eV}$ and a third one at $E = (+3.9 \pm 0.2)\,\mathrm{eV}$.

D. Supporting Information on the Interface Formation between DiMe-PTCDI Molecules and Silver

Growth of DiMe-PTCDI on Silver in the (Sub-)Monolayer Regime

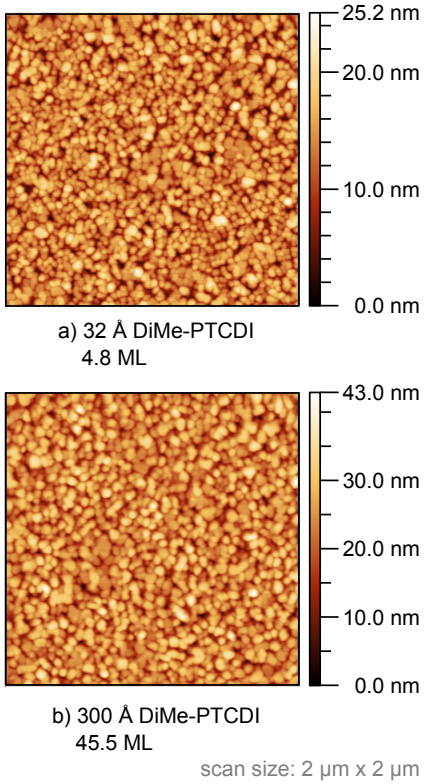

Figure D.1 | AFM images of the DiMe-PTCDI grown on silver: a), b) The scan of the size $(2 \times 2)\,\mu m^2$ shows the morphology of each sample surface in a colour coded image. The sample shown in a) displays the morphology of the 4.8 ML DiMe-PTCDI thin film grown on a silver substrate, while, b) represents that of a 45.5 ML DiMe-PTCDI thin film grown on a comparable substrate.

XPS Investigation of the Molecular Core Level – Silver Substrate

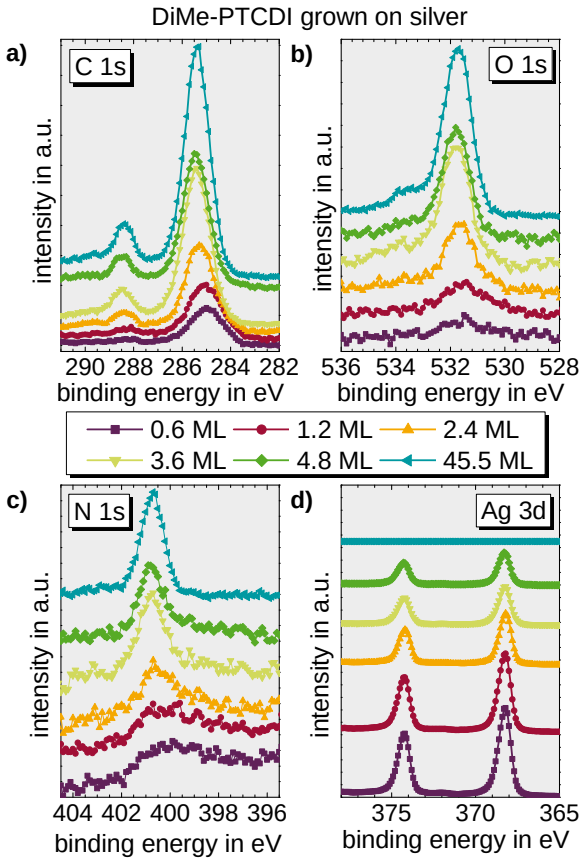

Figure D.2 | Core level spectra of DiMe-PTCDI grown on silver: a) - d) The intensity is plotted in dependence of the binding energy for every spectrum. Each spectrum is endowed with a vertical offset for better comparison. Each colour represents the measurement of a different film thickness.
a) Core level spectra of the C $1s$ revealing a shift from lower to higher binding energies with increasing film thickness.
b) & c) The O $1s$ as well as the N $1s$ spectra of the thinner films show a asymmetric broadening to the low energy side and a shift to lower binding energies, which is not visible for $\Theta_n > 2.4\,\mathrm{ML}$.
d) Core level spectra of the Ag $3d$ level of the metallic substrate illustrating the $3d5/2$ to $3d3/2$ doublet splitting due to spin-orbit coupling. No shift is observed.

Table D.1 | The elemental composition of DiMe-PTCDI grown on silver is determined for different film thicknesses from the high resolution scans C $1s$, N $1s$ and O $1s$ [16, 253]. Within the experimental error, all values match the theoretically expected elemental composition. (Since the cross section of hydrogen atoms is too small to be detected in XPS, the hydrogen atoms of DiMe-PTCDI are not visible.)

Θ_n \ atom	carbon	oxygen	nitrogen
Theory ($C_{26}H_{14}N_2O_4$)	81 %	13 %	6 %
0.6 ML	(80 ± 4) %	(10 ± 4) %	(10 ± 5) %
1.2 ML	(79 ± 4) %	(11 ± 4) %	(10 ± 5) %
2.4 ML	(82 ± 3) %	(10 ± 3) %	(8 ± 3) %
3.6 ML	(81 ± 2) %	(11 ± 2) %	(8 ± 2) %
4.8 ML	(81 ± 2) %	(12 ± 2) %	(7 ± 2) %
45.5 ML	(82 ± 2) %	(11 ± 2) %	(7 ± 2) %

E. Supporting Information on the Interface Formation between DiMe-PTCDI Molecules and Copper

Growth of DiMe-PTCDI on Copper in the (Sub-)Monolayer Regime

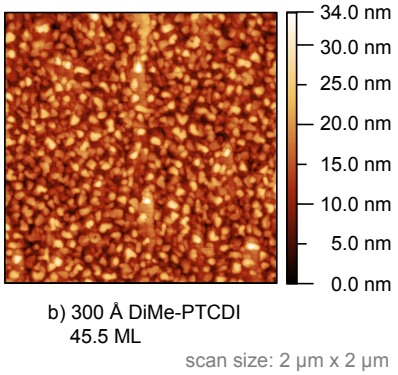

Figure E.1 | AFM images of 45.5 ML DiMe-PTCDI grown on copper: the scan of the size $(2 \times 2)\,\mu\mathrm{m}^2$ shows the morphology of the surface of a 45.5 ML DiMe-PTCDI thin film grown on copper in a colour coded image: the representing height can be inferred from the colour scale on the right side.

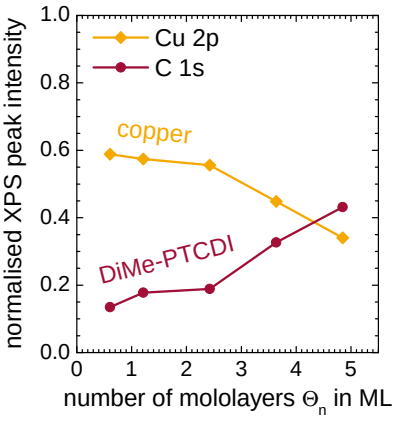

Figure E.2 | Normalised XPS peak intensity as a function of the number of DiMe-PTCDI monolayers: the plot displays the normalised XPS peak intensity $\left(I^{\mathrm{Cu}}/I^{\mathrm{Cu}}_{\mathrm{pristine}}\right)$ of the Cu $2p$ substrate peak (orange) and $\left(I^{\mathrm{C}}/I^{\mathrm{C}}_{\mathrm{bulk}}\right)$ the C $1s$ peak of DiMe-PTCDI (red) as a function of the number of monolayers Θ_{n}. While the curve representing the normalised intensity of the copper substrate decreases linearly with increasing film thickness, the signal caused by the DiMe-PTCDI thin film also increases linearly. This behaviour is comparable to the predicted evolution displayed in Figure 8.3 b).

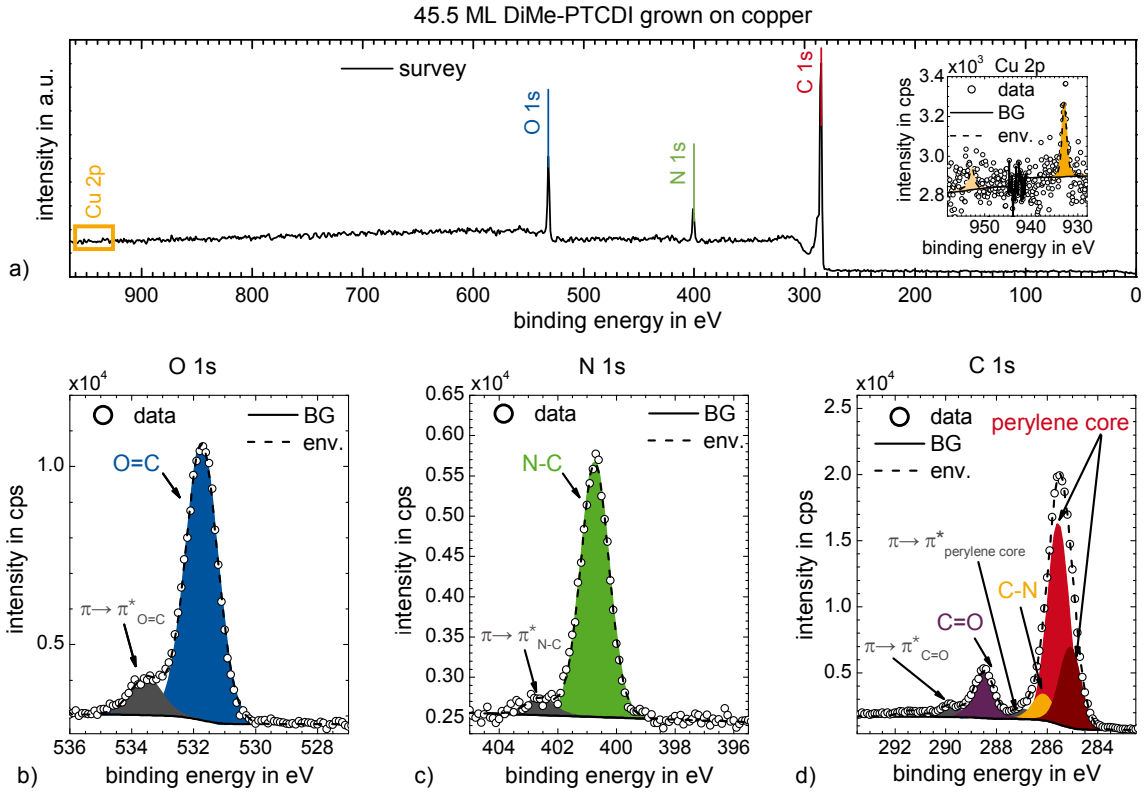

Figure E.3 | XPS spectra of bulk-like DiMe-PTCDI on a copper surface: a) - d) The intensity is plotted in dependence of the binding energy for every spectrum.
a) The survey spectrum confirms the presence of all expected elements. Only photoemission peaks of carbon, nitrogen and oxygen are observed. A high resolution scan of the Cu $2p$ core level hardly shows any XPS emission peaks (see inlay on the right side).
b) - d) High resolution scans of the O $1s$, N $1s$ and C $1s$ core levels:
b) The O $1s$ spectrum is fitted with two peaks. The first represents the oxygen doubly bound to the aromatic ring (O=C) and is centred at $E_B = (531.8 \pm 0.1)\,\mathrm{eV}$. The second peak is centred at $E_B = (533.6 \pm 0.1)\,\mathrm{eV}$ and results from an intramolecular charge transfer (shakeup process) from the aromatic part of the molecule acting like a donor to the accepting functional groups ($\pi \rightarrow \pi*_{O=C}$) [229].
c) The nitrogen bound in the methylimide group (N-C) is represented by a peak centred at $E_B = (400.9 \pm 0.1)\,\mathrm{eV}$ in the N $1s$ spectrum. Additionally, the peak of the $\pi \rightarrow \pi*_{N=C}$ shakeup process is identified at $E_B = (403.2 \pm 0.1)\,\mathrm{eV}$ [229].
d) In principal, the C $1s$ spectrum consists of two well-separated features. The main feature is centred at $(285.5 \pm 0.1)\,\mathrm{eV}$. It originates from the different carbon atoms of the aromatic part (perylene core $E_B = (285.1 \pm 0.2)\,\mathrm{eV}$ and $E_B = (285.6 \pm 0.2)\,\mathrm{eV}$) and the carbon atoms involved in the C-N bond ($E_B = (286.2 \pm 0.3)\,\mathrm{eV}$). The carbon atoms of the C=O bonds contribute to the second peak at $(288.5 \pm 0.1)\,\mathrm{eV}$. In addition, a peak resulting from shakeup processes are found at $E_B = (287.0 \pm 0.2)\,\mathrm{eV}$ for $\pi \rightarrow \pi*_{\text{perylene core}}$ and $E_B = (289.9 \pm 0.1)\,\mathrm{eV}$ for $\pi \rightarrow \pi*_{C=O}$ [229].

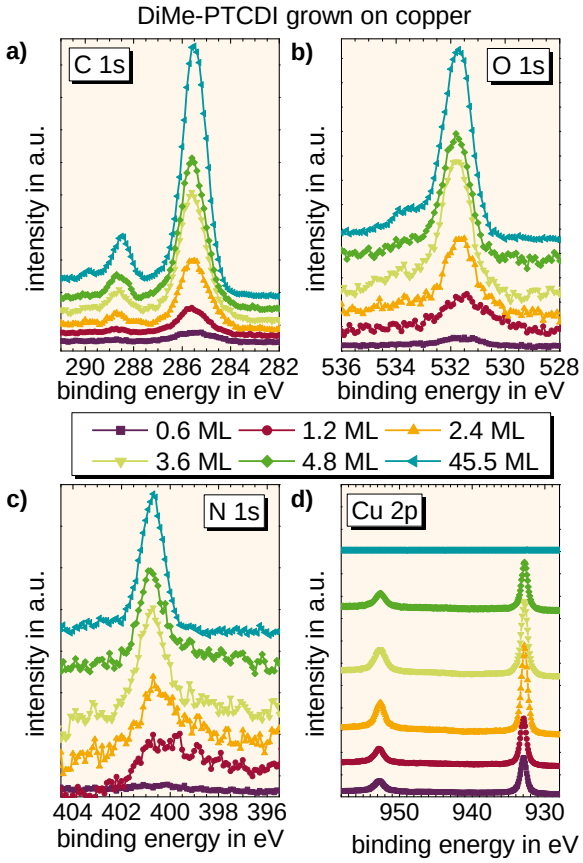

Figure E.4 | Core level spectra of DiMe-PTCDI grown on copper: a) - d) The intensity is plotted in dependence of the binding energy for every spectrum. Each spectrum is endowed with a vertical offset for better comparison. Each colour represents the measurement of a different film thickness.
a) While the peak position of the main peak of the C $1s$ core level spectrum representing the perylene core of DiMe-PTCDI and the C-N bonds stays constant, the peak representing the C=O bonds shifts from higher to lower binding energies with increasing film thickness.
b) The O $1s$ core level spectra hardly reveal any shift or an asymmetric broadening to the low energy side.
c) The N $1s$ spectra of the thinner films show a asymmetric broadening to the low energy side and a shift to lower binding energies.
d) Core level spectra of the Cu $2p$ level of the metallic substrate illustrating the $2p3/2$ to $2p1/2$ doublet splitting due to spin-orbit coupling. No shift is observed.

Table E.1 | The elemental composition of DiMe-PTCDI grown on copper is determined for different film thicknesses from the high resolution scans C $1s$, N $1s$ and O $1s$ [16, 253]. Within the experimental error, all values match the theoretically expected elemental composition. (Since the cross section of hydrogen atoms is too small to be detected in XPS, the hydrogen atoms of DiMe-PTCDI are not visible.)

atom / Θ_n	carbon	oxygen	nitrogen
Theory ($C_{26}H_{14}N_2O_4$)	81 %	13 %	6 %
0.6 ML	(81 ± 4) %	(11 ± 4) %	(8 ± 5) %
1.2 ML	(80 ± 4) %	(13 ± 4) %	(7 ± 5) %
2.4 ML	(82 ± 3) %	(12 ± 3) %	(6 ± 3) %
3.6 ML	(80 ± 2) %	(13 ± 2) %	(8 ± 2) %
4.8 ML	(82 ± 2) %	(11 ± 2) %	(7 ± 2) %
45.5 ML	(81 ± 2) %	(12 ± 2) %	(7 ± 2) %

List of Acronyms

2D	two-dimensional
3D	three-dimensional
AFM	atomic force microscopy or atomic force microscope
AR-IPES	angle-resolved inverse photoemission spectroscopy
ARPES	angle-resolved photoelectron spectroscopy
BaO	barium oxide
BIS	bremsstrahlung isochromat spectroscopy
CaF_2	calcium fluoride
CF	conflat
DiMe-PTCDI	N,N'-dimethyl-3,4,9,10-perylene dicarboximide
DOS	density of states
EGPS-1022	electron gun power supply
ELG-2	electron gun
FWHM	full width half maximum
HOMO	highest occupied molecular orbital
impf	inelastic mean free path
integral PHD	integral pulse height distribution
IPE	inverse photoemission
IPE-AC	inverse photoemission analysis chamber

IPES	inverse photoemission spectroscopy
ITO	In_2O_3:Sn, called tin-doped indium oxide or indium tin oxide
LED	light-emitting diode
LEED	low-energy electron diffraction
LiF	lithium fluoride
LUMO	lowest unoccupied molecular orbital
MO	molecular orbital
MSV mode	mean square voltage mode
NFE	nearly-free-electron
OMBD	organic molecular beam deposition
ORPHEUS	organic photoemission ultra-high vacuum system
PE	photoelectron
PE process	photoelectron process
Perylene	dibenz[de,kl]anthracene
PES	photoelectron spectroscopy
PTCDA	perylene-3,4,9,10-tetracarboxylic dianhydride
PTCDI-C_8	N,N'-dioctyl-3,4,9,10-perylene dicarboximide
SHC	sample handling chamber
SrF_2	strontium fluoride
TSP	titanium sublimation pump
TTL	transistor–transistor logic
UHV	ultra-high vacuum
UPS	ultra-violet photoelectron spectroscopy
XPS	X-ray photoelectron spectroscopy

List of Figures

1.1 Working principle of an OLED stack . . . 2
1.2 Chemical structures of the perylene derivatives PTCDA, DiMe-PTCDI and PTCDI-C_8 . . . 6

2.1 Schematic illustration of a PES experiment . . . 11
2.2 Illustration of the energetic processes in a photoelectron measurement . . . 12
2.3 Escape condition for the photoexcited electron . . . 14
2.4 Hemispherical energy analyser (HSA) . . . 17

3.1 Schematic illustration of an IPES experiment . . . 20
3.2 Energetic diagram of the IPE process . . . 25
3.3 Model of surface states by J. B. Pendry and P. M. Echenique . . . 30

4.1 3D model of the IPE spectrometer . . . 43
4.2 3D model of the sample handling camber . . . 44
4.3 3D model of the sample storage . . . 46
4.4 3D model of the tools used to move a single sample holder . . . 47
4.5 3D model of the manipulator head of the IPE spectrometer . . . 47
4.6 3D model of the analysis camber of the IPE spectrometer . . . 48
4.7 Technical drawing of the length and safety distances . . . 50
4.8 3D model of the electron gun in cross section . . . 51
4.9 Schematic drawing of the photon bandpass detector . . . 53
4.10 Sketch of the filling system of the photon bandpass detector . . . 54
4.11 3D model of interior of the IPE analysis camber . . . 55

5.1 Block diagram of the electron gun ELG-2 . . . 58
5.2 Emission current of the electron gun as a function of the anode voltage . . . 60
5.3 Beam profile of the electron beam in x-direction . . . 62
5.4 2D colour plot of the electron beam as a function of the sample current . . . 63
5.5 Schematic drawing of the determination of the electron beam divergence . . . 63
5.6 Coaxial cylindrical counter and the shape of the applied electrical field . . . 66
5.7 Time development of the pulse in a gaseous ionisation detector . . . 67
5.8 Time evolution of a Townsend avalanche . . . 69
5.9 The different regions of operation of gas-filled detectors . . . 73

5.10 Generation of discrete Townsend avalanches in a proportional counter 74
5.11 The Geiger discharge 75
5.12 Achieving one data point of a counting curve 77
5.13 Exemplary plot of a counting curve of a Geiger-Müller counter 78
5.14 Overview of all measured counting curves for the Geiger-Müller counter 80
5.15 Stability test of the Geiger-Müller counter 81
5.16 Dark count measurement for the Geiger- Müller counter 82
5.17 Exemplary plot of a counting curve of a proportional counter 83
5.18 Overview of all measured counting curves for the proportional counter 84
5.19 Normalised integral pulse height distribution. 85
5.20 Determination of the resolution of the IPE spectrometer 89

6.1 Combined UPS and IPE spectra showing the electronic structure of a well-ordered and highly textured gold (111) thin film 95
6.2 Projected DOS of gold 96
6.3 Band structure of gold 97
6.4 Combined UPS and IPE spectra showing the electronic structure of a well-ordered and highly textured copper (111) thin film 99
6.5 Projected density of states and three dimensional band structure of copper . . 100
6.6 Energy dispersion $E(k_{||})$ of the *Shockley*-type crystal-induced surface state of copper (111) 101

7.1 sp^2 hybridisation in the case of carbon 103
7.2 Electronic system of the benzene ring 104
7.3 Evolution of the electronic structure from a single molecule to an organic solid 105
7.4 Combined UPS and IPE spectra showing the electronic structure of bulk-like DiMe-PTCDI 108
7.5 Comparison of the electronic structure of perylene and substituted perylenes . 112
7.6 Comparison of electronic and optical gab of perylene and substituted perylenes 114

8.1 AFM images of the DiMe-PTCDI thickness series grown on silver 119
8.2 AFM statistics of the DiMe-PTCDI thickness series grown on silver 120
8.3 Schematic representing the behaviour of XPS line intensities of the deposited and the substrate as a function of the amount of deposited material 121
8.4 Normalised XPS peak intensity as a function of the number of DiMe-PTCDI monolayers - silver substrate 122
8.5 XPS spectra of bulk-like DiMe-PTCDI on a silver surface 124
8.6 XPS spectra of 0.6 ML of DiMe-PTCDI on a silver surface 126
8.7 Core level emission peak positions – silver substrate 128
8.8 UPS/IPES spectra of a sub-monolayer in comparison with bulk-like DiMe-PTCDI 129
8.9 Thickness-dependent UPS and IPE spectra of DiMe-PTCDI grown on silver . . 131
8.10 Evolution of the work function of DiMe-PTCDI with increasing number of monolayers - silver substrates 132

8.11 AFM images of the DiMe-PTCDI thickness series grown on copper 133
8.12 AFM statistics of the DiMe-PTCDI thickness series grown on copper 134
8.13 XPS spectra of 0.6 ML of DiMe-PTCDI grown on a copper surface 136
8.14 Core level emission peak positions – copper substrate 137
8.15 Thickness-dependent UPS and IPE spectra of DiMe-PTCDI grown on copper . 138
8.16 Evolution of the work function of DiMe-PTCDI with increasing number of monolayers - silver substrates 139

A.1 Stability test of the proportional counter III
A.2 Dark count measurement for the proportional counter IV

B.1 $\Theta 2\Theta$-XRD pattern of a well-ordered and highly textured 200 nm gold thin film V
B.2 $\Theta 2\Theta$-XRD pattern of a well-ordered and highly textured 200 nm copper thin film VI
B.3 $\Theta 2\Theta$-XRD pattern of a well-ordered and highly textured 200 nm silver thin film VI
B.4 AR-IPE spectra of a well-ordered and highly textured copper (111) thin film as a function of the electron incidence angle Θ VII
B.5 IPE spectrum of a well-ordered and highly textured silver thin film with preferred direction in (111) VIII

C.1 Combined UPS and IPE spectra showing the electronic structure of bulk-like Perylene IX
C.2 Combined UPS and IPE spectra showing the electronic structure of bulk-like PTCDA X
C.3 Combined UPS and IPE spectra showing the electronic structure of bulk-like PTCDI-C_8 XI

D.1 AFM images of the DiMe-PTCDI grown on silver XIII
D.2 Core level spectra of DiMe-PTCDI grown on silver XIV

E.1 AFM image of 45.5 ML DiMe-PTCDI grown on copper XV
E.2 Normalised XPS peak intensity as a function of the number of DiMe-PTCDI monolayers - copper substrate XVI
E.3 XPS spectra of bulk-like DiMe-PTCDI on a copper surface XVII
E.4 Core level spectra of DiMe-PTCDI grown on copper XVIII

List of Tables

3.1 Conceptual comparison of PES and IPES 19
3.2 Energies of surface sates and image potential states 34
3.3 Time needed for building a monolayer at room temperature for different pressures of air, water and hydrogen 38

5.1 Control and driving voltages of the electron gun 59
5.2 Optimal operation parameters found for the Geiger-Müller and the proportional counter 87

7.1 Electronic structure of various bulk-like organic semiconductors 111

8.1 Evolution of the electronic structure of DiMe-PTCDI with increasing with increasing number of monolayers - silver substrate 131
8.2 Evolution of the electronic structure of DiMe-PTCDI with increasing number of monolayers - copper substrate 139

9.1 Operation parameters of the electron gun 145

D.1 Elemental composition of DiMe-PTCDI determined for different film thicknesses - silver substrate XIV

E.1 Elemental composition of DiMe-PTCDI determined for different film thicknesses - copper substrate XVIII

Bibliography

[1] A. Bernanose, "Electroluminescence of organic compounds," *British Journal of Applied Physics*, vol. 6, no. S4, p. S54, 1955. [Online]. Available: http://dx.doi.org/10.1088/0508-3443/6/S4/319 Cited on page 1.

[2] D. Kearns and M. Calvin, "The photovoltaic effect and photoconductivity in laminated organicsystems," *Journal of Chemical Physics*, vol. 29, no. UCRL–8441, 1958. [Online]. Available: http://dx.doi.org/10.1063/1.1744619 Cited on page 1.

[3] C. W. Tang, "Two-layer organic photovoltaic cell," *Applied Physics Letters*, vol. 48, no. 2, pp. 183–185, 1986. [Online]. Available: http://dx.doi.org/10.1063/1.96937 Cited on page 1.

[4] C. W. Tang and S. A. VanSlyke, "Organic electroluminescent diodes," *Applied physics letters*, vol. 51, no. 12, pp. 913–915, 1987. [Online]. Available: http://dx.doi.org/10.1063/1.98799 Cited on page 1.

[5] H. Koezuka, A. Tsumura, and T. Ando, "Field-effect transistor with polythiophene thin film," *Synthetic Metals*, vol. 18, no. 1-3, pp. 699–704, 1987. [Online]. Available: http://dx.doi.org/10.1063/1.96937 Cited on page 1.

[6] (visited: 06.06.2016) The nobel prize in chemistry 2000. [Online]. Available: www.nobelprize.org/nobelprizes/chemistry/laureates/2000/ Cited on page 1.

[7] (visited: 25.07.2016) CES 2016: Hands-on with LG's roll-up flexible screen. [Online]. Available: http://www.bbc.com/news/technology-35230043 Cited on page 1.

[8] (visited: 25.07.2016) 2016: Samsung Flexible Phone prototype unveiled at CES + Samsung galaxy S8 or Note 6 prediction? [Online]. Available: https://www.youtube.com/watch?v=fvLiBtQCIKg Cited on page 1.

[9] S. Mlot. (visited: 01.09.2016) Report: Samsung flexible phones coming in 2017. [Online]. Available: http://uk.pcmag.com/smartphones/82035/news/report-samsung-flexible-phones-coming-in-2017 Cited on page 1.

[10] J. Lee. (visited: 01.09.2016) Samsung may release phones with bendable screens in 2017. [Online]. Available: http://www.bloomberg.com/news/articles/2016-06-07/samsung-said-to-consider-phones-with-bendable-screens-for-2017-ip4tgwz9

[11] P. Briden. (visited: 01.09.2016) Samsung galaxy x launching mwc 2017 will change everything: Flexible smartphones are coming. [Online]. Available: http://www.knowyourmobile.com/mobile-phones/samsung-galaxy-x/23579/samsung-galaxy-x-samsung-galaxy-s8-specs-price-release-date-rumours-features-detailed-flexible-fold Cited on page 1.

[12] IDTechEx. (visited: 06.06.2016) Printed electronics intelligence services. [Online]. Available: http://www.idtechex.com/research/topics/printed-flexible-organic-electronics.asp Cited on page 1.

[13] R. Das, P. Harrop, and IDTechEx. (visited: 06.06.2016) Printed, organic & flexible electronics forecasts, players & opportunities 2016-2026. [Online]. Available: http://www.idtechex.com/research/reports/printed-organic-and-flexible-electronics-forecasts-players-and-opportunities-2016-2026-000457.asp Cited on page 1.

[14] G. Chansin, K. Ghaffarzadeh, H. Zervos, and IDTechEx. (visited: 06.06.2016) Oled display forecasts 2016-2026: The rise of plastic and flexible displays. [Online]. Available: http://www.idtechex.com/research/reports/oled-display-forecasts-2016-2026-the-rise-of-plastic-and-flexible-displays-000477.asp

[15] K. Ghaffarzadeh, N. Bardsley, and IDTechEx. (visited: 06.06.2016) Oled lighting opportunities 2016-2026: Forecasts, technologies, players. [Online]. Available: http://www.idtechex.com/research/reports/oled-lighting-opportunities-2016-2026-forecasts-technologies-players-000472.asp Cited on page 1.

[16] D. Meyer, "Surface functionalization with amino based self-assembled monolayers : tailoring electrode/molecule interfaces for organic electronics," Dissertation, RWTH Aachen University, 2015. [Online]. Available: https://publications.rwth-aachen.de/record/481561 Cited on pages 2, 3, 14, 17, 93, 95, 123, 140, 149, XIV, and XVIII.

[17] N. Koch, "Electronic structure of interfaces with conjugated organic materials," *physica status solidi (RRL)-Rapid Research Letters*, vol. 6, no. 7, pp. 277–293, 2012. [Online]. Available: http://dx.doi.org/10.1002/pssr.201206208 Cited on pages 2, 3, 106, 114, and 117.

[18] M. Schwoerer and H. C. Wolf, *Organic molecular solids*. John Wiley & Sons, 2007. Cited on pages 2, 104, and 105.

[19] N. Koch, "Organic electronic devices and their functional interfaces," *ChemPhysChem*, vol. 8, no. 10, pp. 1438–1455, 2007. [Online]. Available: http://dx.doi.org/10.1002/cphc.200700177 Cited on pages 2 and 117.

[20] K. Hipps, "It's all about contacts," *Science*, vol. 294, no. 5542, p. 536, 2001. [Online]. Available: http://dx.doi.org/10.1126/science.1065708 Cited on pages 2 and 117.

[21] F. Flores and J. Ortega, "Basic theory of the molecule–metal interface," *The Molecule-Metal Interface*, pp. 15–49, 2013. [Online]. Available: http://dx.doi.org/10.1002/9783527653171.ch2 Cited on pages 3 and 117.

[22] N. W. Ashcroft and D. N. Mermin, *Festkörperphysik*. Oldenbourg Verlag, 2012. Cited on pages 3, 60, and 117.

[23] W. R. Salaneck, K. Seki, A. Kahn, and J.-J. Pireaux, *Conjugated Polymer and Molecular Interfaces: Science and Technology for Photonic and Optoelectronic Application*. CRC Press, 2001. Cited on page 3.

[24] A. P. Schulz, "Interface dipole formation in organic surface functionalizations : tailoring metal contacts for organic optoelectronic devices," Dissertation, RWTH Aachen University, 2013. [Online]. Available: http://publications.rwth-aachen.de/record/210329 Cited on page 3.

[25] H. Yoshida, "Near-ultraviolet inverse photoemission spectroscopy using ultra-low energy electrons," *Chemical Physics Letters*, vol. 539, pp. 180–185, 2012. [Online]. Available: http://dx.doi.org/10.1016/j.cplett.2012.04.058 Cited on pages 3 and 4.

[26] H. Lüth, *Solid surfaces, interfaces and thin films*. Springer, 2001, vol. 4. Cited on pages 3, 11, 17, 94, 96, 97, 119, 121, 122, and 134.

[27] N. V. Smith, "Inverse photoemission," *Reports on Progress in Physics*, vol. 51, no. 9, p. 1227, 1988. [Online]. Available: http://dx.doi.org/10.1088/0034-4885/51/9/003 Cited on pages 4, 22, 23, 24, 28, 29, 35, and 36.

[28] P. Johnson and S. Hulbert, "Inverse photoemission," *Review of Scientific Instruments*, vol. 61, no. 9, p. 2277, 1990. [Online]. Available: http://dx.doi.org/10.1063/1.1141352 Cited on pages 4, 36, 37, and 64.

[29] R. Stiepel, R. Ostendorf, C. Benesch, and H. Zacharias, "Vacuum ultraviolet photon detector with improved resolution for inverse photoemission spectroscopy," *Review of scientific instruments*, vol. 76, no. 6, p. 063109, 2005. [Online]. Available: http://dx.doi.org/10.1063/1.1928192 Cited on pages 4, 52, 63, 65, 87, 88, and 144.

[30] A. Kahn, N. Koch, and W. Gao, "Electronic structure and electrical properties of interfaces between metals and π-conjugated molecular films," *Journal of Polymer Science Part B: Polymer Physics*, vol. 41, no. 21, pp. 2529–2548, 2003. [Online]. Available: http://dx.doi.org/10.1002/polb.10642 Cited on pages 4 and 5.

[31] H. Ishii, K. Sugiyama, E. Ito, and K. Seki, "Energy level alignment and interfacial electronic structures at organic/metal and organic/organic interfaces," *Advanced Materials*, vol. 11, no. 8, pp. 605–625, 1999. [Online]. Available: http://dx.doi.org/10.1002/(SICI)1521-4095(199906)11:8<605::AID-ADMA605>3.0.CO;2-Q

[32] G. Heimel, S. Duhm, I. Salzmann, A. Gerlach, A. Strozecka, J. Niederhausen, C. Bürker, T. Hosokai, I. Fernandez-Torrente, G. Schulze, S. Winkler, A. Wilke, R. Schlesinger, J. Frisch, B. Bröker, A. Vollmer, B. Detlefs, J. Pflaum, S. Kera,

K. J. Franke, N. Ueno, J. I. Pascual, F. Schreiber, and N. Koch, “Charged and metallic molecular monolayers through surface-induced aromatic stabilization,” *Nature chemistry*, vol. 5, no. 3, pp. 187–194, 2013. [Online]. Available: http://dx.doi.org/10.1038/nchem.1572 Cited on pages 5, 125, 126, 127, 130, 132, 133, 135, 139, 140, 147, 148, and 149.

[33] F. P. Netzer and M. G. Ramsey, “Structure and orientation of organic molecules on metal surfaces,” *Critical Reviews in Solid State and Material Sciences*, vol. 17, no. 5, pp. 397–475, 1992. [Online]. Available: http://dx.doi.org/10.1080/10408439208243753

[34] S. Braun, W. R. Salaneck, and M. Fahlman, “Energy-level alignment at organic/metal and organic/organic interfaces,” *Advanced Materials*, vol. 21, no. 14-15, pp. 1450–1472, 2009. [Online]. Available: http://dx.doi.org/10.1002/adma.200802893 Cited on pages 4 and 5.

[35] G. Witte, S. Lukas, P. S. Bagus, and C. Wöll, “Vacuum level alignment at organic/metal junctions: "Cushion" effect and the interface dipole,” *Applied Physics Letters*, vol. 87, no. 26, p. 263502, 2005. [Online]. Available: http://dx.doi.org/10.1063/1.2151253 Cited on page 5.

[36] N. Koch, N. Ueno, and A. T. S. Wee, *The molecule-metal interface*. John Wiley & Sons, 2013. Cited on pages 5, 105, 106, and 114.

[37] K. Seki, E. Ito, and H. Ishii, “Energy level alignment at organic/metal interfaces studied by UV photoemission,” *Synthetic Metals*, vol. 91, no. 1, pp. 137–142, 1997. [Online]. Available: http://dx.doi.org/10.1016/S0379-6779(98)80075-1 Cited on page 5.

[38] S. Kera, Y. Yabuuchi, H. Yamane, H. Setoyama, K. Okudaira, A. Kahn, and N. Ueno, “Impact of an interface dipole layer on molecular level alignment at an organic-conductor interface studied by ultraviolet photoemission spectroscopy,” *Physical Review B*, vol. 70, no. 8, p. 085304, 2004. [Online]. Available: http://dx.doi.org/10.1103/PhysRevB.70.085304 Cited on page 5.

[39] X. Crispin, V. Geskin, A. Crispin, J. Cornil, R. Lazzaroni, W. R. Salaneck, and J.-L. Bredas, “Characterization of the interface dipole at organic/metal interfaces,” *Journal of the American Chemical Society*, vol. 124, no. 27, pp. 8131–8141, 2002. [Online]. Available: http://dx.doi.org/10.1021/ja025673r Cited on page 5.

[40] N. Koch, S. Duhm, J. P. Rabe, A. Vollmer, and R. L. Johnson, “Optimized hole injection with strong electron acceptors at organic-metal interfaces,” *Physical review letters*, vol. 95, no. 23, p. 237601, 2005. [Online]. Available: http://dx.doi.org/10.1103/PhysRevLett.95.237601 Cited on page 5.

[41] S. Duhm, A. Gerlach, I. Salzmann, B. Bröker, R. Johnson, F. Schreiber, and N. Koch, “PTCDA on Au (111), Ag (111) and Cu (111): correlation of interface charge transfer to bonding distance,” *Organic Electronics*, vol. 9, no. 1, pp. 111–118, 2008. [Online]. Available: http://dx.doi.org/10.1016/j.orgel.2007.10.004 Cited on pages 5, 6, 125, 127, 130, 132, 139, 140, 147, and 149.

[42] G. Mercurio, O. Bauer, M. Willenbockel, N. Fairley, W. Reckien, C. Schmitz, B. Fiedler, S. Soubatch, T. Bredow, M. Sokolowski, and F. S. Tautz, "Adsorption height determination of nonequivalent C and O species of PTCDA on Ag (110) using x-ray standing waves," *Physical Review B*, vol. 87, no. 4, p. 045421, 2013. [Online]. Available: http://dx.doi.org/10.1103/PhysRevB.87.045421

[43] S. Henze, O. Bauer, T.-L. Lee, M. Sokolowski, and F. Tautz, "Vertical bonding distances of PTCDA on Au (111) and Ag (111): Relation to the bonding type," *Surface Science*, vol. 601, no. 6, pp. 1566–1573, 2007. [Online]. Available: http://dx.doi.org/10.1016/j.susc.2007.01.020

[44] A. Hauschild, K. Karki, B. Cowie, M. Rohlfing, F. Tautz, and M. Sokolowski, "Molecular distortions and chemical bonding of a large π-conjugated molecule on a metal surface," *Physical review letters*, vol. 94, no. 3, p. 036106, 2005. [Online]. Available: http://dx.doi.org/10.1103/PhysRevLett.94.036106

[45] A. Gerlach, S. Sellner, F. Schreiber, N. Koch, and J. Zegenhagen, "Substrate-dependent bonding distances of PTCDA: A comparative x-ray standing-wave study on Cu (111) and Ag (111)," *Physical Review B*, vol. 75, no. 4, p. 045401, 2007. [Online]. Available: http://dx.doi.org/10.1103/PhysRevB.75.045401 Cited on pages 5, 125, 132, 140, 147, and 149.

[46] K. Yonezawa, Y. Suda, S. Yanagisawa, T. Hosokai, K. Kato, T. Yamaguchi, H. Yoshida, N. Ueno, and S. Kera, "Charge transfer states appear in the π-conjugated pure hydrocarbon molecule on Cu (111)," *Applied Physics Express*, vol. 9, no. 4, p. 045201, 2016. [Online]. Available: http://dx.doi.org/10.7567/APEX.9.045201 Cited on page 5.

[47] T. Hosokai, K. Yonezawa, K. Kato, R. Makino, J. Yang, K. R. Koswattage, A. Gerlach, F. Schreiber, N. Ueno, and S. Kera, "Structural requirements for surface-induced aromatic stabilization," in *Symposium GG – Surface/Interface Characterization and Renewable Energy*, ser. MRS Proceedings, vol. 1647, 2014, pp. mrsf13–1647–gg01–03 (6 pages). [Online]. Available: http://journals.cambridge.org/article_S1946427414003480 Cited on page 5.

[48] H. Ishii, K. Kudo, T. Nakayama, and N. Ueno, *Electronic Processes in Organic Electronics*. Springer, 2015. Cited on page 5.

[49] M.-C. Lu, R.-B. Wang, A. Yang, and S. Duhm, "Pentacene on Au (111), Ag (111) and Cu (111): From physisorption to chemisorption," *Journal of Physics: Condensed Matter*, vol. 28, no. 9, p. 094005, 2016. [Online]. Available: http://dx.doi.org/10.1088/0953-8984/28/9/094005 Cited on page 5.

[50] D. Park, S. Kang, H. Kim, M. Jang, M. Noh, K.-H. Yoo, C. Whang, Y. Lee, and M. Lee, "Characteristics of perylene-based organic thin-film transistor with octadecyltrichlorosilane monolayer," *Journal of Vacuum Science & Technology B*, vol. 23, no. 3, pp. 926–929, 2005. [Online]. Available: http://dx.doi.org/10.1116/1.1924418 Cited on page 6.

[51] C. Effertz, S. Lahme, P. Schulz, I. Segger, M. Wuttig, A. Classen, and C. Bolm, "Design of novel dielectric surface modifications for perylene thin-film transistors," *Advanced Functional Materials*, vol. 22, no. 2, pp. 415–420, 2012. [Online]. Available: http://dx.doi.org/10.1002/adfm.201101299 Cited on pages 6 and 113.

[52] V. Kozlov, G. Parthasarathy, P. Burrows, S. Forrest, Y. You, and M. Thompson, "Optically pumped blue organic semiconductor lasers," *Applied physics letters*, vol. 72, no. 2, pp. 144–146, 1998. [Online]. Available: http://dx.doi.org/10.1063/1.120669 Cited on page 6.

[53] W. Herbst and K. Hunger, *Industrielle Organische Pigmente: Herstellung, Eigenschaften, Anwendung*. John Wiley & Sons, 2009. Cited on page 6.

[54] J.-P. Meyer, D. Schlettwein, D. Wöhrle, and N. Jaeger, "Charge transport in thin films of molecular semiconductors as investigated by measurements of thermoelectric power and electrical conductivity," *Thin Solid Films*, vol. 258, no. 1, pp. 317–324, 1995. [Online]. Available: http://dx.doi.org/10.1016/0040-6090(94)06369-9 Cited on page 6.

[55] H. Hoppea and N. S. Sariciftci, "Organic solar cells: An overview," *J. Mater. Res*, vol. 19, no. 7, p. 1925, 2004. [Online]. Available: http://dx.doi.org/10.1557/JMR.2004.0252

[56] D. Lehmann and D. R. Zahn, "The electrical and dielectrical behavior of n-conducting perylene tetracarboxylic diimide derivatives," *Applied Physics A*, vol. 95, no. 1, pp. 203–207, 2009. [Online]. Available: ttp://dx.doi.org/10.1007/s00339-008-5020-2 Cited on page 6.

[57] S. Karak, V. Reddy, S. Ray, and A. Dhar, "Organic photovoltaic devices based on pentacene/N,N'-dioctyl-3,4,9,10-perylenedicarboximide heterojunctions," *Organic electronics*, vol. 10, no. 5, pp. 1006–1010, 2009. [Online]. Available: http://dx.doi.org/10.1016/j.orgel.2009.04.006 Cited on page 6.

[58] N. Hiroshiba, R. Hayakawa, T. Chikyow, K. Matsuishi, and Y. Wakayama, "Ambipolar carrier transport in hetero-layered organic transistors consisting of quaterrylene and N,N'-dioctyl-3,4,9,10-perylenedicarboximide," *Organic Electronics*, vol. 12, no. 8, pp. 1336–1340, 2011. [Online]. Available: http://dx.doi.org/10.1016/j.orgel.2011.05.001

[59] N. Hiroshiba, R. Hayakawa, M. Petit, T. Chikyow, K. Matsuishi, and Y. Wakayama, "Structural analysis and transistor properties of hetero-molecular bilayers," *Thin Solid Films*, vol. 518, no. 2, pp. 441–443, 2009. [Online]. Available: http://dx.doi.org/10.1016/j.tsf.2009.07.050 Cited on page 6.

[60] F. Tautz, "Structure and bonding of large aromatic molecules on noble metal surfaces: The example of PTCDA," *Progress in Surface Science*, vol. 82, no. 9, pp. 479–520, 2007. [Online]. Available: http://dx.doi.org/10.1016/j.progsurf.2007.09.001 Cited on page 6.

[61] M. Rohlfing, R. Temirov, and F. S. Tautz, "Adsorption structure and scanning tunneling data of a prototype organic-inorganic interface: PTCDA on Ag (111)," *Physical Review B*, vol. 76, no. 11, p. 115421, 2007. [Online]. Available: http://dx.doi.org/10.1103/PhysRevB.76.115421

[62] S. Krause, M. Casu, A. Schöll, and E. Umbach, "Determination of transport levels of organic semiconductors by UPS and IPS," *New Journal of Physics*, vol. 10, no. 8, p. 085001, 2008. [Online]. Available: http://dx.doi.org/10.1088/1367-2630/10/8/085001 Cited on pages 88, 109, 110, 113, and 144.

[63] Y. Zou, L. Kilian, A. Schöll, T. Schmidt, R. Fink, and E. Umbach, "Chemical bonding of PTCDA on Ag surfaces and the formation of interface states," *Surface Science*, vol. 600, no. 6, pp. 1240–1251, 2006. [Online]. Available: http://dx.doi.org/10.1016/j.susc.2005.12.050 Cited on pages 117, 127, 132, 138, 140, 147, and 149.

[64] M. Häming, A. Schöll, E. Umbach, and F. Reinert, "Adsorbate-substrate charge transfer and electron-hole correlation at adsorbate/metal interfaces," *Physical Review B*, vol. 85, no. 23, p. 235132, 2012. [Online]. Available: https://doi.org/10.1103/PhysRevB.85.235132 Cited on page 6.

[65] H. Hertz, "Ueber einen einfluss des ultravioletten lichtes auf die electrische entladung," *Annalen der Physik*, vol. 267, no. 8, pp. 983–1000, 1887. [Online]. Available: http://dx.doi.org/10.1002/andp.18872670827 Cited on page 11.

[66] A. Einstein, "Über einen die erzeugung und verwandlung des lichtes betreffenden heuristischen gesichtspunkt," *Annalen der physik*, vol. 322, no. 6, pp. 132–148, 1905. [Online]. Available: http://dx.doi.org/10.1002/andp.200590004 Cited on pages 11 and 13.

[67] S. Hüfner, *Photoelectron spectroscopy: principles and applications - Third Edition*. Springer Science & Business Media, 2003. Cited on pages 11, 14, 28, 29, 30, 34, 93, 94, 96, 97, 98, 101, and 110.

[68] I. Adawi, "Theory of the surface photoelectric effect for one and two photons," *Physical Review*, vol. 134, no. 3A, p. A788, 1964. [Online]. Available: http://dx.doi.org/10.1103/PhysRev.134.A788 Cited on page 13.

[69] J. Endriz, "Calculation of the surface photoelectric effect," *Physical Review B*, vol. 7, no. 8, p. 3464, 1973. [Online]. Available: http://dx.doi.org/10.1103/PhysRevB.7.3464 Cited on page 13.

[70] B. Feuerbacher and R. Willis, "Photoemission and electron states at clean surfaces," *Journal of Physics C: Solid State Physics*, vol. 9, no. 2, p. 169, 1976. Cited on page 13.

[71] C. Berglund and W. Spicer, "Photoemission studies of copper and silver: experiment," *Physical Review*, vol. 136, no. 4A, p. A1044, 1964. [Online]. Available: http://dx.doi.org/10.1103/PhysRev.136.A1044 Cited on pages 13 and 27.

[72] M. Seah and W. Dench, "Quantitative electron spectroscopy of surfaces: a standard data base for electron inelastic mean free paths in solids," *Surface and interface analysis*, vol. 1, no. 1, pp. 2–11, 1979. [Online]. Available: http://dx.doi.org/10.1002/sia.740010103 Cited on page 14.

[73] W. Duane and F. L. Hunt, "On x-ray wave-lengths," *Phys. Rev.*, vol. 6, p. 166, 1915. [Online]. Available: http://dx.doi.org/10.1103/PhysRev.6.166 Cited on page 19.

[74] P. Ohlin, *Arkiv för matematik, astronomi och fysik*, vol. A 29, p. 3, 1942. Cited on page 20.

[75] B. Nijboer, "On the intensity-distribution of the continuous x-ray spectrum near its short-wavelength limit," *Physica*, vol. 12, no. 7, p. 461, 1946. [Online]. Available: http://dx.doi.org/10.1016/S0031-8914(46)80060-0 Cited on page 20.

[76] K. Ulmer and H. Vernickel, "Zur struktur der bremsstrahl-isochromate von wolfram," *Zeitschrift für Physik*, vol. 153, no. 2, p. 149, 1958. [Online]. Available: http://link.springer.com/article/10.1007/BF01332357 Cited on page 20.

[77] V. Dose, "VUV isochromat spectroscopy," *Applied physics*, vol. 14, no. 1, p. 117, 1977. [Online]. Available: http://dx.doi.org/10.1007/BF00882639 Cited on pages 20 and 64.

[78] J. Pendry, "Theory of photoemission," *Surface science*, vol. 57, no. 2, p. 679, 1976. [Online]. Available: http://dx.doi.org/10.1016/0039-6028(76)90355-1 Cited on pages 20, 21, and 24.

[79] ——, "Theory of inverse photoemission," *Journal of Physics C: Solid State Physics*, vol. 14, no. 9, p. 1381, 1981. [Online]. Available: http://dx.doi.org/10.1088/0022-3719/14/9/022 Cited on pages 20, 21, and 24.

[80] D. Woodruff, N. Smith, P. Johnson, and W. Royer, "k-resolved inverse photoelectron spectroscopy and its application to Cu (001), Ni (001), and Ni (110)," *Physical Review B*, vol. 26, no. 6, p. 2943, 1982. [Online]. Available: http://dx.doi.org/10.1103/PhysRevB.26.2943 Cited on pages 21, 26, 27, 28, and 98.

[81] P. Johnson and J. Davenport, "Calculated inverse photoemission cross sections from adsorbed molecules," *Physical Review B*, vol. 31, no. 12, p. 7521, 1985. [Online]. Available: http://dx.doi.org/10.1103/PhysRevB.31.7521 Cited on pages 21, 22, 23, and 24.

[82] R. Hughes, "Theoretical practice: the bohm-pines quartet," *Perspectives on science*, vol. 14, no. 4, p. 457, 2006. [Online]. Available: http://dx.doi.org/10.1162/posc.2006.14.4.457 Cited on page 24.

[83] N. Smith and D. P. Woodruff, "Inverse photoemission from metal surfaces," *Progress in surface science*, vol. 21, no. 4, p. 295, 1986. [Online]. Available: http://dx.doi.org/10.1016/0079-6816(86)90004-3 Cited on pages 24, 29, 30, 34, 93, and 94.

[84] G. Thörner and G. Borstel, "Relativistic theory of photoemission from solids. I. key aspects of the model," *physica status solidi (b)*, vol. 126, no. 2, p. 617, 1984. [Online]. Available: http://dx.doi.org/10.1002/pssb.2221260221 Cited on page 24.

[85] J. Braun, G. Thörner, and G. Borstel, "Relativistic theory of photoemission from solids II. fully dynamical one-step formulation," *physica status solidi (b)*, vol. 130, no. 2, p. 643, 1985. [Online]. Available: http://dx.doi.org/10.1002/pssb.2221300228

[86] G. Borstel, "Theoretical aspects of photoemission," *Applied Physics A*, vol. 38, no. 3, p. 193, 1985. [Online]. Available: http://dx.doi.org/10.1007/BF00616497

[87] J. Braun, G. Thörner, and G. Borstel, "Relativistic theory of photoemission from solids. III. bulk and surface transition matrix elements," *physica status solidi (b)*, vol. 144, no. 2, p. 609, 1987. [Online]. Available: http://dx.doi.org/10.1002/pssb.2221440219

[88] G. Borstel and G. Thörner, "Inverse photoemission from solids: Theoretical aspects and applications," *Surface Science Reports*, vol. 8, no. 1, p. 1, 1988. [Online]. Available: http://dx.doi.org/10.1016/0167-5729(88)90006-4

[89] J. Braun and M. Donath, "Theory of photoemission from surfaces," *Journal of Physics: Condensed Matter*, vol. 16, no. 26, p. S2539, 2004. [Online]. Available: http://dx.doi.org/10.1088/0953-8984/16/26/026 Cited on pages 24 and 37.

[90] F. Himpsel, "Angle-resolved measurements of the photoemission of electrons in the study of solids," *Advances in Physics*, vol. 32, no. 1, pp. 1–51, 1983. [Online]. Available: http://dx.doi.org/10.1080/00018738300101521 Cited on page 26.

[91] F.-J. Himpsel, "Inverse photoemission from semiconductors," *Surface Science Reports*, vol. 12, no. 1, p. 3, 1990. [Online]. Available: http://dx.doi.org/10.1016/0167-5729(90)90005-X Cited on pages 27 and 89.

[92] R. Schneider and V. Dose, "Further topics in low-energy inverse photoemission," in *Unoccupied Electronic States*. Springer, 1992, p. 277. Cited on pages 27 and 28.

[93] W. Shockley, "On the surface states associated with a periodic potential," *Physical review*, vol. 56, no. 4, p. 317, 1939. [Online]. Available: http://dx.doi.org/10.1103/PhysRev.56.317 Cited on pages 29 and 32.

[94] I. Tamm, "Über eine mögliche Art der Elektronenbindung an Kristalloberflächen," *Zeitschrift für Physik*, vol. 76, no. 11-12, p. 849, 1932. Cited on page 29.

[95] P. Echenique and J. Pendry, "The existence and detection of rydberg states at surfaces," *Journal of Physics C: Solid State Physics*, vol. 11, no. 10, p. 2065, 1978. [Online]. Available: http://dx.doi.org/10.1088/0022-3719/11/10/017 Cited on pages 29 and 30.

[96] P. Echenique, J. Pitarke, E. Chulkov, and V. Silkin, "Image-potential-induced states at metal surfaces," *Journal of electron spectroscopy and related phenomena*, vol. 126, no. 1, pp. 163–175, 2002. [Online]. Available: http://dx.doi.org/10.1016/S0368-2048(02)00150-0 Cited on pages 29 and 30.

[97] E. McRae, "Electronic surface resonances of crystals," *Reviews of Modern Physics*, vol. 51, no. 3, p. 541, 1979. [Online]. Available: http://dx.doi.org/10.1103/RevModPhys.51.541 Cited on pages 29 and 30.

[98] N. Smith, C. Chen, and M. Weinert, "Distance of the image plane from metal surfaces," *Physical Review B*, vol. 40, no. 11, p. 7565, 1989. [Online]. Available: http://dx.doi.org/10.1103/PhysRevB.40.7565

[99] N. Smith and C. Chen, "Spectroscopic constraints on the potential barrier at metal surfaces," *Surface Science*, vol. 247, no. 2, p. 133, 1991. [Online]. Available: http://dx.doi.org/10.1016/0039-6028(91)90119-D Cited on page 29.

[100] W. E. Meyerhof, "Contact potential difference in silicon crystal rectifiers," *Physical Review*, vol. 71, no. 10, p. 727, 1947. [Online]. Available: http://dx.doi.org/10.1103/PhysRev.71.727 Cited on page 29.

[101] J. Bardeen, "Surface states and rectification at a metal semi-conductor contact," *Phys. Rev.*, vol. 71, p. 717, May 1947. [Online]. Available: http://link.aps.org/doi/10.1103/PhysRev.71.717 Cited on page 29.

[102] W. H. Brattain and W. Shockley, "Density of surface states on silicon deduced from contact potential measurements," *Physical Review*, vol. 72, no. 4, p. 345, 1947. [Online]. Available: http://dx.doi.org/10.1103/PhysRev.72.345 Cited on page 29.

[103] W. Shockley and G. Pearson, "Modulation of conductance of thin films of semi-conductors by surface charges," *Physical review*, vol. 74, no. 2, p. 232, 1948. [Online]. Available: http://dx.doi.org/10.1103/PhysRev.74.232 Cited on pages 29 and 30.

[104] S. Davison and M. Steslicka, "Basic theory of surface states, clarendon," 1996. Cited on page 29.

[105] S. G. Davison and M. Stęślicka, *Basic theory of surface states*. Oxford University Press, 1992, vol. 46. Cited on pages 29 and 30.

[106] P. Johnson and N. Smith, "Image-potential states and energy-loss satellites in inverse photoemission spectra," *Physical Review B*, vol. 27, no. 4, p. 2527, 1983. [Online]. Available: http://dx.doi.org/10.1103/PhysRevB.27.2527 Cited on page 30.

[107] D. Wesner, P. Johnson, and N. Smith, "Photoemission spectra and band structures of d-band metals. XI. inverse photoemission from Pd (111)," *Physical Review B*, vol. 30, no. 2, p. 503, 1984. [Online]. Available: http://dx.doi.org/10.1103/PhysRevB.30.503 Cited on page 30.

[108] B. Reihl, K. Frank, and R. Schlittler, "Image-potential and intrinsic surface states on Ag (100)," *Physical Review B*, vol. 30, no. 12, p. 7328, 1984. [Online]. Available: http://dx.doi.org/10.1103/PhysRevB.30.7328

[109] V. Dose, W. Altmann, A. Goldmann, U. Kolac, and J. Rogozik, "Image-potential states observed by inverse photoemission," *Physical review letters*, vol. 52, no. 21, p. 1919, 1984. [Online]. Available: http://dx.doi.org/10.1103/PhysRevLett.52.1919

[110] D. Straub and F. Himpsel, "Identification of image-potential surface states on metals," *Physical review letters*, vol. 52, no. 21, p. 1922, 1984. [Online]. Available: http://dx.doi.org/10.1103/PhysRevLett.52.1922 Cited on page 30.

[111] J. Rundgren and G. Malmstrom, "Transmission and reflection of low-energy electrons at the surface barrier of a metal," *Journal of Physics C: Solid State Physics*, vol. 10,

no. 23, p. 4671, 1977. [Online]. Available: iopscience.iop.org/article/10.1088/0022-3719/10/23/004/pdf Cited on page 30.

[112] M. W. Cole and M. H. Cohen, "Image-potential-induced surface bands in insulators," *Physical Review Letters*, vol. 23, no. 21, p. 1238, 1969. [Online]. Available: http://dx.doi.org/10.1103/PhysRevLett.23.1238 Cited on page 30.

[113] P. Gartland and B. Slagsvold, "Transitions conserving parallel momentum in photoemission from the (111) face of copper," *Physical Review B*, vol. 12, no. 10, p. 4047, 1975. [Online]. Available: http://dx.doi.org/10.1103/PhysRevB.12.4047 Cited on page 34.

[114] H. Roloff and H. Neddermeyer, "High-resolution photoemission from Ag (100), Ag (110), and Ag (111)," *Solid State Communications*, vol. 21, no. 6, pp. 561–564, 1977. [Online]. Available: http://dx.doi.org/10.1016/0038-1098(77)90032-1 Cited on page 34.

[115] P. Heimann, H. Neddermeyer, and H. Roloff, "Ultraviolet photoemission for intrinsic surface states of the noble metals," *Journal of Physics C: Solid State Physics*, vol. 10, no. 1, p. L17, 1977. [Online]. Available: http://dx.doi.org/10.1088/0022-3719/10/1/004 Cited on page 34.

[116] S. Kevan, "Evidence for a new broadening mechanism in angle-resolved photoemission from Cu (111)," *Physical review letters*, vol. 50, no. 7, p. 526, 1983. [Online]. Available: http://dx.doi.org/10.1103/PhysRevLett.50.526 Cited on page 34.

[117] G. Hansson and S. Flodström, "Angular-resolved photoemission from low-index crystal faces of silver – bulk and surface contributions," *Physical Review B*, vol. 17, no. 2, p. 473, 1978. [Online]. Available: http://dx.doi.org/10.1103/PhysRevB.17.473 Cited on page 34.

[118] ——, "Photoemission study of the bulk and surface electronic structure of single crystals of gold," *Physical Review B*, vol. 18, no. 4, p. 1572, 1978. [Online]. Available: http://dx.doi.org/10.1103/PhysRevB.18.1572 Cited on page 34.

[119] D. Woodruff, S. Hulbert, P. Johnson, and N. Smith, "Unoccupied surface resonance on Cu (100) and the effect of vacuum-level pinning," *Physical Review B*, vol. 31, no. 6, p. 4046, 1985. [Online]. Available: http://dx.doi.org/10.1103/PhysRevB.31.4046 Cited on page 34.

[120] G. Thörner, G. Borstel, V. Dose, and J. Rogozik, "Unoccupied electronic surface resonance at Cu (001)," *Surface Science Letters*, vol. 157, no. 2, pp. L379–L383, 1985. [Online]. Available: http://dx.doi.org/10.1016/0167-2584(85)91089-8 Cited on page 34.

[121] S. Hulbert, P. Johnson, M. Weinert, and R. Garrett, "Unoccupied surface states on Cu (001): A comparison of experiment and theory," *Physical Review B*, vol. 33, no. 2, p. 760, 1986. [Online]. Available: http://dx.doi.org/10.1103/PhysRevB.33.760 Cited on page 34.

[122] S. Hulbert, P. Johnson, N. Stoffel, W. Royer, and N. Smith, "Crystal-induced and image-potential-induced empty surface states on Cu (111) and Cu (001)," *Physical Review B*, vol. 31, no. 10, p. 6815, 1985. [Online]. Available: http://dx.doi.org/10.1103/PhysRevB.31.6815 Cited on page 34.

[123] M. Ortuo and P. Echenique, "Phase shifts, image planes, and surface states at metal surfaces," *Physical Review B*, vol. 34, no. 8, p. 5199, 1986. [Online]. Available: http://dx.doi.org/10.1103/PhysRevB.34.5199 Cited on page 34.

[124] A. Goldmann, V. Dose, and G. Borstel, "Empty electronic states at the (100),(110), and (111) surfaces of nickel, copper, and silver," *Physical Review B*, vol. 32, no. 4, p. 1971, 1985. [Online]. Available: http://dx.doi.org/10.1103/PhysRevB.32.1971 Cited on page 34.

[125] M. Weinert, S. Hulbert, and P. Johnson, "Image planes and surface states," *Physical review letters*, vol. 55, no. 19, p. 2055, 1985. [Online]. Available: http://dx.doi.org/10.1103/PhysRevLett.55.2055 Cited on page 34.

[126] D. Straub and F. Himpsel, "Spectroscopy of image-potential states with inverse photoemission," *Physical Review B*, vol. 33, no. 4, p. 2256, 1986. [Online]. Available: http://dx.doi.org/10.1103/PhysRevB.33.2256 Cited on pages 34, 93, 94, 96, 102, and 145.

[127] D. Woodruff, W. Royer, and N. Smith, "Empty surface states, image states, and band edge on Au (111)," *Physical Review B*, vol. 34, no. 2, p. 764, 1986. [Online]. Available: http://dx.doi.org/10.1103/PhysRevB.34.764 Cited on pages 34, 93, 94, 96, 97, 102, and 145.

[128] D. Straub and F. Himpsel, "Identification of image-potential surface states on metals," *Physical review letters*, vol. 52, no. 21, p. 1922, 1984. [Online]. Available: http://dx.doi.org/10.1103/PhysRevLett.52.1922 Cited on page 34.

[129] L. Jurczyszyn, "The resonance image states at Cu (111), Au (111), and Al (111) surfaces," *Surface science*, vol. 259, no. 1, pp. 65–69, 1991. [Online]. Available: http://dx.doi.org/10.1016/0039-6028(91)90524-V Cited on page 34.

[130] K. Giesen, F. Hage, F. Himpsel, H. Riess, and W. Steinmann, "Two-photon photoemission via image-potential states," *Physical review letters*, vol. 55, no. 3, p. 300, 1985. [Online]. Available: http://dx.doi.org/10.1103/PhysRevLett.55.300 Cited on page 34.

[131] W. Jacob, V. Dose, U. Kolac, T. Fauster, and A. Goldmann, "Bulk, surface and thermal effects in inverse photoemission spectra from Cu (100), Cu (110) and Cu (111)," *Zeitschrift für Physik B Condensed Matter*, vol. 63, no. 4, pp. 459–470, 1986. [Online]. Available: http://dx.doi.org/10.1007/BF01726194 Cited on page 34.

[132] S. Hulbert, P. Johnson, N. Stoffel, and N. Smith, "Unoccupied bulk and surface states on Ag (111) studied by inverse photoemission," *Physical Review B*, vol. 32, no. 6, p.

3451, 1985. [Online]. Available: http://dx.doi.org/10.1103/PhysRevB.32.3451 Cited on page 34.

[133] K. Giesen, F. Hage, F. Himpsel, H. Riess, and W. Steinmann, "Binding energy of image-potential states: dependence on crystal structure and material," *Physical Review B*, vol. 35, no. 3, p. 971, 1987. [Online]. Available: http://dx.doi.org/10.1103/PhysRevB.35.971 Cited on page 34.

[134] F. Ciccacci, S. De Rossi, A. Taglia, and S. Crampin, "Unoccupied electronic states in Au (100) surfaces," *Journal of Physics: Condensed Matter*, vol. 6, no. 36, p. 7227, 1994. [Online]. Available: http://dx.doi.org/10.1088/0953-8984/6/36/007 Cited on page 34.

[135] Z. Li and S. Gao, "Band-theory calculation of image states on a metal surface," *Phys. Rev. B*, vol. 50, pp. 15 349–15 352, Nov 1994. [Online]. Available: http://link.aps.org/doi/10.1103/PhysRevB.50.15349 Cited on page 34.

[136] W. Altmann, V. Dose, A. Goldmann, U. Kolac, and J. Rogozik, "Angle-resolved bremsstrahlung isochromat spectroscopy of Cu (100) and Cu (110)," *Physical Review B*, vol. 29, no. 6, p. 3015, 1984. [Online]. Available: http://dx.doi.org/10.1103/PhysRevB.29.3015 Cited on page 34.

[137] R. Courths, H. Wern, U. Hau, B. Cord, V. Bachelier, and S. Hufner, "Band structure of Cu, Ag and Au: location of direct transitions on the λ line using angle-resolved photoelectron spectroscopy (ARUPS)," *Journal of Physics F: Metal Physics*, vol. 14, no. 6, p. 1559, 1984. [Online]. Available: http://dx.doi.org/10.1088/0305-4608/14/6/023 Cited on page 34.

[138] G. Binnig, K. H. Frank, H. Fuchs, N. Garcia, B. Reihl, H. Rohrer, F. Salvan, and A. R. Williams, "Tunneling spectroscopy and inverse photoemission: Image and field states," *Phys. Rev. Lett.*, vol. 55, pp. 991–994, Aug 1985. [Online]. Available: http://link.aps.org/doi/10.1103/PhysRevLett.55.991 Cited on page 34.

[139] S. Raj and D. Sarma, "Optimization of a low-energy, high brightness electron gun for inverse photoemission spectrometers," *Review of scientific instruments*, vol. 75, no. 4, pp. 1020–1025, 2004. [Online]. Available: http://dx.doi.org/10.1063/1.1647694 Cited on pages 35 and 36.

[140] A. Zumbülte, A. Schmidt, and M. Donath, "Momentum resolution in inverse photoemission," *Review of Scientific Instruments*, vol. 86, no. 1, p. 013908, 2015. [Online]. Available: http://dx.doi.org/10.1063/1.4906508 Cited on pages 35, 36, 37, 52, 63, and 144.

[141] M. Maniraj and S. R. Barman, "Influence of the contact potential and space-charge effect on the performance of a stoffel-johnson design electron source for inverse photoemission spectroscopy," *Review of Scientific Instruments*, vol. 85, no. 3, p. 033301, 2014. [Online]. Available: http://dx.doi.org/10.1063/1.4866650 Cited on pages 35, 36, and 52.

[142] N. Stoffel and P. Johnson, "A low-energy high-brightness electron gun for inverse photoemission," *Nuclear Instruments and Methods in Physics Research Section A: Accelerators, Spectrometers, Detectors and Associated Equipment*, vol. 234, no. 2, pp. 230–234, 1985. [Online]. Available: http://dx.doi.org/10.1016/0168-9002(85)90910-6 Cited on pages 35 and 36.

[143] J. Lipton-Duffin, A. Mark, G. Mullins, G. Contant, and A. McLean, "An inverse photoemission system with large solid angle of detection and adjustable optical bandpass," *Review of scientific instruments*, vol. 75, no. 2, pp. 445–454, 2004. [Online]. Available: http://dx.doi.org/10.1063/1.1637435 Cited on pages 36, 39, 54, 63, and 144.

[144] P. W. Erdman and E. C. Zipf, "Low-voltage, high-current electron gun," *Review of Scientific Instruments*, vol. 53, no. 2, pp. 225–227, 1982. [Online]. Available: http://dx.doi.org/10.1063/1.1136932 Cited on page 36.

[145] K. P. Inc. (visited: 20.10.2015) ELG-2 / EGPS-1022. [Online]. Available: http://www.kimballphysics.com/elg-2-egps-1022 Cited on pages 36, 51, 52, and 144.

[146] F. Schedin, G. Thornton, and R. Uhrberg, "Windows and photocathodes for a high resolution solid state bandpass ultraviolet photon detector for inverse photoemission," *Review of scientific instruments*, vol. 68, no. 1, p. 41, 1997. [Online]. Available: http://dx.doi.org/10.1063/1.1147844 Cited on pages 36 and 37.

[147] T. Fauster, D. Straub, J. Donelon, D. Grimm, A. Marx, and F. Himpsel, "Normal-incidence grating spectrograph with large acceptance for inverse photoemission," *Review of scientific instruments*, vol. 56, no. 6, pp. 1212–1214, 1985. [Online]. Available: http://dx.doi.org/10.1063/1.1137977 Cited on page 37.

[148] T. Childs, W. Royer, and N. Smith, "Evaluation of LiF lenses as monochromators for inverse photoemission spectroscopy," *Review of Scientific Instruments*, vol. 55, no. 10, pp. 1613–1615, 1984. [Online]. Available: http://dx.doi.org/10.1063/1.1137626 Cited on page 37.

[149] M. Budke, V. Renken, H. Liebl, G. Rangelov, and M. Donath, "Inverse photoemission with energy resolution better than $200\,\mathrm{meV}$," *Review of Scientific Instruments*, vol. 78, no. 8, p. 083903, 2007. [Online]. Available: http://dx.doi.org/10.1063/1.2771096 Cited on pages 37, 52, 65, 87, 88, 89, 98, and 144.

[150] I. Schäfer, W. Drube, M. Schlüter, G. Plagemann, and M. Skibowski, "Bandpass photon detector with high efficiency for inverse photoemission spectroscopy," *Review of scientific instruments*, vol. 58, no. 4, pp. 710–711, 1987. [Online]. Available: http://dx.doi.org/10.1063/1.1139244 Cited on page 37.

[151] V. Dose, "Ultraviolet bremsstrahlung spectroscopy," *Progress in surface science*, vol. 13, no. 3, pp. 225–283, 1983. [Online]. Available: http://dx.doi.org/10.1016/0079-6816(83)90005-9 Cited on page 37.

[152] A. Kovacs, P. Nilsson, and J. Kanski, "A simple apparatus for studies of UV-bremsstrahlung," *Physica Scripta*, vol. 25, no. 6A, p. 791, 1982. [Online]. Available: http://dx.doi.org/10.1088/0031-8949/25/6A/034 Cited on page 37.

[153] I. Hill and A. McLean, "A comparison of two high performance inverse photoemission bandpass detectors," *Review of scientific instruments*, vol. 69, no. 1, p. 261, 1998. [Online]. Available: http://dx.doi.org/10.1063/1.1148506 Cited on pages 37, 64, and 86.

[154] B. Engelkamp, H. Wortelen, H. Mirhosseini, A. Schmidt, D. Thonig, J. Henk, and M. Donath, "Spin-polarized surface electronic structure of Ta (110): Similarities and differences to W (110)," *Physical Review B*, vol. 92, no. 8, p. 085401, 2015. [Online]. Available: http://dx.doi.org/10.1103/PhysRevB.92.085401 Cited on page 37.

[155] C. Thiede, A. B. Schmidt, and M. Donath, "Optimizing the performance of bandpass photon detectors for inverse photoemission: Transmission of alkaline earth fluoride window crystals," *Review of Scientific Instruments*, vol. 86, no. 8, p. 085101, 2015. [Online]. Available: http://dx.doi.org/10.1063/1.4927459 Cited on pages 37 and 52.

[156] K. Jousten, *Handbook of vacuum technology*. Wiley-VCH, 2008. Cited on page 38.

[157] G. Anger, A. Winkler, and K. Rendulic, "Adsorption and desorption kinetics in the systems H_2/Cu (111), H_2/Cu (110) and H_2/Cu (100)," *Surface Science*, vol. 220, no. 1, pp. 1–17, 1989. [Online]. Available: http://dx.doi.org/10.1016/0039-6028(89)90459-7 Cited on page 38.

[158] S. Hofmann, *Auger-and X-ray photoelectron spectroscopy in materials science: a user-oriented guide*. Springer Science & Business Media, 2012, vol. 49. Cited on page 38.

[159] H. C. P. G. G. R. C. for Geosciences. (visited: 13.10.2015) IGRF declination calculator. [Online]. Available: http://www.gfz-potsdam.de/en/section/earths-magnetic-field/services/igrf-declinaion-calculator/ Cited on page 39.

[160] T. M. Company. (visited: 13.10.2015) About MμMetal. [Online]. Available: http://www.mumetal.com/about_mumetal.php Cited on page 39.

[161] P. V. GmbH. (visited: 19.10.2015) 3.2.1.1 edelstahl. [Online]. Available: https://www.pfeiffer-vacuum.com/de/know-how/mechanische-komponenten-im-vakuum/werkstoffe/metallische-werkstoffe/edelstahl/ Cited on page 45.

[162] R. GmbH. (visited: 19.10.2015) V4A-corrosion resistant steel. [Online]. Available: http://en.rime.de/wiki/v4a-steel/ Cited on page 45.

[163] V. V. A. . Switzerland. (visited: 19.10.2015) Series 108 | UHV gate valve. [Online]. Available: http://www.vatvalve.com/products/product?id=10840-CE01 Cited on page 45.

[164] V. V.-A. GmbH. (visited: 19.10.2015) Vab vakuum-anlagenbau GmbH. [Online]. Available: http://www.vab-vakuum.com/ Cited on pages 46 and 49.

[165] V. V. K. &. M. GmbH. (visited: 21.10.2015) WSL / WSLR series. [Online]. Available: http://www.vacom.de/produkte/mechanische-durchfuehrungen/dreh-schiebedurchfuehrungen-und-transfersysteme/serie-wsl-wslr Cited on pages 47 and 48.

[166] K. J. L. Company. (visited: 21.10.2015) Motion feedthroughs. [Online]. Available: http://www.lesker.com/newweb/feedthroughs/feedthroughs_technicalnotes_motion.cfm?pgid=0 Cited on page 48.

[167] V. S. Ltd. (visited: Oct. 2012 - Jan.2013) Chambers and fabrications. [Online]. Available: www.vgscienta.com Cited on pages 48 and 49.

[168] H. P. Barnscheidt, "VG scienta," private communication, Jan. 2013. Cited on page 49.

[169] P. V. GmbH. (visited: 27.10.2015) Hipace®700 with TC 400, DN 160 CF-F. [Online]. Available: https://www.pfeiffer-vacuum.com/en/products/turbopumps/hybrid-bearing/hipace-700/?detailPdoId=4533&request_locale=en_US/ Cited on page 49.

[170] Pneurop. (visited: 27.10.2015). [Online]. Available: http://www.pneurop.eu/index.php Cited on page 49.

[171] V. V. K. &. M. GmbH. (visited: 27.10.2015) Titanium sublimation pumps. [Online]. Available: http://www.vacom.de/en/products/ion-getter-and-titanium-sublimation-pumps/titanium-sublimation-pumps Cited on page 49.

[172] H. GmbH. (visited: 27.10.2015) Einsatz von heizmanschetten. [Online]. Available: http://www.horst.de/heizmanschetten.htm Cited on page 49.

[173] P. V. GmbH. (visited: 27.10.2015) IKR 270, metal sealed, long case, DN 40 CF-F. [Online]. Available: https://www.pfeiffer-vacuum.com/en/products/measurement/activeline/activeline-gauges/?detailPdoId=3867&request_locale=en_US Cited on page 49.

[174] A. Schopphoff, "Pfeiffer vacuum GmbH," private communication, Oct. 2015. Cited on page 49.

[175] V. V. K. &. M. GmbH. (visited: 29.10.2015) Linear translators and aligners. [Online]. Available: http://www.vacom.de/en/products/mechanical-feedthroughs/linear-translators-and-aligners Cited on page 50.

[176] A. Shukla, S. Banik, and S. Barman, "Fabrication of an inverse photoemission spectrometer to study unoccupied electronic states," *Current Science*, vol. 90, no. 4, pp. 490–496, 2006. [Online]. Available: http://repository.ias.ac.in/64615/ Cited on pages 50, 52, 63, 88, and 144.

[177] K. P. Inc., *ELG–2 / EGPS–1022 Electron Gun and Power Supply System – Manual*. 311 Kimball Hill Road, Wilton, NH 03086, United States, 2013. Cited on pages 51, 52, 57, 58, 59, 60, 61, and 62.

[178] J. Yates Jr., *Experimental Innovations in Surface Science*. New York, NY: Springer-Verlag-AIP, 1997. Cited on pages 52 and 53.

[179] K. K. GmbH. (visited: 02.11.2015) Calciumfluorid (CaF_2). [Online]. Available: http://www.korth.de/index.php/material-detailansicht/items/10.html Cited on page 52.

[180] M. Donath, "University of münster," private communication, Sep. 2011. Cited on pages 52 and 144.

[181] C. O. G. G. &. C. K. Dichtungstechnik. (visited: 02.11.2015) FFKM - perfluorelastomer der extraklasse. [Online]. Available: http://www.cog.de/index.php?id=49&L=0 Cited on page 53.

[182] P. V. GmbH. (visited: 29.10.2015) HiCube 80 Eco, DN 63 CF-F, MVP 015 with DCU 002. [Online]. Available: https://www.pfeiffer-vacuum.com/en/products/pumping-stations/turbo-pumping-stations/hicube-eco/?detailPdoId=5165 Cited on page 53.

[183] M. instuments. (visited: 29.10.2015) Baratron® manometers. [Online]. Available: https://www.pfeiffer-vacuum.com/en/products/pumping-stations/turbo-pumping-stations/hicube-eco/?detailPdoId=5165 Cited on page 53.

[184] G. F. Knoll, *Radiation detection and measurement*. John Wiley & Sons, 2010. Cited on pages 54, 64, 65, 66, 73, 75, 79, 80, and 86.

[185] D. Woodruff and N. Smith, "k-resolved inverse photoemission from Cu (001) and Ni (001)," *Physical Review Letters*, vol. 48, no. 4, p. 283, 1982. [Online]. Available: http://dx.doi.org/10.1103/PhysRevLett.48.283 Cited on page 54.

[186] D. Funnemann and H. Merz, "$10\,\mathrm{eV}$ photon detector for inverse photoemission," *Journal of Physics E: Scientific Instruments*, vol. 19, no. 7, p. 554, 1986. [Online]. Available: http://dx.doi.org/10.1088/0022-3735/19/7/011 Cited on pages 54 and 65.

[187] G. G. I. D. Systems. (visited: 04.11.2015) Phosphor screens and scintillators. [Online]. Available: http://www.gids-gmbh.com/9.html Cited on page 55.

[188] W. M. Yen, H. Yamamoto *et al.*, *Phosphor handbook*. CRC press, 2006. Cited on page 55.

[189] K. P. Inc. (visited: 04.11.2015) FC-70. [Online]. Available: http://www.kimballphysics.com/fc-70 Cited on page 55.

[190] H. Charest, "Kimball physics, Inc." private communication, June 2014. Cited on pages 58 and 59.

[191] J. T. Thong, *Electron Beam Testing Technology*. Springer Science & Business Media, 2013. Cited on pages 59 and 87.

[192] C. Child, "Discharge from hot CaO," *Physical Review (Series I)*, vol. 32, no. 5, p. 492, 1911. [Online]. Available: http://dx.doi.org/10.1103/PhysRevSeriesI.32.492 Cited on page 60.

[193] I. Langmuir, "The effect of space charge and residual gases on thermionic currents in high vacuum," *Physical Review*, vol. 2, no. 6, p. 450, 1913. [Online]. Available: http://dx.doi.org/10.1103/PhysRev.2.450 Cited on page 60.

[194] D. Wilkinson, "The geiger discharge revisited part 1.: The charge generated," *Nuclear Instruments and Methods in Physics Research Section A: Accelerators, Spectrometers, Detectors and Associated Equipment*, vol. 321, no. 1 – 2, p. 195, 1992. [Online]. Available: http://dx.doi.org/10.1016/0168-9002(92)90388-K Cited on page 64.

[195] F. Sauli, "Principles of operation of multiwire proportional and drift chambers," *European Organization for Nuclear Research CERN, Geneva (Switzerland)*, Tech. Rep.,1977. [Online]. Available: http://dx.doi.org/10.5170/CERN-1977-009 Cited on pages 65, 66, 67, 69, and 79.

[196] ——, "Gaseous detector fundaments," *"Excellence in Detectors and Instrumentation Technologies", CERN, Geneva, Switzerland*, 31 January 2011 – 10 February 2011. Cited on pages 66 and 69.

[197] Y. I. Davydov, "On the first townsend coefficient at high electric field," *IEEE Transactions on Nuclear Science*, vol. 53, p. 2931, 2006. [Online]. Available: http://arxiv.org/abs/physics/0409156 Cited on pages 69 and 70.

[198] W. Diethorn, "A methane proportional counter system for natural radiocarbon measurements." Ph.D. dissertation, (3rd ed.), Carnegie Institute of Technology, Pittsburgh, Pa, 1956. Cited on page 70.

[199] L. Malter, "Thin film field emission," *Physical Review*, vol. 50, no. 1, p. 48, 1936. [Online]. Available: http://dx.doi.org/10.1103/PhysRev.50.48 Cited on page 72.

[200] S. Banik, A. Shukla, and S. Barman, "Optimal operating conditions and characteristics of acetone/CaF_2 detector for inverse photoemission spectroscopy," *Review of scientific instruments*, vol. 76, no. 6, p. 066102, 2005. [Online]. Available: http://dx.doi.org/10.1063/1.1921507 Cited on pages 79, 80, 83, 86, 88, and 144.

[201] J. Craggs, W. Bosley, and A. Jaffe, "Some experiments with geiger-müller counters," *Journal of Scientific Instruments*, vol. 25, no. 3, p. 67, 1948. [Online]. Available: http://dx.doi.org/10.1088/0950-7671/25/3/302 Cited on pages 79 and 83.

[202] D. H. Wilkinson, *Ionization Chambers and Counters*. Cambridge at the Unsiversity Press, 1950. Cited on pages 79, 80, and 83.

[203] W. M. Trott, N. C. Blais, and E. A. Walters, "Molecular beam photoionization study of acetone and acetone-d6," *The Journal of Chemical Physics*, vol. 69, no. 7, p. 3150, 1978. [Online]. Available: http://dx.doi.org/10.1063/1.437009 Cited on page 80.

[204] A. G. Leiga and H. A. Taylor, "Far-ultraviolet photolysis of acetone," *The Journal of Chemical Physics*, vol. 41, no. 5, pp. 1247–1255, 1964. [Online]. Available: http://dx.doi.org/10.1063/1.1726056 Cited on page 80.

[205] C. Thiede, "Westfälische Wilhelms University of Münster," private communication, June 2014. Cited on pages 82, 83, and 84.

[206] I. Niehues, "Charakterisierung eines Aceton-Zählrohrs für die inverse Photoemission," Bachelorthesis, Westfälische Wilhelms University of Münster, 2012. Cited on pages 82, 83, and 84.

[207] I. Hill, A. Kahn, Z. Soos, and R. Pascal Jr, "Charge-separation energy in films of π-conjugated organic molecules," *Chemical Physics Letters*, vol. 327, no. 3, pp. 181–188, 2000. [Online]. Available: http://dx.doi.org/10.1016/S0009-2614(00)00882-4 Cited on pages 88, 106, 109, and 144.

[208] D. R. Zahn, G. N. Gavrila, and M. Gorgoi, "The transport gap of organic semiconductors studied using the combination of direct and inverse photoemission," *Chemical Physics*, vol. 325, no. 1, pp. 99–112, 2006. [Online]. Available: http://dx.doi.org/10.1016/j.chemphys.2006.02.003 Cited on pages 88, 107, 108, 109, 113, 115, 144, and X.

[209] M. Nakatake, Y. Okamura, S. Akiyama, H. Namatame, and M. Taniguchi, "High-resolution photon detection system for inverse-photoemission spectroscopy," *Journal of electron spectroscopy and related phenomena*, vol. 88, p. 1027, 1998. [Online]. Available: http://dx.doi.org/10.1016/S0368-2048(97)00251-X Cited on page 89.

[210] V. Dose, T. Fauster, and R. Schneider, "Improved resolution in VUV isochromat spectroscopy," *Applied Physics A*, vol. 40, no. 4, p. 203, 1986. [Online]. Available: http://dx.doi.org/10.1007/BF00616595 Cited on page 89.

[211] J. Lipton-Duffin, A. Mark, and A. McLean, "Photon detection with n-propanol and C2H6O isomers," *Review of scientific instruments*, vol. 73, no. 9, p. 3149, 2002. [Online]. Available: http://dx.doi.org/10.1063/1.1499536 Cited on page 89.

[212] F. Reinert, G. Nicolay, S. Schmidt, D. Ehm, and S. Hüfner, "Direct measurements of the L-gap surface states on the (111) face of noble metals by photoelectron spectroscopy," *Physical Review B*, vol. 63, no. 11, p. 115415, 2001. [Online]. Available: http://dx.doi.org/10.1103/PhysRevB.63.115415 Cited on pages 93, 94, 96, 99, and 101.

[213] M. Budke, T. Allmers, M. Donath, and G. Rangelov, "Combined experimental setup for spin-and angle-resolved direct and inverse photoemission," *Review of Scientific Instruments*, vol. 78, no. 11, p. 113909, 2007. [Online]. Available: http://dx.doi.org/10.1063/1.2813345 Cited on pages 100 and 101.

[214] M. Donath and V. Dose, "Temperature behaviour of a magnetic band in nickel," *EPL (Europhysics Letters)*, vol. 9, no. 8, p. 821, 1989. [Online]. Available: http://dx.doi.org/10.1209/0295-5075/9/8/014 Cited on pages 93, 94, 100, and 101.

[215] T. Schäfer, "Diethyl-dithiocarbamatmonolagen als oberflächenmodifikation flür edelmetallelektroden," Masterthesis, RWTH Aachen University, 2012. Cited on pages 93, 94, 96, and 100.

[216] B. Lüssem, S. Karthäuser, H. Haselier, and R. Waser, "The origin of faceting of ultraflat gold films epitaxially grown on mica," *Applied surface science*, vol. 249, no. 1, pp. 197–202, 2005. [Online]. Available: http://dx.doi.org/10.1016/j.apsusc.2004.11.082 Cited on page 93.

[217] P. Schulz, T. Schäfer, C. D. Zangmeister, C. Effertz, D. Meyer, D. Mokros, R. D. van Zee, R. Mazzarello, and M. Wuttig, "A new route to low resistance contacts for performance-enhanced organic electronic devices," *Advanced Materials Interfaces*, vol. 1, no. 5, 2014. [Online]. Available: http://dx.doi.org/10.1103/10.1002/admi.201300130 Cited on pages 96 and 100.

[218] M. M. Traum and N. V. Smith, "Photoemission spectra and band structures of d-band metals. II. Experiments on Rh, Ir, Ni, Pd, and Pt," *Physical Review B*, vol. 9, no. 4, p. 1353, 1974. [Online]. Available: http://dx.doi.org/10.1103/PhysRevB.9.1353 Cited on pages 94 and 96.

[219] B. Yan, B. Stadtmüller, N. Haag, S. Jakobs, J. Seidel, D. Jungkenn, S. Mathias, M. Cinchetti, M. Aeschlimann, and C. Felser, "Topological states on the gold surface," *Nature communications*, vol. 6, 2015. [Online]. Available: http://dx.doi.org/10.1038/ncomms10167 Cited on pages 94 and 97.

[220] N. V. Smith, "Photoemission spectra and band structures of d-band metals. III. model band calculations on Rh, Pd, Ag, Ir, Pt, and Au," *Physical Review B*, vol. 9, no. 4, p. 1365, 1974. [Online]. Available: http://dx.doi.org/10.1103/PhysRevB.9.1365 Cited on page 97.

[221] H. Eckardt, L. Fritsche, and J. Noffke, "Self-consistent relativistic band structure of the noble metals," *Journal of Physics F: Metal Physics*, vol. 14, no. 1, p. 97, 1984. [Online]. Available: http://dx.doi.org/10.1088/0305-4608/14/1/013 Cited on page 100.

[222] M. Ramchandani, "Energy band structure of gold," *Journal of Physics C: Solid State Physics*, vol. 3, no. 1S, p. S1, 1970. [Online]. Available: http://dx.doi.org/10.1088/0022-3719/3/1S/301 Cited on page 97.

[223] P. Heinmann, J. Hermanson, H. Miosga, and H. Neddermeyer, "d-like surface state bands on Cu (100) and Cu (111) observed in angle-resolved photoemission specroscopy," *Phys. Rev. B*, vol. 20, pp. 3059–66, 1979. [Online]. Available: http://dx.doi.org/10.1103/PhysRevB.20.3059 Cited on pages 97 and 100.

[224] R. Jaklevic and J. Lambe, "Experimental study of quantum size effects in thin metal films by electron tunneling," *Physical Review B*, vol. 12, no. 10, p. 4146, 1975. [Online]. Available: http://dx.doi.org/10.1103/PhysRevB.12.4146 Cited on page 96.

[225] K. W. Goodman and V. E. Henrich, "Contribution of nonradiative electron energy losses to the structure of inverse-photoemission spectra," *Physical Review B*, vol. 49, no. 7, p. 4827, 1994. [Online]. Available: http://dx.doi.org/10.1103/PhysRevB.49.4827 Cited on pages 97 and 98.

[226] A. P. Schulz, "National Renewable Energy Laboratory," private communication, May 2015. Cited on page 97.

[227] F. C. Bocquet, "Peter Grünberg Institut (PGI-3) – Forschungszentrum Jülich," private communication, March 2015. Cited on page 97.

[228] A. Goldmann, M. Donath, W. Altmann, and V. Dose, "Momentum-resolved inverse photoemission study of nickel surfaces," *Physical Review B*, vol. 32, no. 2, p. 837, 1985. [Online]. Available: http://dx.doi.org/10.1103/PhysRevB.32.837 Cited on page 98.

[229] D. R. Zahn, G. N. Gavrila, and G. Salvan, "Electronic and vibrational spectroscopies applied to organic/inorganic interfaces," *Chemical reviews*, vol. 107, no. 4, pp. 1161–1232, 2007. [Online]. Available: http://dx.doi.org/10.1021/cr050141p Cited on pages 98, 107, 108, 109, 110, 111, 112, 113, 115, 123, 124, 125, 126, 127, 129, 130, 135, 136, 138, X, and XVII.

[230] S. Ogawa, H. Nagano, H. Petek, and A. Heberle, "Optical dephasing in Cu (111) measured by interferometric two-photon time-resolved photoemission," *Physical review letters*, vol. 78, no. 7, p. 1339, 1997. [Online]. Available: http://dx.doi.org/10.1103/PhysRevLett.78.1339 Cited on page 98.

[231] E. Knoesel, A. Hotzel, and M. Wolf, "Temperature dependence of surface state lifetimes, dephasing rates and binding energies on Cu (111) studied with time-resolved photoemission," *Journal of electron spectroscopy and related phenomena*, vol. 88, pp. 577–584, 1998. [Online]. Available: http://dx.doi.org/10.1103/PhysRevB.59.5926 Cited on page 98.

[232] L. Bürgi, L. Petersen, H. Brune, and K. Kern, "Noble metal surface states: deviations from parabolic dispersion," *Surface science*, vol. 447, no. 1, pp. L157–L161, 2000. [Online]. Available: http://dx.doi.org/10.1016/S0039-6028(99)01102-4 Cited on pages 99, 101, and 102.

[233] B. Reihl, K. Frank, and A. Otto, "Unoccupied surface states on the (111) surface of silver: Evidence for broadening," *Zeitschrift für Physik B Condensed Matter*, vol. 62, no. 4, pp. 473–476, 1986. [Online]. Available: http://dx.doi.org/10.1007/BF01303579 Cited on page 100.

[234] W. Brütting, *Physics of organic semiconductors*. John Wiley & Sons, 2006. Cited on page 104.

[235] N. Ueno and S. Kera, "Electron spectroscopy of functional organic thin films: Deep insights into valence electronic structure in relation to charge transport property," *Progress in Surface Science*, vol. 83, no. 10, pp. 490–557, 2008. [Online]. Available: http://dx.doi.org/10.1016/j.progsurf.2008.10.002 Cited on pages 105 and 106.

[236] W. Warta, R. Stehle, and N. Karl, "Ultrapure, high mobility organic photoconductors," *Applied Physics A*, vol. 36, no. 3, pp. 163–170, 1985. [Online]. Available: http://dx.doi.org/10.1007/BF00624938 Cited on page 105.

[237] R. Farchioni and G. Grosso, *Organic electronic materials: conjugated polymers and low molecular weight organic solids*. Springer Science & Business Media, 2013, vol. 41. Cited on page 105.

[238] H. Yamane, S. Kera, K. K. Okudaira, D. Yoshimura, K. Seki, and N. Ueno, "Intermolecular energy-band dispersion in ptcda multilayers," *Physical Review B*, vol. 68, no. 3, p. 033102, 2003. [Online]. Available: http://dx.doi.org/10.1103/PhysRevB.68.033102 Cited on page 106.

[239] F. Gutmann and L. E. Lyons, *Organic semiconductors*. Wiley, 1967. Cited on page 106.

[240] K. Seki, "Ionization energies of free molecules and molecular solids," *Molecular Crystals and Liquid Crystals*, vol. 171, no. 1, pp. 255–270, 1989. [Online]. Available: http://dx.doi.org/10.1080/00268948908065800 Cited on page 106.

[241] H. Bässler and A. Köhler, "Charge transport in organic semiconductors," in *Unimolecular and supramolecular electronics I*. Springer, 2011, pp. 1–65. Cited on page 106.

[242] J. Ivančo, "Intrinsic work function of molecular films," *Thin Solid Films*, vol. 520, no. 11, pp. 3975–3986, 2012. [Online]. Available: http://dx.doi.org/10.1016/j.tsf.2012.01.035 Cited on pages 107, 108, 113, 115, 146, and X.

[243] G. N. Gavrila, "Electronic Properties and Chemistry of Metal / Organic Semiconductor/ S-GaAs(100) Heterostructures," Dissertation, TU Chemnitz, 2005. [Online]. Available: http://nbn-resolving.de/urn:nbn:de:swb:ch1-200600046 Cited on pages 107, 108, 111, 114, and 115.

[244] P. I. Djurovich, E. I. Mayo, S. R. Forrest, and M. E. Thompson, "Measurement of the lowest unoccupied molecular orbital energies of molecular organic semiconductors," *Organic Electronics*, vol. 10, no. 3, pp. 515–520, 2009. [Online]. Available: http://dx.doi.org/10.1016/j.orgel.2008.12.011 Cited on pages 109, 111, 114, 116, 146, and IX.

[245] S. Krause, A. Schöll, and E. Umbach, "Determination of transport levels of inorganic semiconductors by ultraviolet and inverse photoemission," *Physical Review B*, vol. 91, no. 19, p. 195101, 2015. [Online]. Available: http://dx.doi.org/10.1103/PhysRevB.91.195101 Cited on pages 109, 110, and 111.

[246] N. Koch, "Humboldt-Universität zu Berlin, Institut für Physik," private communication, May 2016. Cited on pages 110, 125, 126, 127, 132, and 147.

[247] W. Wurth, D. Coulman, A. Puschmann, D. Menzel, and E. Umbach, "Relation between x-ray photoemission spectroscopy binding energies and absorption resonance energies for CO adsorbates," *Physical Review B*, vol. 41, no. 18, p. 12933, 1990. [Online]. Available: http://dx.doi.org/10.1103/PhysRevB.41.12933 Cited on page 110.

[248] L. Zhang, X. Zhong, E. Pavlica, S. Li, A. Klekachev, G. Bratina, T. W. Ebbesen, E. Orgiu, and P. Samorì, "A nanomesh scaffold for supramolecular

nanowire optoelectronic devices," *Nature Nanotechnology*, 2016. [Online]. Available: http://dx.doi.org/10.1038/nnano.2016.125 Cited on pages 111 and 114.

[249] C. Effertz, "Organic molecular crystals: from thin-films to devices : investigation of thin-film formation and electronic transport properties of polycrystalline perylene films," Dissertation, RWTH Aachen University, 2011. [Online]. Available: http://publications.rwth-aachen.de/record/65408/files/3778.pdf Cited on page 113.

[250] D. Lide, *Handbook of Chemistry and Physics*. New York: CRC Press, 1997. Cited on page 113.

[251] K. Lament, W. Kamiński, P. Mazur, S. Zuber, and A. Ciszewski, "Molecular recognition of PTCDI-C_8 molecules on the Si (110)-(16$\times$ 2) surface," *Applied Surface Science*, vol. 304, pp. 50–55, 2014. Cited on pages 114, 116, and 146.

[252] I. A. Segger, "Perylene diimide thin films : structure, electrons and excitons," Dissertation, RWTH Aachen University, 2016. [Online]. Available: https://publications.rwth-aachen.de/record/561762 Cited on page 114.

[253] J. H. Scofield, "Hartree-slater subshell photoionization cross-sections at 1254 and 1487 ev," *Journal of Electron Spectroscopy and Related Phenomena*, vol. 8, no. 2, pp. 129–137, 1976. [Online]. Available: http://dx.doi.org/10.1016/0368-2048(76)80015-1 Cited on pages 123, XIV, and XVIII.

[254] CasaXPS: Processing Software for XPS, AES, SIMS and More. [Online]. Available: http://www.casaxps.com/ Cited on page 123.

[255] A. Schöll, Y. Zou, M. Jung, T. Schmidt, R. Fink, and E. Umbach, "Line shapes and satellites in high-resolution x-ray photoelectron spectra of large π-conjugated organic molecules," *The Journal of chemical physics*, vol. 121, no. 20, pp. 10 260–10 267, 2004. [Online]. Available: http://dx.doi.org/10.1063/1.1807812 Cited on page 125.

[256] A. Yang, A. Franco-Cañellas, M. Sato, B. Wang, R.-B. Wang, H. Koike, I. Salzmann, P. K. Thakur, T.-L. Lee, L. Liu *et al.*, "Nitrogen substitution impacts organic-metal interface energetics," *Physical Review B*, vol. 94, no. 15, p. 155426, 2016. [Online]. Available: https://doi.org/10.1103/PhysRevB.94.155426 Cited on pages 126, 127, 135, 139, 140, and 149.

[257] A. Schöll, Y. Zou, T. Schmidt, R. Fink, and E. Umbach, "High-resolution photoemission study of different NTCDA monolayers on Ag (111): Bonding and screening influences on the line shapes," *The Journal of Physical Chemistry B*, vol. 108, no. 38, pp. 14 741–14 748, 2004. Cited on page 127.

[258] N. Koch, S. Duhm, J. P. Rabe, S. Rentenberger, R. L. Johnson, J. Klankermayer, and F. Schreiber, "Tuning the hole injection barrier height at organic/metal interfaces with (sub-) monolayers of electron acceptor molecules," *Applied Physics Letters*, vol. 87, no. 10, p. 101905, 2005. [Online]. Available: http://dx.doi.org/10.1063/1.2041838 Cited on pages 132, 140, 147, and 149.

[259] P. S. Bagus, V. Staemmler, and C. Wöll, "Exchangelike effects for closed-shell adsorbates: Interface dipole and work function," *Physical review letters*, vol. 89, no. 9, p. 096104, 2002. [Online]. Available: https://doi.org/10.1103/PhysRevLett.89.096104 Cited on pages 140 and 149.

[260] N. Koch, "Energy levels at interfaces between metals and conjugated organic molecules," *Journal of Physics: Condensed Matter*, vol. 20, no. 18, p. 184008, 2008. Cited on pages 140 and 149.

[261] D. Meyer, T. Schäfer, P. Schulz, S. Jung, J. Rittich, D. Mokros, I. Segger, F. Maercks, C. Effertz, R. Mazzarello *et al.*, "Dithiocarbamate self-assembled monolayers as efficient surface modifiers for low work function noble metals," *Langmuir*, vol. 32, no. 35, pp. 8812–8817, 2016. [Online]. Available: http://dx.doi.org/10.1021/acs.langmuir.6b01578 Cited on page 150.

Acknowledgments

Diese Dissertation wäre ohne die Unterstützung und Ermutigung von sehr vielen lieben Menschen nicht möglich gewesen. Daher möchte ich hier die Gelegenheit nutzen, um meine tiefe Dankbarkeit auszudrücken.

Allen voran möchte ich meinem Vorgesetzten **Prof. Dr. Matthias Wuttig** danken, der es mir ermöglichte, an seinem Institut dem I. Physikalischen Institut (IA) an der RWTH Aachen University zu promovieren. Dadurch hatte ich die Chance mit vielen hochmotivierten und inspirierenden Forschern, Ingenieuren und Technikern spannende Themen zu bearbeiten. Vielen Dank dafür.

Darüber hinaus danke ich **Prof. Dr. Joachim Mayer**, der sich bereiterklärte mich als zweiter Berichter zu beraten. Vielen Dank für die Unterstützung in der letzten Phase meiner Promotion.

Der Aufbau des IPE- Spektrometers wäre ohne die Unterstützung vieler Menschen, von deren großem Erfahrungsschatz ich lernen durfte, nicht möglich gewesen:

- Allen voran **Prof. Dr. Markus Donath**, der sich nicht nur bereiterklärte, den Photonenbandpassdetektor zu bauen, sondern mich auch in hilfreichen Diskussionen zu IPE und zur Umsetzung des Spektrometers beraten hat. Vielen Dank.

- Mein Dank gebührt ebenfalls **Michael Wlochal** und **Karl-Heinz Dreger**. Mit Hilfe ihres großen Erfahrungsschatzes in der Umsetzung und Konstruktion von Vakuumkammern und -equipment und durch ihr großes Engagement haben wir in zahlreichen, fruchtbaren Diskussionen und mit etlichen Konstruktionsskizzen die beiden Kammern und Teile des Equipments umgesetzt. Ohne Euch wäre der erfolgreiche Abschluss dieses Projektes und somit der Promotion nicht möglich gewesen. Meinen tiefsten Dank.

- Danken möchte ich auch Herrn **Berthold Debye**, der die Vorkammer eigenhändig UHV-dicht zusammengeschweißt hat. Genieße Deinen wohlverdienten Ruhestand.

- Aber eine solche Kammer besteht nicht nur aus Konstruktion und Mechanik. Für die vielen Diskussionen, Dein großes Engagement, die Einführung in Elektrotechnik, sowie Deine Geduld mit mir möchte Dir, **Dipl.-Ing- Axel Groß**, danken.

- Ebenfalls sollen in diesem Zusammenhang auch **Stephan Hermes** und **Sebastian Mohrhenn** nicht unerwähnt bleiben. Von Euch beiden habe ich nicht nur sehr, sehr viel praktisches lernen können, ihr habt mich vor allem auch immer unterstützt, ermutigt und hattet immer ein offenes Ohr und das nicht nur für technische Probleme. Vielen, vielen Dank für die tolle und unkomplizierte Zeit mit Euch.

Ein Dank geht auch an meine "Minions": meine Bachelorstudenten, meine Hiwis und meine Masteranden. Besonders erwähnt werden sollen hier **Miriam Raths** und **Matthias Dück**. Ihr ward jahrelang an meiner Seite und habt Eure Aufgaben immer mit größter Sorgfalt erledigt. Zudem habt ihr mich immer mit kreativen Vorschlägen unterstützt. Ich könnte nicht stolzer auf Euch sein und wünsche Euch weiterhin viel Erfolg für Euren weiteren Weg.

Mit **Dr. Alexandra Yatim**, **Dr. Dominik Meyer** und **Dr. Cathy Jodocy** konnte ich alle Höhen und Tiefen einer Promotion teilen:

- Alex, obwohl wir an ganz unterschiedlichen Themen gearbeitet haben, hat gerade die unterschiedliche Betrachtungsweise dazugeführt, dass wir uns gegenseitig immer wieder weiter gebracht und motiviert haben und nie das Ziel aus dem Auge verloren haben. Zudem hast Du meine gesamte Dissertation sorgfältig korrigiert und mir die langen Abende im Institut versüßt. Du bist mir in all den Jahren ein sehr gute Freundin geworden und gewesen. Ich schulde Dir meinen tiefsten Dank.

- Dominik, obwohl unsere beiden Charaktere doch zweit weilen zur Produktion von Reibungswärme geführt haben, sind wir in all der Zeit zusammen gewachsen und sehr gute Freunde geworden. Mit Dir kann ich immer ehrlich sein und danke Dir für Deine ehrlichen Feedbacks und das nicht nur zu einzelnen Kapiteln meiner Dissertation. Ich schulde Dir meinen tiefsten Dank.

- Cathy, mit Dir konnte ich ebenfalls all meine Höhen und Tiefen teilen. Ich habe unsere nachmittäglichen Teepausen immer genossen. Du warst mir gerade in der letzten Phase der Promotion immer eine motivierende Stütze. Über die Jahre warst Du nicht nur meiner Bürokollegin, sondern warst mir auch eine sehr guten Freundin. Zudem kann ich mit Dir meine Leidenschaft für Sushi ausleben ;-) Ich schulde Dir meinen tiefsten Dank.

Neben den bereits erwähnten Personen, haben mich viele weitere Kollegen aus dem I. Physikalischen Institut (IA) freundlich unterstützt. In diesem Zusammenhang möchte ich herzlichst Danken: Allen voran der alten Organikgruppe **Dr. Dominik Meyer**, **Dr. Cathy Jodocy**,

Dr. Daniel Mokros, **Dr. Ingolf Segger**, **Dr. Christian Effertz** und **Dr. Philip Schulz** für die Unterstützung bei Aufbau der Kammer und die zahlreichen Diskussionen.
Außerdem danke ich **Oliver Lehmann** für seine Unterstützung bei Computerprobleme, denen ich in den letzten Jahren begegnet bin.
Ich möchte **Renate Betz**, **Sarah Schlenter**, **Kathrin Gerth**, **Mara Kallweit** und **Josefine Elbert** danken, die mir nicht nur bei administrativen Problemen immer mit Rat und Tat zur Seite standen, sondern auch immer für eine warme Atmosphäre im Institut sorgten.
Viele meiner Kollegen haben Teile meiner Dissertation sorgfältig gelesen und diese korrigiert. Ich danke **Dr. Alexandra Yatim**, **Dr. Dominik Meyer**, **Dr. Cathy Jodocy**, **Dr. Peter Jost**, **Matthias Dück** und **Sebastian Jung** herzlichst hierfür.
Zudem möchte ich mich bei meinen Ex-Bürokollegen **Dr. Daniel Mokros**, **Dr. Cathy Jodocy** und **Matti Wirtssohn** bedanken. Wir konnten nicht nur über wissenschaftliches sondern auch darüber hinaus diskutieren, haben unsere Probleme geteilt und zusammen Tränen gelacht. Vielen Dank für die schöne Atmosphäre.
Vielen Dank auch an **Dr. Alexandra Yatim**, **Sebastian Mohrhenn**, **Dr. Cathy Jodocy**, **Dr. Dominik Meyer**, **Sonja Wehner**, **Dr. Felix Lange**, **Dr. Peter Jost**, **Julia Benke-Jacob**, **Stefan Jakobs**, **Matthias Dück**, **Sebnem Yazici**, **Mariana Oliveira**, **Dr. Christian Effertz**, **Dr. Philip Schulz**, sowie die anderen Kollegen aus dem I. Physikalischen Institut (IA) dafür, dass ihr ein kooperatives Arbeitsumfeld geschaffen habt und wir gute Freunde geworden sind.

Während meiner Zeit hier in Aachen hast Du, **Martina Horst**, mich in in Deine Familie aufgenommen und mich wie eine Mutter unterstützt. Ich schätze mich sehr glücklich zu Deiner Familie gehören zu dürfen.

Meinen langjährigen Freunden **Sven Horst** und **Sandra Thier** danke ich ebenfalls für ihren Rückhalt:
Sandra, nach Wien konnte ich immer kommen, wenn mir in Aachen mal die Decke auf den Kopf gefallen ist. Deine Türe stand immer offen. Dafür bin ich Dir sehr dankbar.
Sam, wir sind in den letzten Jahren durch dick und dünn gegangen. Du hast mir immer Mut und Kraft gegeben, mich unerlässlich unterstützt und immer an mich geglaubt. Ich danke dir für deinen Rückhalt, mein “großer Bruder”.

Ohne meine Familie, meine Eltern **Heike Wiegand**, **Maria Jacobi** und **Rolf Jacobi**, **Bernd Wiegand**, sowie meine Geschwister **Yvonne Wiegand**, **Nathalie Wiegand**, **Martin Wiegand**, **Franz Jacobi** und **Magdalena Jacobi** wäre ich nicht da, wo ich heute bin. Ihr habt mich immer in meinen Entscheidungen unterstützt und mir stets zur Seite gestanden. Dafür bin ich Euch unendlich dankbar.

Hiermit versichere ich, dass ich die vorliegende Arbeit selbststaendig verfasst und nur die angegebenen Quellen und Hilfsmittel benutzt habe.

Soest, den 08 Januar 2018